

الجمهورية الجزائرية الديمقراطية الشعبية

Democratic and Popular Republic of Algeria

وزارة التعليم العالي و البحث العلمي

Ministry of Higher Education and Scientific Research

University of Mohamed Khider, BISKRA  
Faculty of Exact Sciences and Science of  
Nature and Life  
Department: Material sciences  
Ref.: .....



جامعة محمد خيضر بسكرة  
كلية العلوم الدقيقة وعلوم الطبيعة و الحياة  
قسم: علوم المادة  
المرجع: .....

A thesis submitted to obtain the diploma of:  
**DOCTORATE OF SCIENCE IN: PHYSICS**  
**Option: Physics of materials**

**THEME**

**Elaboration and characterization of nanostructuring  
NiO thin films for gas sensing applications**

Presented by:

**Mr. Mebrouk GHOUGALI**

Publicly defended on: 17/10/2019

In front of the jury committee composed of:

Dr. Abdelouahed CHALA	Prof.	Biskra University	President
Dr. Okba BELAHSEN	MCA	Biskra University	Supervisor
Dr. Omar BENTOUILA	MCA	Ouargla University	Examiner
Dr. Mohammed El Hadi ATTIA	MCA	El Oued University	Examiner

# Acknowledgements

First and foremost, I would like to thank ALLAH for his helping me in making this quest of knowledge possible.

Apart from the efforts of me, the success of this work depends largely on the encouragement and support of many others. I take this opportunity to express my gratitude to the people who have been instrumental in the successful completion of this project.

Initially, I would like to acknowledge my heartfelt gratitude to my supervising guide, *Dr. Okba BELAHSEN* His willingness to motivate me contributed tremendously to my research work. Without his insightful guidance and persistent help, this thesis would never have been accomplished. I am thankful for his guidance, enthusiastic encouragement, valuable suggestions and useful critiques he gave me during the course of this research work.

I express my sincere gratitude and appreciation to my reading committee members, *Professor Abdelouahed CHALA* of Biskra University, *Dr. Omar BENTOUILA* of Ouargla University, and *Dr. Mohammed El Hadi ATTIA* of ElOued University for their precious time to read my thesis and for accepting to judge it.

I would like to extend my special thanks to *Dr. yasin Aoun* For helping me especially at the beginning of this research.

Finally, I express my sincere thanks to all my, family, friends, colleagues, and for everyone who helped me accomplish this research work.

**Mebrouk GHOUGALI**

# Dedicace

**I would like to dedicate this work to:**

- My dear Parents;**
- My dear wife and my dear children;**
- My dear sister and my dear brothers;**
- All my relatives and neighbors;**
- All my friends and colleagues.**

**Mebrouk GHOUGALI**

# Contents

# Contents

---

<b>Acknowledgements</b>	
<b>Dedication</b>	
<b>Contents</b>	<b>I</b>
<b>List of figures</b>	<b>VII</b>
<b>List of tables</b>	<b>XIV</b>
<b>General introduction</b>	<b>1</b>

---

## Chapter 1: Thin films deposition and characterization methods

---

1.1 Introduction	9
1.2 Definition of the thin film (layer)	10
1.3 Thin film Deposition Methods	10
1.4 Chemical Spray Pyrolysis Technique (SPT)	11
1.4.1 Processing steps of spray pyrolysis technique	13
1.4.1.1 Precursor atomization	13
1.4.1.2 Aerosol transport of droplets	14
1.4.1.3 Precursor decomposition	15
1.4.2 Influence of the some main SPT parameters on the quality of the deposited films	16
1.4.2.1 Influence of the temperature	16
1.4.2.2 Influence of precursor solution	17
1.4.2.3 Influence of atomizer (nozzle)-to-substrate distance	17
1.4.3 Growth kinetics of thin films	18
1.5 Films characterization techniques	20
1.5.1 Weight difference method	21
1.5.2 X-Ray diffraction technique (XRD)	21
1.5.2.1 Information obtained from the X-ray diffractogram	22
1.5.3 Scanning Electron Microscopy (SEM)	25
1.5.4 Spectroscopy UV- visible	27

---

1.5.4.1 Information obtained from the UV-Visible transmittance spectra	28
1.5.6 Method of four probes	33
1.6 Nickel Oxide (NiO) thin film	34
1.6.1 Crystallographic and structural properties	35
1.6.2 Electronic and electrical properties	37
1.6.3 Optical properties	40
1.6.4 Doping types in the NiO film	40
1.6.4.1 Extrinsic doping (substitutional)	41
1.6.4.2 Intrinsic doping	42
1.6.5 Review of nickel oxide prepared by SPT	42
1.7 Conclusion	44

## Chapter 2: Chemical gas sensors based on (MOS) thin films

2.1 Introduction	46
2.2 Definition of chemical gas sensor	47
2.2.1 Sensing element of the chemical gas sensor	47
2.2.2 The transducer of the chemical gas sensor	48
2.3 Classification of chemical gas sensors	50
2.4 The main parameters of gas sensor	50
2.4.1 Sensitivity	51
2.4.2 Operating temperature	53
2.4.3 Selectivity	54
2.4.4 Stability	55
2.4.5 Response time	55
2.4.6 Recovery time	56
2.4.7 Reproducibility or repeatability	56
2.4.8 Linearity	57
2.4.9 Sensitivity limit or detection limit	57
2.5 Gas sensing mechanism in(MOS) gas sensors	59
2.5.1 Principles of primary physical interaction	59
2.5.2 Basic phenomena of sensing	59
2.5.3 Working principle	59

2.5.4	Parameters influencing the conductive properties of the sensor	65
2.5.4.1	Influence the morphology and porosity of the sensitive layer	65
2.5.4.2	Influence of grain size	66
2.5.4.3	Influence of the temperature	67
2.5.4.4	Influence of doping	68
2.5.4.5	Influence of film thickness	69
2.6	Role of nanostructures in gas sensors	69
2.7	Review researches of nickel oxide gas sensor	70
2.8	Applications and implications of gas sensors	71
2.8.1	Applications of gas sensors	71
2.8.2	Implications of gas sensors	72
2.9	Conclusion	72

## Chapter 3: Elaboration and characterizations of NiO thin films

3.1	Introduction	74
3.2	Elaboration of NiO thin films	74
3.2.1	Experimental montage of a homemade SPT system	74
3.2.2	Thin film deposition parameters	76
3.2.3	Experimental procedure	76
3.2.3.1	Preparation of substrates	76
3.2.3.2	Preparation method of the precursor solution	77
3.2.3.2	Deposition steps of the NiO thin films	78
3.3	Characterizations of prepared NiO thin films	79
3.3.1	Effect of precursor molarity on properties of NiO thin films	79
3.3.1.1	Preparation of samples	79
3.3.1.2	Devices and measurements	80
3.3.1.3	Results and discussions	80
3.3.1.3.a	Structural properties	80
3.3.1.3.b	Optical properties	82
3.3.1.3.c	Electrical properties	86
3.3.2	Effect of annealing on physical properties of NiO thin films	87
3.3.2.1	Preparation of samples	87

3.3.2.2	Devices and measurements	88
3.3.2.3	Results and discussions	88
3.3.2.3.a	Structural properties	88
3.3.2.3.b	Optical properties	89
3.3.2.3.c	Electrical properties	92
3.3.3	Effect of cobalt doping on physical properties of NiO thin films	93
3.3.2.1	Preparation of samples	93
3.3.3.2	Devices and measurements	94
3.3.3.3	Results and discussions	95
3.3.3.3.a	Structural and surface morphological properties	95
3.3.3.3.b	Optical properties	101
3.3.3.3.c	Electrical properties	104
3.3.4	Effect of copper doping on physical properties of NiO thin films	105
3.3.4.1	Preparation of samples	105
3.3.4.2	Devices and measurements	107
3.3.4.3	Results and discussions	107
3.3.4.3.a	Structural and surface morphological properties	107
3.3.4.3.b	Optical properties	114
3.3.4.3.c	Electrical properties	119
3.4	Conclusion	120

## Chapter 4: Gas sensing performance of NiO thin films

4.1	Introduction	122
4.2	Fabrication of gas sensor	123
4.3	Gas sensing measurement	124
4.4	Principle and mechanism of gas sensor	126
4.5	Gas sensing performance	128
4.5.1	Gas sensing performance of undoped NiO thin films	128
4.5.1.1	Operating temperature	128
4.5.1.2	Selectivity	129
4.5.1.3	Sensitivity	130
4.5.1.4	Response and recovery times	131
4.5.1.5	Detection limit	131

---

4.5.1.6 Stability	132
4.5.2 Gas sensing performance of Co-doped NiO thin films	133
4.5.2.1 Operating temperature	133
4.5.2.2 Selectivity	133
4.5.2.3 Sensitivity	134
4.5.2.4 Response and recovery times	135
4.5.2.5 Detection limit	136
4.5.2.6 Stability	137
4.5.3 Gas sensing performance of Cu-doped NiO thin films	138
4.5.3.1 Operating temperature	138
4.5.3.2 Sensitivity	139
4.5.3.3 Selectivity	141
4.5.3.4 Response and recovery times	141
4.5.3.5 Detection limit	141
4.5.2.6 Stability	143
4.6 Comparative study	144
4.6.1 Resistance	144
4.6.2 Response and recovery times	144
4.6.3 Operation temperature	146
4.6.4 Sensitivity	146
4.6.5 Stability	147
4.6.6 General comparison between our results and results of other works	147
4.7 Conclusion	148
<hr/>	
<b>General conclusion and Future Works</b>	151
<b>Appendix</b>	157
<b>References</b>	164

# List of Figures

---

<b>Figures of general introduction</b>		
<b>Figure 1</b>	Number of articles on gas sensors only on the "science direct" reference basis	4
<b>Figure 2</b>	Global chemical gas sensor market, 2009-2016 (Millions of dollars)	4
<b>Figure 3</b>	GDP, Number of dead workers related to industrial gas accidents, and shipped gas detectors in Japan	4
<b>Figure 4</b>	Number of citations with the keyword "nickel oxide" in the 20 years, (ISA knowledge website)	5
<b>Figures of chapter 1</b>		
<b>Figure 1.1</b>	Schematic of thin film deposited on a glass substrate	10
<b>Figure 1.2</b>	Diagram of the some chemical deposition processes	11
<b>Figure 1.3</b>	Schematic sketch of chemical spray pyrolysis process	13
<b>Figure 1.4</b>	Diagram of the different process stages for the aerosol droplet evolution as it approaches the hot substrate for two cases: (a) Constant initial droplet size and increasing substrate temperature, and (b) constant substrate temperature and decreasing initial droplet size	14
<b>Figure 1.5</b>	Schematic depicting different deposition processes that occur as the nozzle-to-substrate distance and deposition temperature change	18
<b>Figure 1.6</b>	Various stages of nucleation and growth of thin films	18
<b>Figure 1.8</b>	Schematic of X-ray diffraction according to Bragg	22
<b>Figure 1.9</b>	Full width at half maximum (FWHM) of an arbitrary peak	23
<b>Figure 1.10</b>	Schematic representation of scanning electron microscope	26
<b>Figure 1.11</b>	Schematic representation of UV-Visible spectrometer	27
<b>Figure 1.12</b>	Presents the transmittance curve of a thin film of metal oxide semiconductor	28
<b>Figure 1.13</b>	Direct (a) and indirect (b) band gap band transition	30
<b>Figure 1.14</b>	Determination of the energy gap $E_g$ by the extrapolation method	31

---

---

	from the variation of $(\alpha hv)^2$ as a function of $hv$ for a thin layer.	
<b>Figure 1.15</b>	Scheme of Urbach tails	32
<b>Figure 1.16</b>	Determination of the Urbach energy from the variation of $\ln(\alpha)$ as a function of $hv$ for a thin layer.	33
<b>Figure 1.17</b>	Schematic diagram of four point probe method	33
<b>Figure 1.18</b>	Ni-O phase diagram	35
<b>Figure 1.19</b>	Crystallographic structure (a) of nickel (b) nickel oxide	36
<b>Figure 1.20</b>	Type of defects inside NiO crystal	37
<b>Figure 1.21</b>	Schematic of NiO energy levels	37
<b>Figure 1.22</b>	Diagram of NiO band structure	39
<b>Figure 1.23</b>	Energy diagram of density of states (pseudo-particle) in NiO	39
<b>Figure 1.24</b>	Band structure diagrams of n-type and p-type doped semiconductor materials: showing promotion of the electrons over a small defect ionization energy level. $E_f$ is the Fermi level (the highest electronically occupied energy level)	41
<b>Figures of chapter 2</b>		
<b>Figure 2.1</b>	Schematic of a chemical gas sensor	47
<b>Figure 2.3</b>	Classification of gas sensing methods	49
<b>Figure 2.3</b>	Schematic response-curve of a chemical gas sensor	52
<b>Figure 2.4</b>	Sensitivity variation as a function of temperature at a specific concentration of gas, for the determination of operating Temperature and $S_{max}$ values	52
<b>Figure 2.5</b>	Gas sensor responses of NiO sensor for different operating temperatures under 3000 ppm of $H_2$ and $CH_4$ and 75 ppm of $NH_3$	53
<b>Figure 2.6</b>	Sensors response for different gases, at the corresponding operating temperatures ( $T_o$ )	53
<b>Figure 2.7</b>	Variation of the values and forms of response as a function of the temperature variation for a different gases having the same concentration	54
<b>Figure 2.8</b>	Selectivity tests of gas sensors based on NiO films, the concentration of $NH_3$ is 50 ppm, and the concentration of other organic gases is higher than 300 ppm	55
<b>Figure 2.9</b>	Long-term stability of sensor signal to ozone gas with different concentrations	56

---

<b>Figure 2.10</b>	Percentage response as a function of (a) ethanol concentration and (b) working temperature, (c) limit of detection as a function of the sensor operating temperature (Polycrystalline NiO nanowires) and (d) selectivity plot at 200°C for 100 ppm of gas	57
<b>Figure 2.11</b>	The phenomenon of: (a) scattering, (b) trapping and (c) sticking	59
<b>Figure 2.12</b>	Leonard-Jones model for physisorption and chemisorption	60
<b>Figure 2.13</b>	Schematic of metal oxide thin film gas sensor	61
<b>Figure 2.14</b>	Gas sensing mechanism of metal oxide semiconductor	63
<b>Figure 2.15</b>	Schematic diagram of the change in sensor resistance for n- and p-type MOS in the presence of the target gas (reducing gas)	63
<b>Figure 2.16</b>	Simple schematic of the band diagram of a semiconductor	64
<b>Figure 2.17</b>	Schematic view of gas sensing reaction in (a) compact layer and (b) porous layer	65
<b>Figure 2.18</b>	Influence of crystallite size on sensitivity ( $R_a/R_g$ ) at 300°C	66
<b>Figure 2.19</b>	Schematic model of the effect of the crystallite size on the sensitivity of metal-oxide gas sensors: (a) $D \gg 2L$ (GB control); (b) $D \geq 2L$ (neck control); (c) $D < 2L$ (grain control)	67
<b>Figure 2.20</b>	Electrical resistance in air as well as gas sensor response 800 ppm $H_2$ and 800 ppm Co as function of film thickness at 350°C	69
<b>Figure 2.21</b>	Studies on n- and p-type oxide semiconductor gas sensors	70
<b>Figures of chapter 3</b>		
<b>Figure 3.1</b>	The homemade SPT system	75
<b>Figure 3.3</b>	Nickel (II) nitrate hexahydrate $[Ni(NO_3)_2 \cdot 6 H_2O]$	77
<b>Figure 3.4</b>	Electronic scale and magnetic stirrer used in our work	77
<b>Figure 3.5</b>	XRD patterns of the deposited NiO thin films on glass substrate at different precursor molarity.	81
<b>Figure 3.6</b>	The variation of crystallite size, mean strain and dislocation Density of NiO thin films as a function of the precursor molarity	82
<b>Figure 3.7</b>	Absorbance spectra of NiO samples for different precursor molarity	83
<b>Figure 3.8</b>	Plot of $(\alpha h\nu)^2$ versus incident photon energy ( $h\nu$ ) of NiO thin films at different precursor molarity	83
<b>Figure 3.9</b>	Transmission spectra of NiO samples for different precursor molarity	84

<b>Figure 3.10</b>	Reflectance profiles of NiO thin film for different precursor molarity	84
<b>Figure 3.11</b>	Plot of $\text{Ln}(\alpha)$ versus incident photon energy ( $h\nu$ ) of NiO thin films at different precursor molarity	85
<b>Figure 3.12</b>	The variation Urbach energy and band gap energy of NiO thin films as a function of the precursor molarity	86
<b>Figure 3.13</b>	The correlation between the crystallite size and thickness with band gap energy of NiO thin films as a function of the precursor molarity	86
<b>Figure 3.14</b>	The variation of the crystallite size, the thickness and the electrical conductivity of NiO thin films as a function of the precursor molarity	87
<b>Figure 3.15</b>	The annealing oven	88
<b>Figure 3.16</b>	XRD patterns of the as-deposited and annealed NiO thin films	89
<b>Figure 3.17</b>	Absorbance spectra of the as-deposited and annealed NiO thin films	90
<b>Figure 3.18</b>	Plot of $(\alpha h\nu)^2$ versus incident photon energy ( $h\nu$ ) of the as-deposited and annealed NiO thin films	91
<b>Figure 3.19</b>	Transmission spectra of the as-deposited and annealed NiO thin films	91
<b>Figure 3.20</b>	Reflectance profiles of the as-deposited and annealed NiO thin films	92
<b>Figure 3.21</b>	Plot of $\text{Ln}(\alpha)$ versus incident photon energy ( $h\nu$ ) of the as-deposited and annealed NiO thin films	92
<b>Figure 3.22</b>	Cobalt (II) chloride hexahydrate	93
<b>Figure 3.23</b>	XRD patterns of the deposited Co-doped NiO thin films on glass substrate at different cobalt percentages	96
<b>Figure 3.24</b>	Texture coefficient values for all peaks of Co-doped NiO thin films at different cobalt percentages	97
<b>Figure 3.25</b>	Variation of the $\Delta(2\theta)$ values as function of Co-doping percentages	97
<b>Figure 3.26</b>	Correlation between crystallite size, mean strains and dislocations density of Co-doped NiO thin films at different cobalt percentages	98

<b>Figure 3.27</b>	Variation of crystallite size and lattice constant of Co-doped NiO thin films at different cobalt percentages	98
<b>Figure 3.28</b>	SEM and Gwyddion program images of Co-doped NiO thin films different cobalt percentages.	100
<b>Figure 3.29</b>	Transmittance of Co-doped NiO thin films at different Co percentages	101
<b>Figure 3.30</b>	Absorbance of Co-doped NiO thin films at different cobalt percentages	102
<b>Figure 3.31</b>	Plot of $(\alpha h\nu)^2$ versus incident photon energy ( $h\nu$ ) of Co-doped NiO thin films at different cobalt percentages.	103
<b>Figure 3.32</b>	Plot of $\ln(\alpha)$ versus incident photon energy ( $h\nu$ ) of Co-doped NiO thin films at different cobalt percentages	103
<b>Figure 3.33</b>	Reverse correlation between optical band gap energy and Urbach energy of Co-doped NiO thin films at different cobalt percentages	104
<b>Figure 3.34</b>	Close correlation between of Co-doped NiO thin films at different cobalt percentages	105
<b>Figure 3.35</b>	Copper (II) chloride dihydrate	106
<b>Figure 3.36</b>	XRD patterns of the deposited Cu-doped NiO thin films on glass substrate at different copper percentages	108
<b>Figure 3.37</b>	Variation of the $\Delta(2\theta)$ values as function of Cu-doping percentages	109
<b>Figure 3.38</b>	Texture coefficient values for all peaks of Cu-doped NiO thin films at different copper percentages	110
<b>Figure 3.39</b>	Determination of the average crystallite size ( $D$ ) and the microstrain ( $\epsilon_\mu$ ) by Williamson-Hall plot method	111
<b>Figure 3.40</b>	Comparison between the values of the average crystalline size ( $D$ ) determined by the Williamson Hall plot and the Shearer method	112
<b>Figure 3.41</b>	Comparison between the values of the Microstrain ( $\epsilon_\mu$ ) determined by Williamson-Hall plot method and eq.(1.8).	112
<b>Figure 3.42</b>	Correlation between structural parameters of Cu-doped NiO thin films at different copper percentages	113
<b>Figure 3.43</b>	SEM and Gwyddion program images of Cu-doped NiO thin film with 6 at.% at different scales.	114

<b>Figure 3.44</b>	Transmission spectra of Cu-doped NiO thin films at different copper percentages	115
<b>Figure 3.45</b>	Absorbance spectra of Cu-doped NiO thin films at different copper percentages	116
<b>Figure 3.46</b>	Plot of $(\alpha h\nu)^2$ versus incident photon energy ( $h\nu$ ) of Cu-doped NiO thin films at different copper percentages	116
<b>Figure 3.47</b>	Plot of $\ln(\alpha)$ versus incident photon energy ( $h\nu$ ) of Cu-doped NiO thin films at different copper percentages	118
<b>Figure 3.48</b>	Variation of microstrain, dislocation density and Urbach energy of Cu-doped NiO thin films at different copper percentages	118
<b>Figure 3.49</b>	Variation of optical band gap energy and Urbach energy of Cu-doped NiO thin films at different copper percentages	118
<b>Figure 3.50</b>	Variation of electrical conductivity, optical band gap energy and crystallite size of Cu-doped NiO thin films at different copper percentages	119
<b>Figures of chapter 4</b>		
<b>Figure 4.1</b>	The most important components of the homemade gas sensor	123
<b>Figure 4.2</b>	Schematic diagram of sensing element with two silver strips used as electrodes	124
<b>Figure 4.3</b>	Voltage-current Plot (in air) of undoped and Co and Cu-doped NiO thin films at different operating temperature	125
<b>Figure 4.4</b>	Response curves of undoped NiO based sensor towards methanol, ethanol and acetone (1000 ppm) at different operating temperatures	129
<b>Figure 4.5</b>	Response of undoped NiO based sensor towards 1000 ppm of methanol, ethanol and acetone at the optimum operating temperatures	131
<b>Figure 4.6</b>	Variation of the sensitivity of undoped NiO based sensor as function of concentration of methanol, ethanol and acetone vapors	132
<b>Figure 4.7</b>	Stability characteristics of undoped NiO based sensor	133
<b>Figure 4.8</b>	Sensor response curves of Co-doped NiO based sensors towards methanol, ethanol and acetone (1000 ppm) at different operating temperatures	132
<b>Figure 4.9</b>	Response of Co-doped NiO based sensors towards 1000 ppm of	133

---

	ethanol, acetone and methanol at the optimum operating temperatures	
<b>Figure 4.10</b>	Variation of the sensitivity of the Co-doped NiO based sensors as function of concentration of methanol, ethanol and acetone vapors	137
<b>Figure 4.11</b>	Stability characteristics of Co-doped NiO based sensors	138
<b>Figure 4.12</b>	Sensor response curves of Cu-doped NiO based sensors towards methanol, ethanol and acetone (1000 ppm) at different operating temperatures	139
<b>Figure 4.13</b>	Responses of Cu-doped NiO based sensors towards 1000 ppm of ethanol, acetone and methanol at the optimum operating temperatures	140
<b>Figure 4.14</b>	Variation of the sensitivity of Cu-doped NiO based sensors as function of concentration of vapors	142
<b>Figure 4.15</b>	Stability characteristics of Cu-doped NiO based sensors	143
<b>Figure 4.16</b>	Variation of resistance (in air) of undoped and Co and Cu-doped NiO based sensors at different temperature	144
<b>Figure 4.17</b>	Comparison between undoped and Co and Cu-doped NiO based sensors in terms of different response times values obtained	145
<b>Figure 4.18</b>	Comparison between undoped and Co and Cu-doped NiO based sensors in terms of different recovery times values obtained	145
<b>Figure 4.19</b>	Comparison between undoped and Co and Cu-doped NiO based sensors in terms of different optimum operating temperature values obtained	146
<b>Figure 4.20</b>	Comparison between undoped and Co and Cu-doped NiO based sensors in terms of sensitivity values obtained towards 1000 ppm from target gases	147

---

# List of Tables

---

<b>Tables of chapter 1</b>		
<b>Table 1.1</b>	General properties of nickel oxide	34
<b>Table 1.2</b>	Crystallographic properties of nickel oxide	36
<b>Table 1.3</b>	Summary of major reviewed parameters for NiO thin films using spray pyrolysis technique	43
<b>Tables of chapter 2</b>		
<b>Table 2.1</b>	Classification according to the response of sensing element	48
<b>Table 2.4</b>	Relationship between chemical recognition and transduction mode	48
<b>Table 2.3</b>	The operating principle of a various families of chemical sensors	50
<b>Table 2.4</b>	Some factors affecting the parameters of the chemical gas sensor	58
<b>Table 2.5</b>	Comparative study of the characteristics of the large families of sensors	58
<b>Table 2.6</b>	Classification of metal oxides based on the conductivity type	64
<b>Table 2.7</b>	Literature review of different elaborated NiO thin films which are used for gas sensor application	71
<b>Tables of chapter 3</b>		
<b>Table 3.1</b>	The optimum values range of some NiO thin film deposition parameters	76
<b>Table 3.2</b>	Some physic-chemical properties of nickel nitrates hexahydrate	78
<b>Table 3.3</b>	Structural parameters of NiO thin film at different precursor molarity.	81
<b>Table 3.4</b>	Optical and electrical parameters of NiO thin film at different precursor molarity.	83
<b>Table 3.5</b>	Structural parameters of as-deposited and annealed samples of NiO thin film at 0.15 mol/L of precursor molarity	89
<b>Table 3.6</b>	Optical and electrical parameters of as-deposited and annealed NiO thin film	91
<b>Table 3.7</b>	Some physic-chemical properties of cobalt (II) chloride hexahydrate	94
<b>Table 3.8</b>	X-ray diffraction data of Co-doped NiO thin films at different	96

---

---

	cobalt percentages.	
<b>Table 3.9</b>	Structural parameters of Co-doped NiO thin films at different cobalt percentages.	97
<b>Table 3.10</b>	Optical and electrical parameters of Co-doped NiO thin films at different cobalt percentages	104
<b>Table 3.11</b>	Some physic-chemical properties of copper (II) chloride dihydrate.	106
<b>Table 3.12</b>	X-ray diffraction data of Cu-doped NiO thin films at different copper percentages.	109
<b>Table 3.13</b>	Structural parameters of Cu-doped NiO thin films at different copper percentages	111
<b>Table 3.14</b>	Optical and electrical parameters of Cu-doped NiO thin films at different copper percentages	117
<b>Tables of chapter 4</b>		
<b>Table 4.1</b>	Some chemical properties of the methanol, ethanol and acetone	124
<b>Table 4.2</b>	Gas sensing performance of undoped NiO thin film towards methanol, ethanol and acetone vapors	130
<b>Table 4.3</b>	Gas sensing performance of Co-doped NiO based sensors towards methanol, ethanol and acetone vapors	134
<b>Table 4.4</b>	Gas sensing performance of Cu-doped NiO based sensor towards methanol, ethanol and acetone vapors	140
<b>Table 4.5</b>	Results of some previous works	146
<b>Tables of appendix</b>		
<b>Table A.1</b>	JCPDS cards of NiO	157
<b>Table A.2</b>	Gas exposure limits for some toxic and flammable gases	162

---

# General introduction

# General introduction

## A. Prelude

The ever increasing progress of technology for the human needs, have benefited humanity in all the fields. This progress, which has benefits, also involves serious issues related to our environment. All the industry somehow influences our environment. From the industrial solid waste to the emission of different toxic and hazardous gases such as CO [1], H<sub>2</sub>[2, 3], CH<sub>4</sub> [4], NH<sub>3</sub> [5, 6], Volatile Organic Compounds (VOCs) [7], NO<sub>2</sub> [8, 9], sulfur compounds released from industries and also from automobiles like H<sub>2</sub>S [10, 11], and the chemical vapors in the laboratories such as ethanol, methanol, and acetone it can be polluting the air of our laboratories [12,13]. Neglecting the facts related to environmental issues is causing serious problems. Exposure of these hazardous gases to human body causes different diseases, shortness of breath, nausea, swelling of tissues in the throat, and it can lead to death. Another key topic associated to sensors is related to the so called comfort applications, for example in air monitoring inside buildings or cars, where the target gas may not be highly hazardous or toxic, but its detection and elimination from the environment can improve the air quality. There is an urgent need to find the solutions that comply with the requirements needed to the environmental security [14].

Ability to detect these above mentioned gases in industry and homeland security is important. Recent developments in sensing technology have provided simple yet efficient way to deal with these environmental issues [15]. It is easy to understand that highly sensitive and possibly selective devices are mandatory for these applications; moreover an ideal sensor should also be as much miniaturized as possible, stable in a wide range of temperatures and environments, cheap, user-friendly, long-lasting and it should also allow in situ measurements with the operator being at safety distance from the hazardous source.

A device able to convert a target chemical or physical variation to be monitored into an easily processable signal can be defined as a sensor, the sensing element has to fulfill essentially two different tasks: first, it has to interact with the target gas through various mechanisms like surface adsorption, charge transfer, ionic exchange (receptor task), then this interaction has to be transformed into an easily processable signal, like for example a change in electrical conductivity or in optical transmission

(transducer task). A lot of research and development is done to design small and affordable gas sensors which possess high sensitivity, selectivity and stability with respect to a given application.

Although extensive research and development for over 40 years (See figure 1), the chemical sensors (in the broad sense) and gas sensors in particular are still in full development until today. On the industrial side, the global market for chemical and biochemical sensors is experiencing the strongest growth since the end of the 2000s as shown in figure 2 [16]. Japan has a global market share of approximately 20%. Japanese trends in GDP, the number of workers killed by gas accidents, the number of industrial gas alarms and gas detectors shipped are shown in figure 3.

The technology favors the development of sensors with ever-decreasing size and power consumption. However, decreasing the size of the active area may lead to a decrease in sensitivity. Therefore, nanostructuring of the active layers has been the active and competitive area of research over the last few years. In particular, nanoscience and nanotechnology are enabling the growth of well-known gas-sensitive materials with better controlled morphology, crystalline size and chemical composition. Such materials nanowires [17- 19], nanotubes [19, 20], nanorods [21, 22], nanoparticles [23- 25], nanocomposite films [26, 27] offer not only significantly enlarged surface to volume ratio, thus better sensitivity, but also many new and extraordinary properties [14]. Semiconducting metal oxides possess a broad range of chemical and physical properties that are often highly sensitive to changes in their chemical environment. Many Researchers have studied metal oxide thin films as electronic materials due to their semiconducting behavior, structural simplicity and low cost. In the field of gas chemical sensing, it has been known that the electrical conductivity of semiconductors varies with the chemical composition of the gas surrounding it. Semiconductor oxide-based gas sensors are classified according to the direction of the conductance change due to the exposure to reducing gases as n-type (conductance increases, e.g,  $\text{In}_2\text{O}_3$  [28],  $\text{V}_2\text{O}_5$  [29],  $\text{WO}_3$  [30],  $\text{ZnO}$  [31- 33], and  $\text{SnO}_2$  [34, 35]) or to oxidising gases as p-type (conductance decreases, e.g.,  $\text{NiO}$  [36],  $\text{SnO}$  [37],  $\text{Cu}_2\text{O}$  [38, 39],  $\text{CuO}$  [40]). This classification is related to the (surface) conductivity type of the oxides, which is determined by the nature of the dominant charge carriers at the surface, that is electrons or holes. A chemical gas sensor operates of two functions: the first is to identify the nature of chemical gas on the surfaces of semiconductor particles; the second is to convert the chemical signal on the surface of the semiconductor through the micro or nanostructure of the sensing semiconductor material into the measurable output signals like resistance, voltage, dielectric constant, mass of the sensing element due to adsorption of gas etc.

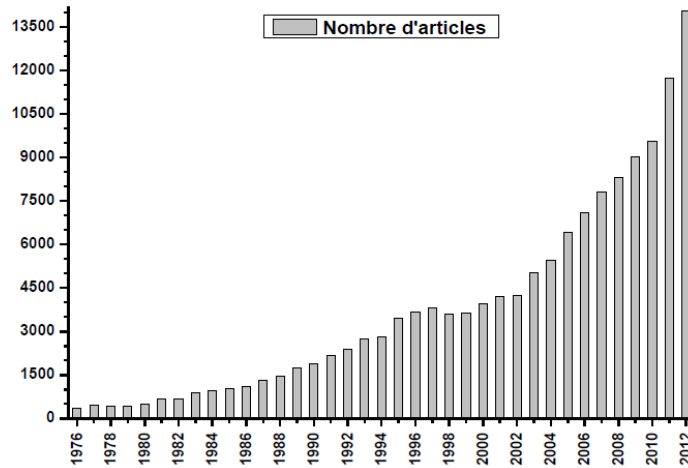


Figure 1: Number of articles on gas sensors only on the "science direct" reference basis [16].

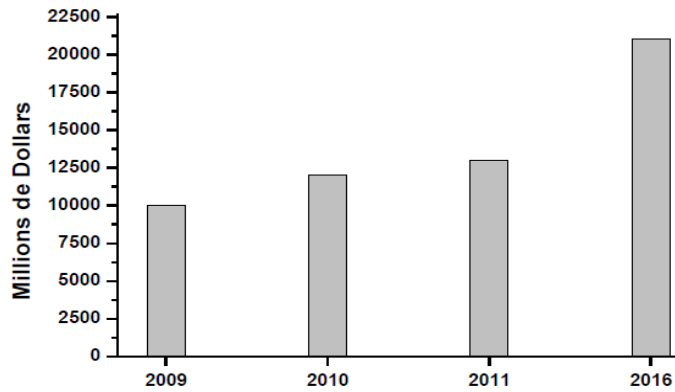


Figure 2: Global chemical gas sensor market, 2009-2016 (Millions of dollars) [16].

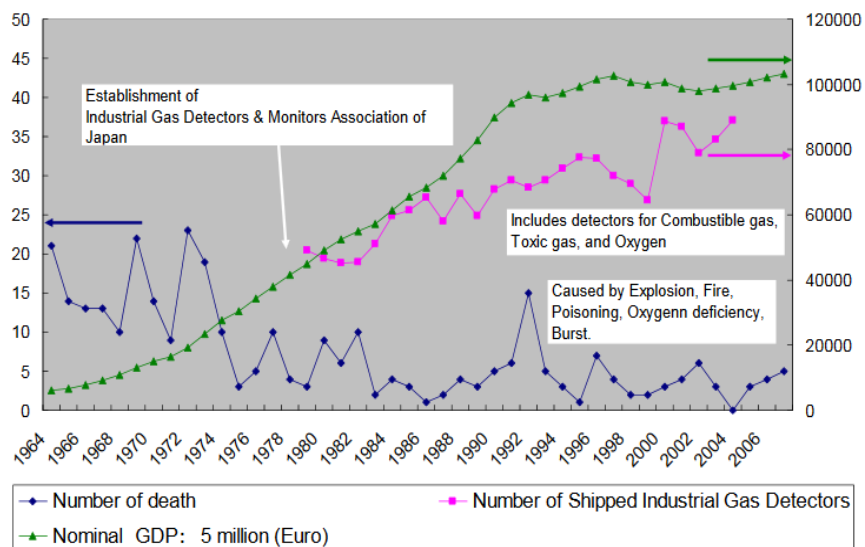
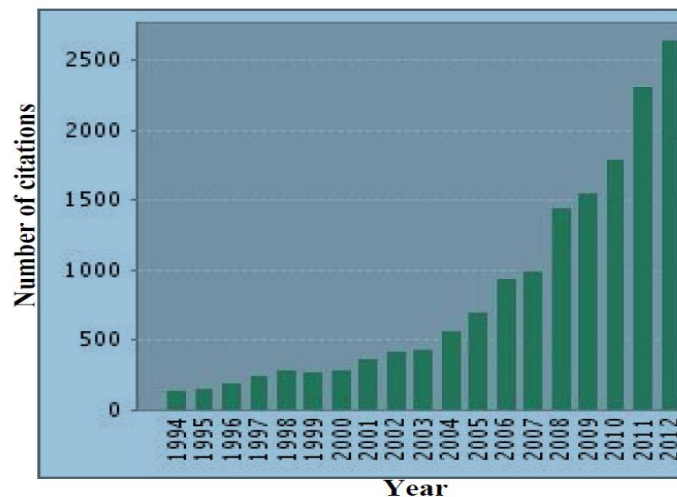


Figure 3: GDP, Number of dead workers related to industrial gas accidents, and shipped gas detectors in Japan [17].

In order to improve the sensitization characteristics of the semiconducting Metal oxides of gas sensors, several methods can be used, the metal doping is the most important like Co [42], Cu [43], Pd [44], Al [45], Sn [46], In [47] etc., Where modifying the Fermi level position as appropriate. The addition of different metallic species to semiconductor gas sensing materials improves the gas detection of a determinate gas in most of the cases. Metal oxides semiconductors (MOS) at elevated temperature show change in conductivity according to the composition of the gas to which they are exposed. The effects are dependent upon the nature of the oxide material, its microstructure and the temperature. It has been reported that by using an appropriate synthesis technique, semiconducting metal oxides with highly nanostructure can be obtained which is an important requisite for gas sensing applications.

There are various published research of semiconducting metal oxides of gas sensors which operate in the temperature range (200–500°C) [48, 49]. And now lot of efforts are undergoing to utilize metal oxide as gas sensor at relatively low operating temperature. Nickel oxide is considered among the most interesting transition metal oxide materials, it have been the subject of extensive experimental and theoretical investigations for the past several years (Figure 4).



**Figure 4:** Number of citations with the keyword “nickel oxide” in the 20 years, (ISA knowledge website) [50].

Nickel oxide (NiO) exhibits wide features in its the optical, magnetic and electrical properties behavior related to electronic structure. Which forms the basis for the enormous range of applications. Such as supercapacitor [50], electrochromic device [51], photo-catalytic [52] and gas sensor [53, 54]. It is an anti-ferromagnetic semiconductor oxide. It can be prepared in the form of a conducting thin films by various

techniques that involve: electron beam evaporation [55], magnetron sputtering [56], chemical deposition [57], sol-gel [58] and spray pyrolysis technique (SPT) [59, 60].

In our present work, will be chose the spray pyrolysis method to prepare thin films of nickel oxide on glass samples because it is simple and low cost. Then will be studied some of the structural, optical and electrical properties of these films for use it in gas sensor applications.

## B. Research motivation

In recent years nanotechnology has developed into one of the most prominent and exciting forefront fields in Physics, chemistry, engineering and biology. Nanoparticles and nanostructures fabricated with the use of nanotechnology present new properties and characteristics that can be utilized in a wide variety of applications. It's impacts a broad range of fields such as engineering, medicine, energy, environment, defense, security, electronics and materials.

Nanotechnology is the understanding and control of matter at the nanoscale, at dimensions between approximately 1 and 100 nanometers. Nanotechnologies aim to study, manufacture and manipulate matter on the scale of molecules or atoms. It is therefore very promising to use these technological developments, where unique phenomena enable novel applications. The nanoscopic scale is a lower bound to the mesoscopic scale for most solids. For technical purposes, the nanoscopic scale is the size at which materials properties play a significant role for the detection and monitoring of poisonous hazardous gas and vapors. Scientific community and researchers around the globe thus are trying to develop novel chemical sensors with superior performances. According to this context, there were two main motives for this research:

- The first is the desire to enter the experimental world of nanotechnology, to see the microscopic changes that occur in the material and how we can exploit them scientifically in different applications.
- The second is the desire to contribute to the development of gas sensors, for public health safety, from the effects of poisonous and hazardous gases and vapors.

## C. Research aims and objectives

This study aims to achieve the following objectives:

1. installation of a homemade device, allows the preparation of thin films of metal oxides, by method of chemical spray pyrolysis.

2. Preparation of nanostructuring thin films of nickel oxide, and study their structural, optical and electrical properties.
3. Installation of a homemade device, acts as a chemical sensor depends on the changes of electrical resistance. Then, use this device to study the allergic properties of nickel oxide films prepared, for some toxic chemical vapors.

## D. Structure of the dissertation

This thesis consists of four chapters organized as follows.

It was starting with a general introduction.

In the first chapter, we will define the thin film. Then we will explain some preparation methods of films and we will focus on the method of spraying pyrolysis, followed by an explanation of the devices used in the study of the properties of films prepared. At the end of the chapter, we will present a bibliographic study of nickel oxide, which illustrates the structural, optical and electrical properties.

The second chapter will contain some basic definitions and concepts of chemical gas sensors based on metal oxides. We will define the gas sensor and explained its characteristics, types and its sensing mechanism. At the end of the chapter we will provide a review of the gas sensors based on nickel oxide.

The third chapter will provide a detailed explanation of the method of preparation of the films undoped and Co and Cu doped NiO thin films, followed by a study of the structural, electrical and optical characteristics of these films.

In the fourth chapter, we will be interested in applying these films in the field of gas sensing, where we used the samples prepared in advance in the sensing of some chemical vapors such as ethanol, methanol and acetone.

Finally, there will be a conclusion present the synthesis of main results obtained, concluding remarks and suggestions for future works.

# Chapter one

1/4

Thin films deposition  
and characterization  
methods

# CHAPTER 1

## Thin films deposition and characterization methods

### 1.1 Introduction

Metal oxides are an important class of materials from both scientific and technological point of view. They found huge interesting applications in different technological fields. Oxide semiconductors are gaining interest as new materials that may challenge the supremacy of silicon. Metal oxide thin films are known for many years ago due to the industrial interest on their unique properties [61]. The physicochemical properties of metal oxide thin layers are closely related to preparation processes and operating conditions. Indeed, it is possible to obtain thin films having an amorphous or crystalline structure. Thereafter, films structural, electrical and optical properties can be tailored by varying the condition and the deposition process. Control of film properties is therefore key parameters of metal oxide films preparation to be used in wide applications such as: fabrication of microelectronic circuits, sensors, piezoelectric devices, fuel cells, coatings against corrosion, and as catalysts.

Earlier, research in the field has been devoted to bulk metal oxides before interest in their thin films aspect. the most important of these oxides are zinc oxide (ZnO), tin oxide (SnO<sub>2</sub>), titan oxide (TiO<sub>2</sub>), tungsten oxide (WO<sub>3</sub>), cuprous oxide (Cu<sub>2</sub>O) and cadmium oxide (CdO). Recently, several metallic oxide thin films have emerged such as vanadium oxide (V<sub>2</sub>O<sub>5</sub>), cupric oxide (CuO), molybdenum oxide (MoO<sub>2</sub>) and nickel oxide (NiO). Among these oxides, nickel oxide thin films exhibit an interesting combination of multifunctional proprieties including: optical, semiconducting, magnetic, electronic, and optoelectronic. NiO thin films find many applications in electronic devices such as: gas sensors, solar cells and catalysts, etc.

### 1.2 Definition of the thin film (layer)

It is possible to define a thin film of a material that is an element of this material so that its thickness is greatly reduced, which is expressed with nanometers. (Layer

quasi two-dimensionality). The small distance between the two boundary surfaces gives a disturbance of the physical, chemical and mechanical properties (Figure 1.1).

The essential difference between the material in its bulk state and its thin state is related to the fact that the role of the boundaries in the properties is usually neglected in the bulk state of materials, but in the thin state, on the contrary, the effects related to the boundaries are preponderant and very important [62]. It is quite obvious that the lower the thickness, the greater the bidimensionality effect. Conversely, when the thickness of a thin layer exceeds a certain threshold, the effect of thickness will become minimal and the material will return to the well-known properties of the solid state of material [63]. The second essential characteristic of a thin layer is that, whatever the procedure used for its manufacture, a thin layer is always integral with a substrate on which it is built (even if it sometimes happens that one separates the thin film of said substrate). Consequently, it will be imperative to take into account this major fact in the design, namely that the substrate has a very strong influence on the structural properties of the layer deposited therein. Thus a thin layer of the same material, of the same thickness may have substantially different physical properties depending on whether it will be deposited on an amorphous insulating substrate such as glass, or a monocrystalline silicon substrate, for example. The interest of thin film is to give particular properties to the surface of the substrate.

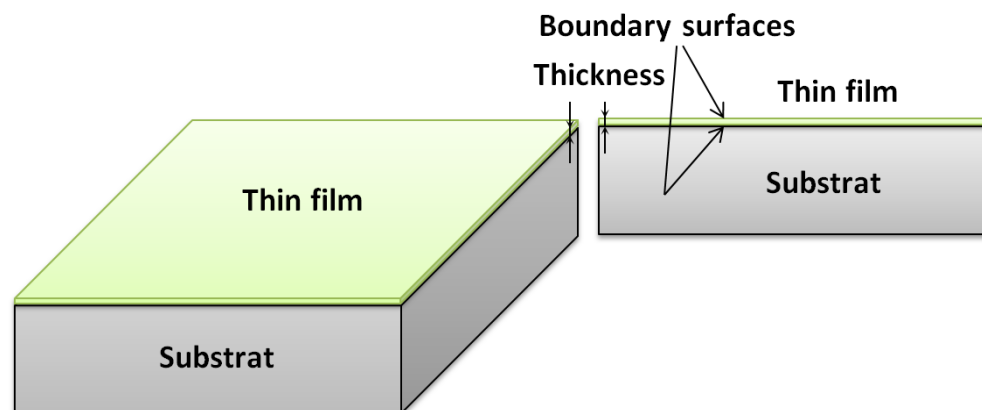
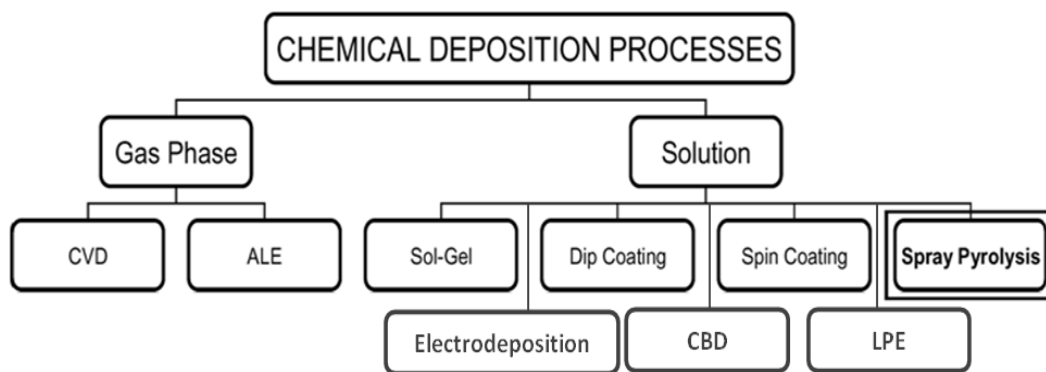


Figure 1.1: Schematic of thin film deposited on a glass substrate.

### 1.3 Thin film deposition methods

Over the years, various materials have been synthesized in the form of thin films due to their prospective technological significance and scientific interest in their properties. They have very extensive range of applications and extend from nanostructures

to coatings of several square meters on window glasses. Based on the nature of the deposition process, the techniques employed for thin film deposition can be classified into two groups, namely, physical and chemical deposition processes. The physical methods include physical vapor deposition (PVD), laser ablation [64], molecular beam epitaxy [65] and magnetron sputtering [66, 67]. While the chemical methods comprise gas phase and liquid phase deposition methods (Figure 1.2). The gas phase methods are chemical vapor deposition (CVD) and atomic layer epitaxy (ALE) [68], while spray pyrolysis [69, 70], sol-gel [71], electrodeposition [72], chemical bath deposition (CBD) [73], liquid phase epitaxy (LPE) [74], spin-coating [75] and dip-coating [76] are liquid phase methods .



**Figure 1.2:** Diagram of the some chemical deposition processes.

## 1.4 Chemical Spray Pyrolysis Technique (SPT)

Spray pyrolysis processing technique is most popular today because of its applicability to produce variety of conducting and semiconducting materials [77]. The basic principle involved in spray pyrolysis technique (SPT) shown in Figure 1.3.

Figure 1.3 shows the schematic representation of a SPT set-up which is generally used. SPT set-up consists of an atomizer, precursor solution, substrate heater, temperature controller, air compressor or other source of carrier gas. Thin film deposition, using the SPT, involves spraying a metal salt solution (precursor solution) onto a pre-heated substrate. Droplets impact on the substrate surface, spread into a disk shaped structure, and undergo thermal decomposition. The shape and size of the disk depends on the momentum and volume of the droplet, as well as the substrate temperature. Consequently, the film is usually composed of overlapping disks of metal salt being converted into oxides on the heated substrate. The surface of the substrate must be sufficiently hot to initiate chemical reaction between the precursors in the droplet so-

lution. Specifically, the droplet must still contain enough reactants in solution after reaching the substrate [78].

The spray pyrolysis is useful for the production of thin films of simple oxides and mixed oxides, from these, thin films the metal oxide materials prepared by spray pyrolysis technique have matching properties for wide variety of potential applications. Spray pyrolysis has been developed extensively by Chamberlin and coworkers [79]. After that, many research articles and review articles [80, 81] related to spray pyrolysis processing and the range of thin films deposited by this method for various applications have appeared in the literature. Recently a comprehensive review of all possible thin film materials that could be deposited by spray pyrolysis technique for various applications has been published [82].

In our work chemical spray pyrolysis technique has been chosen for preparation of NiO nanostructured layers because has a number of advantages [83, 84].

1. Spray pyrolysis is a simple and low cost technique for the preparation of semiconductor thin films.
2. It has capability to produce large area, high quality adherent films of uniform thickness.
3. Spray pyrolysis technique does not require high quality targets or substrates nor does it require vacuum at any stage, which is a great advantage if the technique is to be scaled up for industrial applications.
4. The deposition rate and the thickness of the films can be easily controlled over a wide range by changing the spray parameters.
5. A major advantage of this method is operating at moderate temperature (200–600°C) and can produce films on less robust materials.
6. Not like high-powered strategies like frequency electron tube sputtering (RFMS), it doesn't cause native heating that may be prejudicial for materials to be deposited. There are nearly no restrictions on substrate material, dimension or its surface profile.
7. By dynamic composition of the spray solution throughout the spray method, it is often used to create bedded films and films having composition gradients throughout the thickness.
8. It's believed that reliable elementary kinetic information are additional seemingly to be obtained on significantly well characterized film surfaces, provided the films area unit quiet compact, uniform which no aspect effects from the substrate occur. SPT offers such a chance.

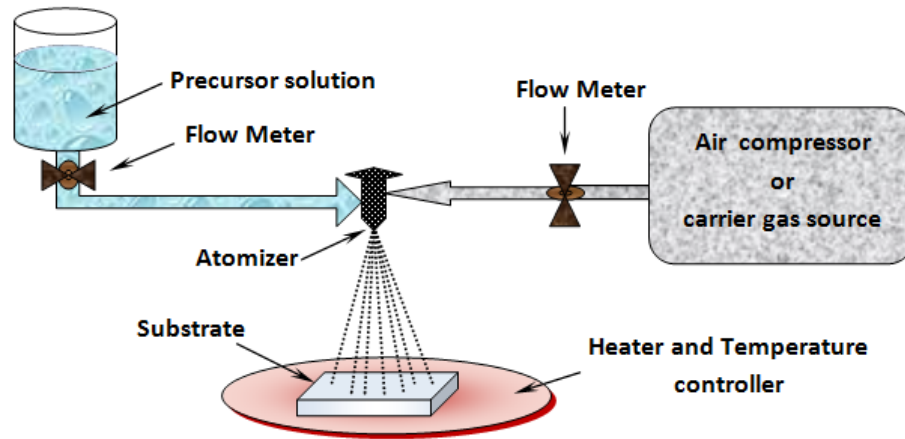


Figure 1.3: Schematic sketch of chemical spray pyrolysis process.

### 1.4.1 Processing steps of spray pyrolysis technique

Spray pyrolysis involves many processes occurring either simultaneously or sequentially. The most important of these steps are three processing steps that are presented and analyzed as follows:

1. Atomization of the precursor solution;
2. Aerosol transport of the droplet;
3. Decomposition of the precursor to initiate film growth;

#### 1.4.1.1 Precursor atomization

The atomization procedure is the first step in the spray pyrolysis deposition system. The idea is to generate droplets from a spray solution and send them, with some initial velocity, towards the substrate surface. Spray pyrolysis normally uses air blast, ultrasonic, or electrostatic techniques [84]. The atomizers differ in resulting droplet size, rate of atomization, and the initial velocity of the droplets. It has been shown that the size of the generated droplet is not related to any fluid property of the precursor solution and depends solely on the fluid charge density level. The mass of a droplet  $m$ , assuming a spherical shape depends on its density  $\rho_q$ , it is given the following relationship [85].

$$m = \frac{4\pi}{3} \rho_q r^3 \quad (1.1)$$

where  $r$  is the droplet radius. The initial leaving velocity of the droplet is an important parameter as it determines the rate at which the droplets reach the substrate surface, the heating rate of the droplet, and the amount of time the droplet remains in transport.

Due to its ease of production, a pressure, or air blast, atomizer uses high speed air in order to generate an aerosol from a precursor solution. Increasing the air pressure causes a direct decrease in the generated mean droplet diameter. Inversely, increasing the liquid pressure causes a direct increase in the mean droplet diameter [84].

### 1.4.1.2 Aerosol transport of droplets

After the droplet leaves the atomizer, it travels through the ambient with an initial velocity determined by the atomizer. In the aerosol form, the droplets are transported with the aim of as many droplets as possible reaching the surface. As the droplets move through the ambient, they experience physical and chemical changes depicted in Figure 1.4. As the droplet traverses the ambient, there are four forces simultaneously acting on it, describing its path. Those forces are gravitational [86], electrical [87], thermophoretic [88] and the Stokes force [89]. As shown in Figure 1.4, the droplets experience evaporation during their flight, which affects the influence of the forces on their trajectory. Some experimental results indicate that solid particles could form, when the reactor temperature is low, when the precursor solution concentration is high, and when the flow rate of the carrier gas is low.

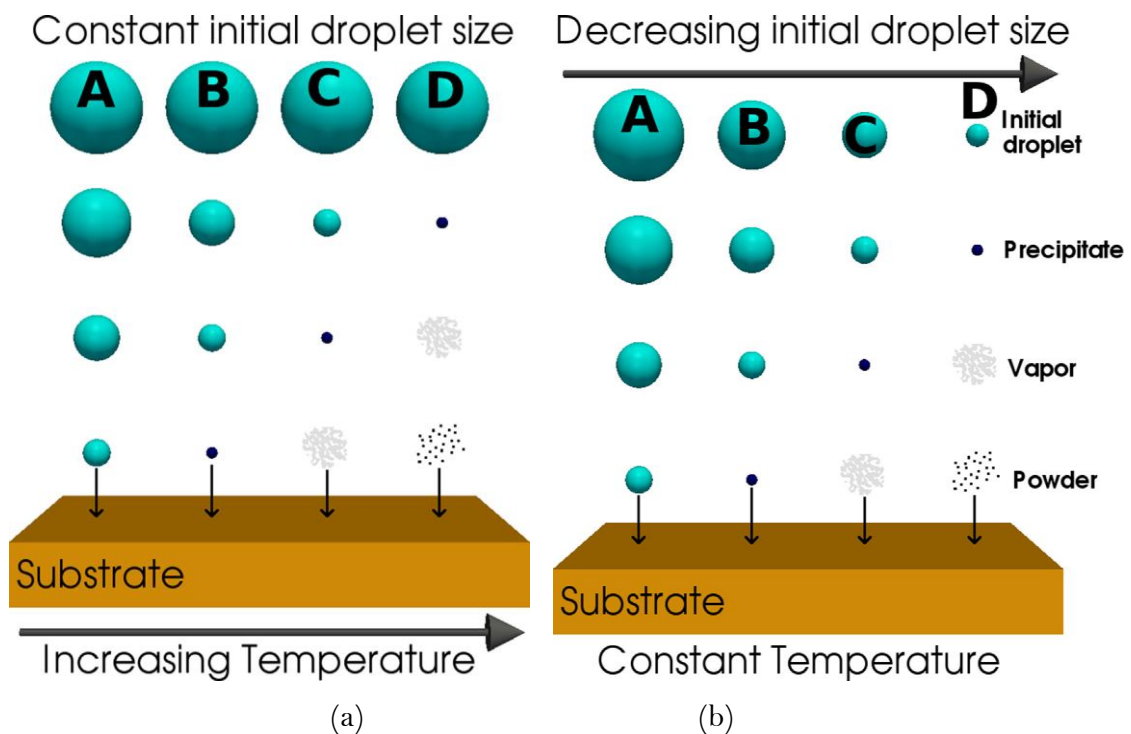


**Figure 1.4:** Diagram of the different process stages for the aerosol droplet evolution as it approaches the hot substrate for two cases: (a) Constant initial droplet size and increasing substrate temperature, and (b) constant substrate temperature and decreasing initial droplet size [89-90].

### 1.4.1.3 Precursor decomposition

The precursor, as it moves through the heated ambient undergoes various changes, which are shown in figure 1.4 and figure 1.5. Evaporation, precipitate formation, and vaporization all occur depending on the droplet size, ambient temperature and atomizer-to-substrate distance. Figure 2.4 and Figure 2.5 shows the four physical forms in which the droplet may interact with the substrate surface. Although all processes occur during deposition, process C is the optimal process for obtaining dense, homogeneous films, like the CVD deposition is desired to yield a dense high quality film [89, 90].

**a. Process A: ( low temperature/large initial droplet)**

When the large droplets approach a heated substrate and the temperature is not sufficiently high to fully evaporate the solution, they will impact with the substrate and decompose. Upon contact, the droplet is entirely vaporized and a dry precipitate is left behind. Because droplet vaporization requires some heat, the substrate temperature is slightly decreased at the impact point, adversely affecting the reaction kinetics. This process has a weak sticking probability [91].

**b. Process B: (Low intermediate temperature/Large medium droplet size)**

When Large medium droplet sizes are initially formed, some evaporation occurs. Just as the droplet reaches the surface, however, it forms a precipitate as an amorphous salt and a dry precipitate hits the surface, where decomposition occurs. Some particles evaporate and condense into gaps between particles, where surface reaction occurs. However, this process has a medium sticking probability [89, 92].

**c. Process C: (A medium temperature/A medium droplet size)**

When the processing environment causes droplets to evaporate prior to reaching the substrate vicinity, a precipitate will form early. As the precipitate reaches the immediate vicinity of the substrate, it is converted into a vapor state and it undergoes a heterogeneous reaction through the following steps [78, 84, 89]:

- 1- Reactant molecules diffuse to the surface.
- 2- Adsorption of some molecules at the surface.
- 3- Surface diffusion and a chemical reaction, incorporating the reactant into the lattice.
- 4- Desorption and diffusion of the product molecules from the surface.

This is a classical CVD reaction, which results in a high quality film deposition and a high sticking probability.

**d. Process D: ( A high temperature/A small droplet size)**

When small initial droplets are formed, or the temperature is high enough, the droplet quickly forms a precipitate. As the precipitate approaches the substrate, it is vaporized and a chemical reaction subsequently occurs in the vapor phase. This homogeneous reaction leads to the condensation of molecules into crystallites in the form of a powder precipitate. The powder falls to the substrate surface, but without a deposition reaction [92].

## **1.4.2 Influence of the some main SPT parameters on the quality of the deposited films**

This section deals with the influence of the some main SPT parameters on properties of the deposited films.

### **1.4.2.1 Influence of the temperature**

The deposition temperature is involved in all mentioned processes, except in the aerosol generation. Consequently, the substrate surface temperature is the main parameter that determines the shape and properties of the film [69]. By increasing the temperature, the film morphology can change from a cracked to a porous microstructure. In many studies the deposition temperature was reported indeed as the most important spray pyrolysis parameter. The properties of deposited films can be varied and thus controlled by changing the deposition temperature; it influences structural, optical and electrical properties of thin films [93].

The influence of substrate temperature on the structural, optical and electrical properties of ZnO films prepared by the spray pyrolysis method using aqueous solution of zinc acetate has been investigated by Afify et al [94]. The films are polycrystalline and X-ray diffraction measurements show a strong preferred orientation along the (002) plane which is strongly dependent on the substrate temperature. Optical absorption spectra, show high transparency of the film (90–95% transmission) in the visible range, with a sharp absorption edge around 375 nm wavelength of light which closely corresponds to the intrinsic band gap of ZnO (3.3 eV). ZnO films with the lowest resis-

tivity, which is due to the increased mobility resulting from the improvement of the crystallinity of the films, can be prepared at a substrate temperature of 490°C.

#### 1.4.2.2 Influence of precursor solution

The precursor solution is the second important process variable. The solvent, salt type, salt concentration and additives affect the physical and chemical properties of the precursor solution. Thus, many properties of the deposited film can be changed by changing the composition of the precursor solution. Such as film thickness, morphology, chemical structure, and electrical and optical properties [89]. Lehraki et al. [95] they deposited thin films of zinc oxide (ZnO) by pyrolysis technique using different liquids. Three starting solutions salts namely: zinc acetate, zinc chloride and zinc nitrate were used. The properties of these solutions and their influence upon ZnO films growth rate are investigated. The obtained results indicate that the dissociation energy of the starting solution plays an important role on films growth rate. A linear relationship between the solution dissociation energy and the growth rate activation energy was found. However, the surface tension of the used solution controls the droplet shape impact. Both solution surface tension and dissociation enthalpy alter the microstructure of the formed film. Films deposited with zinc acetate are characterized by a smooth surface, dense network and high transparency, while films deposited with zinc chloride have a better crystallinity and low optical transmittance [95].

#### 1.4.2.3 Influence of atomizer (nozzle)-to-substrate distance

In the case of changing atomizer (nozzle)-to-substrate distance there are four types of processes that may occur during deposition are shown in figure 1.5. In process 1, the droplet splashes on the substrate, vaporizes, and leaves a dry precipitate in which decomposition occurs. In process 2, the solvent evaporates before the droplet reaches the surface and the precipitate impinges upon the surface where decomposition occurs. In process 3, the solvent vaporizes as the droplet approaches the substrate, then the solid melts and vaporizes (or sublimates) and the vapor diffuses to the substrate to undergo a heterogeneous reaction there. This is true CVD [96]. In process 4, at the highest temperatures, the metallic compound vaporizes before it reaches the substrate and the chemical reaction takes place in the vapor phase.

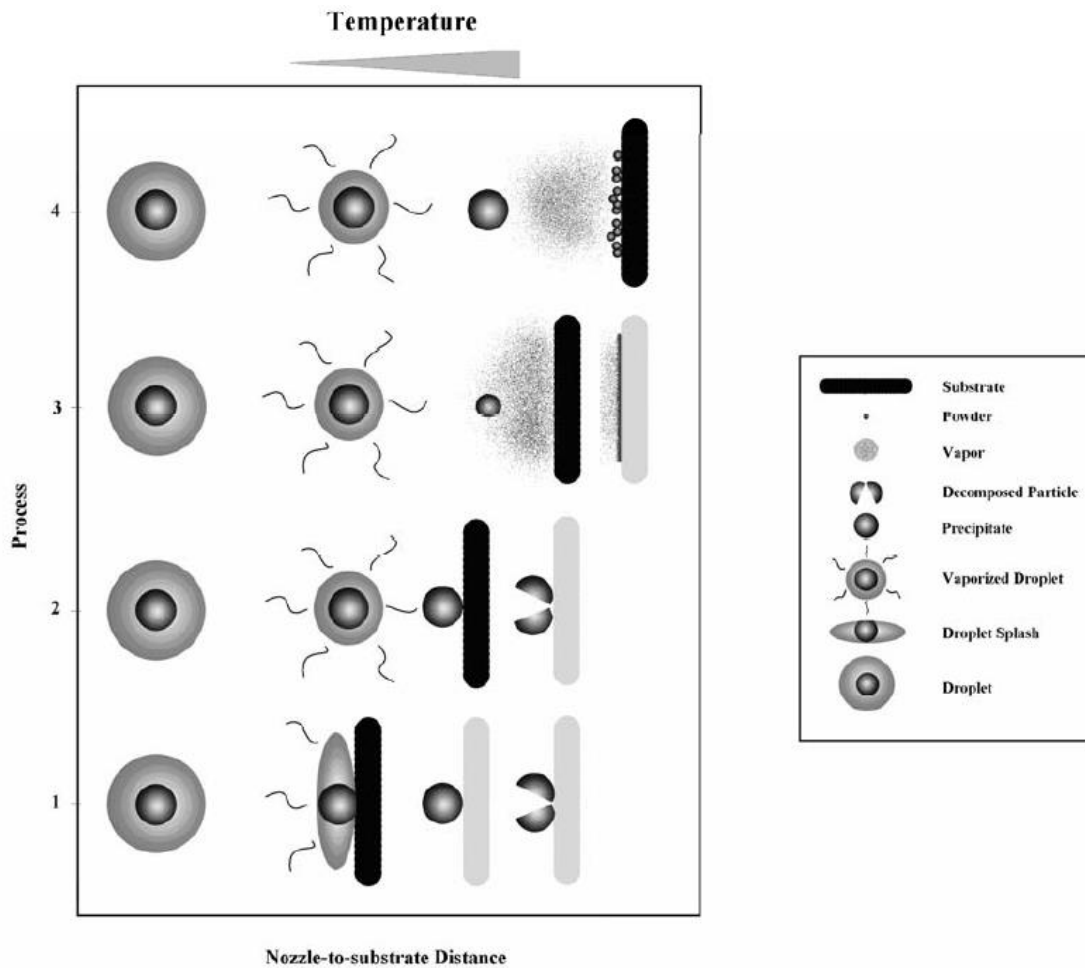


**Figure 1.5:** Schematic depicting different deposition processes that occur as the nozzle-to-substrate distance and deposition temperature change [96].

### 1.4.3 Growth kinetics of thin films

Thin film is prepared by deposition of the film materials (metals, semiconductors, insulators, dielectric, etc.) on a substrate through a phase transformation. Sufficient time interval between the two successive deposition of atoms or molecules and also layers are required so that these can occupy the minimum potential energy configuration. In thermodynamically stable films, all atoms (or molecules) will take up positions and orientations energetically compatible with the neighboring atoms of the substrate or to the previously deposited layers, and then the effect substrate or the initial layers will diminish gradually [97].

The deposition process of a film can be divided into three basic phases:

1. Preparation of the film forming particles (atoms, molecules, cluster);
2. Transport of the particles from the source to the substrate;
3. Adsorption of the particles on the substrate and film growth;

These phases can depend the specific deposition process on the choice of the deposition parameters be considered as either independent or as influencing one another. The former is desirable since it allows controlling the basic steps independently and therefore yields a high flexibility in the deposition process.

The importance of coatings and the synthesis of new materials for industry have resulted in a tremendous increase of innovative thin film processing technologies. The properties of thin film strongly depend on their structure. So it is important to know the factors that govern the structure of the film.

The theory of nucleation and growth of thin films is reviewed. The basic phenomena on the substrate have been described. The ideal condition of the film formation involves the deposition of the material atom by atom, molecule by molecule and layer by layer from the vapor phase of a material. Atomistic condensation takes place at the earliest stage of observation, in the form of a three dimensional nuclei which then grow to form a continuous film by diffusion-controlled processes. This condensation is the net result of equilibrium between the absorption and desorption processes taking place in the vicinity of the substrate surface. Many theoretical models of condensation are proposed by various researchers that are consistent with the experimental observations [97]. The sequential growth stages in the formation of thin films are schematically shown in figure 1.6. There are several stages in the growth process from the initial nucleation of the deposits to the final continuous three dimensional film formation stages. These stages are as given below [98- 102].

1. In the nucleation stage, randomly distributed, three-dimensional nuclei are first formed if the supersaturation condition is fulfilled. These nuclei then grow to form observable islands, whose shapes are determined by interfacial energies and deposition conditions.
2. Further deposition increases the size of the islands and often has tendencies to develop crystallographic facets during the early stage of their growth. Island density rate can be controlled by the deposition conditions.
3. When the island distribution reaches a critical state, a rapid large-scale coalescence of islands results. After reaching saturation, the island density decreases with increasing substrate temperature and with subsequent film growth. The rate of decrease of island density is more rapid also with increasing smoothness of the substrate [99].
4. Continuous coalescence results film channels in between. These channels need not remain void and soon some secondary nuclei starts to grow within this void

space in the channel. Sometimes these channels may not be completely filled up even with increasing film thickness thus leaving some holes or gaps in the aggregate mass.

5. The final stage of growth is a slow process of filling the empty channels that requires a considerable amount of deposit. In an ideal film, there should not be any gap and this stage can be attained when the film has certain average thickness. The minimum film thickness for the continuous stage is also dependent on the nature of the deposits, deposition parameters etc.

The above sequence is qualitatively common to all types of vapor deposited films; however, the kinetics of each stage may vary markedly depending on the deposition parameter and the deposited film-substrate combinations.

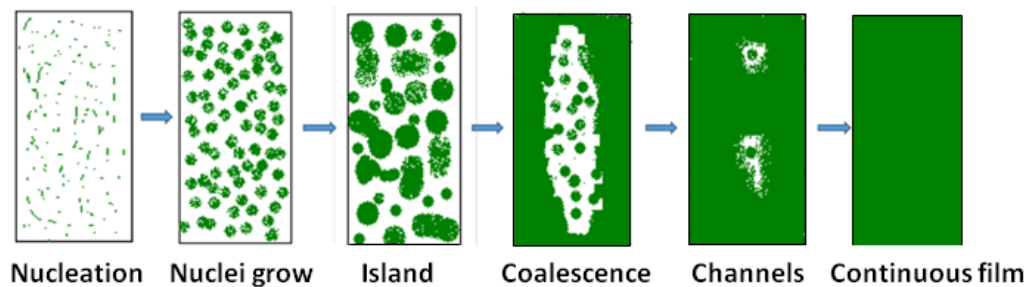


**Figure 1.6:** Various stages of nucleation and growth of thin films.

## 1.5 Films characterization techniques

Characterization techniques Recently nanostructured semiconducting materials are synthesized by different physical and chemical methods. The structural and electronic properties as well as the primary particle size distribution are strongly dependent on the preparation method. Once the synthesis of an appropriate material is done, the first goal is to perform the characterizations of that particular material. In order to perform this in a systematic way, one needs a diverse array of characterization techniques. An important issue is the correct interpretation of the experimental results obtained by characterization tools. To confirm this, in this element we will describe the various characterization techniques utilized in our work.

1. Weight difference method;
2. X-Ray diffraction technique (XRD);
3. scanning electron microscopy (SEM);
4. Ultra violet-visible spectroscopy (UV-Vis);

5. Method of four probes;

### 1.5.1 Weight difference method

Film thickness is one of the very important attributes of the films to be determined. The reason is that many properties of the films are dependent on the film thickness and other parameters such as mass density can be derived from thickness. There are various methods to measure the film thickness, Among them optical method (Hebal Optics) and weight difference method. In this work, both techniques have been used. The weight difference method is simple and available only need a precise electronic balance, the thickness is measured in this method using the following formula [103]:

$$t(nm) = \frac{\Delta m}{S \eta} \quad (1.2)$$

Where ( $t$ ) is the thickness of the film, ( $\Delta m$ ) is the weight gain, ( $S$ ) is the area of the coated film and ( $\eta$ ) is the density of NiO in bulk state.

### 1.5.2 X-Ray diffraction technique (XRD)

X-Ray diffraction technique (XRD) is one of the most useful characterization methods as it can provide a great deal of information about the film without requiring much sample preparation. As part of our study, were used, Bruker - AXS D8 kind, X-rays were generated from a source  $Cu K_{\alpha}$  radiation having a wavelength of 1.541838 Å, with an acceleration voltage of 30 kV and a current of 40 mA.

X-ray diffraction can be used to study the crystallographic properties of the thin films prepared such as determine of the crystalline structure, the orientation of the crystallites in a sample, the crystalline quality and the crystallite sizes.

Two critical advantages of X-ray diffraction for thin film analysis are [104]:

1. The wavelengths of X-rays are of the order of atomic distances in condensed mater, which especially qualifies their use as structural probes.
2. X-ray scattering techniques are non-destructive and leave the investigated sample intact.

X-ray diffraction has been used to identify the crystalline phases of the materials based on the Bragg's law. As shown in figure 1.8, condition at which diffraction occurs in a crystalline material satisfying the Bragg's law is described as [105]:

$$n\lambda = 2d_{hkl} \sin(\theta_{hkl}) \quad (1.3)$$

Where ( $\lambda$ ) is the wave length of the X-ray beam, ( $d_{hkl}$ ) is the spacing between the parallel planes in the atomic lattice, ( $h, k$  and  $l$ ) are the miller indices of the corresponding lattice planes ( $hkl$ ),  $\theta_{hkl}$  is the angel between the incident ray and the scattering planes, and  $n$  is an integer. Waves that satisfy this condition interfere constructively and result in a reflected wave of significant intensity.

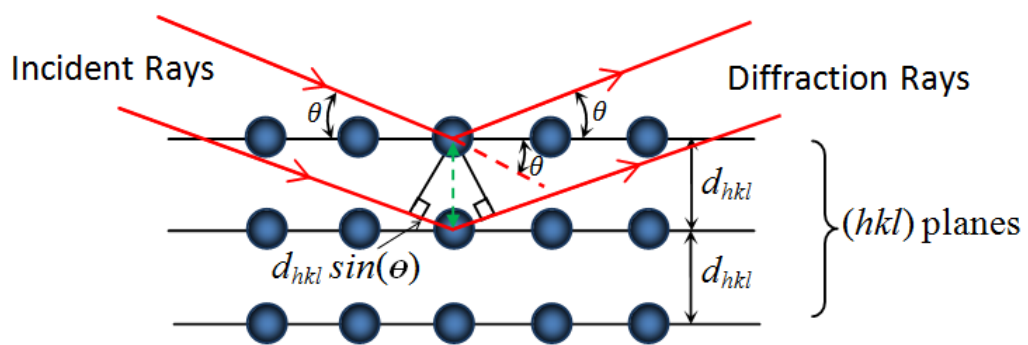


**Figure 1.8:** Schematic of X-ray diffraction According to Bragg.

A diffraction pattern is obtained by measuring the intensity of scattered waves from a sample as a function of scattering angle. Very strong intensities known as Bragg peaks are obtained in the diffraction pattern at the points where the scattering angles satisfy Bragg condition. X-ray diffraction studies gives a whole range of information about the crystal structure, orientation and average crystalline size of the films. The diffraction patterns obtained experimentally of the sample are compared with the standard patterns of the likely elements and compounds present in the sample. Based on this comparison conclusions can be drawn about crystal structure and orientation of the sample.

### 1.5.2.1 Information obtained from the X-ray Diffractogram

There are much information that we can deduce from the X-ray Diffractogram, some of which are presented below.

#### A. grain size:

From the X-ray diffraction pattern, the width generated in a peak which known as full width at half maximum (FWHM) (See figure 1.9), can be used to calculate the

mean crystallites sizes of the film in a direction perpendicular to the respective  $(hkl)$  planes, by using the Scherrers formula [106, 107], which is given as:

$$D_{hkl} = \frac{0.9 \lambda}{\beta_{hkl} \cos(\theta_{hkl})} \quad (1.4)$$

Where  $(D_{hkl})$  is the average grain size obtaining from the peak  $(hkl)$ ,  $(\lambda)$  is the wave length of the X-ray beam,  $(\beta_{hkl})$  is the full width at half maximum intensity of the peak  $(hkl)$  and  $(\theta_{hkl})$  is the angel between the incident ray and the  $(hkl)$  scattering planes.

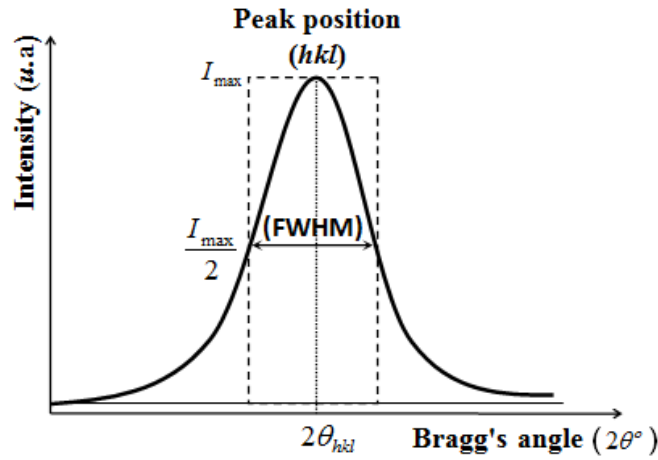


**Figure 1.9:** Full width at half maximum (FWHM) of an arbitrary peak.

### B. Lattice parameters

The distance between the two adjacent lattice planes is derived from the experimental peak position by means of Bragg formula. Experimentally, the Bragg law can be utilized by using X-rays of known wavelength  $(\lambda_0)$  and measuring  $(\theta_{hkl}^{\text{exp}})$ , we can determine the interplanar spacing  $(d_{hkl}^{\text{exp}})$  of various planes in a crystal.

$$d_{hkl}^{\text{exp}} = \lambda_0 / 2 \sin \theta_{hkl}^{\text{exp}} \quad (1.5)$$

The experimental lattice parameter values  $(a_{hkl}^{\text{exp}})$  for Cubic systems can be calculated from the following equation using the  $(hkl)$  parameters and the interplanar spacing  $(d_{hkl}^{\text{exp}})$  [108].

$$d_{hkl}^{\text{exp}} = \frac{a_{hkl}^{\text{exp}}}{\sqrt{h^2 + k^2 + l^2}} \quad (1.6)$$

The lattice parameters are substrate dependent. This gives rise to a mismatch between the substrate and the deposited thin films. The latter is responsible of the resulting strains and stresses. The strain ( $\varepsilon$ ) values of the films were estimated from the observed shift, in the diffraction peak between their positions in the XRD spectra via the formula [109, 110]:

$$\varepsilon = (a_{hkl}^{\text{exp}} - a_{hkl}^{\text{the}}) / a_{hkl}^{\text{the}} \quad (1.7)$$

Where ( $\varepsilon$ ) is the mean strain in thin films,  $a_{hkl}^{\text{exp}}$  is the lattice constant of thin films and  $a_{hkl}^{\text{the}}$  the lattice constant of bulk.

We can be also estimating the lattices microstrain ( $\mu_\varepsilon$ ) using another relationship [111, 112]:

$$\mu_\varepsilon = \beta \cos(\theta) / 4 \quad (1.8)$$

A dislocation is an imperfection within the crystal associated with the misregistry of the lattice in one part of the crystal with that in another part. Unlike vacancies and interstitial atoms, dislocations are not equilibrium imperfections, i.e. thermodynamic considerations are insufficient to account for involving dislocation as a matter of importance [113]. The dislocation density ( $\delta$ ) is the dislocation lines per unit area of the crystal can be evaluated from the grain size ( $D$ ) using the formula [112, 114]:

$$\delta = 1/D^2 \text{ (Lines / m}^2\text{)} \quad (1.9)$$

### C. Texture

Usually, the polycrystalline is such a crystal aggregates whose orientations may deviated widely from complete randomness, which is said to possess texture. In order to compare the reflex intensities of different orientations they are usually normalized with the tabulated peak heights of the powder diffractograms. We are looking for a normalization of the x-ray peaks that yield quantities that are proportional to the fraction of the material with the corresponding crystalline orientation. For such a normalization, approximately equal values for the total normalized scattering power are to be expected for crystalline films with the same thickness [103]. Crystallographic texture in thin films, i.e. the preferred orientation of particular crystal planes relative to the film substrate, is a common and frequently useful phenomenon.

The texture coefficient (TC) represents the texture of the particular plane, deviation of which from unity implies the preferred growth. The (TC) of the samples can be calculated by using the relations [115]:

$$TC(hkl) = \frac{I(hkl)/I_0(hkl)}{\frac{1}{N} \sum_N I(hkl)/I_0(hkl)} \quad (1.10)$$

Where  $I(hkl)$  is the measured intensity of a plane (hkl),  $I_0(hkl)$  is the standard intensity of the plane (hkl) taken from the JCPDS data and  $N$  is the number of diffraction peaks. The value  $TC(hkl)=1$  represents films with randomly oriented crystallites, while higher values indicate the abundance of grains oriented in a given (hkl) direction [115].

### 1.5.3 Scanning electron microscopy (SEM)

The scanning electron microscope (SEM) is a multipurpose and commonly employed electron beam mechanism. Its reputation in scientific world developed from its simple interpretation methods of the generated micrographs, variety of information types that it can produce and combination of images with their analytical information counterpart [116, 117].

SEM's are used for material characterization involving image and quantitative data representation. It offered an insight into the two dimensional and three dimensional imaging of the microstructure, chemical composition, crystallography and electronic properties. Light microscopes (LM) operate using light to illuminate the surface to observe the structure; this limits resolution of these microscopes to the wavelength of light. Optical microscopes generally observe an optical limit around 300nm, whereas electron microscopes (EM) offer atomic resolution [117].

The morphological and compositional characterization of the semiconducting thin films in this work are carried out using scanning electron microscope TESCAN VEGA3, equipped with energy dispersive analysis of x-rays (EDAX) facilities operated at 20 keV.

A schematic representation of a typical SEM is shown in figure 1.10. Electrons emitted from an electron gun pass through a series of lenses to be focused and scanned across the sample. Electron beams having energies ranging from 0.5 keV to 30 keV, is

focused by one or two condenser lenses. The beam then passes through pairs of scanning coils or pairs of deflector plates in the electron column, typically in the final lens.

When the electron beam interacts with the sample, the electrons lose energy by repeated random scattering and absorption. The energy exchange between the electron beam and the sample results in the reflection of high-energy electrons by elastic scattering, emission of secondary electrons by inelastic scattering and the emission of electromagnetic radiation, each of which can be detected by detectors. The beam current absorbed by the specimen can also be detected and used to create images of the distribution of specimen current. Electronic amplifiers of various types are used to amplify the signals, which are displayed as variations in brightness on a cathode ray tube (CRT) [117, 118]. The raster scanning of the CRT display is synchronized with that of the beam on the specimen in the microscope, and the resulting image is therefore a distribution map of the intensity of the signal being emitted from the scanned area of the specimen. The image can be digitally captured and displayed on a computer monitor and saved to a computer's hard disk.

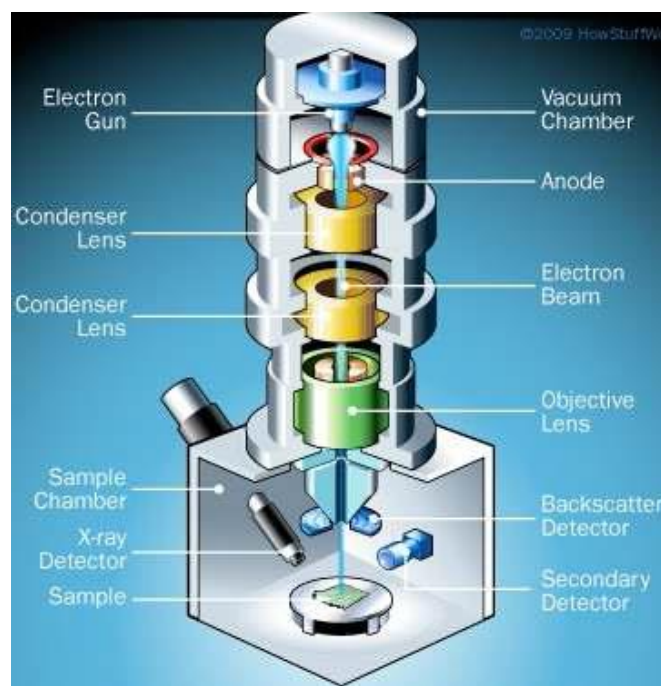


**Figure 1.10:** Schematic representation of scanning electron microscope [119].

#### 1.5.4 Spectroscopy UV- visible

The thin layers has optical properties interesting for various applications. So, Optical absorption characterization has become an important tool for optically character-

izing transparent samples. By way of example, it is strongly used to highlight the effects of quantum confinement induced by the small size of the crystallites. Using a spectrometer it is possible to measure the transmittance, the optical gap, the activation energy, the extinction coefficient, the absorption coefficient.

In this work, some parameters of the optical properties of thin films were determined by exploiting curves representing the variation of the transmittance as a function of the wavelength in the field of UV-visible. we used a UV-Visible spectrometer (UV.1601PC) whose spectral range extends from the UV-Visible ( 200-900 nm). The operating principle of this device is shown in figure 1.11.

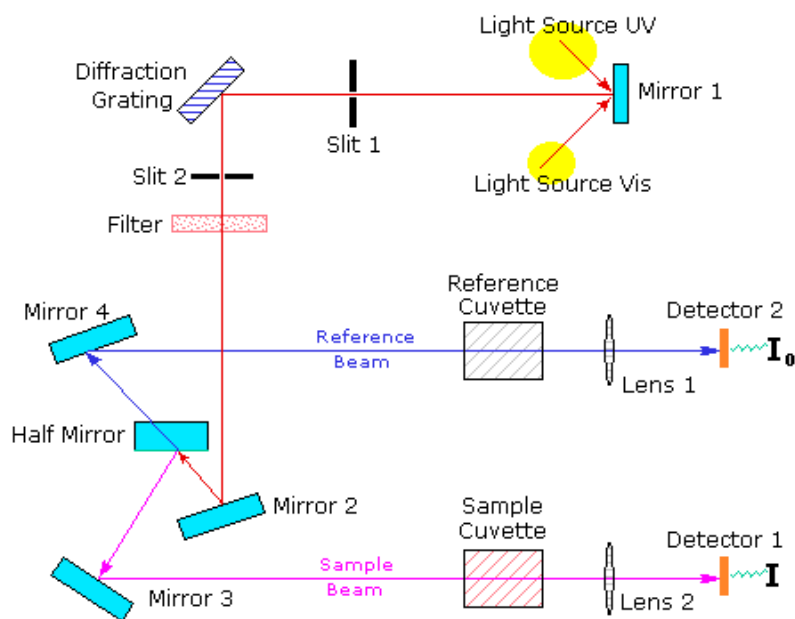


**Figure 1.11:** Schematic representation of UV-Visible spectrometer [120].

When a substance absorbs light in the In the ultraviolet and visible domains, the energy absorbed causes disturbances in the electronic structure of atoms, ions or molecules. One or more electrons absorb this energy to jump from a low energy level to a high energy level. These electron transitions are in the visible range, from 350 to 800 nm and ultraviolet between 200 and 350 nm. A homogeneous medium traversed by the light absorbs a part of it, the different radiations constituting the incident beam are differently absorbed according to their energies, the transmitted radiations are then characteristic of the medium [121, 122].

The absorption of energy of photon equal or more than the band gap of the semiconductor induces a photo-excitation, while transmittance can be defined as the frac-

tion of light of a given wavelength incident to a material that passes through that material.

Figure 1.12 presents the transmission curve of an arbitrary transparent thin film semiconductor. Incident photons with energies  $h\nu \geq E_g$  are absorbed, this absorption determined by the properties of the film (e.g. thickness & impurities), since there are numerous valence band electrons and the conduction band contains many empty states into which these electrons can be excited. A photon with energy  $h\nu < E_g$  is unable to excite a valence band electron to the conduction band, and as consequence they are transmitted, this explains why some semiconductors are transparent in certain wavelength ranges. Thus, for pure (intrinsic) semiconductors. There is negligible absorption of photons with  $h\nu < E_g$ , a photon will be absorbed only if there are available energy states in the forbidden band gap due to chemical impurities or physical defects, this process is called extrinsic transition [103].

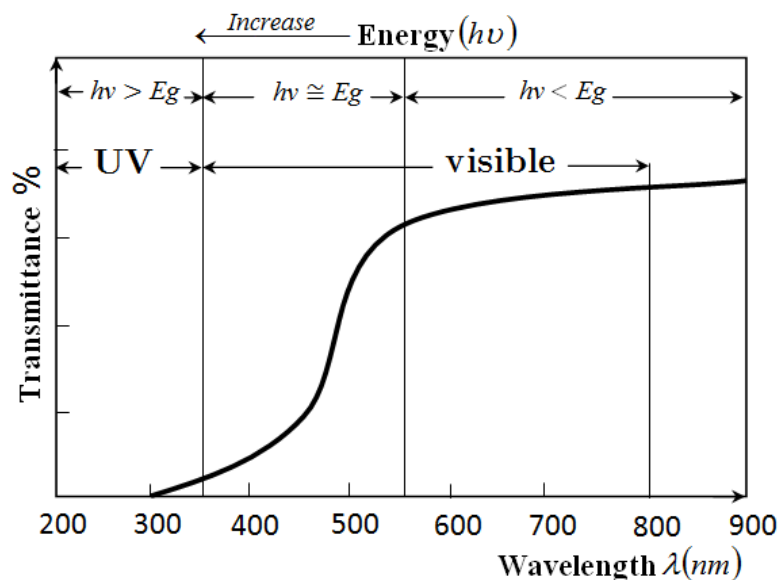


**Figure 1.12:** Presents the transmittance curve of a thin film of metal oxide semiconductor.

#### 1.5.4.1 Information obtained from the UV-Visible transmittance spectra

Much information is obtained about the properties of materials when they interact with electromagnetic radiation. When the light beam (photons) is an accident on an object, there is some expected absorption, determined by the properties of the material. In the following we will integrate the properties of films that can be deduced from the transmittance spectrum.

### A. Absorption coefficient

Absorption coefficient expresses the decrease in the intensity of a beam of photons at its passage through a particular substance or medium.

When radiation of intensity ( $\phi_0$ ) is incident on material of thickness ( $t(nm)$ ) the transmitted intensity ( $\phi$ ) is given by Lambert-Beer-Bouguer's law [123]:

$$\phi = \phi_0 \exp(-\alpha t) \quad (1.11)$$

For pure absorption, the constant ( $\alpha$ ) is the absorption coefficient. For scattering, obeying by Lambert-Beer-Bouguer's law, ( $\alpha$ ) is the scattering coefficient. And for the total attenuation including both is the extinction coefficient given by the sum of the absorption and scattering coefficient.

The transmittance ( $T$ ) and the absorbance ( $A$ ) are defined as follows [124]:

$$T = \phi / \phi_0 = \exp(-\alpha t) \quad (1.12)$$

$$A = -\log_{10}(T) \quad (1.14)$$

A relation between transmittance ( $T$ ), spectral absorbance ( $A$ ) and spectral reflectance ( $R$ ), according to the law of conservation of energy is given by [125]:

$$T + R + A = 1 \quad (1.15)$$

Based on the equations (1.12) we can obtain the following expression of absorption coefficient [124-126]:

$$\alpha = -\frac{\ln(T)}{t} \approx 2.303 \frac{A}{t} \quad (1.16)$$

We are using equation (1.14) for calculating the reflectance and equation (1.15) for calculating the absorption coefficient in this work .

For ( $h\nu < E_g$ ), no electron hole pairs can be created, the material is transparent and ( $\alpha$ ) is small. For ( $h\nu \geq E_g$ ) absorption should be strong and it is clear that ( $\alpha$ ) must be strong. The absorption coefficient ( $\alpha$ ) is related to the incident photon energy ( $h\nu$ ) and the optical band gap energy of the material as [103, 126]:

$$(\alpha h\nu) = C(h\nu - E_g)^n \quad (1.17)$$

Where  $C$  is a constant is a constant depending upon the transition probability,  $E_g$  is the optical band gap, it is shown in figure 1.13, it is the separation energy between bottom of the conduction band and top of the valence band.  $(h\nu)$  is the photon energy, where  $(\nu)$  is the frequency of the incident photon,  $(h)$  is the Planck's constant and  $(n)$  is a constant it is equal to  $1/2$  or  $3/2$  depending on whether transition is allowed or forbidden. For allowed direct transitions ( $n = 1/2$ ) and for allowed indirect transition ( $n = 2$ ). Thus if the plot of  $(\alpha h\nu)^2$  against  $h\nu$  is linear then the transition is direct allowed [123].

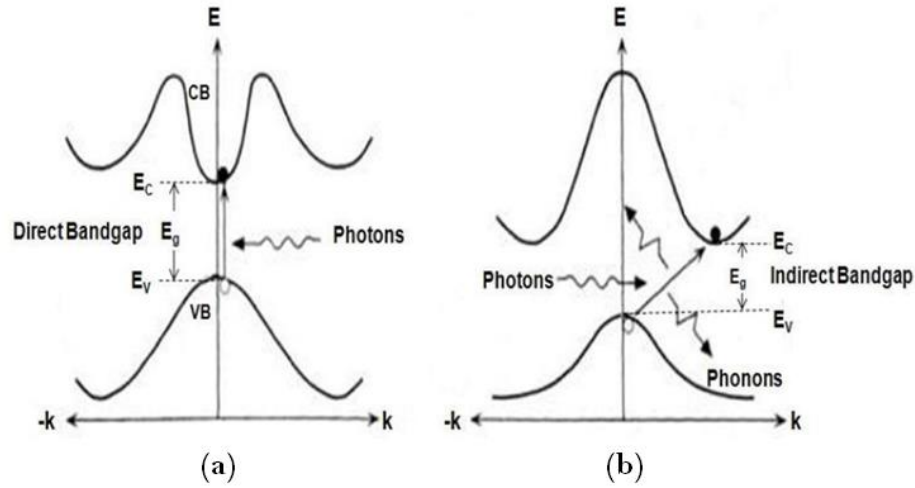


**Figure 1.13:** Direct (a) and indirect (b) band gap.

From the calculated absorption coefficient ( $\alpha$ ) values the extinction coefficient ( $k$ ) of the films were calculated over visible and NIR wavelengths using the following formula [127]:

$$k = \frac{\alpha \lambda}{4\pi} \quad (1.18)$$

Where  $\lambda$  is the wavelength of the incident photon. The rise and fall in the extinction coefficient are directly related to the absorption of light. In the case of polycrystalline films, extra absorption of light occurs at the grain boundaries [126]. This leads to non-zero value of  $k$  for photon energies smaller than the fundamental absorption edge.

## B. Energy band gap

The energy band gap and transition type can be determined from mathematical treatment of data obtained from optical transmittance versus wavelength. According to Tauc's relation for direct band gap semiconductor such as NiO [126, 127]:

$$(\alpha h\nu)^2 = A(h\nu - E_g) \quad (1.19)$$

Where  $(A)$  is a constant,  $(E_g)$  is the optical gap energy. Figure 2.14 shows the plot of  $(\alpha h\nu)^2$  versus  $(h\nu)$ , it reveals the linear nature of the plot near absorption edge indicates the existence of the direct transition between bands. Hence, this linear relationship is a clear indication that the material is direct band gap semiconductors. Extrapolating the straight line portion of the absorption spectrum in Figure 1.14 intersects the zero absorption coefficients  $(\alpha = 0)$  (energy axes) [128]. The value of energy at this interesting point indicates the energy of band  $(E_g)$ .

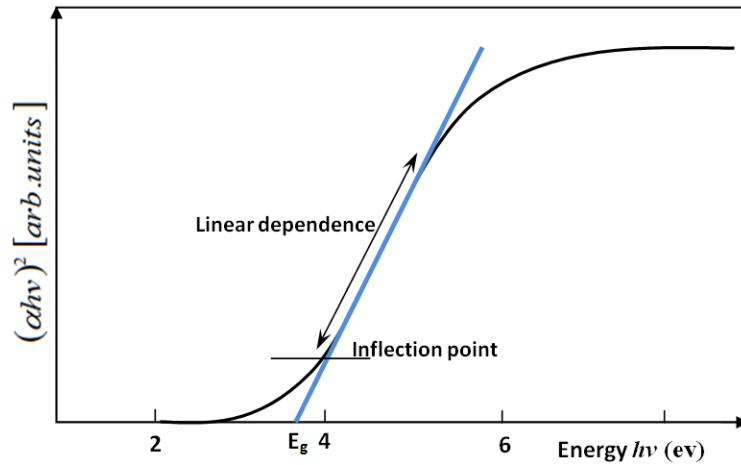


**Figure 1.14:** Determination of the energy gap  $E_g$  by the extrapolation method from the variation of  $(\alpha h\nu)^2$  as a function of  $h\nu$  for a thin layer.

#### D. Urbach energy

Mott and Dais noted that oppositely to pure crystalline structures, where the fundamental edge is mainly determined by conduction and valence levels, ion-doped binary semiconductor compounds present a particular optical absorption edge profile. In these materials, the absorption coefficient profile increases exponentially with the photon energy beneath the energy gap. This variation results in “blurring” of the valence-conduction bands and narrows slightly the band gap by the occurrence of the so called Urbach tails (Figure 1.15).

Urbach tailing has been attributed, to various causes. Earliest investigations tried to relate it to the thermally induced lattice disorder [129, 130]. Generally, at optical absorption, near band edges, an electron from the top of the valence band gets excited to the bottom of the conduction band across the energy band gap. During this transition process, if these electrons encounter disorder, it causes changing in density of their states  $\zeta(h\nu)$ , tailing into the energy gap. This tail of  $\zeta(h\nu)$  extending into the energy band gap is termed as Urbach tail. Consequently, absorption coefficient  $\alpha(h\nu)$  also tails off in an exponential manner and the energy associated with this tail is referred to as Urbach energy and can be calculated by the following equation [130].

$$\alpha = \alpha_0 \exp\left(\frac{h\nu}{E_u}\right) \quad (1.20)$$

$$\ln \alpha = \frac{1}{E_u}(h\nu) + \ln \alpha_0 \quad (1.21)$$

Where ( $\alpha_0$ ) is the pre-exponential factor, ( $h\nu$ ) the photon energy and ( $E_u$ ) is the band tail width commonly called Urbach energy. The band tail width is also related to the disorder in the film network [130, 131]. The Urbach energy, or the disorder, can be estimated from the inverse slope of the linear plot of  $\ln(\alpha)$  versus ( $h\nu$ ) as represented in figure 1.15.

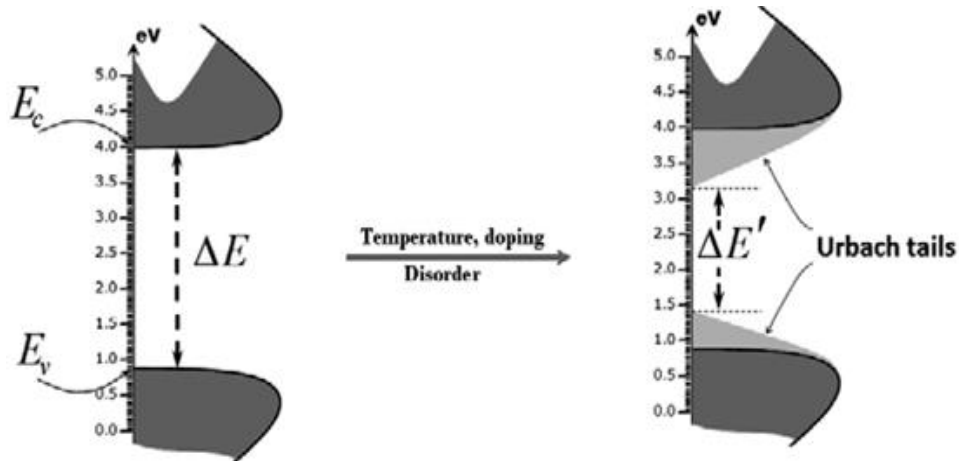


**Figure 1.15:** Scheme of Urbach tails [129].

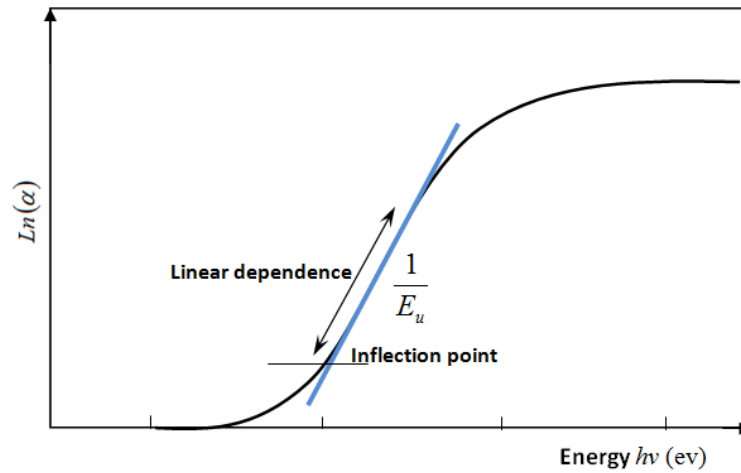


**Figure 1.16:** determination of the Urbach energy from the variation of  $\ln(\alpha)$  as a function of  $h\nu$  for a thin layer.

### 1.5.5 Method of four probes

The four probes is commonly used technique to measure the semiconductor resistivity. It is an absolute measurement without recourse to calibrated standards and is sometimes used to provide standards for other resistivity measurements. The schematic diagram of four probes measurement technique is shown in figure 1.17. It is seen that by applying current ( $I$ ) between outer probes in the figure 1.17 and measuring voltage ( $V$ ) between inner probes one can calculate the resistivity ( $\rho$ ) and conductivity ( $\sigma$ ) of the film using following equation [132].

$$\frac{1}{\sigma} = \rho = \frac{\pi}{\ln 2} t \frac{V}{I} = 4.53236t \frac{V}{I} \quad (2.23)$$

Where ( $t$ ) is the film thickness.

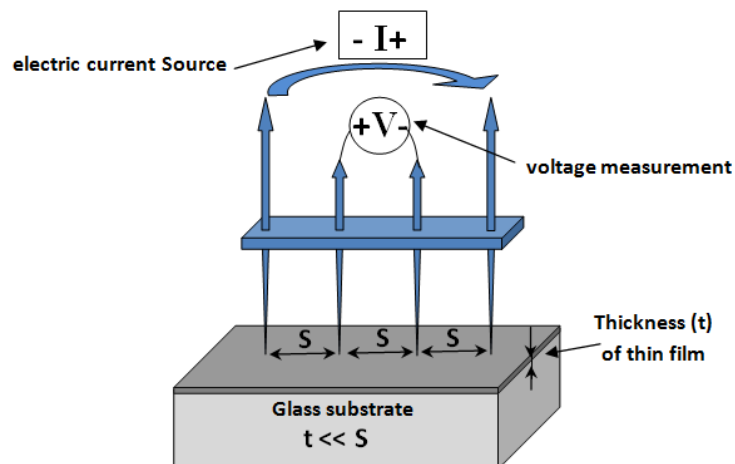


**Figure 1.17:** Schematic diagram of four probes method.

## 1.6 Nickel Oxide (NiO) thin film

Nickel oxide known as (bunsenite) is a basic oxide. It is in the form of a greenish gray powder depending on the method of preparation. It is a transition and antiferromagnetic material [133]. Their Néel temperature is 523 K, it is a temperature that characterizes the antiferromagnetic materials. Below this temperature the sub-lattice atoms spontaneously magnetize in the manner of a ferromagnetic lattice and its curie temperature has taken little of 2000 K [134].

The antiferromagnetic order of Nickel oxide related to the symmetry properties of the crystal (body-centered cubic structure, face-centered cubic, perovskite). Its high chemical stability and thermodynamic [135], it's very resistant to oxidation [136]. The table 1.1 shows some general properties of NiO.

The mineralogical form of NiO is rare. Therefore, it must be synthesized. There are many kinds of routes to synthesize NiO. Among those, the most well known route is a pyrolysis of Ni<sup>2+</sup> compounds such as hydroxide, nitrate and carbonate, which yield a light green powder. Heating in oxygen or air atmosphere leads to black NiO powder which indicates nonstoichiometry. Nonstoichiometry is accompanied by a color change from green to black due to the existence of Ni<sup>3+</sup> resulting from Ni vacancies [137].

**Table 1.1:** General properties of nickel oxide.

The Property	The value	Reference
Chemical formula	NiO	[138]
Boiling point	> 2000 (° C)	[134]
Solubility in water [18]	1.1(mg / L) at 20 ° C insoluble	[134]
Melting point	1955 (° C)	[135]
$\Delta H_f$ for metal oxide formation per oxygen atom at 298k	245.2 (KJ / mole of atoms)	[138]
Entropy S <sup>0</sup>	38.00(JK <sup>-1</sup> .mol <sup>-1</sup> )	[138]
Molar mass	74.6928 (g/mol)	[138]
Volumetric Density	6.67	[134]
Type of conductivity	P-type	[139]
Dielectric constant	10	[139]
Refractive index (n <sub>D</sub> )	2.18	[139]

Figure 1-18 shows the phase diagram of a Ni-O binary system. The stable crystal structure of nickel oxide at a high temperature is polymorph bunsenite. By cooling the crystal, the crystal structure converts to rhombohedral. It should be noted that these crystal structures form during thermodynamically stable transitions. Different fabrication techniques produce a nonstoichiometric structure [139].

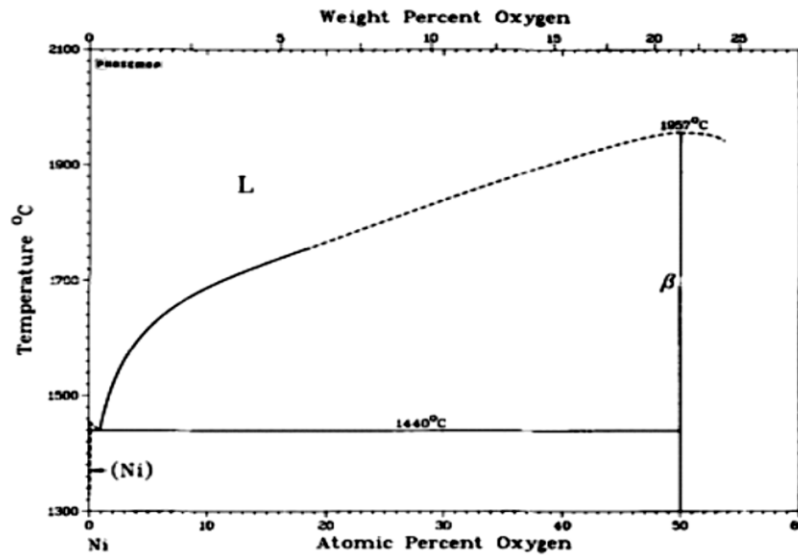
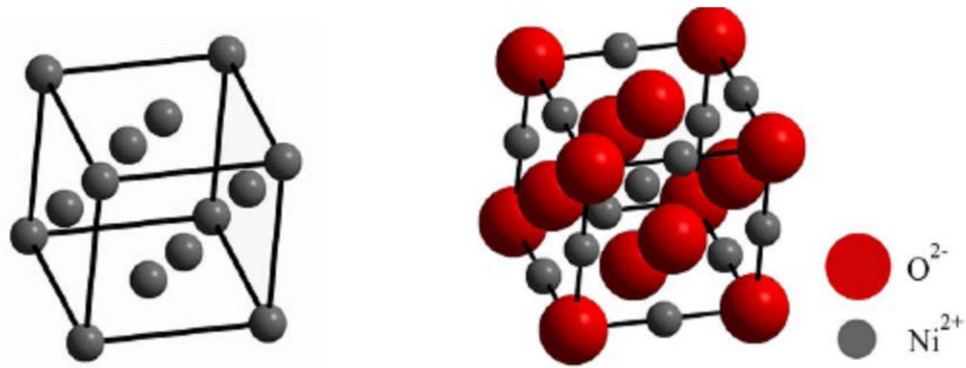


Figure 1.18: Ni-O phase diagram [140].

### 1.6.1 Crystallographic and structural properties

Nickel oxide (NiO) crystallizes in a NaCl structure (rock salts), it's shown in figure 1.19. It has a face-centered cubic structure-type (FCC) [141, 142]. This cubic structure is composed of two similar subnetworks A and B, so that every atom of subnet A has only neighbors belonging to subnet B and vice versa. The anionic subnetwork ( $O^{2-}$ ) and the cationic subnetwork ( $Ni^{2+}$ ) have a FCC structure. The plane (100) is a mixed plane composed of 50% nickel and 50% oxygen. The planes (111) are alternately pure Ni and pure O. The face (111) is a polar face (non-stable) against the face (100) is a non-polar face (stable) [134]. The interplanar spacing between two different planes is 0.120 nm and is almost double between the nature of two similar planes. The main crystallographic properties of this oxide are summarized in table 1.2.

Crystalline solids show a periodic in its crystal structure. Perfect stoichiometric metal oxides are an insulators but by introducing different defects inside the crystal, its electrical, optical and mechanical properties changes. It should be noted that the existence of the defects depends on the growth method and the material development conditions.



**Figure 1.19:** Crystallographic structure (a) of nickel (b) nickel oxide [134].

**Table 1.2:** Crystallographic properties of nickel oxide.

The Property	The value	Ref
Crystalline parameter	$a = 4.177 \text{ (\AA)}$	JCPDS No.47-1049
	$a = 4.194 \text{ (\AA)}$	JCPDS No.89-7130
Space Group	Fm3m	JCPDS No.47-1049 JCPDS No.89-7130
Coordination	6	-
Atomic coordinates of base	$\text{O}^{2-}(0,0,0), \text{Ni}^{2+}(0.5,0,0)$	-

On the other hand, the concentration of a type of defects in a crystal depends on its formation energy. The following types of defects can be found:

- E. point defects (interstitials, substitutionals, Vacancies).
- F. linear defects (dislocations...)
- G. plane defects (grain boundaries...)

Dislocations (edge, screw or mixed) are examples of line defects. Planar defects can be categorized into grain boundaries and stacking faults. The grain boundaries occur when different crystallographic planes reach together. The stacking fault structure is common in closed packed structures such as FCC and HCP, and is caused by misalignment of several layers of atoms in a preferred orientation. The properties of a sample can be altered by changing the number of defects in the crystal. Fabrication process, the annealing temperature and percentage of impurities have strong effects on the properties of the fabricated films [139]. Figure 1.20 shows different point defects in structure of NiO crystal.

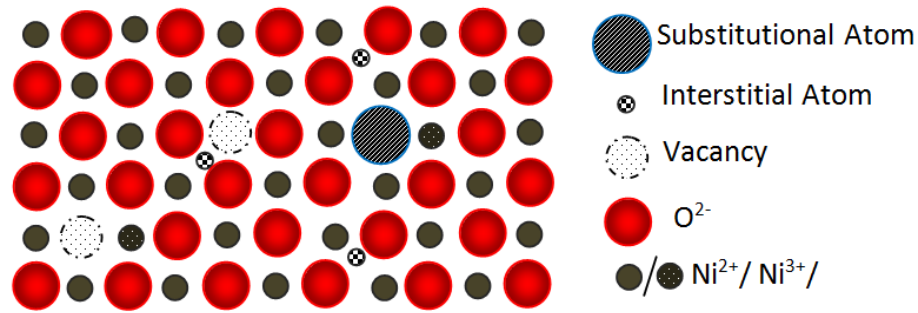


Figure 1.20: Types of point defects inside of NiO crystal.

## 1.6.2 Electronic and electrical properties

The transition metal oxides are characterized by band structures, depending on the values of the forbidden bands, the present oxide has an insulating or semiconductor character. Nickel oxide is the transition metal which form an important family by their applications. Their magnetic property is due to the presence of a band of energy called "band d". The 3d wave functions are relatively localized in the vicinity of the atomic nucleus. The band d can contain a total of 10 electrons and its width is of the order of 5eV [143]. The level of 3d electronic sub-layer energy responsible for magnetism was slightly higher than that of the 4s conduction sub-layer. The orbitals of the oxide ions in recovery with the 3d orbitals of nickel constitute the low energy binder level that level and the  $t_{2g}$  level are electronically complete; the level antibonding  $e_g$  only has two electrons. The electronic configurations of nickel and oxygen are: Ni: (Ar)  $3d^8 4s^2$ , O: (He) $2s^2 2p^4$  [134].

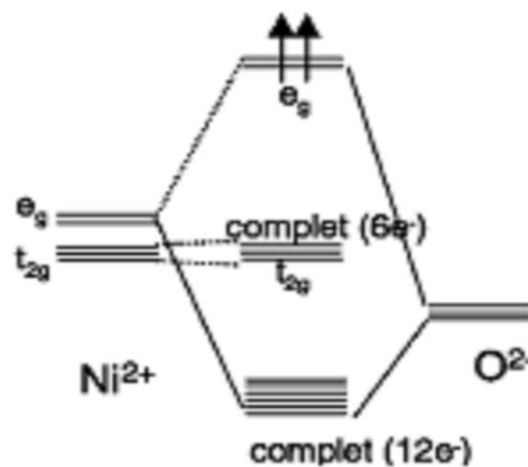


Figure 1.21: Schematic diagram of NiO energy levels.

Pure stoichiometric NiO is an excellent insulator. Conduction mechanism of NiO has not clearly explained yet, so there is no common agreement about its electrical properties [144]. Firstly, it was believed that stoichiometric NiO is Mott insulator [145]. Then, it is corrected that it behaves as Mott-Hubbard type insulator [146]; however, when it is oxidized, it becomes a p-type conductor [147]. However, my conflicting results reveal that conduction mechanism and electronic structure of NiO is quite complex [148].

Various theories have been done to explicate the insulating behavior of NiO; they include localized electron theory, band theory, chemical band approach and cluster theory. After intense theoretical and experimental investigations, the electronic structure of NiO remains controversial [149]. The conduction mechanism of NiO has been explained as percolative, small polaronic and grain boundary controlled. Similarly, the conflictive results about Hall conductivity of NiO has been also reported [148].

Electronic conduction in undoped NiO is suggested to the appearance of nickel vacancies or excess of oxygen. In the ionic crystal of NiO, the orientation of the film is usually affected by the orientation of  $O^{2-}$  when the active species of nickel and oxygen impinge separately on the growth of the film surface. This is because NiO has no directivity of a mixture between  $Ni^{2+}$  and  $O^{2-}$  and the radius of  $O^{2-}$  (0.140 nm) is superior to that of  $Ni^{2+}$  (0.069 nm) [120]. The oxygen atom is too large to permit any considerable concentration of interstitial O atoms in the structure. As a resulting overload of O in NiO create vacancies in the normally occupied Ni sites as in Figure I.14. However, to preserve overall electrical neutrality in the crystal, two  $Ni^{2+}$  ions should be converted to  $Ni^{3+}$  for every vacant  $Ni^{2+}$  site. The  $Ni^{3+}$  ions introduced within the crystal in this way can be advised to be positive centers capable of jumping from one  $Ni_2$  site to another. When an electron hops from a  $Ni^{2+}$  to a  $Ni^{3+}$  site, it is as if a positive hole moves around the  $Ni^{2+}$  sites. Thus overload of oxygen makes the NiO as p-type semiconductor [120].

In fact, nickel oxide is an insulator with an optically measured band gap of 3.6 to 4 eV (Figure 1.22), but its structural defects that make it a semiconductor at high temperatures. It was claimed that the optical gap forms between the ligand electrons and metal 3d electron exchange states. It has been that d electrons are localized and conduction takes place in  $O2p$  bands. The smallest ionization energy which accounts for the optical gap is not a single hole picture, rather it leads to a many body hole state.

The schematic of density of states in NiO is shown in figure 1.23. In NiO, the Fermi energy level is said to be at 0.4 eV above the valence band. Conducting states are shown to the left of vertical line. Right side shows non-conducting states. Shaded states are full, whereas unshaded states are empty. NiO is an insulator at room temperature with resistivity well exceeding  $\sim 10^6 \Omega \cdot \text{cm}$ , with values as high as  $\sim 10^{13} \Omega \cdot \text{cm}$  [120].

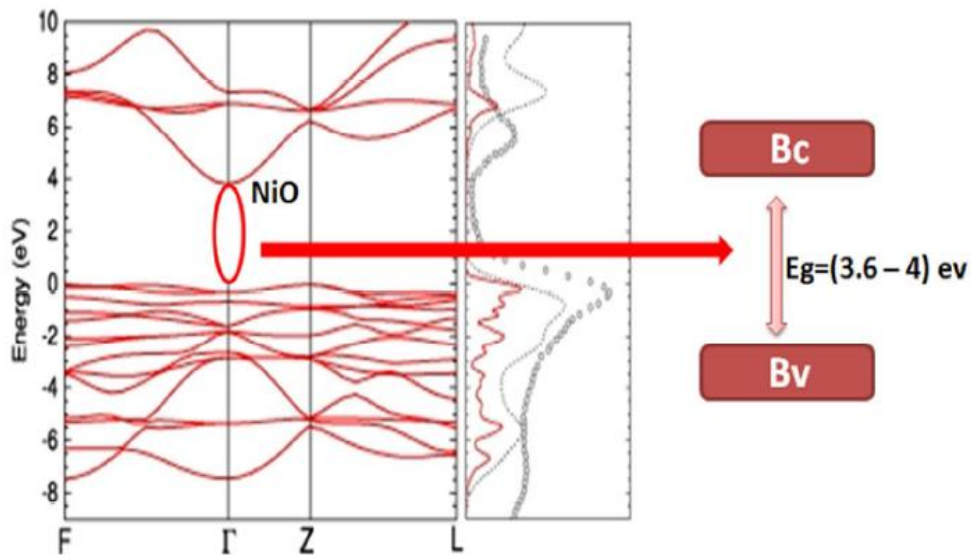


Figure 1.22: Diagram of NiO Band structure.

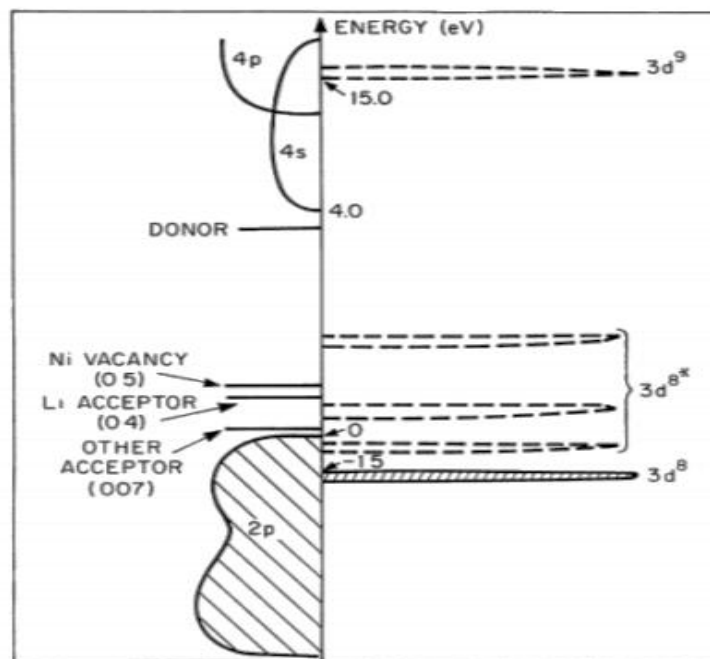


Figure 1.23: Energy diagram of density of states (pseudoparticle) in NiO.

### 1.6.3 Optical properties

The material nickel oxide from the transparent conductive oxides (TCO) which have high conductivity and lighting gap energy directly, NiO is green due to strong absorption in violet (2.75 – 2.95 eV) and red 1.75 eV. In case of excess oxygen, namely Ni is oxidized by directly oxygen or doping with Li<sup>+</sup>, high absorption coefficient of the green range (1.75 – 2.75 eV) is expanded and NiO appears as black [148]. Band gap of NiO thin films changes with the deposition technique in between 3.6 and 4 eV. To understand the electronic structure of NiO, various optical experiments have been carried out such as photoemission or inverse photoemission studies [143]. Theoretical calculations about optical spectra have also been reported. There are some significant points about conduction band, valence band and optical band gap of NiO to be noticed:

1. Ni 3d states dominates the conspicuous structure at valence band edge [151].
2. Ni 4s is located at the conspicuous structure of conduction band edge, but the structure on the small shoulder ( $(E_c - E) \sim 0.8$  eV) is detected and considered as localized Ni states [152].
3. The gap of band structure is clean due to its nature; however, mid-gap structure is quite sensitive susceptible to thin film deposition and defects [148].

### 1.6.4 Doping types in the NiO film

Doping in both n and p-type metal oxide materials is the result of the addition of, the dopant atom sits in place of one of the constituent atoms in the bulk, in the case the n-type doping, can resulting in a non-bonding electron which creates an donor energy level close to that of the conduction band (Figure 1.24). This allows facile promotion from the donor energy level, and delocalized conductivity in the now partially filled conduction band.

In a p-type doping, the dopant atom causes an electronic deficiency in the ionic bonding, thus creating an empty acceptor energy level just above the valence band, which can accept an electron from that valence band, and leaves behind a positive 'hole'. This allows conduction via doping species to a bulk semiconducting or insulating lattice structure [153].

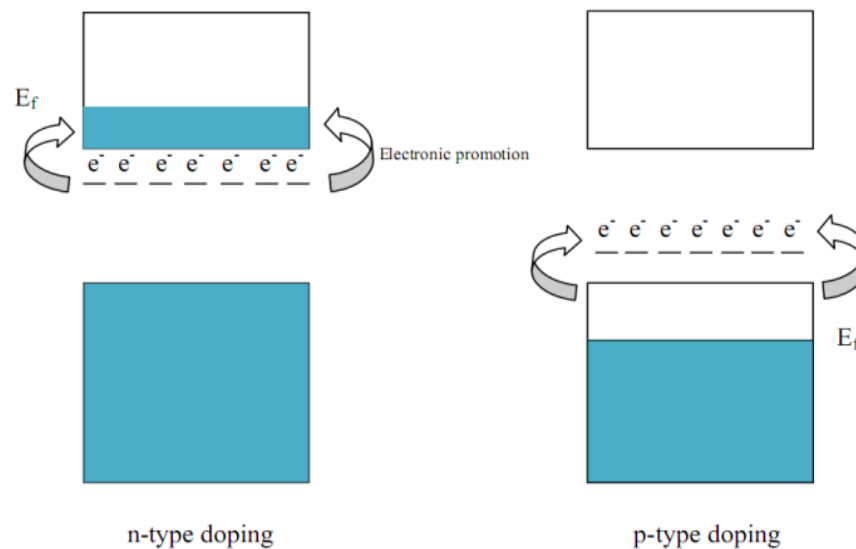


**Figure 1.24:** Band structure diagrams of n-type and p-type doped semiconductor materials: showing promotion of the electrons over a small defect ionisation energy level.

$E_f$  is the Fermi level (the highest electronically occupied energy level) [153].

#### 1.6.4.1 Extrinsic doping (substitutional)

It is done by changing the original ions  $Ni^{2+}$  or oxygen ions  $O^{2-}$  (anions) with ions having respectively a higher or lower valence, the charge carriers concentration can be increased. This increase leads to shifting in the Fermi level within the conduction band, if the opposite occurs, the Fermi level shifting within the valence band [120]. The introduction of impurities into the crystal lattice creates energy levels in the gap and either donors or acceptors, which are responsible for changing the optical and electrical properties. There are also linear defects (dislocation) and plane defects (grain boundaries). Transition metals (TM) doped nickel oxide have been studied mainly for their dielectric and magnetic properties. However, the major focus has been confined to the evolution of magnetic property in NiO with TM doping. High-permittivity dielectric materials with good thermal stability have been played a significant role in microelectronics. Giant dielectric response has been observed for (Li, Fe) and (Li, V) doped NiO [154]. The effects of transition metal like Fe, Cu, Co, Mn etc. doping can drive a non-magnetic semiconductor into a semiconductor with ferromagnetism. This has led to the emergence of a new field of research, the diluted magnetic semiconductors (DMS). The table shows some characteristics of the NiO films doped by the transition metals [155].

### 1.6.4.2 Intrinsic doping

By introducing excess oxygen atoms in the interstitial position, or by creating nickel gaps. The major defects in nickel oxide are cationic vacancies  $\text{Ni}^{2+}$ . NiO can be written  $\text{Ni}_{1-y}\text{O}$ , or there is the difference of the stoichiometry, the oxygen atoms in interstitial positions. The conductivity of nickel oxide increases with temperature, that is to say their semiconductor behavior is interpreted by the presence of defects in the crystal lattice. When there are vacant crystallographic sites in this case it is possible to envisage an electrical conduction by jump, a cation ( $\text{Ni}^{2+}$ ) passing from a occupied site to a vacant site produces the displacement of the vacant site, such a displacement of charges is more efficient at high temperature .

### 1.6.5 Review of nickel oxide prepared by SPT

Nickel oxide thin layers have been prepared by various techniques that involve: electron beam evaporation [156], magnetron sputtering [157], chemical deposition [158], sol-gel [159] and spray pyrolysis technique (SPT) [160].

Among various methods, spray pyrolysis is one through which the films can be coated for large area. In the present work, we are used this method for elaboration the NiO thin films. In this item we present a scheduled review by K. O. Ukoba et all [161] (Table 1.3), This study reviews NiO film deposition using the Spray Pyrolysis Technique (SPT). Physical and chemical methods can be used to deposit NiO film. This review looks at different precursors and their characterization methods for spray deposition of NiO thin film. The usefulness of SPT emanates from this method being simple, low cost, and viable for mass production. It gives high product purity for metallic and non-metallic material deposition. Nickel chloride, nickel acetate, nickel nitrate, nickel hydroxide, nickel sulfate, and nickel formate are the major precursors for NiO thin film deposition. Nickel chloride and nickel acetate are the most used and highly available precursors. Unlike nickel acetate, nickel chloride precursors corrode the deposition equipment (spray gun).

Table 1.3: Summary of major reviewed parameters for NiO thin films using spray pyrolysis technique [161].

Precursor Used	Optical Band Gap (eV)	Molarity (M)	Substrate Temperature (°C)	Major Focus	Film Thickness	Other Parameters
Nickel chloride	3.58 for 30 ml, 3.55 for 40 ml, 3.49 for 60 ml 3.40 for 75 ml	0.05	350	Vol of sprayed (30 ml, 45 ml, 60 ml and 75 ml) on solution on NiO films	0.028 μm (30 ml) to 0.23 μm for (75 ml).	
Nickel chloride		0.05	350	Electrochromic properties of nickel oxide thin films prepared by spray pyrolysis technique.		
Nickel chloride	3.4–3.8 eV for 0.1–0.05 M respectively	0.025, 0.05, 0.075 and 0.1	280, 320, 360 and 400	Study focused on the effect of varying the concentration (0.025 M, 0.05 M, 0.075 M and 0.1 M) and the deposition temperature (280 °C, 320 °C, 360 °C and 400 °C)	0.21 μm 5–0.91 μm.	Spraying nozzle height, rate of spray and deposition time are 35 cm, 15 cm <sup>3</sup> /min and 6 s respectively.
Nickel chloride	3.25	0.5	350 °C, annealed at a temperature of 500 °C for one hour	Focused on the antireflection coating of NiO thinfilms in solar cells	161 nm	Spray rate of 1 ml/min, substrate to nozzle distance of 18 cm.
Nickel chloride		0.1	225 to 420	study focused on substrate temperature as it affects the films properties	Decrease of the film thickness with increasing the substrate temperature (220 nm for 225 °C to 50 nm for 420 °C.	Substrate to nozzle distance of 40 cm, deposition time of 40 s, and flow rate of 15 cm <sup>3</sup> /min.
Nickel chloride	3.54 eV, 3.43 eV and 3.37 eV for 350 °C, 400 °C and 450 °C respectively	0.3	350 °C, 400 °C and 450 °C	Evaluating the oscillator parameters (optical dispersions) of the NiO thin films	Film thickness increased as the transmittance decreased.	Nozzle to substrate distance of 7 cm, volume of 0.5 ml per min and an optimized airflow of 1.2 kg/cm <sup>2</sup> .
Nickel chloride	3.25 eV, 3.04 eV, 3.16 eV and 3.28 eV for 425 °C, 450 °C, 475 °C and 500 °C respectively	0.5	425 °C, 450 °C, 475 °C and 500 °C	Influence of substrate temperature on electrochemical supercapacitive performance of spray deposited NiO thin films	280 nm, 350 nm, 310 nm and 275 nm for 425 °C, 450 °C, 47 °C 5 and 500 °C respectively.	Distance between spray nozzle and substrate is kept constant at 30 cm. Spray rate employed was 3 mlmin <sup>-1</sup> .
Nickel acetate	3.6 eV for freshly prepared solution and aged 3.5 eV	0.1	330 °C	Focused on the effect of ageing on NiO thin films	631 nm for freshly prepared and 676 nm for aged.	
Nickel acetate	383 eV for 225 °C and 3.14 eV for 350 °C	0.05	225 °C to 350 °C	The work varied the substrate temperature with a view to finding the structural and optical dispersion properties of NiO thin films	The film thickness decreased with increased substrate temperature (225 °C was 200 nm while 350 °C was 40 nm).	Nozzle diameter of 0.7 mm, deposition time of 15 s, period between spraying of 3 min, spraying height of 35 cm and spraying rate was 15 cm <sup>3</sup> /min.
Nickel acetate	The optical band gap of the films decreased with increase in film thickness from 4.3 to 3.65 eV.	0.1	350 °C and 450 °C	The study showed that the morphology of the films is principally controlled by the substrate temperature.	At 350 °C the thickness was 230 nm for 20 ml/h, 505 nm for 40 ml/h and 842 nm for 60 ml/h. At 450 °C the thickness was 80 nm for 20 ml/h, 130 nm for 40 ml/h and 170 nm for 60 ml/h.	Substrate thickness of 1 mm, volume of solution varied between 20 to 60 ml/h, nozzle to substrate distance of 20 cm, spray time varied between 7.5 min and 180 min
Nickel chloride and nickel acetate.		0.05 M for both	473 K and 523 K.	To study the effect of substrate temperature on the structural and electrical properties of NiO using two precursors.		
NiCl <sub>2</sub> ·6H <sub>2</sub> O, Ni(NO <sub>3</sub> ) <sub>2</sub> ·6H <sub>2</sub> O, Ni(OH) <sub>2</sub> ·6H <sub>2</sub> O, NiSO <sub>4</sub> ·4H <sub>2</sub> O.	3.59 eV for all precursors	0.2 and 0.3	350 °C post annealed at 425 °C for 3 h.	Used four precursors of NiO films to study the properties of the film using SPT with perfume atomizer to grow the aerosol with varying molarity.		The volume of the solution for each deposition was 60 ml. 30 min was necessary for 60 ml. The substrate to nozzle distance was 30 cm.

## 1.7 Conclusion

In this chapter, we defined the thin film. Then we explained some preparation methods of films and we focused on the method of spraying pyrolysis, followed by an explanation of the devices used in the study of the properties of films prepared. At the end of the chapter, we presented a bibliographic study of nickel oxide, which illustrated the structural, optical and electrical properties. In the next chapter we will study chemical gas sensors based on thin films of metal oxide semiconductors.

# Chapter two

2/4

Chemical gas sensors  
based on  
(MOS) thin films

## CHAPTER 2

# Chemical gas sensors based on (MOS) thin films

### 2.1 Introduction

During the past few decades, the demand for detection methods for chemical species and more particularly for gaseous species has increased considerably. This interest is mainly due to environmental, safety, process control or industrial waste considerations. The necessity to constantly monitor and control these gases emitted sprouted the need to gas sensors, which can continuously and effectively detect these gasses to avoid most of the probable dangers [162].

In recent years, metal oxide semiconductors (MOS) chemical gas sensors have become a prime technology in several domestic, commercial, and industrial gas sensing systems. These sensors are based on electrochemical behavior, catalytic combustion, or resistance modulation of MOS [163]. Among the available gas sensing methods, the MOS chemical gas sensor devices have several unique advantages such as low cost, high sensitivity (ppm levels), small size, measurement simplicity, durability and ease of fabrication. In addition, most MOS based sensors tend to be long-lived and somewhat resistant to poisoning. For these reasons, they have rapidly grown in popularity, becoming the most widely used gas sensors available these days. All above listed characteristics have been the subject of extensive research for the past two decades [164]. But still the quest for developing a sensor that has all the properties listed is still far from reaching an end.

This chapter will begin with definition of chemical gas sensor, its Classifications and its main parameters. Then we describe the sensing mechanism of chemical gas sensor. At the end of the chapter, we present the role of nanotechnology in gas sensor, and applications and implications of gas sensor.

## 2.2 Definition of chemical gas sensor

A chemical gas sensor is a system that transforms chemical information, which arises from the physico-chemical interactions of the gaseous specimens with the sensor, into a usable signal. A gas sensor consists of two main parts: a sensing element (it is the sensitive film in the MOS sensors) for recognizing the gas with which it interacts and a transforming system (transducer) transforming the interaction between the gas and the sensing element into a certain analytical signal (usually an electrical signal) (Figure 2.1). Usually, the sensing element and the transducer are merged in the MOS sensors [165].

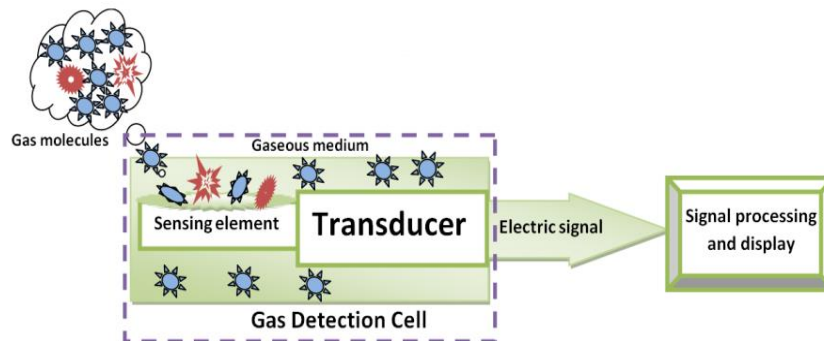


Figure 2.1: Schematic of a chemical gas sensor.

### 2.2.1 Sensing element of the chemical gas sensor

The operating principle of chemical sensors is based on the choice of the sensitive layer on which the emitted signal depends which is due to the physical and/or chemical interaction between a sensitive material and the chemical species. These materials are chosen to react specifically with a chemical species, so good selection is ensured. The physico-chemical adsorption on the surface of the sensor leads to the modification of a physical quantity which is most often the resistivity of the material and sometimes the variation of the mass of the sensitive element [166]. According to the material used as a base material for the manufacture of the chemical sensor, it is possible to distinguish two types of sensors based on deposition of the material (case of metal oxides and polymers) or by immobilization of the biological material (case of bio-receivers) on the surface of the transducer.

If metal oxides are used as Sensing elements in chemical gas sensors, then called Metal Oxide Semiconductor (MOS) sensors. The MOS sensors are one of the most

important chemical gas sensors, it is designed to react with one class of gases. Whereby the sensitive film In the MOS sensors undergoes reduction and oxidation. This process causes the sensitive film to exchange electrons with the target gas at a certain characteristic rate, thereby affecting the sensor's resistance and yielding a certain electrical signal. The electrical resistance of the MOS sensor changes drastically (increase or decrease), when exposed to the molecules of analyzing gas. This increase or decrease depends on the nature (or type) of MOS material and the gas (Table 2.1).

**Table 2.1:** Classification according to the response of sensing element [167, 168].

Classification	n-type	p-type	Example gases
<b>Reducing gas</b>	Resistance decrease	Resistance increase	H <sub>2</sub> , H <sub>2</sub> S, CO, NH <sub>4</sub> , CH <sub>4</sub> , Acetone, Methanol, Ethanol
<b>Oxidizing gas</b>	Resistance increase	Resistance decrease	O <sub>2</sub> , O <sub>3</sub> , NO <sub>x</sub> , CO <sub>2</sub>

### 2.2.2 The transducer of the chemical gas sensor

All chemical sensors contain a transducer that transforms the chemical, physical or biological response into a generally usable signal in electrical form. The choice of transducer also depends on the application of the sensor, the type of reaction, and the substance released or consumed. The transducer ensures the transformation of the signal emitted by the sensitive element in contact with the target substance. However, the choice of transducer is related to the type of reaction and the substances released or consumed [166]. The relationship between chemical recognition and that of the transduction mode is shown in table 2.2.

**Table 2.2:** Relationship between chemical recognition and transduction mode.

chemical recognition	Mode of transduction	Transducer
Change in concentration	Amperometry	Amperometric electrode
	Potentiometry	Potentiometric electrode
Modification of the conductivity	Conductivity	Conductivity cell
Heat of reaction	Thermometry	Thermistor, thermocouple
Mass modification	Piezoelectric Biosensors	Quartz Microbalance Surface Acoustic wave (SAW)

## 2.3 Classification of chemical gas sensors

there are a large variety of gas sensors based on different sensing principles, e.g. semiconductor sensors, optical sensors, calorimetric sensors, quartz microbalance sensors and electrochemical sensors. The sensing phenomena in all these devices rely on different chemical and physical changes such as:

- ❖ Changes in electrical properties (conductivity, impedance, capacitance...)
- ❖ Optical properties (absorption, reflection, luminescence, refractive index...)
- ❖ Physical properties (mass, thermal conductivity, acoustic waves propagation)
- ❖ Measuring the reaction heat.
- ❖ Analyzing specific electrochemical or biochemical recognition.

In order to give a clear introduction of sensing principles, we can classify gas sensing technologies by methods into two groups: methods based on variation of electrical properties and methods based on variation of other properties, as shown in Figure 2.2.

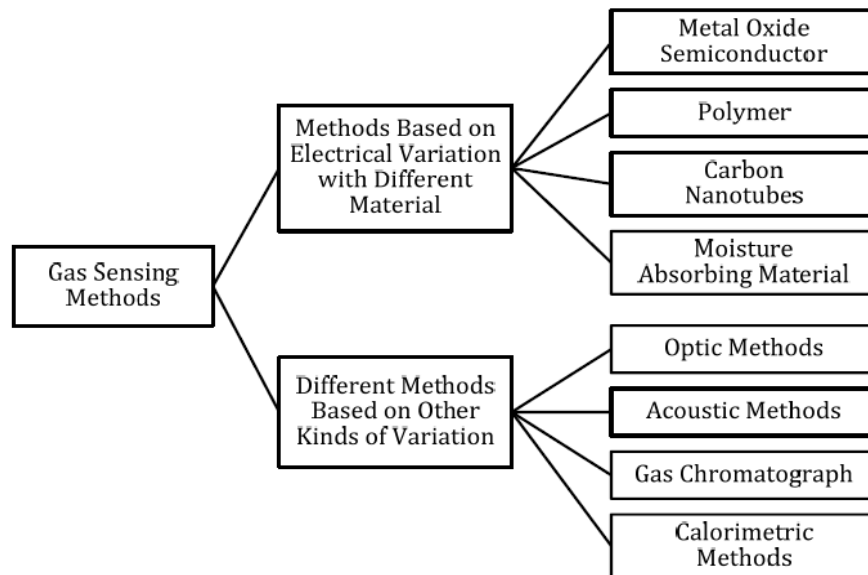


**Figure 2.2:** Classification of gas sensing methods [169].

Table 2.3 provides an overview of the operating principle of a various families of chemical sensors.

**Table 2.3:** The operating principle of a various families of chemical sensors [167-171].

Family	Operating principle
<b>Chemical sensors</b>	Their principle is based on oxidation-reduction reactions. The absorption of the gas gives rise to a specific electrochemical reaction, which induces an electromotive force linked to the transfer of charges between the gas and the cell.
<b>Surface acoustic wave sensors</b>	A sensitive layer for adsorbing the substance to be detected, it is deposited on the path of a wave between two electrodes. The adsorption of the target compound modifies the propagation of the wave and therefore its frequency.
<b>Field Effect transistor (FET) sensors</b>	Their principle is to integrate on the FET grid a membrane sensitive to the species to be detected. Upon absorption of an acceptor or electron donor gas, there will be a change in the surface potential resulting in a change in the charge carrier concentration at the channel and finally a change in the conductance.
<b>Quartz Microbalance sensors</b>	Their principle is based on the variation of the resonance frequency of the sensitive (piezoelectric) material when a species adsorbs on its surface.
<b>Semiconductor-based sensors</b>	Their principle is based on the measurement of the electrical conductivity variation of a metal oxide when a gas reacts with the oxygen adsorbed on its surface.
<b>Optical sensors</b>	Their principle is based on the modification of the optical properties of sensor when exposed to the target gas, where are utilized the spectroscopic, surface plasmon resonance, ellipsometric or measurements of Absorbance, reflectance, luminescence, fluorescence, refractive index, etc.
<b>Calorimetric sensors</b>	These sensors make use of temperature changes that are caused by interactions of sensitive solid surfaces with molecules of target gas.
<b>Capacitive sensors</b>	Absorption of gas molecules into the dielectric (most commonly polymers) of a capacitor results in changes of its electrical capacitance.

## 2.4 The main parameters of gas sensor

The performance of a gas sensor is commonly governed According to the following parameters, Sensitivity, Selectivity and Stability, reversibility, the response time, recovery time and the reproducibility [171- 173]. These parameters are largely dependent on the nature of the sensitive material as well as its physicochemical and microstructural properties. A typical response curve, that is, variation of resistance of

sensor with time on exposure and withdrawal of analyzing gas, is schematically depicted in figure 2.3. The above parameters are detailed below:

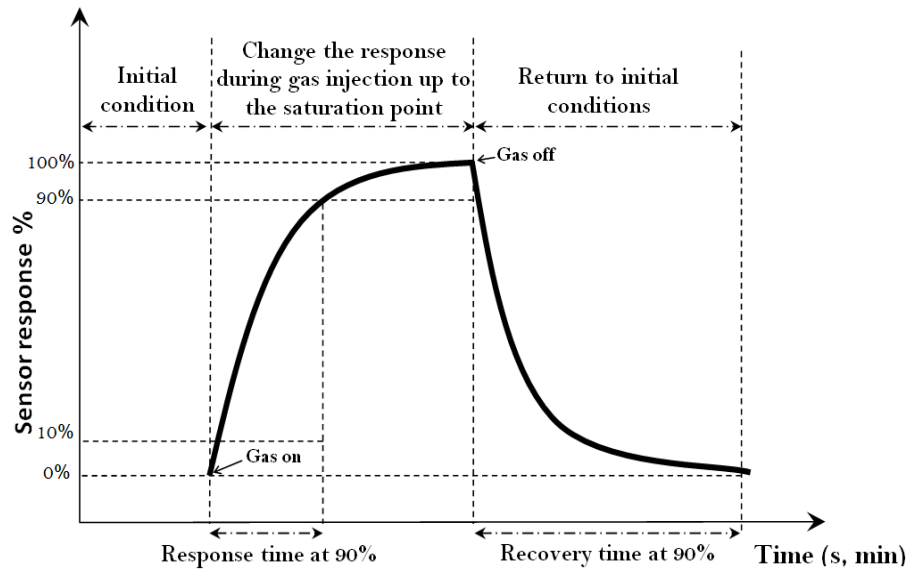


Figure 2.3: Schematic response-curve of a chemical gas sensor.

### 2.4.1 Sensitivity

Sensitivity represents the ability of the component to perceive a variation in a physical and/or chemical property of the sensitive material under gaseous exposure. Sensitivity is therefore a parameter that expresses the variation of the sensor response as a function of the gas concentration. Since the response of the gas sensors is generally nonlinear, the sensitivity is not constant. The sensitivity is generally defined as the ratio of the resistance of the sensing element in the target gas to that in air, in the case reducing gases, and the inverted in the case the oxidizing gases. Usually, in order to be able to compare the sensitivities of sensors we use the relative response.

In the case the relative difference measurement, the relative response ( $S$ ) is calculated using the formulas [174, 175].

- for the reducing gas:

$$S(\%) = \frac{|R_a - R_g|}{R_a} \times 100 \quad (2.1)$$

- for the oxidizing gas:

$$S(\%) = \frac{|R_g - R_a|}{R_g} \times 100 \quad (2.2)$$

In the case the relative measurement, the relative response (S) is calculated using the formulas [175- 177].

- for the reducing gas:

$$S(\%) = \frac{R_g}{R_a} \times 100 \quad (2.3)$$

- for the oxidizing gas:

$$S(\%) = \frac{R_a}{R_g} \times 100 \quad (2.4)$$

Where ( $R_a$ ) is the sensor resistance under the air at a given temperature (T) and ( $R_g$ ) is the sensor resistance under the target gas at the same temperature (T).

A sensor is all the more sensitive if as a small variation in the concentration of the gas will cause a significant variation in the measured resistance. Sensitivity (or relative response) is one of the strengths of MOS sensors whose variation in resistance can be measured for concentrations of the order of ppm (parts per million) or even hundred ppb (part per billion) [178].

In MOS sensors the sensitivity is highly dependent on films porosity, its thickness, its morphology, its microstructure, operating temperature, presence of additives and crystallite size (Table 2.4). In order to improve it, it will be of great interest to work with the most appropriate sensing material in every case and reach its optimum detecting temperature (Figure 2.4). working with nanostructure materials will give a higher surface area in front of gas. Taking into account that sensing reactions take place mainly on sensor layer surface, the control of semiconductor grain size will be one of the first requirements for enhancing the sensitivity of the sensor.

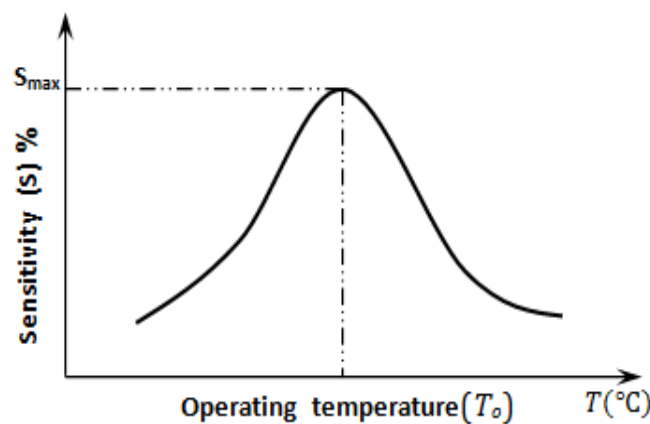


**Figure 2.4:** Sensitivity variation as a function of temperature at a specific concentration of gas, for the determination of operating Temperature and  $S_{\max}$  values.

## 2.4.2 Operating temperature

It is the temperature that corresponds to maximum sensitivity (Figure 2.5), obviously it is The operating temperature should be specified for any sensor. It is a function of the semiconductor oxide composition and of the gas which is to be detected (Figure 2.6). It is important to define this parameter because with respect to single gas, the sensor reaches the maximum of its sensitivity at a precisely fixed temperature.

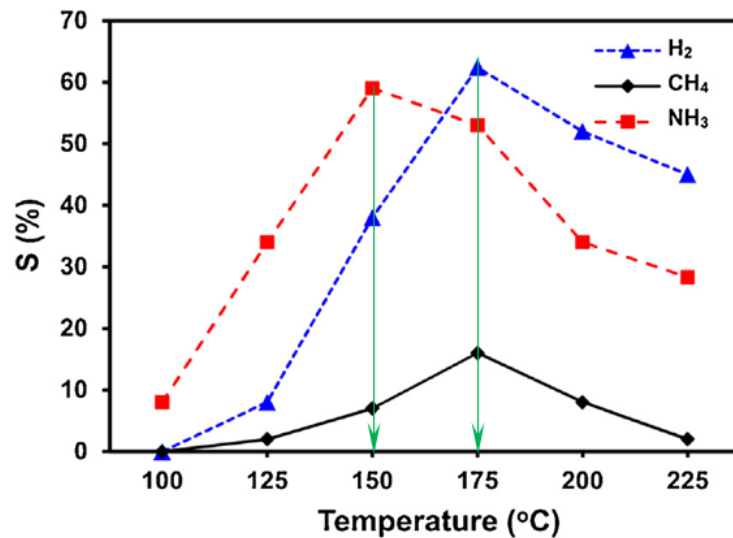


**Figure 2.5:** Gas sensor responses of NiO sensor for different operating temperatures under 3000 ppm of H<sub>2</sub> and CH<sub>4</sub> and 75 ppm of NH<sub>3</sub> [180, 181].

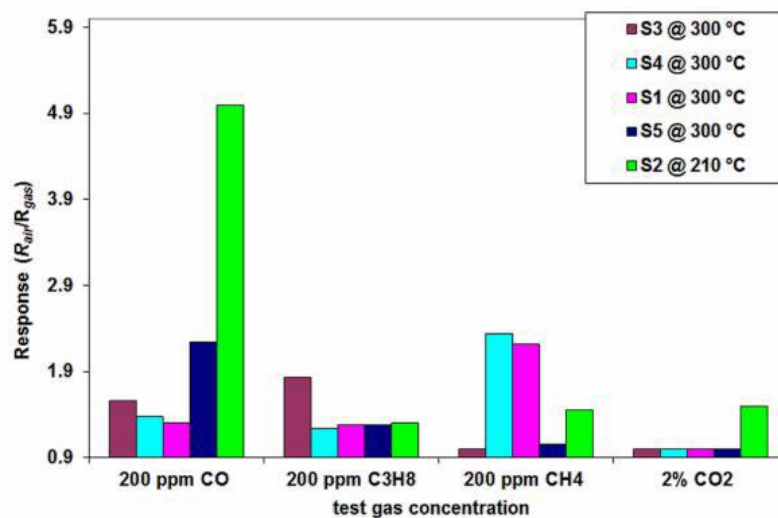


**Figure 2.6:** Sensors response for different gases, at the corresponding operating temperatures [182].

### 2.4.3 Selectivity

This characteristic is related to the discrimination capacity of a sensor towards a mixture of gases. Selectivity plays a major role in gas identification. Generally, a ‘fingerprinting’ method relies on a unique signature of the target gas signal. However, gases often produce very similar sensor responses (except when comparing reducing to oxidizing gases). For example, gases such as ethanol, carbon monoxide, and methane have appreciable cross-sensitivity that hinders the development of a domestic gas sensor that can distinguish these species [171]. Common techniques of improving the selectivity of gas sensors include controlling the sensor operating temperature, selective gas filters used in series with gas sampling, and using additives. Different operating temperatures allow the control of the sensitivity toward a particular gas when there is a unique  $T_C$  (critical temperature/optimum temperature with maximum sensor response) for each gas (Figure 2.7). thus allowing the sensor to produce distinguishable signals for two gases at a selected temperature. The film morphology and sensor architecture can also play a key role in selectivity [171]. Distinguishing poorly reactive gases from reactive gases can be facilitated by placing electrodes further inside the bulk of the sensing material to allow reactive materials to be filtered by the sensing material near the surface of the sensor. Another technique uses catalysts, which generally reduce the operating temperature of a gas sensor for a particular gas species and thus allow the target gas to be distinguished from other gases due to the differences in sensitivity (Figure 2.8). In other words, addition of catalysts can maximize the sensitivity of target gases to produce a distinct signal.

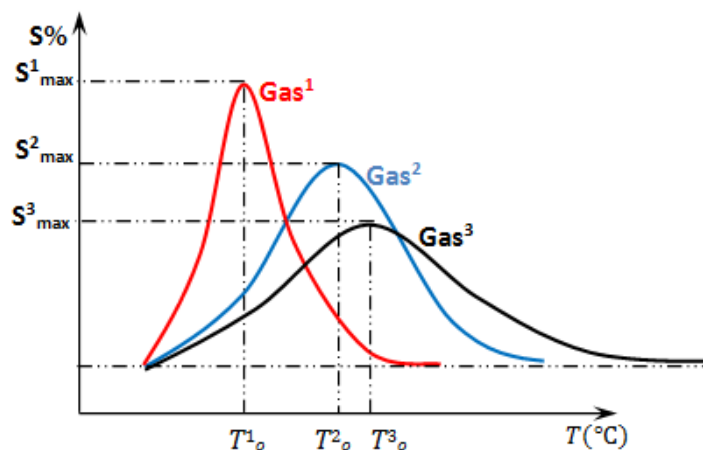


**Figure 2.7:** Variation of the values and forms of response as a function of the temperature variation for different gases having the same concentration.

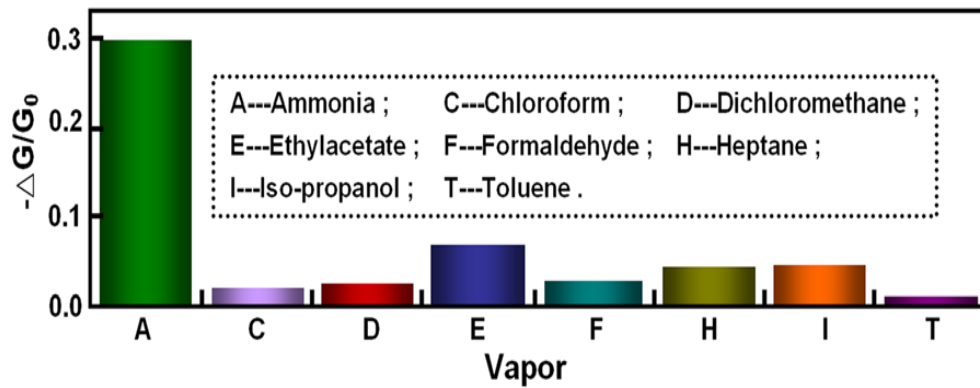


**Figure 2.8:** Selectivity tests of gas sensors based on NiO films, the concentration of  $\text{NH}_3$  is 50 ppm, and the concentration of other organic gases is higher than 300 ppm [183].

#### 2.4.4 Stability

It is a characteristic that takes into account the repeatability of device measurements after a long use. The success of the sensor will be limited if the sensor performance is not demonstrated as repeatable and stable over long-term testing (Figure 2.9). Problems of stability, may be attributing to three primary areas of concern. The first is that a surface conductive sensor can suffer from surface contamination. Second, changes in the sensor characteristics (such as intergranular connectivity) can occur due to thermal expansion coefficient mismatch or interfacial reactions at the metal electrode interface. Last the film morphology may change over time due to the relatively high operating temperatures of the sensor, which may change over time due to the relatively high operating temperatures of the sensor, which may also cause migration of additives. To avoid the effects of non-repeatability after repeated use, the sensor materials are submitted to a thermal pretreatment; during these treatments samples are submitted to high calcinations temperatures to avoid instabilities during their working life.

#### 2.4.5 Response time

The response time is the time interval over which resistance attains a fixed percentage (usually 90%) of final value when the sensor is exposed to full scale concentration of the gas. Time response is especially dependent on the sensor characteristics such as crystallite size, additives, electrode geometry, electrode position, diffusion rates, etc. A small value of response time is indicative of a good sensor.

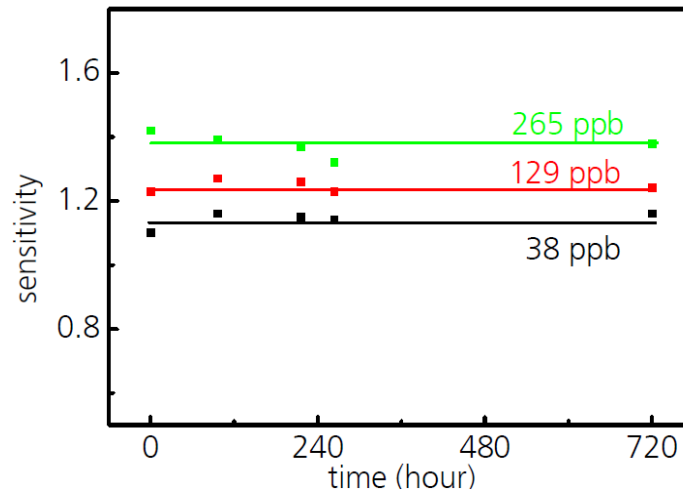


**Figure 2.9:** Long-term stability of sensor signal to ozone gas with different concentrations [184].

#### 2.4.6 Recovery time

This is the time interval over which the sensor resistance reduces to 10% of the saturation value when the sensor is exposed to full scale concentration of the gas and then placed in clean air. A good sensor have a small recovery time so that sensor can be used over and over again.

#### 2.4.7 Reproducibility or repeatability

This parameter is probably the most important for both physical and chemical sensors. It is the ability of a sensor to give, under defined conditions, very similar responses when repeatedly applying the same input signal, this includes retaining the sensitivity, selectivity, response, and recovery time. That is to say, we talk about the repeatability or reproducibility if the sensor responds to a gas in the same way regardless of the number of measurements and the time between measurements. In other words, the repeatability of a gas sensor reflects its ability to produce the same response for a given gas atmosphere. Reproducibility can also be applied under changed conditions of measurement for the same measurand to check, that the results are not an artifact of the measurement procedures.

#### 2.4.8 Linearity

Linearity is the relative deviation of an experimentally determined calibration graph from an ideal straight line [185].

### 3.5.9 Sensitivity limit or detection limit

This is the smallest value of the measurable quantity to be detected under given conditions, or minimum detectable target gas concentration, far from the range of uncertainty of experimentation, particularly at a given temperature (Figure 2.10) [185].

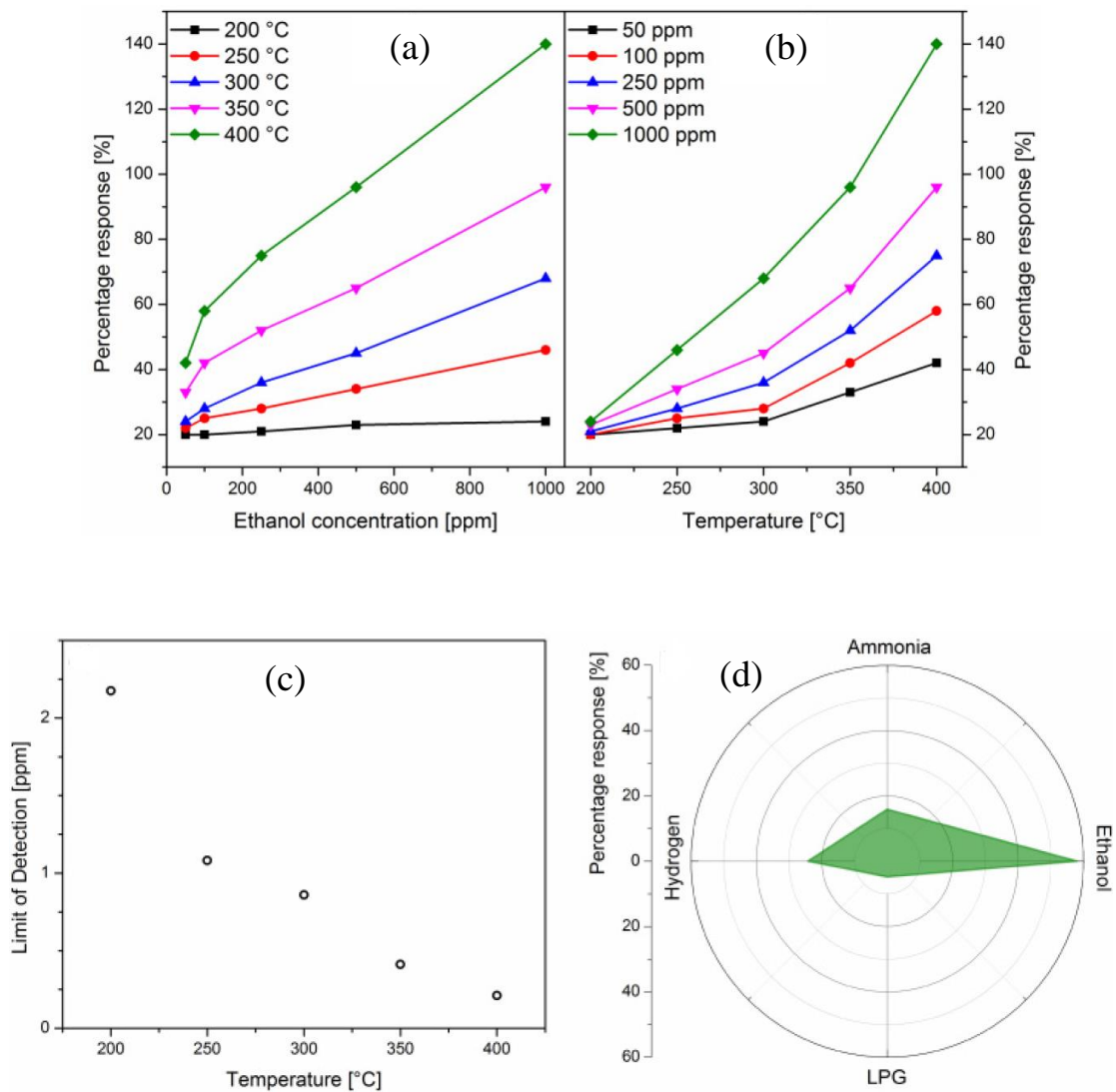


**Figure 2.10:** Percentage response as a function of (a) ethanol concentration and (b) working temperature, (c) limit of detection as a function of the sensor operating temperature (Polycrystalline NiO nanowires) and (d) selectivity plot at 200 °C for 100 ppm of gas [186].

Table 2.4 shows the effect of some factors on the parameters of the chemical gas sensor. While the table 2.5 shows a comparative study among different large families of sensors.

**Table 2.4:** Some factors affecting the parameters of the chemical gas sensor [172].

Sensor parameter	Some influencing factors
Sensitivity	<ul style="list-style-type: none"> <li>• Nature of sensitive material</li> <li>• Structure (porosity, morphology, crystallinity ...)</li> <li>• Doping (copper, platinum, cobalt ...)</li> <li>• Operating temperature</li> </ul>
Stability and Repeatability	<ul style="list-style-type: none"> <li>• Stability of the sensitive material</li> <li>• Operating temperature</li> <li>• Measurement Conditions (temperature, humidity, pressure...)</li> </ul>
Selectivity	<ul style="list-style-type: none"> <li>• Doping</li> <li>• Selective filters</li> <li>• Operating mode</li> </ul>
Reversibility	<ul style="list-style-type: none"> <li>• Nature of sensitive material vis-à-vis gas to detect</li> <li>• Structure</li> <li>• Operating temperature</li> </ul>

**Table 2.5:** Comparative study of the characteristics of the large families of sensors [164, 178].

Classification	Semiconductor	Catalytic	Electrochemical	Thermal conductivity	Infrared absorption
Sensitivity	++	+	+	--	++
Selectivity	-	--	+	--	++
Precision	+	+	+	+	++
Response time	++	+	--	+	-
Stability	+	+	-	+	+
Durability	+	++	-	+	++
Maintenance	++	++	+	+	-
Cost	++	++	+	+	-
Portability	++	+	-	+	--
Integration in an embedded system	++	+	-	+	--

## 2.5 Gas sensing mechanism in (MOS) gas sensors

The semiconductor gas sensors consist of oxide semiconductor grains and have electrons or holes conductivity. The external exposure of any gas influences the conductivity. It can change the conductivity of the bulk or the grain surface. The gas molecules are active particles in semiconductor oxides and create donor or acceptor states of the grain surface [187].

### 2.5.1 Principles of primary physical interaction

When a surface of oxide semiconductor grains is placed in the presence of a gaseous medium, it will interact with the middle. The gas molecules will collide with the surface of the host material through thermal agitation. We can then distinguish three cases (Figure 2.11) [178]:

- The phenomenon of "scattering", the gaseous molecule hits the surface under a elastic shock, loses very little energy and bounces off the surface.
- The phenomenon of "trapping", the gaseous molecule loses energy during the collision but can't be mobile on the surface.
- The "sticking" phenomenon, the gaseous molecule dissipates a lot of energy and remains immobile at the surface after the collision. This is the phenomenon on which the gas-sensor interaction is based on which our work will be based.

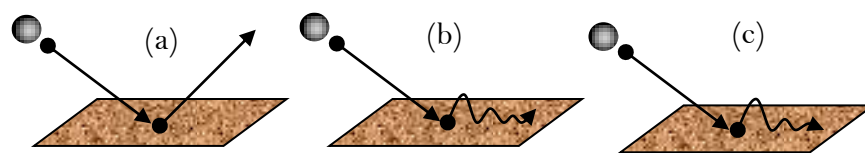


Figure 2.11: The phenomenon of: (a) scattering, (b) trapping and (c) sticking.

### 2.5.2 Basic phenomena of sensing

Thin films of metal oxides like ZnO, SnO<sub>2</sub>, WO<sub>3</sub>, NiO etc. when heated in the range of 100°C to 400°C in air sensitively respond to a wide range of oxidizing and reducing test gases via resistance changes. The process involved in sensing is described below [187, 188]:

1. Diffusion of reactants to the active region;
2. Adsorption of reactants on to the active region;

3. Surface reaction;
4. Desorption of products from the active region;
5. Diffusion of products away from the active region;

Diffusion of reactants to active region depends on the ambient temperature of the measurement and atmosphere. Once the molecules of gas diffuse into the active layer; they tend to adhere to the sensing surface. This process is called adsorption, it's of three types namely physisorption, chemisorption and ionosorption.

If the gas molecules are in contact with metal oxide surface, they can adsorb with physisorption or chemisorption. Physisorption is a weak adsorption between adsorbate and adsorbent which the heat of adsorption is less than 6 Kcal.mol<sup>-1</sup>. In the chemisorption process, the gas molecules interact more strongly with a solid atom and the heat of adsorption is greater than 15 Kcal.mol<sup>-1</sup>. Figure 1.12 shows Lennard-Jones model for physisorption and chemisorption process. It can be seen that the heat of adsorption  $\Delta H_{\text{physis}}$  relatively smaller than  $\Delta H_{\text{chem}}$ . It should be noted that the heat of chemisorption is comparable to a heat of compound formation [180, 181].

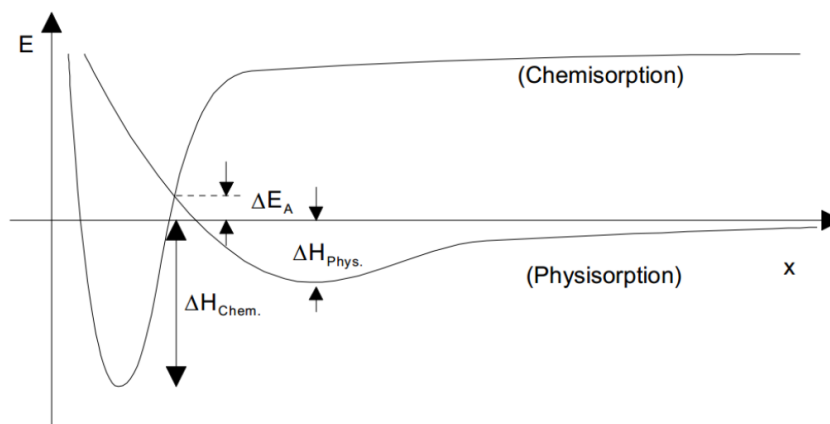


**Figure 2.12:** Leonard-Jones Model for physisorption and chemisorption [180].

### 2.5.3 Working principle

The gas-detection principle of metal oxide is based on the variations of the depletion layer at the grain boundaries in the presence of reducing or oxidizing gases, which lead to modulations in the height of the energy barriers for free charge carriers to flow, thus leading to a change in the resistance of the sensing material. In other words, gas molecules interacting with the metal oxides either act as a donor or acceptor of charge carriers (Receptor function), and alters the resistivity of the metal oxide

(Transduction function) and it is shown in figure 2.13. In the atmosphere, oxygen is the second largest element after nitrogen. Oxygen plays a predominant role in the adsorption process due to its high electronegativity of about 3.65 and lone pairs of electrons, making it easily adsorbed on the surface of metal oxides. Diatomic oxygen is a non-reactive species in the gas phase, while interacting with the metal oxide surface, it acts as an electron acceptor and gets ionized and forms an ionic layer on the surface.

When the sensor is exposed to combustible gases for example, the surface oxygen species react to form combustion products. This reaction lowers the oxygen species coverage, returns the free electron charge carriers to the bulk of the oxide material and decreases resistance. This surface reaction modulated resistance serves as a gas response signal of the sensor.

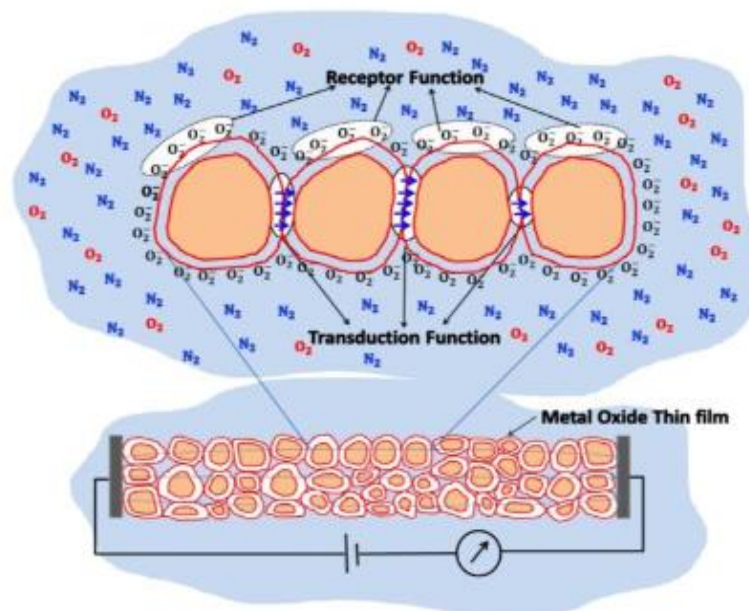


**Figure 2.13:** Schematic of metal oxide thin film gas sensor [189].

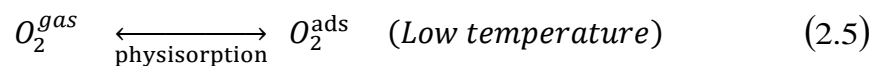
This helps in sorption of other gas molecules on to the metal oxide surface. In dry atmosphere, chemisorbed oxygen molecule strongly influenced the receptor function. Thus, the principle of metal oxide gas sensor mainly depends upon the oxygen concentration and its rate of adsorption and desorption. During the adsorption process, the oxygen molecule gains an electron from the metal oxide surface and turned to ionic form as,  $O_2^-$ ,  $O^-$  and  $O^{2-}$  [189, 190], Thus electrons trapped on the surface of grains (Figure 2.14), and results in the increase of the width of space charge region and hence the height of potential barrier. This in turn, reduces the conduction of electron be-

tween the grains, which influence the transduction process of the metal oxide surface. In addition, the grain boundary resistance also plays a crucial role in determining the surface resistance of the sensing element.

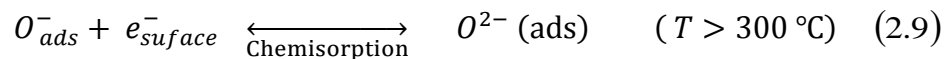
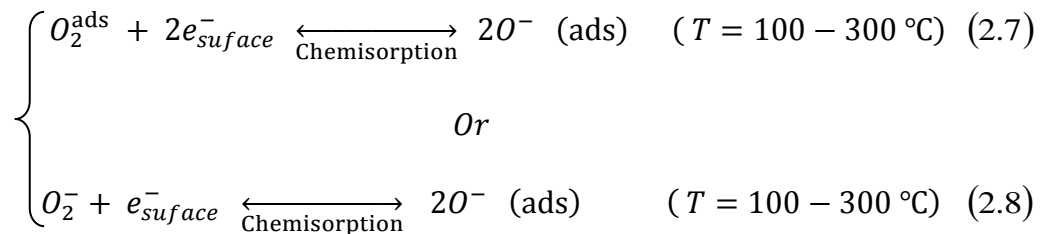
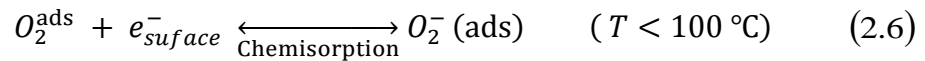
When the sensor is exposed to combustible gases for example, the surface oxygen species react to form combustion products. This reaction lowers the oxygen species coverage, returns the free electron charge carriers to the bulk of the oxide material and decrease resistance. This surface reaction modulated resistance serves as a gas response signal of the sensor.

At elevated temperatures, reactive oxygen species such as  $O_2^-$ ,  $O^-$  and  $O^{2-}$  are adsorbed on the surface of metal oxide semiconductor [190, 191]. The sequence of processes involved in the adsorption of oxygen on the metal oxide surface can be described by the following formulas [189, 192]:

- Physisorption



- Chemisorption



In n-type semiconductor, the majority charge carriers are electrons. When it interacts with a reducing gas, a decrease in resistance occurs. On the other hand, an oxidizing gas depletes the charge carriers, leading to an increase in resistance (Figure 2.16). Similarly, in the case of p-type semiconductors, where positive holes are the majority charge carriers, a decrease in the resistance is observed in the presence of an oxidizing gas (the target gas increases the number of positive charge carriers or holes) (Figure 2.15). On the other hand an increase in resistance is observed in the presence

of reducing gas, where negative charge introduced into the material reduces the positive (hole) charge carrier concentration. Table 2.1 summarizes the response of the sensing element towards oxidizing and reducing gases; some n and p-type metal oxide semiconductor elements are listed in table 2.6.

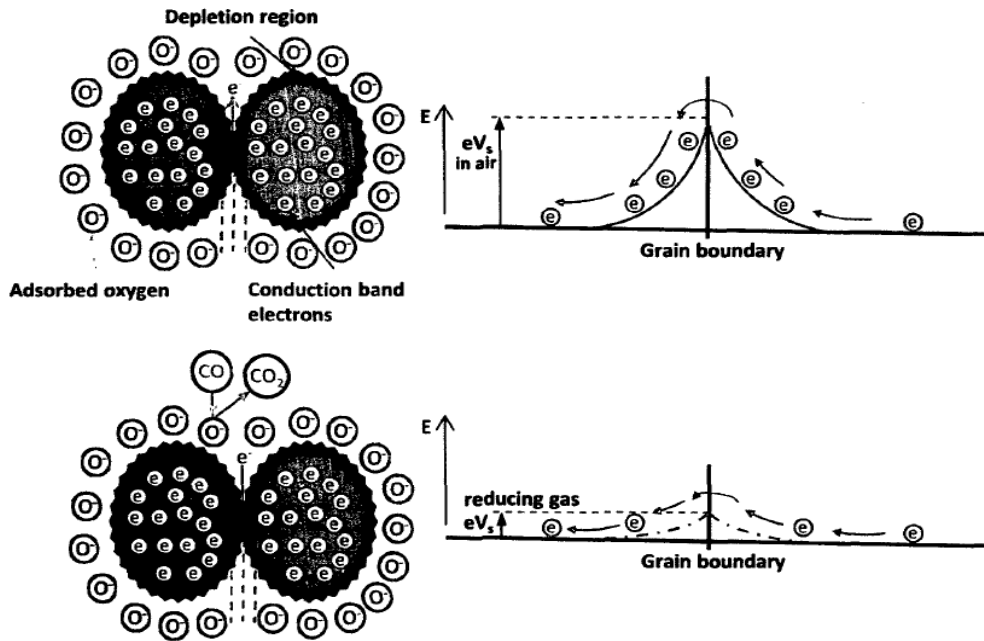


Figure 2.14: Gas sensing mechanism of metal oxide semiconductor [190].

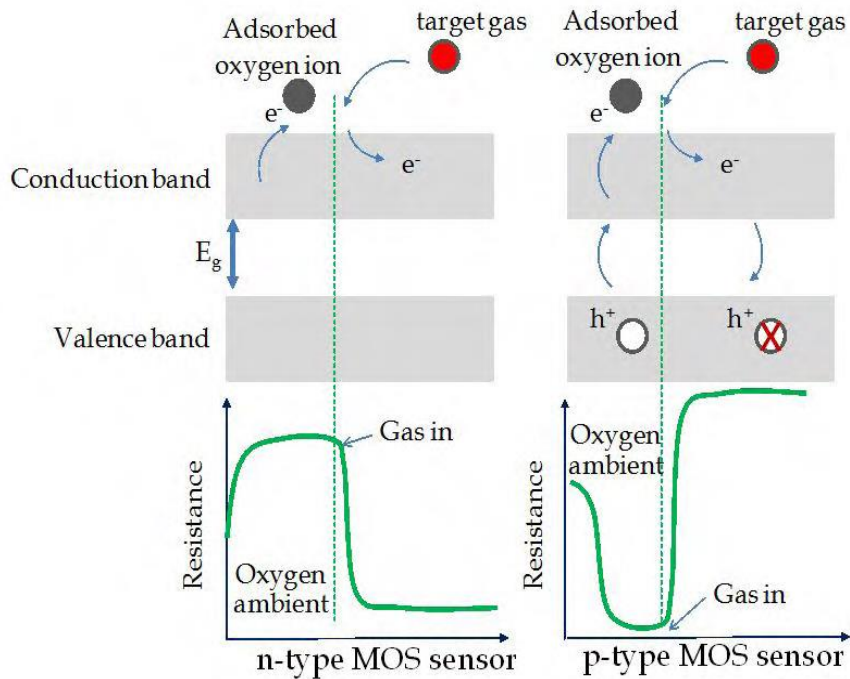
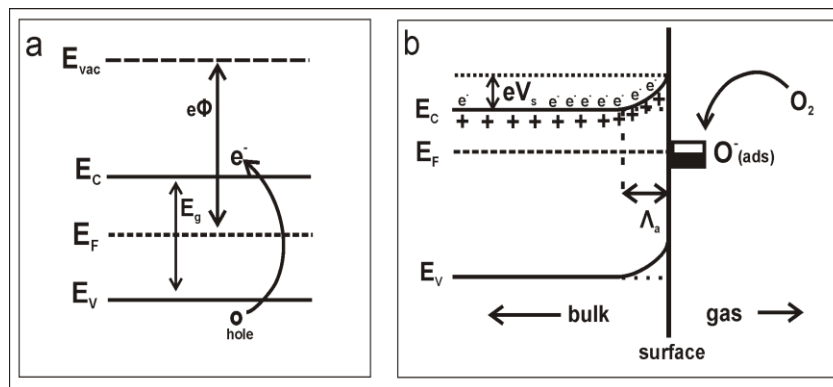


Figure 2.15: Schematic diagram of the change in sensor resistance for n- and p-type MOS in the presence of the target gas (reducing gas) [193].

**Table 2.6:** Classification of metal oxides based on the conductivity type [180].

Type of Conductivity	Metal oxides
n-type	ZnO, MgO, CaO, TiO <sub>2</sub> , WO <sub>3</sub> , SnO <sub>2</sub> , In <sub>2</sub> O <sub>3</sub> , Al <sub>2</sub> O <sub>3</sub> , Ga <sub>2</sub> O <sub>3</sub> , V <sub>2</sub> O <sub>5</sub> , Nb <sub>2</sub> O <sub>5</sub> , ZrO <sub>2</sub>
p-type	Y <sub>2</sub> O <sub>3</sub> , La <sub>2</sub> O <sub>3</sub> , CeO <sub>2</sub> , Mn <sub>2</sub> O <sub>3</sub> , NiO, PdO, Ag <sub>2</sub> O, Bi <sub>2</sub> O <sub>3</sub> , Sb <sub>2</sub> O <sub>3</sub> , TeO <sub>2</sub>

Trapping of electrons by the adsorbed molecules leads to band bending, this affects the conductivity of the metal oxides. The upward bending of the energy bands due to the negative charges trapped in these oxygen species leads to a decrease in the conductivity. As shown in figure 2.16, when O<sub>2</sub> molecules are adsorbed on the surface of metal oxides, they would extract electrons from the conduction band E<sub>c</sub> and form ions. This will lead to band bending and an electron depleted region (space charge region). The thickness of this space charge region is equivalent to the length of band bending region.



**Figure 2.16:** a) Simple schematic of the band diagram of a semiconductor. E<sub>v</sub>, E<sub>F</sub>, E<sub>c</sub>, E<sub>vac</sub>, E<sub>g</sub> denote the energy of the valence band, Fermi level, conduction band, vacuum level and band gap and Φ represents the work function. At 0 K, the conduction band is completely empty and at higher temperatures, electrons can jump to the conduction band leaving holes in the valence band. b) A simplified model of band bending at the surface of an n-type semiconductor after chemisorption of charged species is illustrated. Λ<sub>a</sub> denotes the thickness of the space charge layer and eV<sub>s</sub> denotes the potential barrier formed in the space charge region. The Fermi energy has the same value everywhere in the material. As a result of the surface charges accumulated on the surface due to gas adsorption, the bands bend close to the surface to keep the Fermi energy constant [188].

## 2.5.4 Parameters influencing the conductive properties of the sensor:

There are several parameters that affect the detection of gases. We can count among these parameters, the morphology of the sensitive layer, the temperature and the relative humidity present in the gaseous environment.

### 2.5.4.1 Influence the morphology and porosity of the sensitive layer

The structure of the sensitive layer takes into account the morphology of this layer. We can control the morphology of the sensitive layer by the parameters of deposition techniques. The porosity of the material has a significant effect on the sensor's response to the gases entering into operation. The interaction of dense (compact) or porous layers with gases is different. The porous layers are accessible to gases because of their large internal surface, whereas the dense layers interact with gases only on the surface of the layer (See figure 2.17). We can therefore expect greater sensitivity and greater immunity to sensor poisoning in the case of porous layers. Thus, the diffusion of the gaseous molecules through the porous material increases with the size of the grains according to the Knudsen equation [168].

$$D_k = \frac{4r}{3} \sqrt{2RT/\pi M} \quad (2.10)$$

Where  $D_k$  is the Knudsen diffusion constant,  $r$  is the grain radius,  $R$  is the perfect gas constant,  $T$  is the temperature and  $M$  is the molecular weight .

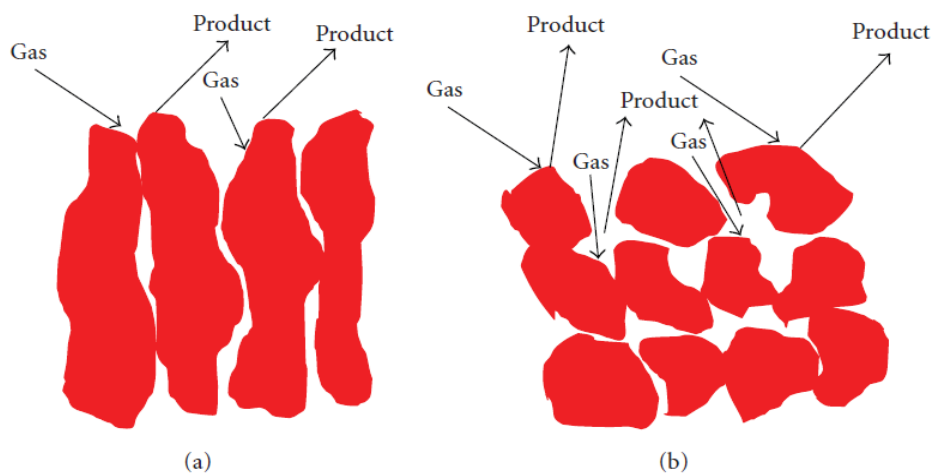


**Figure 2.17:** Schematic view of gas sensing reaction in (a) compact layer and (b) porous layer [194].

### 2.5.4.2 Influence of grain size

The sensitive layer is a polycrystalline material with defects such as grain boundaries that influence the electrical properties of the metal oxide. This influence is more or less important depending on the size and shape of the grains. Indeed, there are three main contributions: the "heart" of the grain, the grain boundary materialized by the zone of depletion or accumulation and the semiconductor metal interface located at the electrodes .

Yamazoe et al [195] studied the effect of the size of SnO<sub>2</sub> thin film crystallites on the sensitivity to detect CO and H<sub>2</sub>. The authors followed the variation of the resistance and sensitivity at 300°C of these layers consisting of crystallites of different sizes (5-27nm). The Sensitivity values were highest for samples with the lowest crystallite sizes (around 5-10 nm), and varies linearly with the ratio 1/D (Figure 3.18), where D is the size of the crystallites. Expressed otherwise, for crystallites of spherical shape (ratio: surface/volume = 6/D), the sensitivity is proportional to the surface/volume ratio.

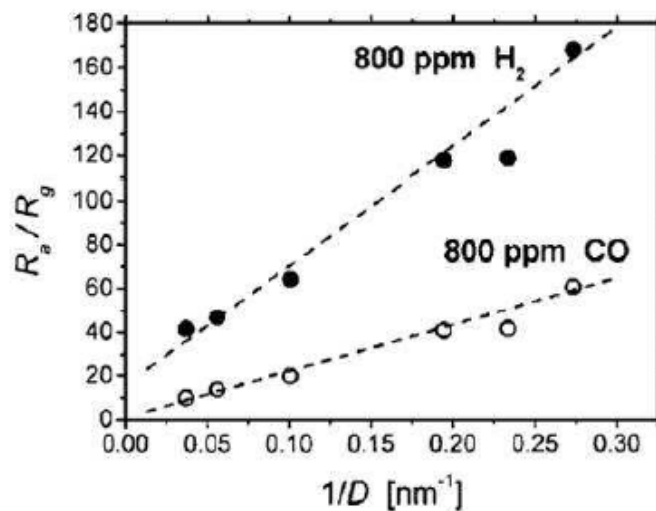


**Figure 2.18:** Influence of crystallite size on sensitivity ( $R_a/R_g$ ) at 300°C [196].

To explain this phenomenon, a schematic representation is presented in Figure 2.19. The model takes into account a thin film consisting of small grains (5 to 30 nm in diameter) connected together by collars and forming small clusters. According to the size of the crystallites (D) and the thickness of the depletion zone (L), Yamazoe distinguishes three modes of conduction [195]:

- For large grains ( $D \gg 2L$ ), no influence of the gaseous phase on the volume of the crystallites, the depletion zone is poorly conductive on the surface of the grain

- clusters and the conductance of the whole is controlled by the grain boundaries (grain boundaries control).
- In the case where ( $D \approx 2L$ ), a surface part of the grains is occupied by the zone of Depletion and conductance of the layer is determined by the transport of electrons through each interface (interface control).
  - When ( $D < 2L$ ), the depletion zone then occupies the whole grain volume and the conductance is controlled by the grain (grain control).

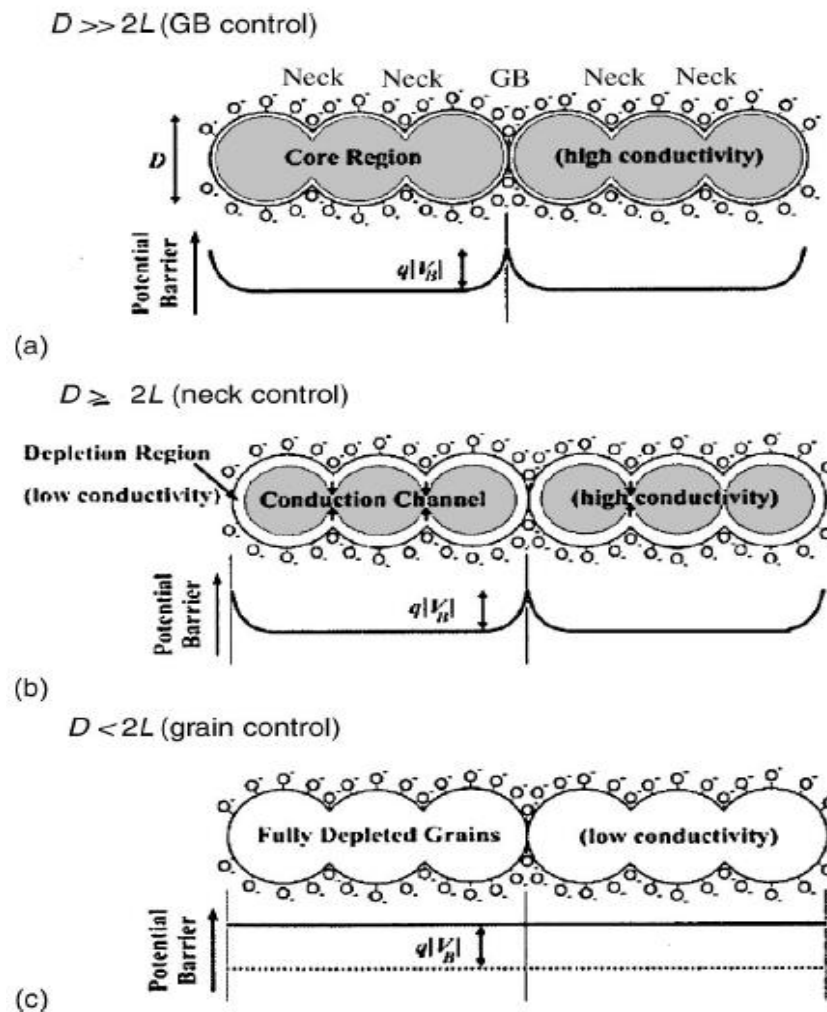


**Figure 2.19:** Schematic model of the effect of the crystallite size on the sensitivity of metal-oxide gas sensors: (a)  $D \gg 2L$  (GB control); (b)  $D \geq 2L$  (neck control); (c)  $D < 2L$  (grain control) [196].

### 2.5.4.3 Influence of the temperature

Since the temperature involved in the main physico-chemical mechanisms (adsorption and desorption) occur on the surface of oxides, most metal oxide-based sensors are

optimal at temperatures above 200°C. Temperature is a parameter very important in the process of gas detection, but it also has an impact on the physical properties of the sensitive layer, in particular the electrical conductivity, as well as on the dynamic properties of the sensor, such as the response time. Using too low a temperature can result in long response times.

#### 2.5.4.4 Influence of doping

We have seen that the selectivity of sensors based on semiconductor oxides appears to be their main disadvantage and that in some cases it may be bypassed by the operating temperature. However, if the working temperature is set, for practical reasons and/or safety reasons, improvement of the selectivity is no longer possible. The most common method used to improve the selectivity of these sensors is to resort to doping. The principle consists of adding a small quantity of a metal or its oxide .

The effect of doping is multiple: the sensitivity for a given gas is increased but in parallel, the sensitivities for the other gases are reduced. There is also an improvement in the reaction times and a change in the optimum operating temperature, but it remains difficult to associate a dopant with a specific gas and the use of mixed doping may be necessary to detect a gas within a mixture.

To explain the effect of doping on the sensitivity of the sensitive layer. Two mechanisms are proposed [178].

1. The first is a mechanism based on the "spillover" effect of the additive. In this mechanism, the dopant will dissociate molecules such as O<sub>2</sub> or H<sub>2</sub> on its surface and these will then migrate to the sensitive layer; similarly to the dissociation of H<sub>2</sub> on the palladium Pd particles. This has the consequence of increasing the surface concentration of the active species H<sub>2</sub> and therefore increase the charge transfer between the sensitive layer and surface oxygen.
2. The second mechanism is based on an electron transfer between the dopant and the sensitive material. The surface additive will be oxidized by the oxygenated species and in turn will accept the electrons from the sensitive layer. Due to the presence of the dopant, the amount of oxygen species adsorbed on the surface is greater.

The doping of a sensitive layer of metal oxide seems to be a means of improving the selectivity defects thereof and increasing their sensitivities. The care should be taken not to poison the surface by adding too much dopants.

### 2.5.4.5 Influence of film thickness

As reported in the literature, the sensitivity of a sensor increases if the thickness of the sensitive layer decreases (Figure 2.20). However, it has been observed that below one critical thickness (about  $\sim 110$  nm) [168], the sensitivity decreases with the thickness, because the porosity in this case is considerably reduced, and therefore the active sites allowing the adsorption of gaseous molecules are reduced.

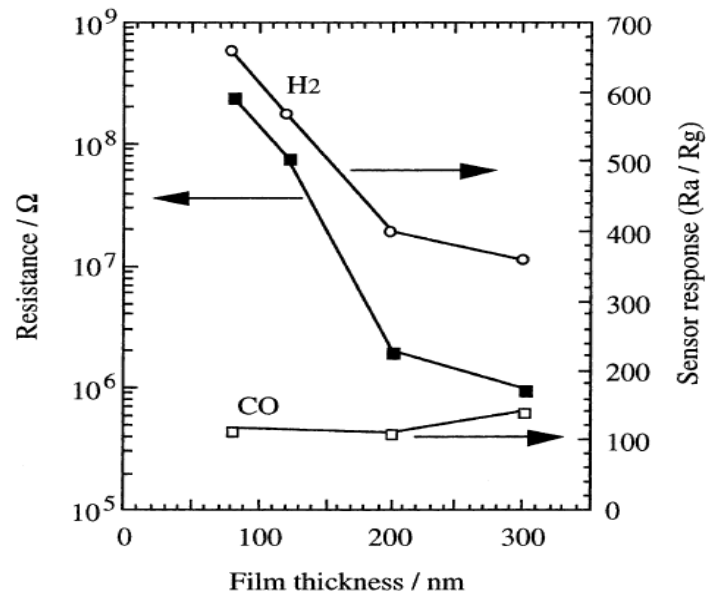


**Figure 2.20:** Electrical resistance in air as well as gas sensor response 800 ppm H<sub>2</sub> and 800 ppm CO as function of film thickness at 350°C [197].

## 2.6 Role of Nanostructures in gas sensors

Coarse grained, micron scaled polycrystalline metal oxides were the first materials commonly used in the construction of gas sensors. However, their sensing signal and resulting sensitivity is very poor. But if these oxides prepared in nanoscale dimensions, such as nanoparticles, it would be quite different. Nanostructuring of metal oxides can enhance the performance of functional materials as it gives them unique properties such as: increased surface-to-volume ratio, which provides more surface area for both chemical and physical interactions; significantly altered surface energies that allow tuning and engineering of the material's properties, as atomic species near the surface have different bond structures than those embedded in the bulk; quantum confinement effects, due to the inherently small size of nanostructured materials, that significantly influences charge transport, electronic band structure and optical properties. Since then, the particular focus is put on nanosensors and their peculiar behavior, mostly due

to quantum nature of observed effects. Nanosensors of non-porous, uniform nanoparticles potentially perform better. As it is known sensing signal results from the interaction of gas molecules with the surface layer of the semiconductor metal oxides. Thickness of this layer  $d$  is usually less than 100 nm. Using materials composed of coarse grains of a radius  $r$  greater than  $d$  ( $r \gg d$ ), the value of sensing signal is diminished by the factor of  $d/r$ . Therefore, nanomaterials with decreased particle size and increased specific surface area (high surface to volume ratio) are highly recommended for gas sensing applications [180]. In such case, the surface phenomenon overtakes the chemistry and physics of the bulk. This effect is also important for the miniaturization trend of the gas sensing devices. Consequently by use of nanosensors the following improvements of sensor performance parameters can be introduced: increased sensitivity, lower and broader detection limits, fast response and recovery time, possibility of direct detection.

## 2.7 Review researches of nickel oxide gas sensor

Metal oxides stand out as one of the most common, diverse and, most likely, largest class of materials due to their extensive structural, physical and chemical properties and functionalities. The most common metal oxides utilized as sensing layer in chemoresistive devices are binary oxides such as  $\text{SnO}_2$ ,  $\text{ZnO}$ ,  $\text{TiO}_2$  and  $\text{NiO}$ . The researcher G. Neri [198] summed up Results of a search study on semiconductor metal oxides used as sensing materials for chemoresistive gas sensors, including both the n-type and p-type oxides, are summarized in the graph shown in figure 2.21. There are extensive studies on optical/electrical properties of  $\text{NiO}$  in the literature, but there are few studies on the gas sensing property of  $\text{NiO}$  [180]. The table 2.7 shows a literature review of different elaborated  $\text{NiO}$  thin films which are used for gas sensor application.

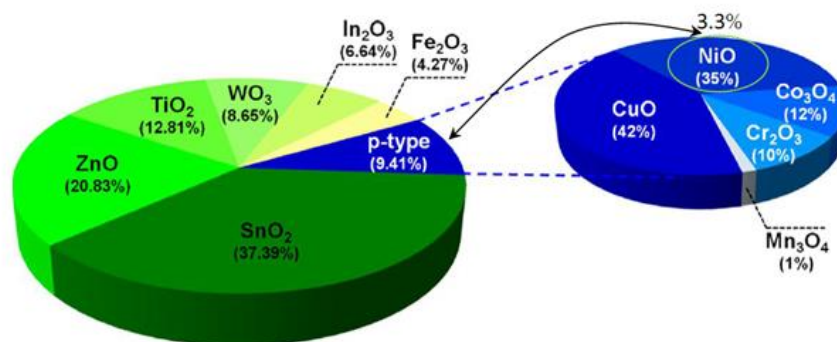


**Figure 2.21:** Studies on n- and p-type oxide semiconductor gas sensors [198].

**Table 2.7:** Literature review of different elaborated NiO thin films which are used for gas sensor application.

Method	Material	Target gas	C (ppm)	OT (°C)	Response	Ref
Sol-gel spin coating	NiO Films	NO <sub>2</sub>	200	200	23	[199]
Electrodeposition	NiO nanoroses	Ethanol	5	230	9.11	[200]
		Methanol	5	230	8.36	
		Acetone	5	230	6.44	
Template-free	Hollow NiO-SnO <sub>2</sub> nanospheres	NH <sub>3</sub>	5	300	10	[201]
CBD	nanostructures NiO films	NH <sub>3</sub>	25-150	300	114.3-41.3	[202]
CSP					31.7-142.5	
Citrate-gel	Li, Ti doped NiO	Chloroform toluene	1000	RT	4-10	[180]
Sol-gel	SiO <sub>2</sub> -NiO	H <sub>2</sub>	20-850	50	9	[203]
		CO	10-500	300	> 1	
Magnetron Sputtering	TiO <sub>2</sub> -NiO	H <sub>2</sub>	500	250	5-25	[180]
Pulsed laser deposition	NiO	H <sub>2</sub>	3000	80	12-14	[180]
				210	40	
RF sputtering	NiO Films	H <sub>2</sub>	5000	600	55	[204]
Solvothermal	NiO nanoparticles	Ethanol	450	90	40-82	[205]
		Acetone	67	80	21-30	
		Ammonia	50	80	10-11	
RF magnetron sputtering	NiO Films	H <sub>2</sub>	0.3	145-130	-	[205]

## 2.8 Applications and implications of gas sensors

Gas sensors are essential for many aspects of our daily lives. Some examples of applications and effects of gas sensors are given below [206, 207].

### 2.8.1 Applications of gas sensors

- 1. Automotive industry:** control of the concentration of the gases in the engine, to guarantee the highest possible efficiency of the combustion process. The same concept can also be applied to power plants, as the energy is generated by combustion.
- 2. Safety at work:** monitoring toxic gases in a working environment, for instance in a factory where dangerous chemicals are used.

3. **Domestic safety:** detection of poisonous gases or smoke in households, due to accidents such as fires, explosions, etc.
4. **Public security:** detection of substances dangerous for the safety of the general public, such as flammable gases and explosives.
5. **Environment:** monitoring toxic gases present in the atmosphere, due to industrial emissions.
6. **Food quality control:** detection of particular molecules, which are formed when food starts to rot and it is no longer good for consumption.

## 2.8.2 Implications of gas sensors

The correct and appropriate use of gas sensors is important for our society, as it can have implications at many different levels. For instance:

1. Monitoring toxic gases and automotive emissions is a vital tool in maintaining cleaner air, especially in big cities.
2. This can decrease the incidence of respiratory system illnesses; consequently, people will have a better quality of life. This is particularly true for children and elderly people.
3. This will also have an economic impact on society, as it will help to reduce the costs associated with the treatments of these illnesses.
4. The use of gas sensors in a power plant can make the process of energy generation more efficient.

This means less fuel will be necessary to produce the same amount of energy; this will benefit the society economically.

## 2.9 Conclusion

This chapter contained some basic definitions and concepts of chemical gas sensors based on metal oxides. We defined the gas sensor and explained its characteristics, types and its sensing mechanism. At the end of the chapter we provided a review of the gas sensors based on nickel oxide. In the next chapter we will prepare and characterize of NiO thin films.

# Chapter three

3/4

Elaboration and  
characterizations  
of NiO thin films

## CHAPTER 3

# Elaboration and characterizations of NiO thin films

### 3.1 Introduction

Nickel oxide (NiO) thin films can be prepared by various techniques and for this purpose has also been developed. SPT is the most commonly used technique adopted for the deposition of metal oxides, alloys and many compounds. Hydrolysis and pyrolysis are the main chemical reactions involved in the process. In this technique, the chemicals vaporized and react on the substrate surface after reaching on it. SPT is particularly attractive because of its simplicity, efficiency and efficacy. The SPT is used basically a chemical deposition method in which fine droplets of the desired material are sprayed onto a heated substrate. A continuous film is formed on the hot substrate by thermal decomposition of the material droplets. Various steps of the preparation of NiO thin films on glass substrates by SPT and its characterization techniques used to measure their optical and structural properties is discussed below.

### 3.2 Elaboration of NiO thin films

#### 3.2.1 Experimental montage of a homemade SPT system

The homemade SPT system, which we used to obtain our thin layers of NiO is shown in figure 3.1, where three processing steps can be viewed and analyzed. The three processing steps for spray pyrolysis deposition are:

- a. Atomization of the precursor solution;
- b. Aerosol transport of the droplet;
- c. Evaporate the droplets scattered towards the substrate and decompose the precursor salt to begin the growth of the film;

The main elements of the homemade SPT system are:

1. **A transparent glass bottle:** that can hold 50 ml of the Precursors solution. It feeds by gravity a low flow atomizer.
2. **A substrate heater and holder:** It is an electrical resistance, topped by a ceramic plate, heated by Joule effect whose temperature is regulated by means of a digital temperature controller which is connected to a thermocouple. The temperature range of this device is between 25°C and 550°C.
3. **An atomizer and flow solution controller:** The location which we can control the flow of precursors solution and transforming it into spray with small droplets by compressed air.
4. **An atomizer holder:** The atomizer holds, with it we can change the distance between the atomizer and the substrate.
5. **Air compressor:** It is reservoir type electrical air compressor. A rotary pump in this section mode draws atmospheric air and keeps it reserved in a large capacity air tank. At the outlet of the tank a pressure gauge is attached which records the pressure of the air at the time of supplying it from the tank. There is a bypass control valve which can keep the output pressure constant. Where compressed air is transferred to the atomizer through a non-expandable tube.

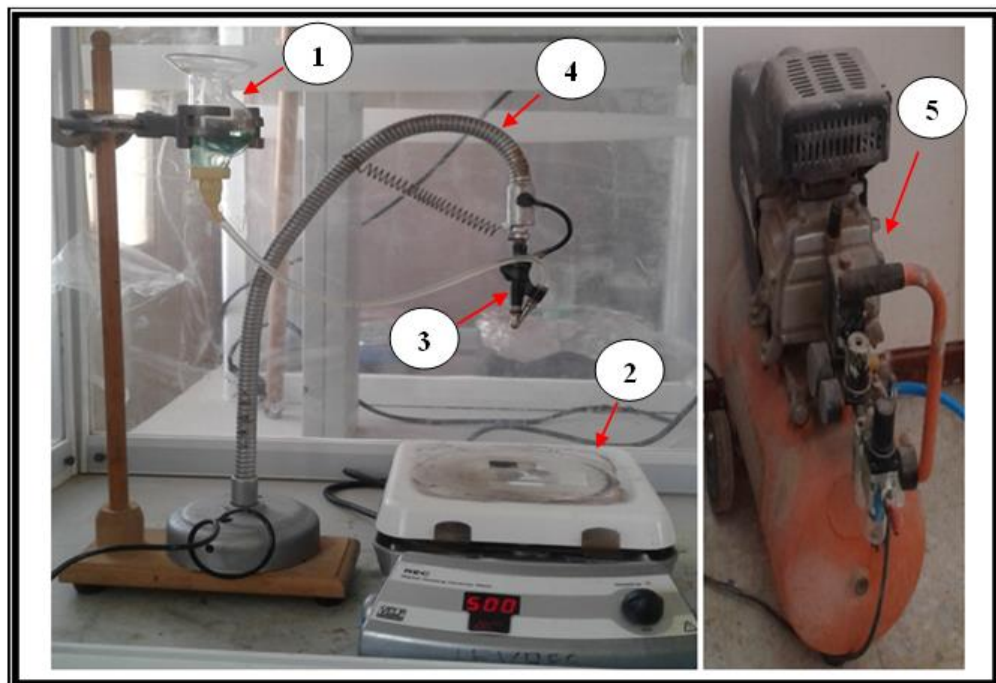


Figure 3.1: The homemade SPT system.

### 3.2.2 Thin film deposition parameters

In the chemical spray deposition technique the structure, composition and other characteristics of the deposited films depend on a number of process variables [deposition parameters]. The variable quantities such the substrate temperature, solution and air flow rate, deposition time, quality of the substrate material, size of atomized droplets, distance between substrate and atomizer, and solution concentration, etc. are affected on the film properties.

To study the effect of any one of these parameters on the film properties we keep the other parameters fixed. For the deposition of thin film, all the above mentioned parameters were kept at their optimum values (See table 3.1).

**Table 3.1:** The optimum values range of some NiO thin film deposition parameters

Parameters	Optimum values
Air pressure	1-2 bar
Temperature substrate	400-500 °C
Flow of the solution	1.5-5 ml/min
Distance between the atomizer and the substrate	18-53 cm
Concentration of the precursor solution	0.05-0.2 mol/L
Deposition time	5-10 min
Volume of precursor solution	> 5 ml

### 3.2.3 Experimental procedure

#### 3.2.3.1 Preparation of substrates

The glass substrates used in this work is (CITOPLUS-REF-0302-0004), which are an optical microscope slides in size of (75×25×1 mm<sup>3</sup>) for their availability, low price, and allowing us to study film properties, especially the optical ones. On the other hand, the glass has a thermal expansion coefficient very close to the thermal expansion coefficient of nickel oxide (NiO), that reduce the surface stresses applied from the surface of the substrate on the prepared film.

The substrates used must be clean and of good adhesion. Cleaning of substrates is a very important step to eliminate the presence of grease, dust and all other dirt and contaminations. The substrates are cleaned as follows:

1. Washes with Tap water then rinsed with distilled water.
2. Immerses one by one in the HCl acid then in the acetone solution (C<sub>3</sub>H<sub>5</sub>OH), then rinse with distilled water.

3. Finally, dry with a hairdryer and paper towels.

After that the glass substrates become usable.

### 3.2.3.2 Preparation method of the precursor solution

In order to obtain a specific molar concentration of the precursor solution, we are dissolving of a known quantity of nickel (II) nitrate hexahydrate  $[\text{Ni}(\text{NO}_3)_2 \cdot 6 \text{H}_2\text{O}]$ , which has been weighed by an electronic scale, in a known volume of doubly distilled water ( $\text{H}_2\text{O}$ ). As has been added a few drops of HCl acid to the solution. After that, The solution has been stirring with a magnetic stirrer at  $60^\circ\text{C}$  for an one to two hours, to yield a clear, transparent the homogeneous green solution. The solution then becomes usable for the SPT.



**Figure 3.3:** Nickel (II) nitrate hexahydrate  $[\text{Ni}(\text{NO}_3)_2 \cdot 6 \text{H}_2\text{O}]$ .

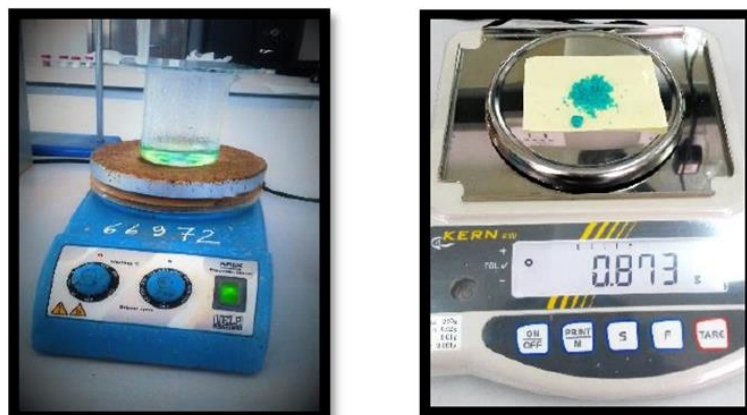


**Figure 3.4:** Electronic scale and magnetic stirrer used in our work.

To calculate the mass of nickel (II) nitrate hexahydrate  $[\text{Ni}(\text{NO}_3)_2 \cdot 6 \text{H}_2\text{O}]$ , the expression (3.1) is used, which gives the mass of nickel nitrate  $m(\text{g})$  as a function of the

molar mass  $M$  (g/mol), the molar concentration  $C$  (mol/L) of nickel nitrate and the volume of doubly distilled water  $V$  (L).

$$m = M.C.V \quad (3.1)$$

The table 3.2 shows some physic-chemical properties of nickel nitrates hexahydrate.

**Table 3.2:** Some physic-chemical properties of nickel nitrates hexahydrate

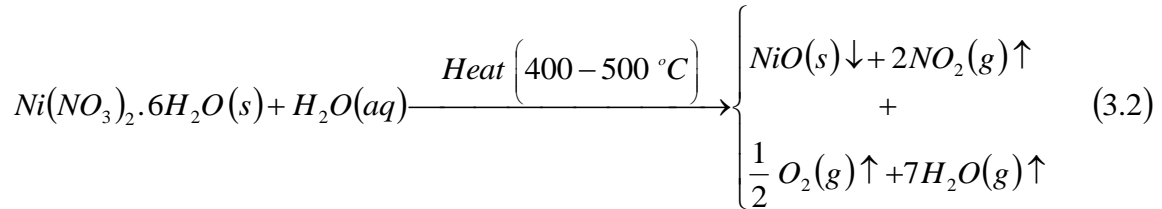
Property	Value
Physical state	Solid
Chemical formula	$\text{Ni}(\text{NO}_3)_2 \cdot 6 \text{H}_2\text{O}$
Molecular weight	290.80 g/mol
Melting point	56.7°C
Boiling point	136.7°C
Density	2.05
Water solubility	2385 g/L at 0°C
Purity	98%

### 3.2.3.3 Deposition steps of the NiO thin films

The deposition procedure comes after the preparation of the substrates and precursor solutions and is presented in According to the following steps:

1. Filling a certain amount of the prepared precursor solution in its own bottle.
2. Setting of The distance between the atomizer and the substrate holder by changing the position of the atomizer by changing atomizer holder position.
3. Adjusting of the air pressure through the tap built into the compressor with the pressure gauge.
4. Adjusting of flow the liquid through the button built into the sprayer.
5. The glass substrate is placed above a ceramic plate (substrate holder) of the electric heater containing a temperature regulator.
6. The glass substrate is heated to the required temperature (400-500°C).
7. Once the substrate reaches the desired temperature, a quantity of precursors is sprayed onto the hot substrate. Since the temperature will be reduced after a short period of spraying, spraying is done sporadically, allowing the electric heater to adjust the temperature.

8. The reaction of pyrolysis between the precursor solution and air in the hot medium creates a thin layer, so that the water evaporates and the oxygen and nitrogen dioxide are released due to an endothermic reaction, which is described by the following chemical equation [208, 209]:



9. At the end of the deposition process, the heating is stopped and the substrates are allowed to cool gradually over the substrate carrier to room temperature, In order to avoid thermal shocks that could break the glass substrate.

### 3.3 Characterizations of prepared NiO thin films

The films are prepared in almost the same way, with a slight difference in some parameters of depositing. Undoped and doped NiO thin films were deposited onto glass substrates. Then the films were examined by different methods and devices, it has been reported and discussed below.

#### 3.3.1 Effect of precursor molarity on properties of NiO thin films

In this section, undoped nanostructured (NiO) thin films were elaborated using (SPT). In order to get better physical properties of NiO thin films elaborated with (SPT), the precursor molarity has an essential parameter to get films with good quality. Effects of precursor molarity on the structural, optical and electrical properties of prepared films are studied and reported.

##### 3.3.1.1 Preparation of samples

NiO thin films were prepared onto a highly cleaned glass substrates using SPT. Nickel (II) nitrate hexahydrate  $[Ni(NO_3)_2 \cdot 6 H_2O]$  was dissolved in 50 ml of doubly distilled water to obtain the following precursor molarity (molar concentrations): 0.05, 0.10, 0.15, 0.20 mol/L. The produced mixtures (Precursor solutions) were stirred at 60°C for 2 hours in order to obtain a clear and homogenous green solution.

The heating temperature of the substrates was fixed at 480°C, the atomizer-substrate distance was kept 18 cm, the spray rate was 1.5 ml/min, and each spray

takes five second, whereas the time interval between two successive sprays was 30 second to avoid the substrate temperature fall. Different precursor solutions of fixed volume (50 ml) were sprayed separately on heated glass substrates leading to undoped NiO thin films. After deposition, the films were allowed to cool till room temperature.

### 3.3.1.2 Devices and measurements

The X-ray diffraction (XRD) spectra of the NiO nanostructured thin films prepared with different precursor molarity were measured to verify its structure. X-ray diffraction (XRD) was measured by using BRUKER-AXS-8D diffractometer with Cu  $K_{\alpha}$  radiation ( $\lambda = 1.5406 \text{ \AA}$ ) operated at 40 KV and 40 mA in the scanning range of ( $2\theta$ ) between  $20^{\circ}$  and  $80^{\circ}$ . The spectral dependence of the NiO transmittance (T) and the absorbance (A), on the wavelength ranging 300 –1100 nm are measured using an ultraviolet-visible spectrophotometer (Perkin-Elmer Lambda 25). Whereas the electrical conductivity of the films was measured in a coplanar structure of four golden stripes on the deposited film surface; the measurements were performed with Keithley model 2400 low voltage source meter instrument. All measurements were carried out at room temperature.

### 3.3.1.3 Results and discussions

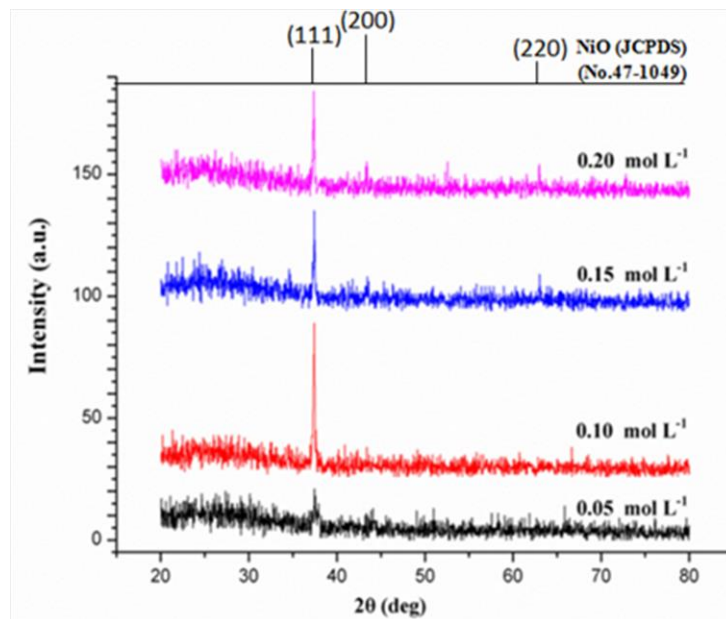
#### 3.3.1.3.a Structural properties

Figure 3.5 shows the XRD patterns of NiO thin films elaborated on a glass substrate at  $480^{\circ}\text{C}$ . The X-ray diffraction was used in this work in order to understand the structure of the deposited NiO thin films with the different molar concentrations of precursor solutions (precursor molarity).

The indexed peak (111) at  $2\theta \approx 37.2^{\circ}$  and other weak peaks (200) and (220), especially at concentrations 0.15 and 0.20 mol/L approves that the NiO films are polycrystalline in nature and matched well to the face-centered cubic (FCC) crystalline structure of NiO phase, which are consistent with the JCPDS (No.47-1049). Figure 3.5 shows that the diffraction intensity increased for precursor molarity 0.10 mol/L; it shows that the best crystalline quality of the film is achieved for this precursor molarity. The crystalline size was calculated using Debye–Scherrer formula. The increasing of the intensity of the diffraction peak may indicate to the resulted of the good crystallinity [210].

Diverse structural parameters such as lattice constants, mean strain, dislocation

density, and crystallite size of NiO thin films has been calculated using equations (1.5), (1.6), (1.8) and (1.3) respectively and included in table 3.3. It can be observed that the lattice parameter values from all obtained films are smaller than to the bulk standard lattice parameter ( $a_0=4.177 \text{ \AA}$ ) of NiO, this variation in lattice parameter corresponds to the existence of internal strain, defects and impurities in the films, similar results are also reported by other researchers [211, 212]. The negative sign in the mean strain expression means that the strain is a compressive strain, and therefore we will use the absolute value in the figure 3.6.



**Figure 3.5:** XRD patterns of the deposited NiO thin films on glass substrate at different precursor molarity.

**Table 3.3:** Structural parameters of NiO thin film at different precursor molarity.

Precursor molarity (mol/ L)	Bragg's angel $2\theta(\text{deg})$	Lattice constant $a(\text{\AA})$	Crystallite size D(nm)	Mean strain $\varepsilon(\%)$	Dislocation density $\delta(\text{lines/m}^2) \cdot 10^{16}$
0.05	37.565	4.143	09.720	-0.814	1.060
0.10	37.300	4.172	40.610	-0.120	0.061
0.15	37.423	4.158	46.620	-0.455	0.046
0.20	37.346	4.167	33.290	-0.239	0.090

Figure 3.6 shows that the crystallite size contrary proportional to mean strain, this may be attributed to the increment of the defects and empty spaces in the crystal-line structure as crystallite size decreases. The deviation in the values of the lattice constant of the as-prepared NiO films from the bulk value indicates the presence of

strain in the films. The origin of internal strain is related to the grain size of the film, which depends upon to deposition condition of the films [213]. This is confirmed by the compatibility between the changes in mean strain and the dislocation density according to changes the precursor molarity, as clearly in the figure 3.6. Also it can be noticed that the film with the best structural properties has smallest mean strain value, which effects in the crystallization level [214].

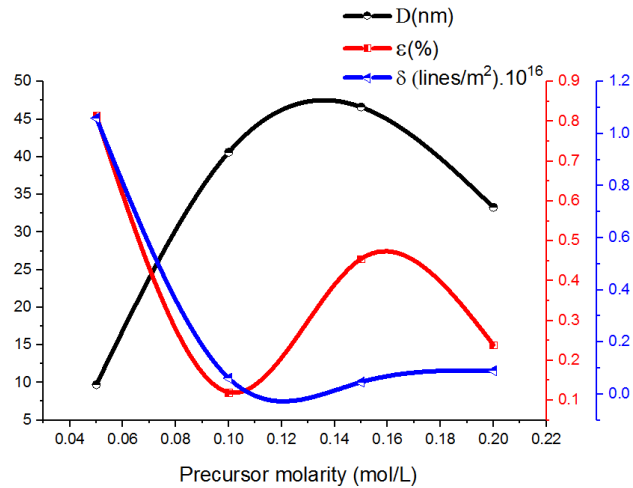


**Figure 3.6:** The variation of crystallite size, mean strain and dislocation Density of NiO thin films as a function of the precursor molarity.

### 3.3.1.3.b Optical properties

Figure 3.7 shows the optical absorption spectra of NiO thin films. The absorption edge of 0.05 mol/L was found to be at 326 nm and of 0.20 mol/L was found to be at 343 nm. The absorption spectra of 0.05 mol/L show that the absorption edge is slightly shifted towards shorter wavelength when compared to other precursor concentration. The absorption edge of a degenerate semiconductor is shifted to shorter wavelengths with increasing carrier concentration. This shift predicts that there is an increase in band gap value ( $E_g=3.86$  eV), which is due to the reduction in particle size ( $D = 9.72$  nm). The fundamental absorption, which corresponds to the electron transition from the valance band to the conduction band, can be used to determine the nature and value of the optical band gap. The optical absorption study was used to determine the optical band gap of the nanoparticles, which is the most familiar and simplest method.

For direct bang gap semiconductor such as NiO, the absorption coefficient ( $\alpha$ ) and the incident photon energy ( $h\nu$ ) are related by the Tauc's relation Eq. (1.19). As it was shown in figure 3.8 a typical variation of  $(\alpha h\nu)^2$  as a function of photon energy ( $h\nu$ ) of NiO thin films, used for deducing optical band gap  $E_g$ , The optical band gap values have

been determined by extrapolating the linear portion of the curve to meet the energy axis ( $h\nu$ ) [215]. The band gap values were given in table 3.4.

**Table 3.4:** Optical and electrical parameters of NiO thin film at different precursor molarity.

Precursor molarity $C(\text{mol L}^{-1})$	Thickness $t(\text{nm})$	Urbach energy $E_U(\text{eV})$	Band gap energy $E_g(\text{eV})$	Conductivity $\sigma(\Omega.\text{cm})^{-1}$
0.05	194	0.472	3.86	0.03306
0.10	234	0.288	3.82	0.08961
0.15	274	0.284	3.64	0.04125
0.20	242	0.292	3.68	0.00698

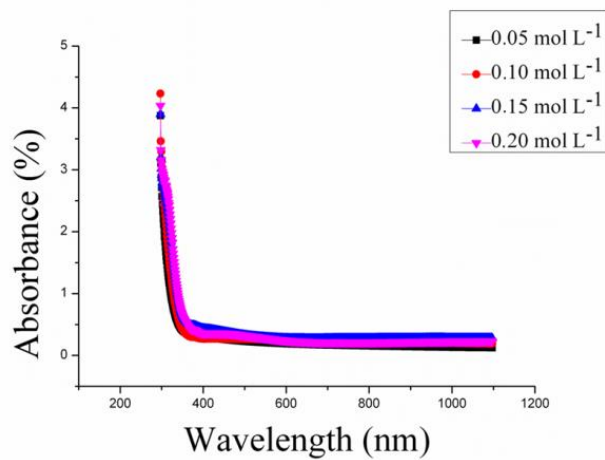


**Figure 3.7:** Absorbance spectra of NiO samples for different precursor molarity.

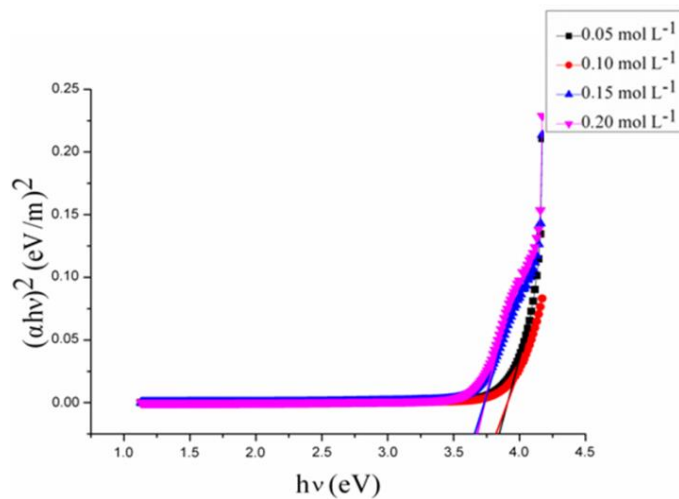


**Figure 3.8:** Plot of  $(\alpha h\nu)^2$  versus incident photon energy ( $h\nu$ ) of NiO thin films at different precursor molarity.

For a transmittance study (Figure 3.9), the NiO layer showed very high transmittance of 75 %, averaged in the wavelength ( $\lambda$ ) of 300 -1100nm. Suppression of light re-

Reflection at a surface is an important factor to absorb more photons in semiconductor materials. We obtained the reflectance profiles of NiO-coated (Figure 3.10). The averaged reflectance values (300–1100nm) were significantly lower than 0.203 %. Moreover, NiO-coating drives a substantially suppressed reflectance under 0.20 % in  $\lambda \in (500, 1100 \text{ nm})$ . This notifies that the NiO-coating is an efficient design scheme to introduce the incident light into substrate.

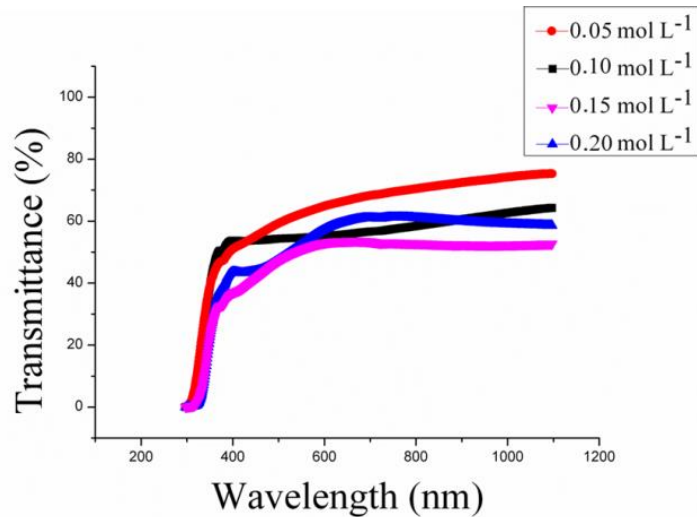


**Figure 3.9:** Transmission spectra of NiO samples for different precursor molarity.

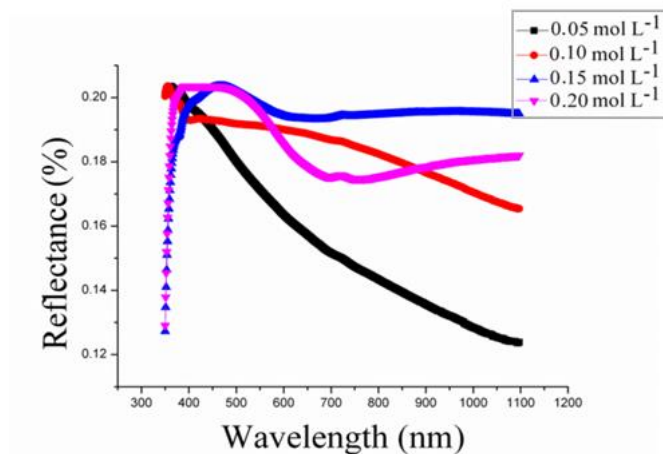


**Figure 3.10:** Reflectance profiles of NiO thin film for different precursor molarity.

SPT is a deposition method in which the growth of the film is by pyrolytic reaction. In this situation, the atoms that arrive on the substrate can stick to the point of their landing. Therefore, the atoms in the film network are not generally in an ideal position, hence the appearance of gaps in the width of the NiO bonds. In this case, the edges of bands delimited by  $E_v$  and  $E_c$  of the lattice crystalline will be extended. We observe what are called localized states formed at strip tails at the boundaries of the forbidden band, in the valence band ( $B_v$ ) and conduction ( $B_c$ ). For energies higher than

$E_c$  and lower than  $E_v$ , are the extended states [216, 217]. In addition, the tail width, also called Urbach energy, is synonymous with disorder or a width of the localized states available in the optical band gap of the films affects the optical band gap structure and optical transitions, which is related directly to a similar exponential tail for the density of states of either one of the two band edges and refers to the width of the exponential absorption edge [218]. The Urbach tail of the films can be determined by the Eq. (1.19). Figure 3.11 shows the variation of  $(\ln(\alpha))$  versus photon energy ( $h\nu$ ) for the films. The  $E_U$  values were calculated as the reciprocal of the straight line slopes shown in the same figure. Urbach energy decreases as the molarity increasing. The obtained  $E_U$  values are given in table 3.4. The  $E_U$  values change between 0.472 and 0.284 eV with a different precursor molarity. This changing is attributed to the disorder in the film due to the creation of new localized energy states near the band edges [219].

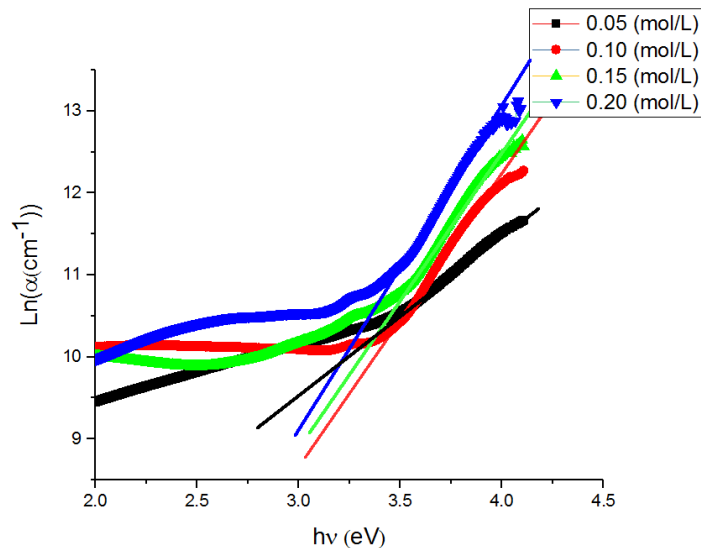


**Figure 3.11:** Plot of  $\ln(\alpha)$  versus incident photon energy ( $h\nu$ ) of NiO thin films at different precursor molarity.

Figure 3.12 shows the variation of Urbach energy and the optical band gap versus precursor molarity for the films. At first, the  $E_U$  values change similarly to the optical band gap values of NiO films. But in value 0.20 mol/L their values are changed inversely. This may be due to fluctuations in the density of defects, thickness and crystallite size. The changing in the crystallites size and thickness leads to the changes in optical properties i.e. band gap energy decreasing with increased thickness and crystallite size as shown in figure 3.13.

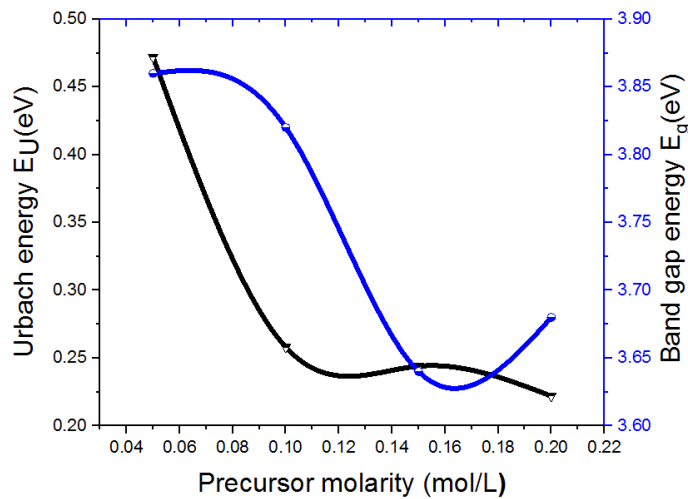


**Figure 3.12:** The variation Urbach energy and band gap energy of NiO thin films as a function of the precursor molarity.

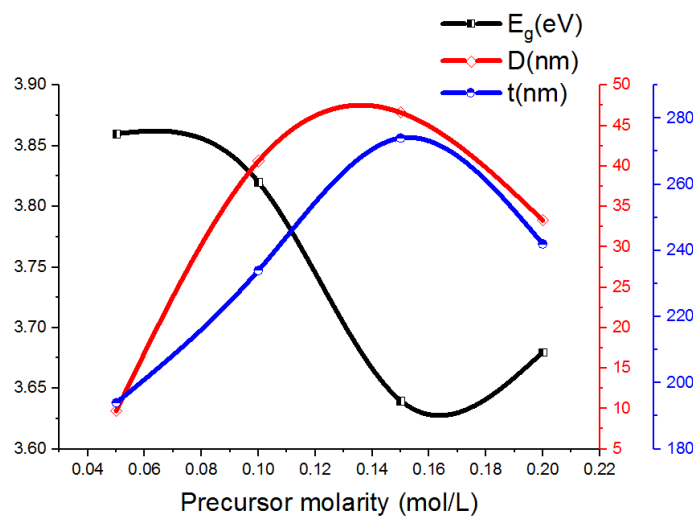


**Figure 3.13:** The correlation between the crystallite size and thickness with band gap energy of NiO thin films as a function of the precursor molarity.

### 3.3.1.3.c Electrical properties

The electrical conductivity ( $\sigma$ ) of the NiO films is summarized in Table 3.4. Figure 3.14 shows the variation of the thickness, crystallite size and electrical conductivity of NiO thin films as a function as precursor molarity. It was observed that the changes of the thickness have a clear effect on the electrical conductivity [220].

As can be seen, deposited films have a good conductivity. The maximum recorded value was  $0.0896 (\Omega \cdot \text{cm})^{-1}$  for the NiO thin film deposited using the molarity 0.10 mol/L. The increase of the electrical conductivity can be explained by the increase in the carrier concentration. Patil et al. [220] have reported that the increase of the electrical conductivity is due to the increase in activation energy with increasing film thickness.

This was explained by difference in the experimental conditions of spraying solution, spray rate and cooling of the substrates during decomposition. However, with 0.10 mol/L precursor molarity, the crystal structure of the film is significantly improved and the grain size is increased, leading to a reduced concentration of structural defects such as dislocations and grain boundaries. Thus, the decrease of the concentration of crystal defects leads in the increase of free carrier concentration. The improvement of crystal quality reduces the carrier scattering from structural defects, leading to higher electric mobility [221].

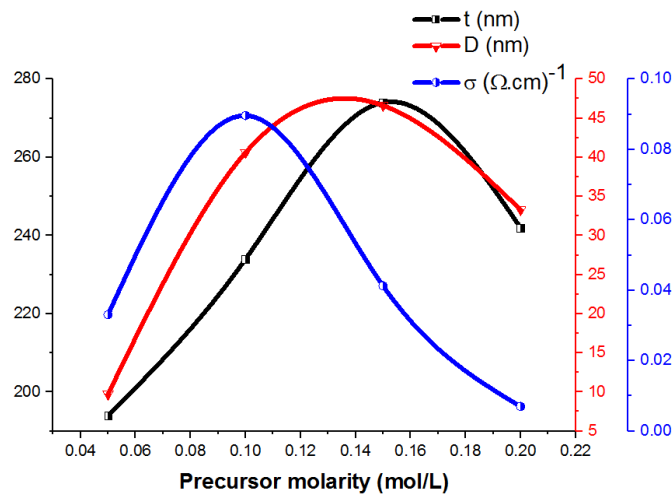


**Figure 3.14:** The variation of the crystallite size, the thickness and the electrical conductivity of NiO thin films as a function of the precursor molarity.

### 3.3.2 Effect of annealing on physical properties of NiO thin films

In this section, low cost thermal pyrolysis technology (SPT) is used to prepare thin films of pure nickel oxide with only 0.15 mol /L of precursors. One of them is annealed and the other leaves as it is. The structural, optical and electrical properties of the thin layers of nickel oxide are then examined.

#### 3.3.2.1 Preparation of samples

Two samples of NiO thin films were prepared onto a highly cleaned glass substrates using SPT. Nickel (II) nitrate hexahydrate was dissolved in 50 ml of doubly distilled water to obtain the precursor molarity 0.15 mol/L. The Precursor solutions were stirred at 60°C for 2 hours in order to obtain a clear and homogenous green solution. The heating temperature of the substrates was fixed at 480°C, the atomizer-substrate distance was kept 21cm, the spray rate was 1.5 ml/min, and each spray takes five second, whereas the time interval between two successive sprays was 30 second to

avoid the substrate temperature fall. The 50 ml of precursor solutions with molarity of 0.15 mol/L were sprayed separately on heated glass substrates leading to NiO thin films. After deposition, the films were allowed to cool till room temperature. After preparing the two samples, one leaves it as deposited and the other annealed at 500°C in an electrical oven for two hours.

### 3.3.2.2 Devices and measurements

The X-ray diffraction (XRD) spectra of the NiO thin films were measured to verify the structure. X-ray diffraction (XRD) was measured by using BRUKER-AXS-8D diffractometer with Cu K $\alpha$  radiation ( $\lambda = 1.5406 \text{ \AA}$ ) operated at 40 KV and 40 mA in the scanning range of ( $2\theta$ ) between 20° and 80°. The spectral dependence of the NiO transmittance (T) and the absorbance (A), on the wavelength ranging 300–900 nm are measured using an ultraviolet–visible spectrophotometer (Shmatzu 1800). The reflectance (R) was calculated by the well-known equation as (T+R+A = 1). Whereas the electrical conductivity of the films was measured in a coplanar structure of four golden stripes on the deposited film surface; the measurements were performed with Keithley model 2400 low voltage source meter instrument. The annealing process was performed by an electric oven. It was manufactured by the German company Nabertherm (Figure 3.15).



Figure 3.15: The annealing oven.

### 3.3.2.3 Results and discussions

#### 3.3.2.3.a Structural properties

Figure 3.16 shows the XRD patterns of the films deposited on glass substrates in as deposited and annealed at 500°C. Can be observed two XRD lines of the grown NiO thin films, showing the broadening of the line, which is a characteristic of the formation of films. The X-ray diffraction was used in this work in order to understand the

structure of the as-deposited and the annealed NiO nanostructured thin films. The indexed peak (111) at  $2\theta \approx 37.2^\circ$  correspond to the cubic structure of NiO nanoparticles which are consistent with the JCPDS (No.47-1049). Figure 3.16 shows that the diffraction intensity increased for annealed sample; it shows that the best crystalline quality of the film is achieved for this annealed sample.

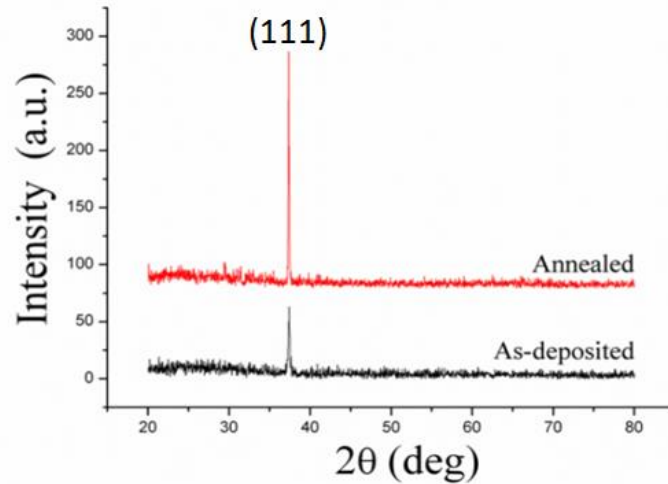


**Figure 3.16:** XRD patterns of the as-deposited and annealed NiO thin films.

The crystalline size was calculated using the well-known Debye–Scherrer formula (Eq. (1.3)). The increasing of the diffraction peaks may indicate to the resulted of the NiO in good crystallinity [223]. The crystalline size is found in the range of 46.62 nm for as-deposited sample and 119.89 nm for annealed one. Table 3.5 shows a decrease in the absolute value of the mean strain and the dislocation density after the annealing, which explains also good crystallization of annealed sample.

**Table 3.5:** Structural parameters of as-deposited and annealed samples of NiO thin film at 0.15 mol/L of precursor molarity.

Sample	Bragg's angle $2\theta(\text{deg})$	Lattice constant $a(\text{\AA})$	Crystallite size D(nm)	Mean strain $\epsilon(\%)$	Dislocation density $\delta(\text{lines/m}^2) \cdot 10^{16}$
As-deposited	37.423	4.158	46.62	-0.455	0.046
Annealed	37.290	4.173	119.89	-0.100	0.007

### 3.3.2.3.b Optical properties

Figure 3.17 shows the optical absorption spectra of NiO thin films. The absorption spectra of as-deposited sample show that the absorption edge is slightly shifted

towards shorter wavelength when compared to the annealed one. The absorption edge of annealed sample is shifted to longer wave-lengths. This shift predicts that there is a decrease in band gap value from ( $E_g=3.64$  eV) to ( $E_g=2.98$  eV), which is due to an enlargement in crystallite size from ( $D = 46.62$  nm) to ( $D = 119.89$  nm).

The fundamental absorption, which corresponds to the electron transition from the valance band to the conduction band, can be used to determine the nature and value of the optical band gap [222, 223]. The optical absorption study was used to determine the optical band gap of the films, which is the most familiar and simplest method. The changing in the crystallites size leads to the changes in optical properties i.e. band gap energy increased with decreasing of crystallites size as shown in table 3.6.

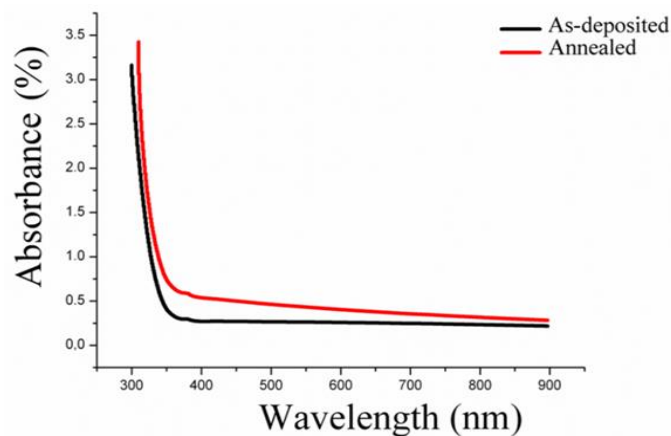


**Figure 3.17:** Absorbance spectra of the as-deposited and annealed NiO thin films.

As it was shown in figure 3.18 a typical variation of  $(\alpha h\nu)^2$  as a function of photon energy ( $h\nu$ ) of NiO thin films. The optical band gap values have been determined by extrapolating the linear portion of the curve to meet the energy axis ( $h\nu$ ) depending on equation (1.17) [224]. The band gap values were given in Table 3.6.

For a transmittance study (Figure 3.19), the as-deposited NiO showed high transmittance, averaged in the wavelength ( $\lambda$ ) of 300–900nm. Suppression of light reflection at a surface is an important factor to absorb more photons in semiconductor materials.

We obtained the reflectance profiles of NiO coated as deposited and annealed (Figure 3.20). The averaged reflectance values (300–900nm) were significantly lower than 0.203 %. Moreover, NiO coating drives a substantially suppressed reflectance un-

der 0.20 % in  $400 \text{ nm} < \lambda < 900 \text{ nm}$ . This notifies that the NiO coating is an efficient design scheme to intro-duce the incident light into substrate.

**Table 3.6:** Optical and electrical parameters of as-deposited and annealed NiO thin films.

Sample	Urbach energy $E_U(\text{eV})$	Band gap energy $E_g(\text{eV})$	Conductivity $\sigma(\Omega.\text{cm})^{-1}$
As-deposited	0.284	3.64	0.04125
Annealed	0.391	2.98	0.09241

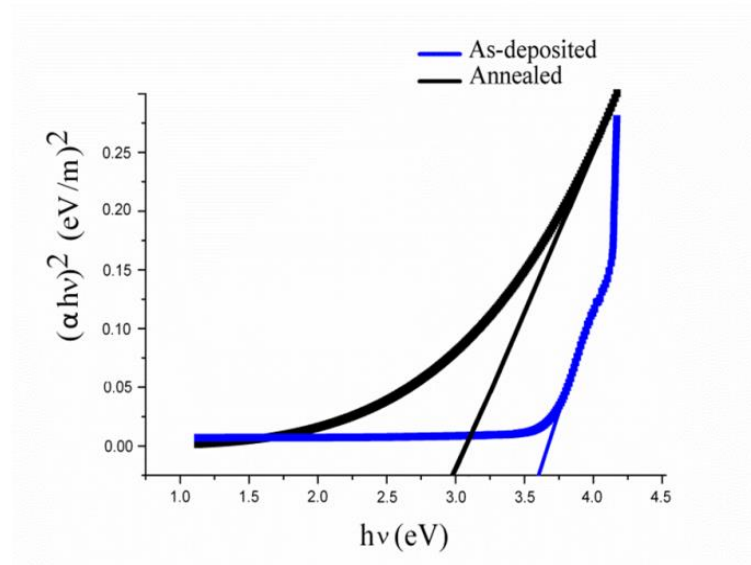


**Figure 3.18:** Plot of  $(\alpha hv)^2$  versus incident photon energy ( $hv$ ) of the as-deposited and annealed NiO thin films.

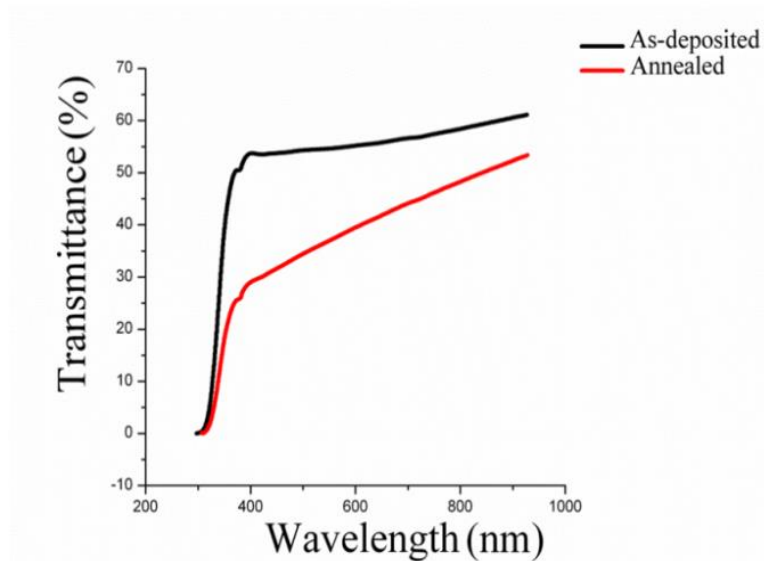


**Figure 3.19:** Transmission spectra of the as-deposited and annealed NiO thin films.

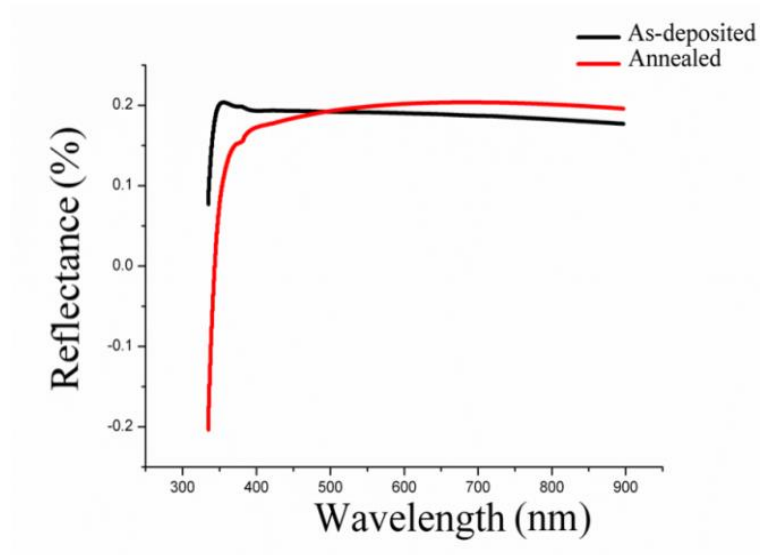


**Figure 3.20:** Reflectance profiles of the as-deposited and annealed NiO thin films.

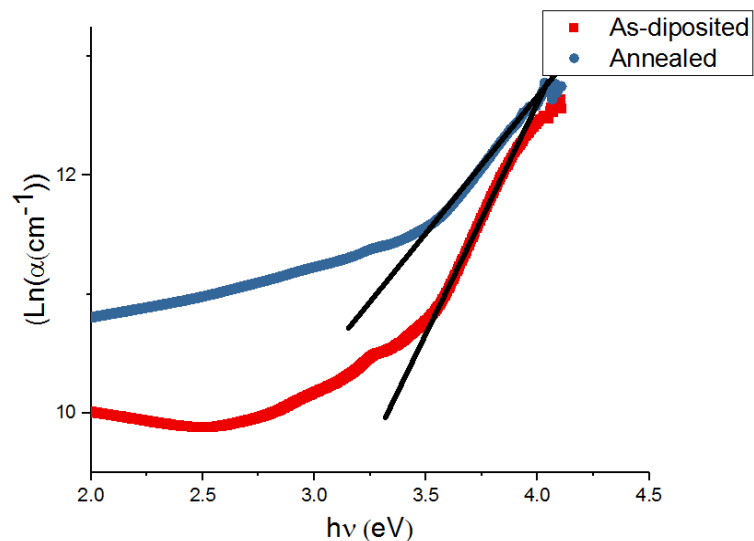


**Figure 3.21:** Plot of  $\text{Ln}(\alpha)$  versus incident photon energy ( $h\nu$ ) of the as-deposited and annealed NiO thin films.

### 3.3.2.3.c Electrical properties

The electrical conductivity ( $\sigma$ ) of the NiO films is summarized in table 3.6. The as-deposited films have good conductivity  $0.04125 (\Omega.\text{cm})^{-1}$ , after annealing the conductivity increase at  $0.09241 (\Omega.\text{cm})^{-1}$ . The increase of the electrical conductivity can be explained by the increase in the carrier concentration. Patil et al. [225] have reported that the increase of the electrical conductivity is due to the increase in activation energy. This was explained by the crystal structure of the film which is significantly improved and the grain size which is increased, leading to a reduced concentration of

structural defects such as dislocations and grain boundaries. Thus, the decrease of the concentration of crystal defects leads in the increase of free carrier concentration. The improvement of crystal quality reduces the carrier scattering from structural defects, leading to higher mobility [221].

### 3.3.3 Effect of cobalt doping on physical properties of NiO thin films

In this section, Co-doped NiO thin films were prepared using SPT. In order to obtain better physical properties of thin films, it has been doped at specific atomic ratios, after that the effects of doping on the structural, optical and electrical properties of the films were studied and reported bellow.

#### 3.3.3.1 Preparation of samples

NiO thin films were prepared onto a highly cleaned glass substrates (Standard glass CITOPLUS-REF-0302-0004) using SPT. The 5.816 g of nickel (II) nitrate hexahydrate [ $\text{Ni}(\text{NO}_3)_2 \cdot 6 \text{H}_2\text{O}$ ] was dissolved in 100 ml of doubly distilled water to obtain the solution with molar concentration of 0.20 mol/L. Then the 4.758 g of cobalt (II) chloride hexahydrate [ $\text{CoCl}_2 \cdot 6 \text{H}_2\text{O}$ ] (See figure 3.22 and table 3.7) dissolved in 100 ml of doubly distilled water to obtain the 0.20 mol/L of precursor solution. The two Precursor solutions were stirred at 60°C for 2 hours in order to obtain a clear and homogenous solution. To obtain the Co/Ni atomic doping ratios, we use certain proportions of the precursor solutions calculated from equation (3.3).

$$\text{Co}(at\%) = \frac{V_{S_a}}{V_{S_a} + V_{S_b}} \times 100 \quad (3.3)$$



**Figure 3.22:** Cobalt (II) chloride hexahydrate.

**Table 3.7:** Some physic-chemical properties of cobalt (II) chloride hexahydrate.

Property	Value
Physical state	Solid
Appearance	rose red crystals
Chemical formula	CoCl <sub>2</sub> .6H <sub>2</sub> O
Molecular weight	237.93 g/mol
Melting point	86 °C
Boiling point	1049 °C
Density	1,924 g/cm <sup>3</sup>
Water solubility	52.9 g/100 mL (20 °C) 105 g/100 mL (96 °C)

The appropriate cobalt (II) chloride dihydrate solution (S<sub>a</sub>) is added to nickel (II) nitrate hexahydrate solution (S<sub>b</sub>) for obtain the Co/Ni atomic ratios: 0, 3, 6, 9, 12 at.%. The mixture solution was stirred at 60°C for half an hour to obtain a homogeneous solution. After that, the solution was sprayed on heated substrates at 480°C. Where the atomizer-substrate distance was kept 53 cm, the spray rate was 5 ml/min, and each spray takes five second, whereas the time interval between two successive sprays was 30 second to avoid the substrate temperature fall. Different precursor solutions of fixed volume (15 ml) were sprayed separately for getting on the Co-doped NiO thin films. After deposition, the films were allowed to cool till room temperature.

### 3.3.3.2 Devices and measurements

The X-ray diffraction (XRD) spectra of the Co-doped NiO nanostructured thin films prepared were measured to verify its structure. X-ray diffraction (XRD) was measured by using PROTO-MANUFACTURING diffractometer with CuK<sub>α</sub> radiation ( $\lambda=1.5406 \text{ \AA}$ ) operated at 40 KV and 40 mA in the scanning range of ( $2\theta$ ) between 30° and 80°. The spectral dependence of the NiO transmittance (T) on the wavelength ranging 200–900 nm is measured using an ultraviolet-visible spectrophotometer (Shmatzu 1800). Whereas the electrical conductivity of the films was measured in a coplanar structure of four golden stripes on the deposited film surface; the measurements were performed with keithley model 2400 low voltage source meter instrument. In order to preview the surface morphology, the images were taken by a scanning electron microscope (SEM) TESCAN VEGA3. All measurements were carried out at room temperature.

### 3.3.3.3 Results and discussions

#### 3.3.3.3.a Structural and surface morphological properties

Figure IV.10 shows the XRD patterns of undoped NiO and Co-doped NiO thin films with different Co doping percentage. It can be seen three main diffraction peaks positioned at  $2\theta \approx 37.3^\circ$ ,  $43.3^\circ$  and  $79.4^\circ$  assigned to the (111), (200) and (222) crystal planes respectively (See Table 3.8). These peaks correspond precisely to the NaCl crystalline structure of NiO and matched well with the standard spectrum (JCPDS, No.47-1049) under the space group Fm $\bar{3}$ m. The presence of such peaks indicates that the films are polycrystalline in nature. From the XRD analysis, there is secondary phase at  $2\theta \approx 39.4^\circ$  that corresponds to (60 $\bar{2}$ ) peak in cobalt dioxide (CoO $_2$ ) can be observed, it is according to JCPDS (No. 98-008-7942), this peak is signalized by a square (■) in figure 3.23, which could be due to the difference of the ionic radius of the Co and Ni ( $R_{Ni^{2+}} \approx 0.69 \text{ \AA}$ ,  $R_{Co^{2+}} \approx 0.74.5 \text{ \AA}$ ) [226]. That may cause internal stress in the host lattice. This can be attributed to the fact that at lower doping cobalt ions replace Ni ions substitutionally but at higher doping much more Co ions may occupy the octahedral sites and affect the crystalline nature of films [227].

The intensity of (111) diffraction peak is higher compared with other observed peaks indicating the preferred orientation and The its intensity is found to decrease with increasing Co doping percentage rations (See table 3.8), this is confirmed by the Texture coefficient values witch shown in figure 3.24. Furthermore, we can clearly see from the inset of figure 3.25 that the position of the all diffraction peaks changing with increasing Co-doping percentage. Where, most angle values are shifted to lower values so that the difference  $\Delta(2\theta) = 2 (\theta_{\text{Doped film}} - \theta_{\text{Undoped film}})$  decreases with increasing Co-doping percentage. The structural parameters such as crystallite size, lattice constants, mean strain and dislocation density of NiO thin films has been calculated using equations (1.5), (1.6), (1.8) and (1.3) respectively and included in table 3.9. It can observed that, the lattice parameter value from undoped film is smaller than to the bulk standard lattice parameter, but for Co-doped films the lattice parameter value are greater ( $a_0 = 4.177 \text{ \AA}$ ). Generally, this variation in lattice parameter corresponds to the existence of internal strain, defects or impurities in the films. In this case, the doping is what led to the expansion of conventional crystal-lattice of the NiO, which likely to be due to the difference of the ionic radius of the Co and Ni. The negative sign of the mean strain expression means that the strain is a compressive strain [228]. Converse-

ly, the positive sign means it is an extensive strain and therefore we will use the absolute value in the figure 3.25.

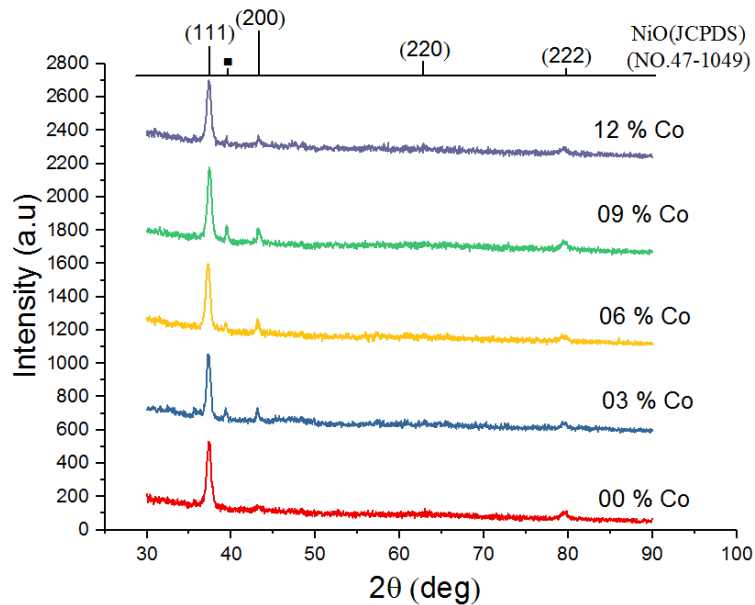


**Figure 3.23:** XRD patterns of the deposited Co-doped NiO thin films on glass substrate at different cobalt percentages.

**Table 3.8:** X-ray diffraction data of Co-doped NiO thin films at different cobalt percentages.

Cobalt percentage (at.%)	Peak (hkl)	Bragg's angel $2\theta(\text{deg})$		Intensity (u.a)		FWHM $B(\text{deg})$
		Observed	Reported	Observed	Reported	
00	111	37.466	37.249	82	61	0.118
	200	43.291	43.276	5	100	0.708
	222	79.608	79.409	7	8	0.827
03	111	37.37	37.249	64	61	0.108
	200	43.072	43.276	11	100	0.288
	222	79.664	79.409	5	8	0.76
06	111	37.302	37.249	63	61	0.236
	200	43.093	43.276	13	100	0.236
	222	79.553	79.409	5	8	0.354
09	111	37.326	37.249	41	61	0.118
	200	43.168	43.276	7	100	0.118
	222	79.572	79.409	4	8	0.59
12	111	37.466	37.249	54	61	0.111
	200	43.283	43.276	7	100	0.18
	222	79.597	79.409	3	8	0.472

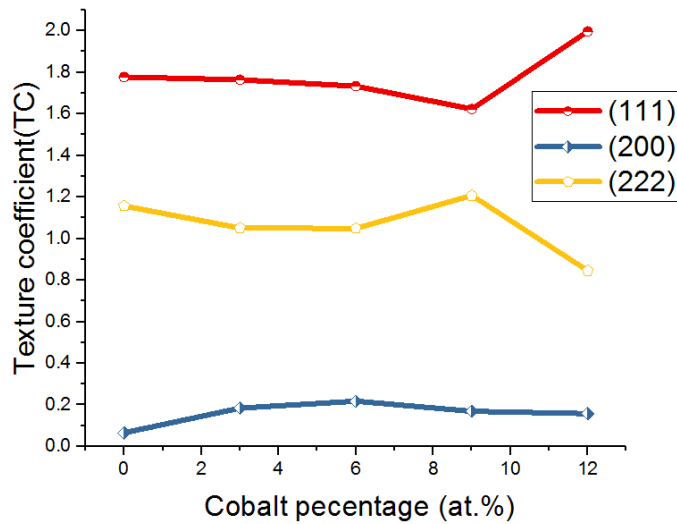


**Figure 3.24:** Texture coefficient values for all peaks of Co-doped NiO thin films at different cobalt percentages.

**Table 3.9:** Structural parameters of Co-doped NiO thin films at different cobalt percentages.

Cobalt percentage (at.%)	Lattice constant $a(\text{Å})$	Crystallite size $D(\text{nm})$	Mean strain $\varepsilon$ (%)	Dislocation density $\delta(\text{lines/m}^2) \cdot 10^{16}$
00	4.169	31.890	-0.186	0.098
03	4.179	40.312	0.041	0.062
06	4.187	33.644	0.247	0.088
09	4.178	53.672	0.032	0.035
12	4.178	48.318	0.016	0.043

The figure 3.25 shows the negative effect of crystalline defects such as strains and dislocations on crystallite size at different doping rates of Co. There is a clear correlation between changes in mean strain and dislocation, which negatively affected the crystallization of the films prepared.

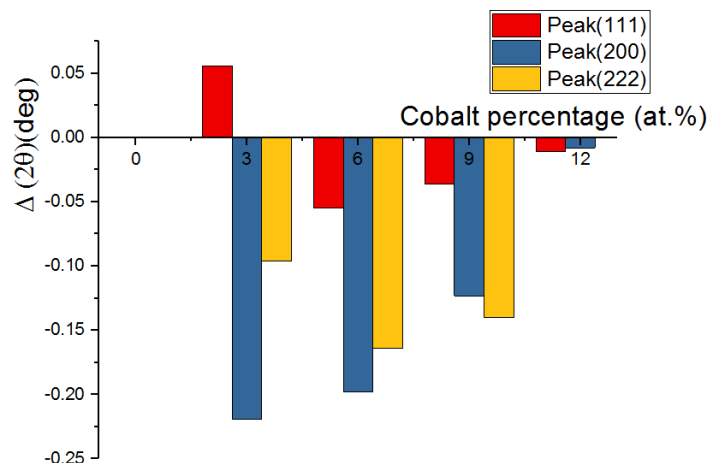


**Figure 3.25:** Variation of the  $\Delta(2\theta)$  values as function of Co-doping percentages.

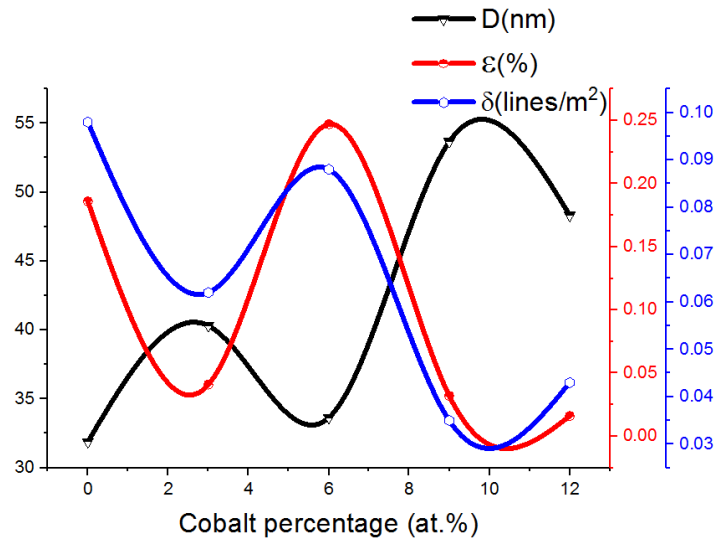


**Figure 3.26:** Correlation between crystallite size, mean strain and dislocation density of Co-doped NiO thin films at different cobalt percentages.

From the figure 3.27 it can be observed that the doping has improved crystallization by increasing the crystallite size with varying values, which positively affects the lattice constant. The latter shows values close to the theoretical value whenever the crystallite size is large.

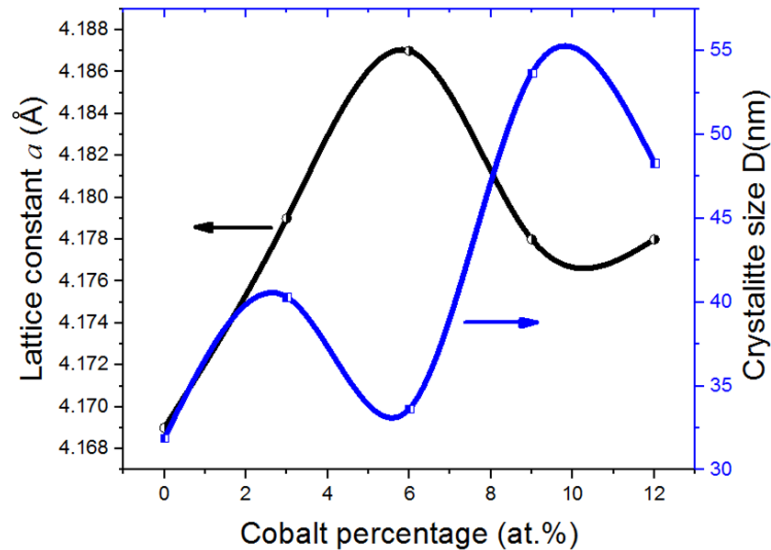
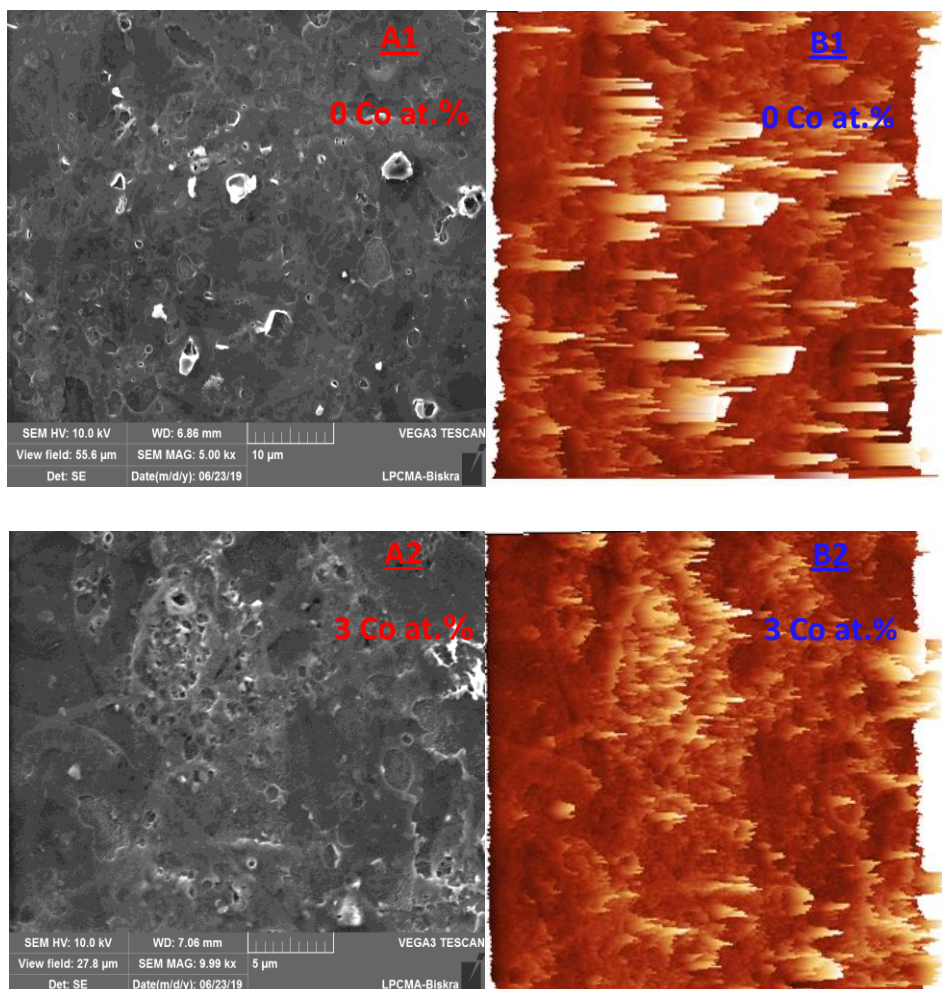


**Figure 3.27:** Variation of crystallite size and lattice constant of Co-doped NiO thin films at different cobalt percentages.

The films surfaces were studied by scanning electron microscopy (SEM). SEM micrographs were taken for thin films of undoped and Co-doped NiO at 3, 6, 9 and 12 at.% are embedded in figure 3.28. Figure 3.28 also shows images in three dimensions of the same samples taken by the Gwyddion program [229, 230]. The SEM images

revealed films show that the deposited films have relative homogeneity on its surface; the shape of the grains and aggregates of grains boundaries does not appear clearly, where the surfaces of the undoped and Co-doped NiO films have a wrinkle network structure. This morphology appears to be clearer and denser as the cobalt concentration increases.

In general, the surfaces of the NiO thin films have a wrinkle network structure, and are influenced by the incorporation of dopants. The incorporation of Cobalt ions into the NiO thin films synthesized by SPT, modified the surface morphology of the surface, due to the more impurities included in the NiO crystal, resulting in more defects in the structure. In this study, the morphology of the structure observed in Co-doped NiO films can be attributed to the fact that Co dopant promotes nucleation and growth in certain directions at random.



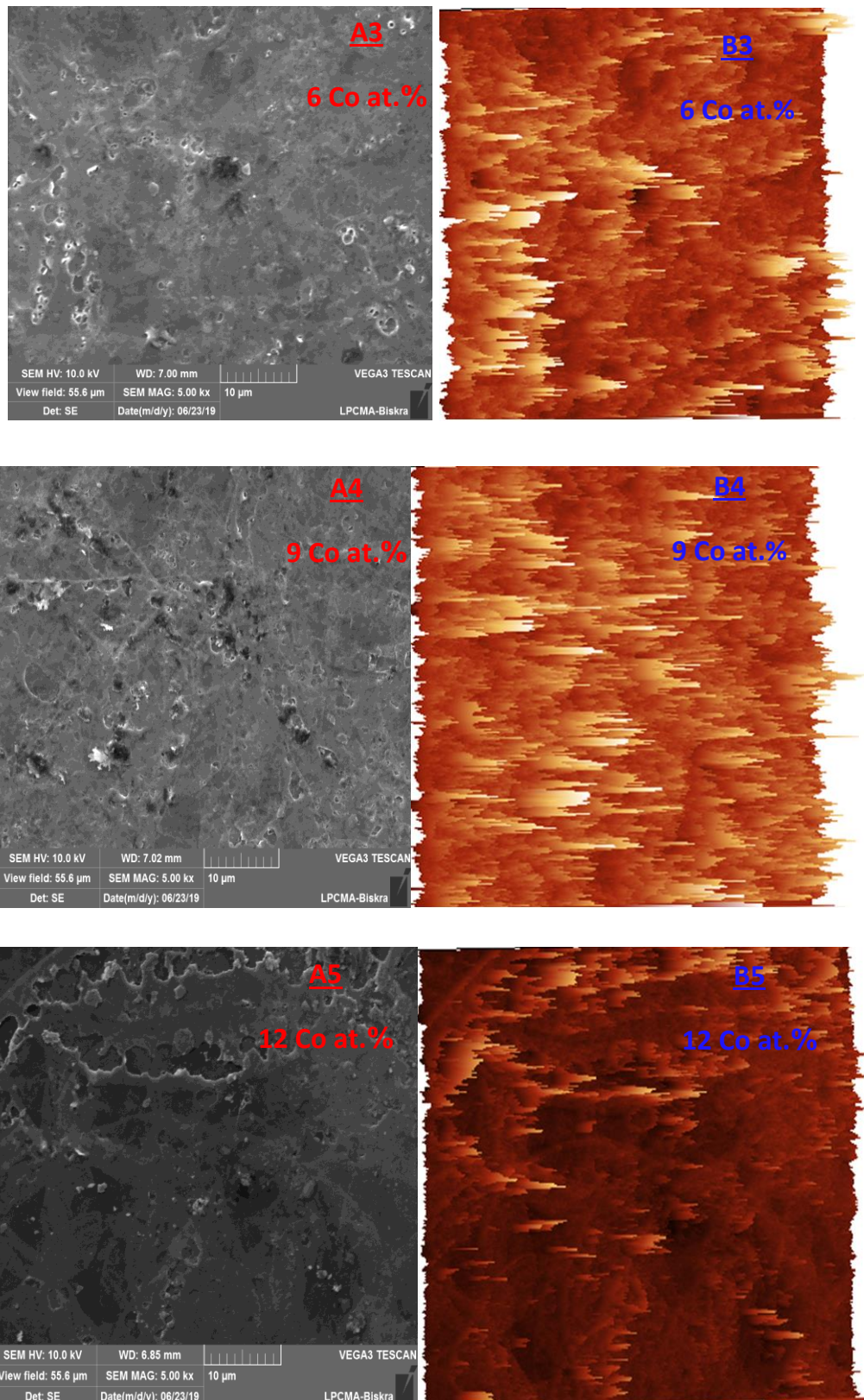


**Figure 3.28:** SEM and Gwyddion program images of Co-doped NiO thin films different cobalt percentages.

### 3.3.3.3.b Optical properties

Figure 3.29 shows the transmittance spectra in the UV-Visible range (300-900 nm) of undoped and Co-doped NiO thin films in the doping range of 0 to 12 at.%. The transmittance for all thin films increases as the wavelength increases in the range of (300-375 nm), and then increases slowly at higher wavelengths. The spectrum shows relatively low transmittance in the visible and near-infrared regions range of 45-55%. The reduction of the transmittance for the all samples is due to the surface roughness of the films, because the latter generates at the film/air interface of the refractions of the radiations, so these radiation will be diffused in several directions instead of being reflected. In the range of (375-650 nm), we observed a significant reduction in the transmittance values of all grafted films compared to the pure sample, but after 650 nm, the transmittance values of the grafted films improved to exceed the transmittance pure sample, that for samples 6 and 12 at.%.

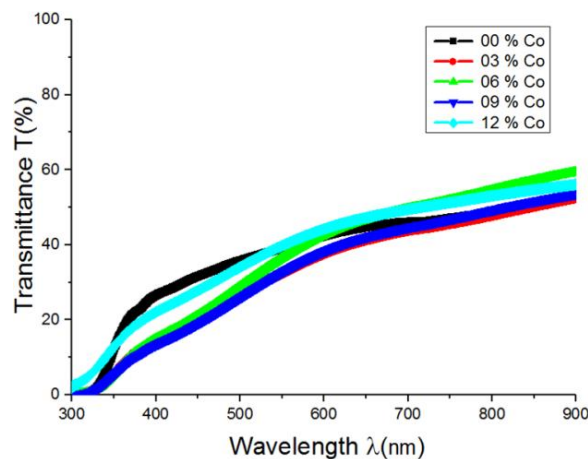


**Figure 3.29:** Transmittance of Co-doped NiO thin films at different Co percentages.

The variation of the absorbance spectrum with wavelength is opposite to the transmittance spectrum. The study of absorbance was in the range of (300– 900 nm). Figure 3.30 shows the relation between absorbance ( $A$ ) and wavelength for Co-doped NiO thin films. The absorbance decreases rapidly at short wavelengths (high energies) corresponding to the energy gap of the film, (when the incident photon has an energy equal or more than the energy gap value). This evident increase of energy is due to the interaction of the material electrons with the incident photons which have enough energy for the occurrence of electron transitions, this attribute to decrease the energy gap of the film. Nickel oxide is a high band gap semiconductor with the absorption edge in the UV region and no absorption in the visible region. NiO thin films show an

absorption in the visible region in this study. There may be three possible explanations for the above process. The first one is that the main stoichiometry of the film is NiO, and Ni<sub>2</sub>O<sub>3</sub> is present as a minority phase that could not be detected by XRD [8, 18]. The second possibility is that two adjacent divalent nickel ions become Ni<sup>3+</sup> due to charge transfer process caused by presence of nickel vacancy. Third possibility is that the stoichiometry of the film is NiO, but excess oxygen together with the hydrogen may be present in the film as OH groups which may show a significance absorption in the visible region of the spectrum [216, 225].

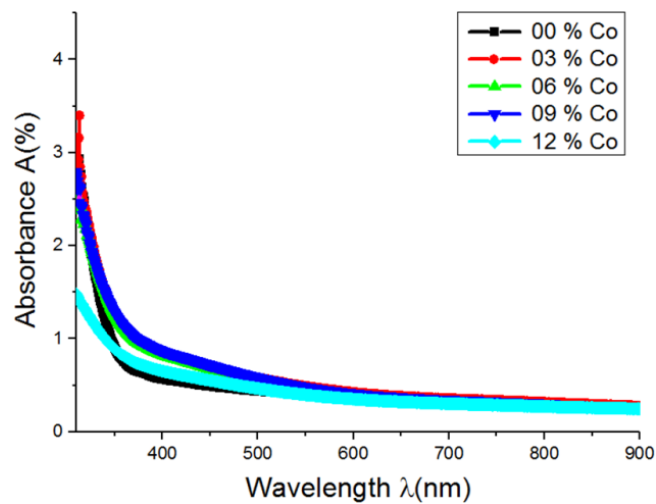


**Figure 3.30:** Absorbance of Co-doped NiO thin films at different cobalt percentages.

Energy band gap values depend in general on the films crystal structure (disorder and its regularity) [231]. The optical band gap for of all samples is determined using the Tauc's equation. Figure 3.31 shows  $(\alpha h\nu)^2$  as a function of  $h\nu$  for the Co-doped NiO thin films at various Co-doping parentage.  $E_g$  values are summarized in Table 3.10. The value of band gap  $E_g$  is 3.61 eV for undoped NiO film, whereas the value of  $E_g$  gradually decreases from 3.60 to 3.48 eV for samples prepared as of Co doping concentration increased from 3 to 12 at.%. This was in good accord with the earlier reports on the band gap of NiO films from 3.4 eV to 4.0 eV by different research groups [232, 233]. The band gap is found to decrease with an increase in the Co doping concentration; this suggests a change in the NiO electronic structure. This may refer to the crystallite growth, defects or vacancies in the NiO crystal which can create new energy level. This behavior leads to the reduction in the band gap energy [235]. At near the band edge the extent of the exponential tail of the absorption edge is characterized by the Urbach energy ( $E_U$ ) indicating the width of band tails of the localized states within the optical band gap and is given by equation (1.10).

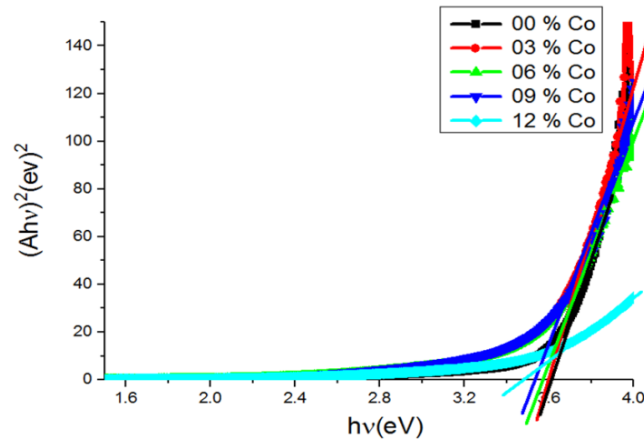


**Figure 3.31:** Plot of  $(\alpha h\nu)^2$  versus incident photon energy ( $h\nu$ ) of Co-doped NiO thin films at different cobalt percentages.

The  $E_U$  is also known as band tail width and is due to the disorder in the thin film material. The variation of bond length and bond angle from their standard value in the crystalline material is called disorder [236]. The Urbach energy of undoped NiO thin films depends on the structural defects, dislocations density and some defects of the vacancy and interstitial states in the films [237]. In the case of Co-doped NiO films, doping ions can create more number of localized states that reduce the energy gap under the influence of the Roth effect. Urbach energy can be determined from the reciprocal gradient of the linear portion of  $\ln(\alpha)$  versus  $(h\nu)$  plots.  $E_U$  values are shown in figure 3.32 and summarized in table 3.10. It is obviously seen that  $E_U$  increases if the percentage of Co-doping increases as opposite of gap energy as shown in figure 3.33.

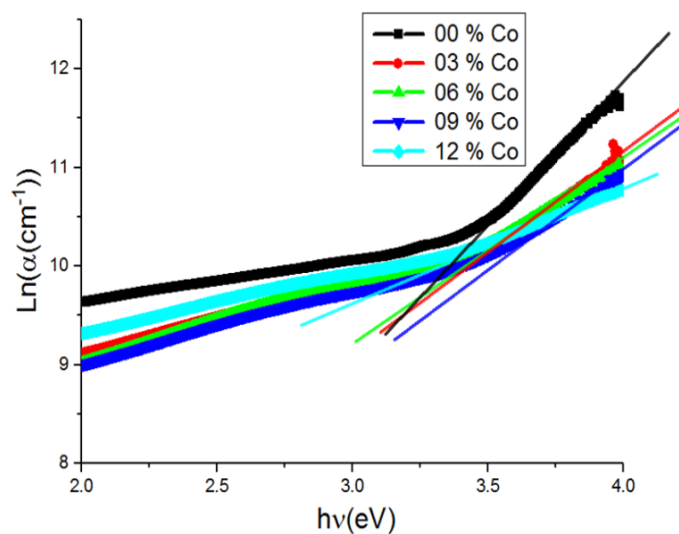


**Figure 3.32:** Plot of  $\ln(\alpha)$  versus incident photon energy ( $h\nu$ ) of Co-doped NiO thin films at different cobalt percentages.

**Table 3.10:** Optical and electrical parameters of Co-doped NiO thin films at different cobalt percentages.

Cobalt percentage (at.%)	Thickness t (nm)	Urbach energy $E_U$ (eV)	Band gap energy $E_g$ (eV)	Conductivity $\sigma$ ( $\Omega \cdot \text{cm}$ ) <sup>-1</sup>
00	264	0.353	3.61	0.0169
03	288	0.531	3.60	0.0730
06	269	0.641	3.57	0.0157
09	268	0.655	3.56	0.0240
12	305	0.915	3.48	0.0690

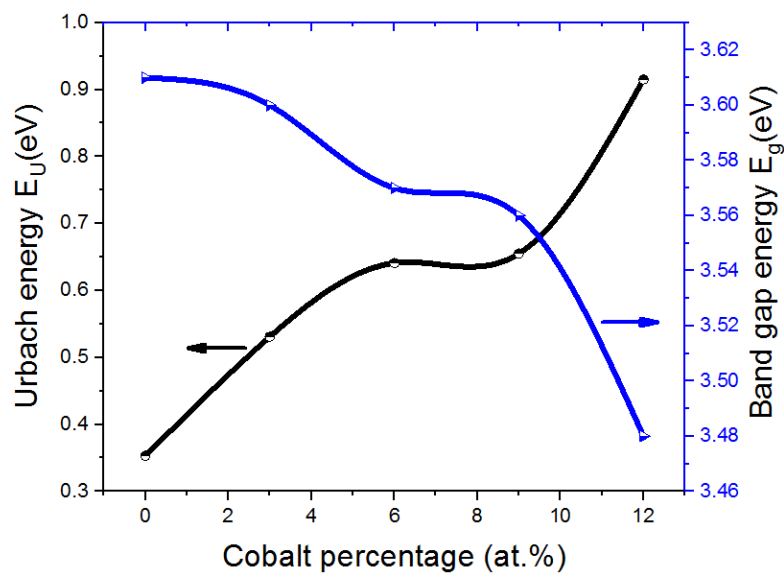


**Figure 3.33:** Reverse correlation between optical band gap energy and Urbach energy of Co-doped NiO thin films at different cobalt percentages.

### 3.3.3.3.c Electrical properties

The type of the NiO thin films was determined using hot probe method (Seebeck's effect). Where it was confirmed that the nature of conductivity of all films deposited were of p-type as specified in many of the literature. Whereas resistivity of NiO films was measured by the four probe method using the relation (1.23). The conductivity of the NiO thin films prepared at different percentage of Co-doping is shown in figure 3.33. It was clear that the electrical properties of NiO thin films are affected by doping. The films showed high electrical conductivity ranging from 0.0157 to 0.0730 ( $\Omega \cdot \text{cm}$ )<sup>-1</sup> at percentage of 6 and 3 at.% respectively. Generally, The electrical resistivity of NiO thin films has a strong dependence on the microstructural defects existing in NiO crystallites, such as nickel vacancies and interstitial defects therefore the electrical

properties of films depend strongly on surface effects, the grain size and the boundaries between them [238, 239].

Figure 3.34 also shows the close correlation between crystallite size and thickness of membranes with electrical conductivity, which is clearly affected in case of increasing or decreasing. Except in the case of doping 12 at.%, which suggests that the effect of thickness in this case is more important than the effect of the crystallite size of films.

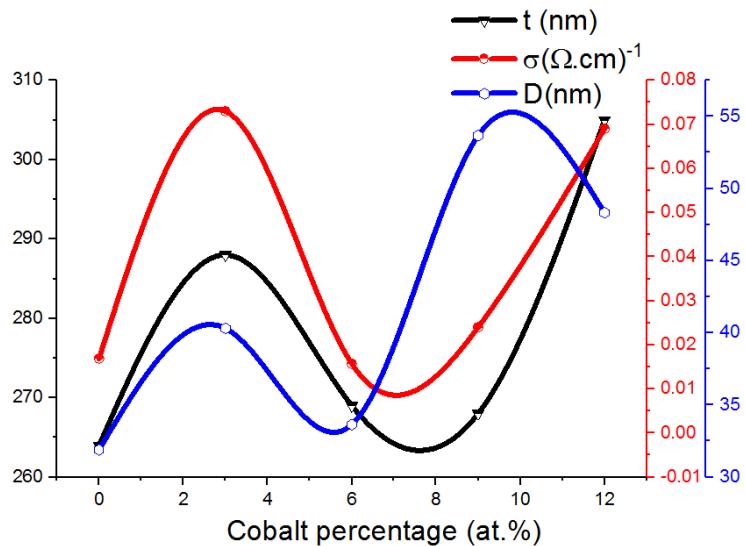


**Figure 3.34:** Close correlation between of Co-doped NiO thin films at different cobalt percentages.

### 3.3.4 Effect of copper doping on Physical properties of NiO thin films

In this section, Cu doped NiO thin films were prepared using SPT. In order to obtain better physical properties of thin films, it has been doped at specific atomic ratios, after that the effects of doping on the structural, optical and electrical properties of the films were studied and reported.

#### 3.3.4.1 Preparation of samples

NiO thin films were prepared onto a highly cleaned glass substrates (Standard glass CITOPPLUS-REF-0302-0004) using SPT. The 2.908 g of nickel (II) nitrate hexahydrate [ $\text{Ni}(\text{NO}_3)_2 \cdot 6 \text{H}_2\text{O}$ ] was dissolved in 100 ml of doubly distilled water to obtain the solution with molar concentration of 0.10 mol/L. Then the 1.705 g of copper (II) chloride dihydrate [ $\text{CuCl}_2 \cdot 2 \text{H}_2\text{O}$ ] (See figure 3.35 and table 3.7) dissolved in 100 ml of doubly distilled water to obtain the 0.10 mol/L of precursor solution. The two Precursor solutions were stirred at 60°C for 2 hours in order to obtain a clear and homoge-

nous solution. To obtain the Cu/Ni atomic doping ratios, we use certain proportions of the precursor solutions calculated from equation (3.1).

$$Cu(at\%) = \frac{V_{S_1}}{V_{S_1} + V_{S_2}} \times 100 \quad (3.4)$$



**Figure 3.35:** Copper (II) chloride dihydrate.

**Table 3.11:** Some physico-chemical properties of copper (II) chloride dihydrate.

Property	Value
Physical state	Solid
Chemical formula	$CuCl_2 \cdot 2 H_2O$
Molecular weight	170.48 g/mol
Melting point	100 °C
Boiling point	993 °C
Density	2.51 g/cm <sup>3</sup>
Water solubility	70.6 g/100 mL at (0 °C)
	75.7 g/100 mL at (25 °C)
	107.9 g/100 mL at (100 °C)

The appropriate copper (II) chloride dihydrate solution ( $S_1$ ) is added to nickel (II) nitrate hexahydrate solution ( $S_2$ ) for obtain the Cu/Ni atomic ratios: 0, 3, 6, 9, 12 at.%. The mixture solution was stirred at 60°C for half an hour to obtain a homogeneous solution. After that, the solution was sprayed on heated substrates at 400°C. Where the atomizer-substrate distance was kept 30 cm, the spray rate was 5 ml/min, and each spray takes five second, whereas the time interval between two successive sprays was 30 second to avoid the substrate temperature fall. Different precursor solutions of fixed volume (15 ml) were sprayed separately for getting on the Cu doped NiO thin films. After deposition, the films were allowed to cool till room temperature.

### 3.3.4.2 Devices and measurements

The X-ray diffraction (XRD) spectra of the Cu doped NiO nanostructured thin films prepared with different copper percentages were measured to verify its structure. X-ray diffraction (XRD) was measured by using BRUKER-AXS-8D diffractometer with Cu  $K_{\alpha}$  radiation ( $\lambda=1.5406 \text{ \AA}$ ) operated at 40 KV and 40 mA in the scanning range of ( $2\theta$ ) between  $30^{\circ}$  and  $80^{\circ}$ . The spectral dependence of the NiO transmittance (T), on the wavelength ranging 200–900 nm is measured using an ultraviolet-visible spectrophotometer (Shmatzu 1800). Whereas the electrical conductivity of the films was measured in a coplanar structure of four golden stripes on the deposited film surface; the measurements were performed with Keithley model 2400 low voltage source meter instrument. In order to preview the surface morphology, the images were taken by a scanning electron microscope (SEM) TESCAN VEGA3. All measurements were carried out at room temperature.

### 3.3.4.3 Results and discussions

#### 3.3.4.3.a Structural and surface morphological properties

The X-ray diffraction patterns for the Cu-doped NiO thin films from 0 to 12 at.% are shown in figure 3.36. From the figure it is obvious that the four peaks are indexed as (111), (200), (220) and (311) corresponding to diffraction angles  $2\theta$  Included in Table 3.8, that correspond to face centered cubic structure of NiO nanoparticles which are in consistent with the JCPDS (No.89-7130) data. It is possible to estimate that the sample with 6 at.% has higher peaks than other samples, which means that it has better crystallization. It can be also observed that no peaks correspond to the Cu-doping exist in the XRD patterns. In fact, doping with low concentration impurities does not result in the appearance of new XRD peaks, but instead leads to a shift in the lattice parameters of the host material. This shift may arise from the strain induced when the dopant is incorporated into the crystal lattice [240]. Where we can observe that there is a little shift of  $2\theta$  location, from 3 to 6 at.% towards the lower values and then from 9 to 12 at.% towards the larger values with varying degrees (Figure 3.37). The shift in peak position is may be due to the variation of the ionic radius of the Cu dopant ( $R_{Cu} \approx 0.73 \text{ \AA}$ ) [224].

The wide variety of textures observed at varying deposition conditions provides detailed information about the structural properties of the films. The texture coeffi-

cient for each of the four diffraction peaks in the Cu-doped NiO films was calculated from their intensities relative to each other and to the standard powder pattern JCPDS (No.47-1049), as per equation (1.10). The texture coefficient  $TC(hkl)$  represents the texture of a particular plane; deviation of a plane from unity implies that this is the preferred direction of growth. For a preferential orientation, the  $TC(hkl)$  values should be greater than one [241, 242]. The degree of preferred orientation denoted by the calculated coefficient of texture using Eq.(1.10) is presented in figure 3.38. When the  $TC(hkl)$  values were investigated, all of the Cu-doped NiO thin films demonstrated a clear preference for growth along the (111) planes. This effect, i.e., preferential growth, becomes less predominate with increasing dopant percentage. The highest TC value was obtained for the (111) plane of the 3 at.% Cu-doped NiO thin film.

The average crystallite size of Cu-doped NiO thin films, with different copper percentage, was determined using the Scherrer formula (1.5) and Williamson–Hall (W-H) method. Williamson-Hall method is a classical method to obtain qualitative information of anisotropy in broadening, where crystal imperfections and distortion of microstrain induced peak broadening are related.

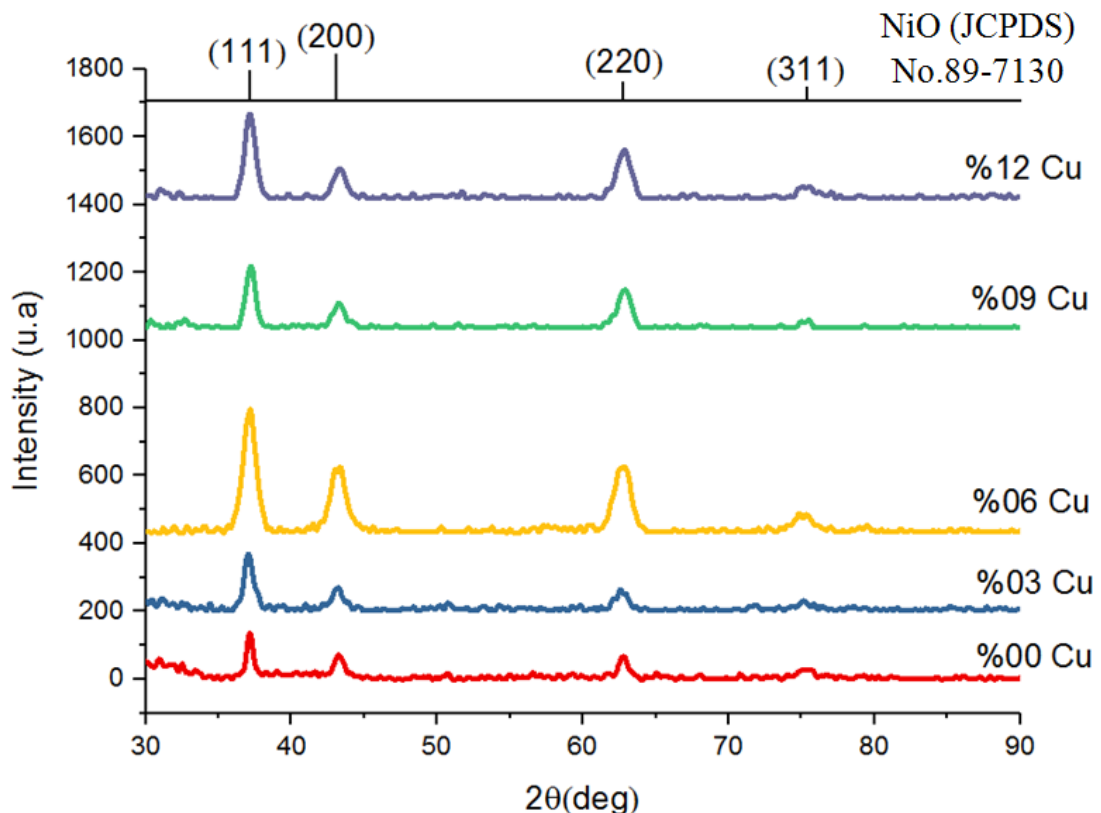


**Figure 3.36:** XRD patterns of the deposited Cu-doped NiO thin films on glass substrate at different copper percentages.

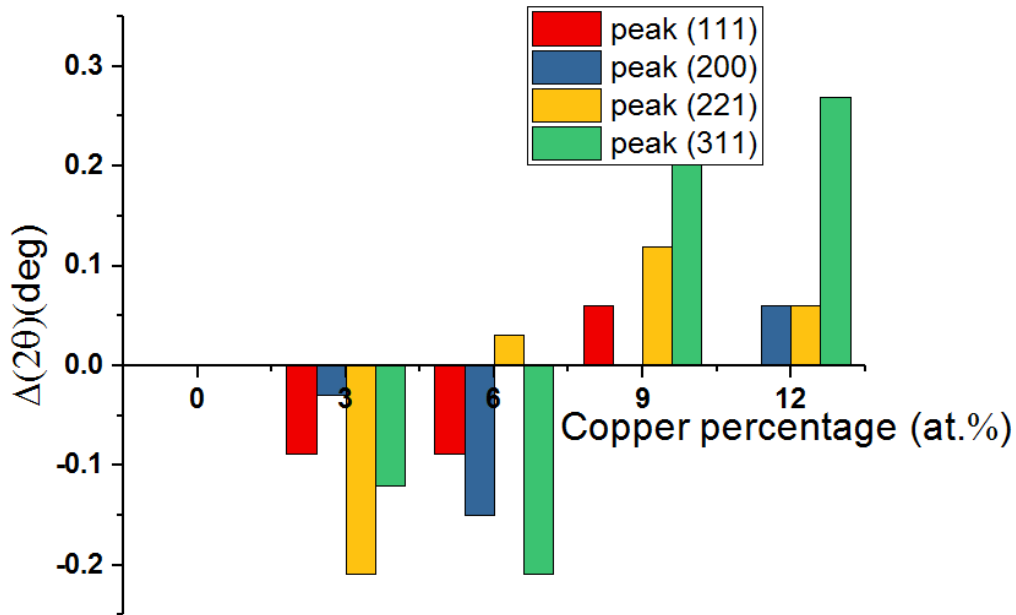
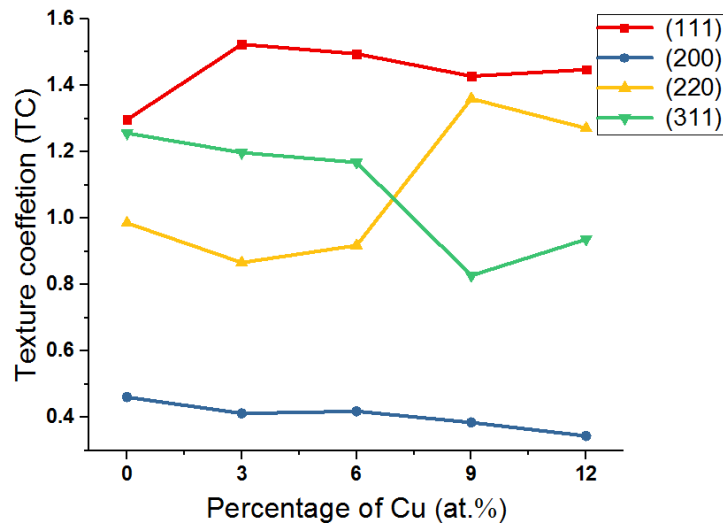


Figure 3.37: Variation of the  $\Delta(2\theta)$  values as function of Cu-doping percentages.

Table 3.12: X-ray diffraction data of Cu-doped NiO thin films at different copper percentages.

Copper percentage (at.%)	Plane (hkl)	Bragg's angel $2\theta$ (deg)		Intensity (u.a)		FWHM $B$ (deg)
		Observed	Reported	Observed	Reported	
00	111	37.143	37.095	134.61	67.4	0.267
	200	43.241	43.098	71.1	99.9	0.426
	220	62.789	62.590	66.51	43.8	0.367
	311	75.283	75.048	27.86	14.4	0.669
03	111	37.054	37.095	164.48	67.4	0.363
	200	43.211	43.098	66.02	99.9	0.4026
	220	62.580	62.590	60.8	43.8	0.559
	311	75.163	75.048	27.62	14.4	0.378
06	111	37.054	37.095	272.84	67.4	0.463
	200	43.091	43.098	113.38	99.9	0.570
	220	62.819	62.590	108.87	43.8	0.550
	311	75.074	75.048	45.55	14.4	0.441
09	111	37.203	37.095	181.31	67.4	0.383
	200	43.241	43.098	72.57	99.9	0.497
	220	62.908	62.590	112.24	43.8	0.530
	311	75.492	75.048	22.46	14.4	0.449
12	111	37.143	37.095	248.52	67.4	0.426
	200	43.301	43.098	87.75	99.9	0.510
	220	62.849	62.590	141.8	43.8	0.594
	311	75.552	75.048	34.36	14.4	0.636



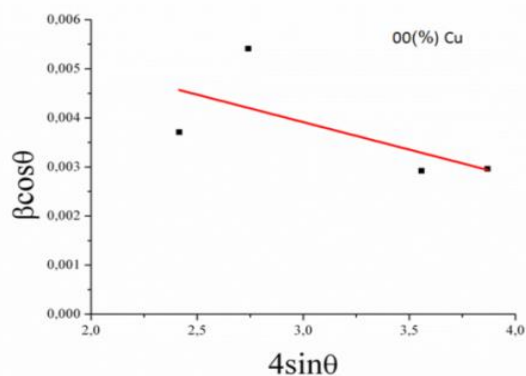
**Figure 3.38:** Texture coefficient values for all peaks of Cu-doped NiO thin films at different copper percentages.

Williamson and Hall assumed that both size and strain broadened profiles are Lorentzian. Based on this assumption, a mathematical relation was established between the full width at half maximum intensity ( $\beta$ ), average crystallite size ( $D$ ) and the microstrain ( $\varepsilon_\mu$ ) as follows [243, 244].

$$\beta \cos(\theta) = \frac{0.9 \lambda}{D} + 4\varepsilon_\mu \sin(\theta) \quad (3.5)$$

Where ( $\lambda$ ) is the wave length of the X-ray beam and ( $\theta$ ) is the Bragg's angel.

Figure 3.39 shown the plot of  $\beta \cos(\theta)$  versus  $4 \sin(\theta)$  which gives the value of the microstrain from the slope and crystallite size from the ordinate intercept. If the points in the W-H plot are scattered, i.e., if  $\beta \cos(\theta)$  is not a monotonous function of  $4 \sin(\theta)$ , the broadening is termed as anisotropic [243, 244]. The values of the average crystallite size ( $D$ ), the microstrain ( $\varepsilon_\mu$ ) and Dislocation density ( $\delta$ ) were given in table 3.12.



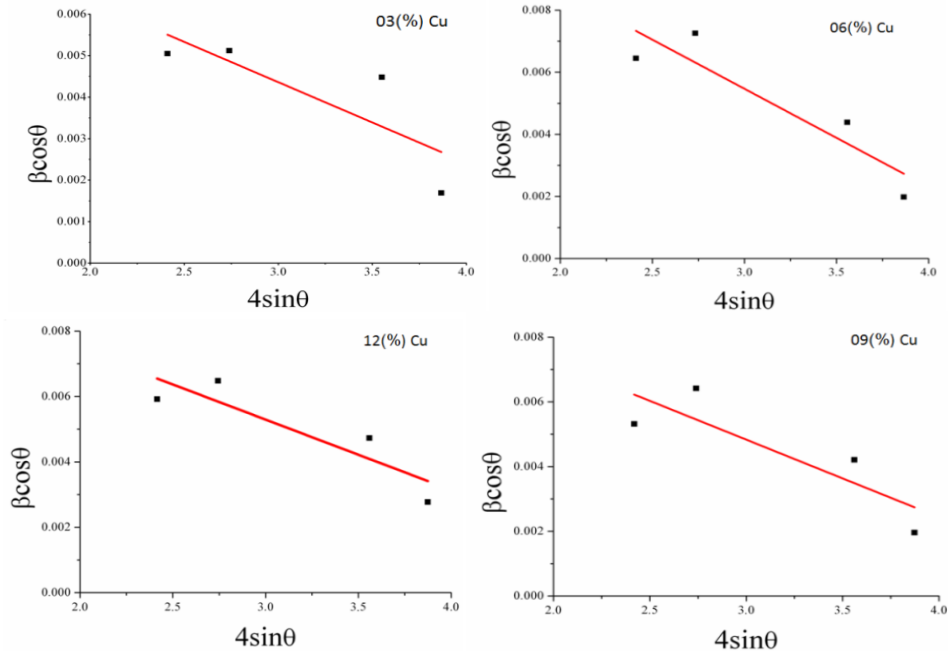


**Figure 3.39:** Determination of the average crystallite size ( $D$ ) and the microstrain ( $\varepsilon_{\mu}$ ) by Williamson-Hall plot method.

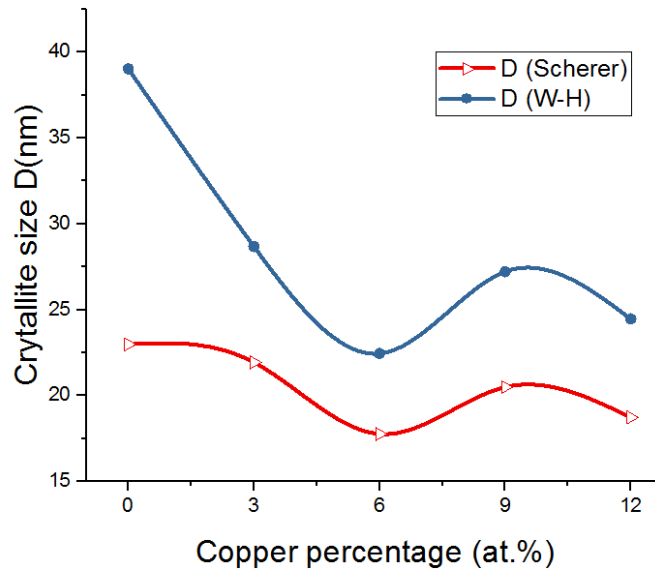
**Table 3.13:** Structural parameters of Cu-doped NiO thin films at different copper percentages.

Copper percentage (at.%)	Lattice constant $a(\text{\AA})$	Crystallite size $D(\text{nm})$		Microstrain $\varepsilon_{\mu}$ (%)		Dislocation density $\delta(\text{lines/m}^2) \cdot 10^{16}$
		Scherrer	W-H	W-H	Eq.(1.8)	
00	4.1847	22.98	39.03	-0.112	0.162	0.656
03	4.1924	21.93	28.68	-0.194	0.163	1.216
06	4.1927	17.76	22.45	-0.316	0.195	1.984
09	4.1789	20.49	27.22	-0.240	0.178	1.350
12	4.1793	18.73	24.46	-0.215	0.206	1.671

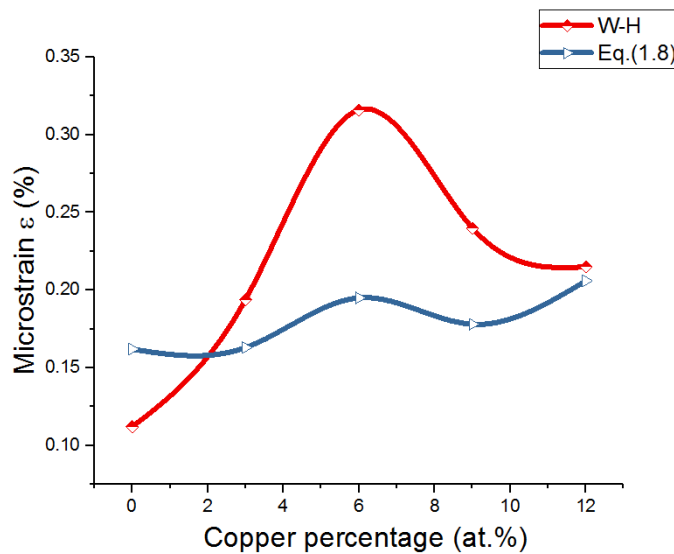
Figure 3.40 shows a clear correlation between the changes in the jellied volume values calculated in Williamson-Hall method and the Scherrer method. However, the values calculated with the first method are greater due to the different approximations adopted by the both methods. It also shows that the granular size decreases with the increase in Cu doping percentage in general.

Figure 3.41 shows a clear correlation between the changes in the microstrain values calculated with William Hall method and the equation (1.8). However, the values calculated with the first method are greater due to the different approximations adopt-

ed by the both methods. It also shows that the microstrain increases with the increase in Cu doping percentage in general.

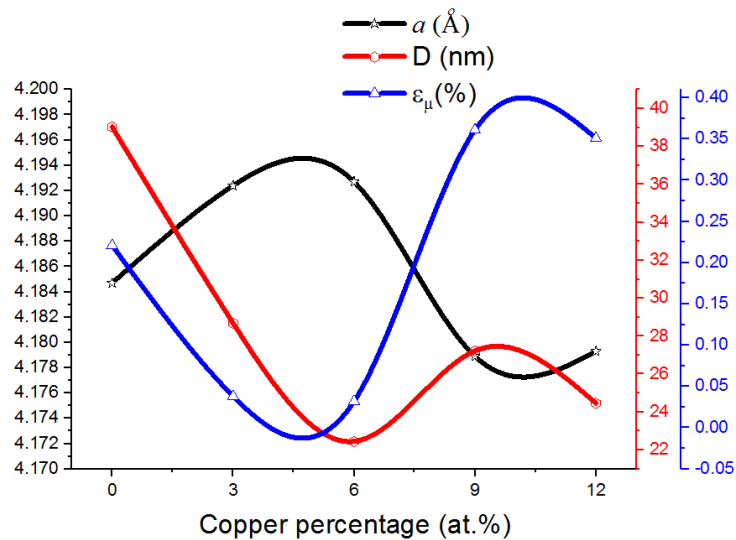


**Figure 3.40:** Comparison between the values of the average crystallite size ( $D$ ) determined by the Williamson Hall plot and the Scherer method.



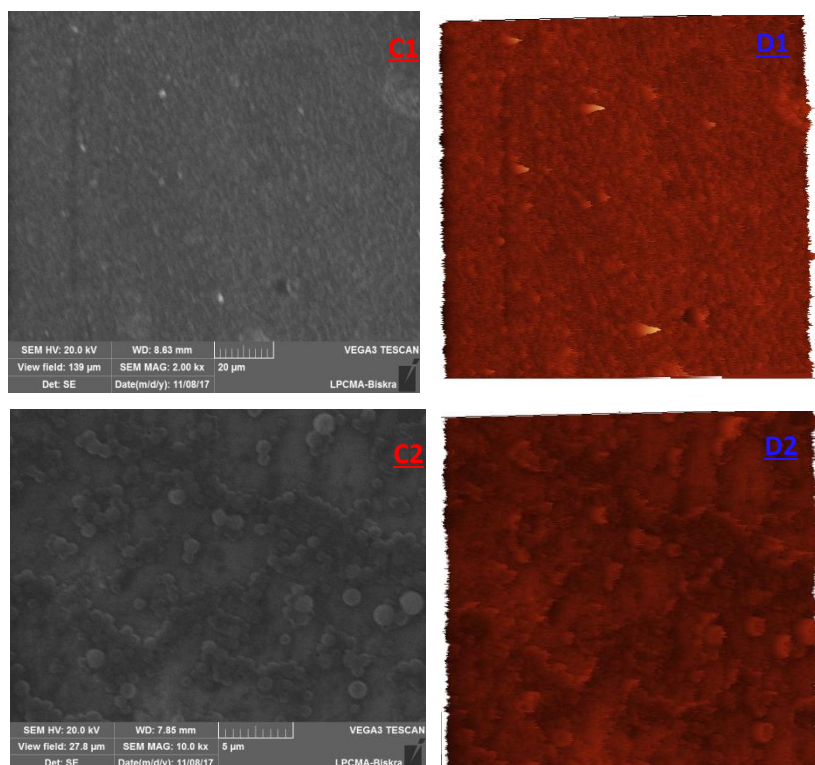
**Figure 3.41:** Comparison between the values of the Microstrain ( $\epsilon_\mu$ ) determined by Williamson-Hall plot method and Eq. (1.8).

Figure 3.42 shows changes of the values of the average crystallite size ( $D$ ), the microstrain ( $\epsilon_\mu$ ) and lattice constant ( $a$ ) with different percentages of copper doping. From the Figure, it is possible to observe the compatibility of changes between crystallite size and lattice constant, but in a reverse way the microstrain changes. It can be noticed that the film with the best structural properties has smallest microstrain value, which effects in the crystallization level.



**Table 3.42:** Correlation between structural parameters of Cu-doped NiO thin films at different copper percentages.

Scanning electron microscope images of NiO sample doped with 6 at.% of Cu are shown in figure 3.43. The effect of copper doping on the morphology of thin films was studied; it was found to be homogenous and it covers the entire substrate. At first, the film looks rather smooth in picture C1, showing a regular distribution of grain in all directions, while it appears coarser in images C2 and C3 due to the emergence of clusters of grains in the form of discs on the surface. We can note that these clusters of grains have heterogeneous sizes between 3 and 6 microns.



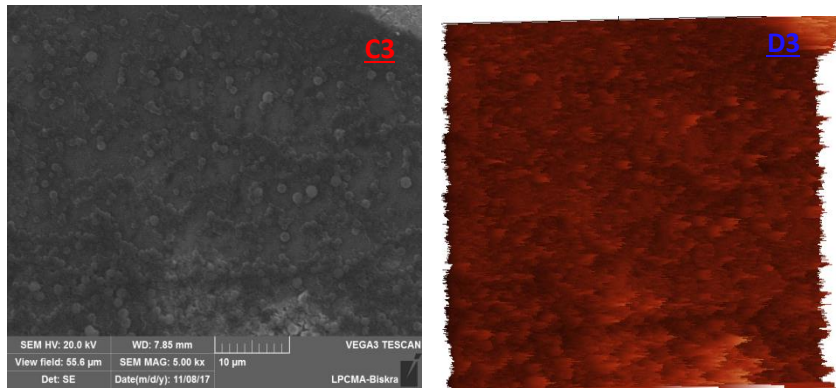


**Figure 3.43:** SEM and Gwyddion program images of Cu-doped NiO thin film with 6 at.% at different scales.

Accordingly, we can conclude that doping has an effect on the formation of the film, which is porous, with aggregates that are not uniform in size.

### 3.3.4.3.b Optical properties

Figure 3.44 shows the transmittance spectra in the UV-Visible range (300 - 900 nm) of undoped and Cu-doped NiO thin films in the doping range of 0 to 12 at.%. The transmittance for all thin films increases as the wavelength increases in the range of (300- 375 nm), and then increases slowly at higher wavelengths. The spectrum shows high transmittance in the visible and near-infrared regions range of 65-89%, and low in the ultraviolet region. Also, one can observe in this figure that the fundamental absorption edge (absorption edge which separates the high absorption region and the low absorption region or the window region) is sharp in the visible region at the wavelength (375 nm) of the spectrum.

To see the effect of doping on transmittance, the transmittance spectra of Cu-doped NiO thin films found that the layers are transparent in the visible and have an absorption edge in the near UV with a shift from this edge to the short waves under the Burstein-Moss effect (B-M) [245, 246] or length waves under the Roth effect [247]. The shift of the absorption edge of the films can be explained by B-M effect, according to which the increase in carrier concentration due to doping results makes a shift of the Fermi level, by approaching the conduction band or valence band, and to block certain low energy-states at the tail of conduction band or high energy states at the tail of valence band, thus causing the widening of the band gap; this widening expresses the shift of the absorption tail towards the short wave-length (high energy). This widening of the forbidden band is also responsible for the improvement of transmission in the UV region. The opposite effect, which causes the gap narrowing that is

observed for semiconductors heavily doped. When the Fermi level passes in the conduction band, which causes the narrowing of the gap following the fusion of donor bands and conduction and which is called the Roth effect [247].

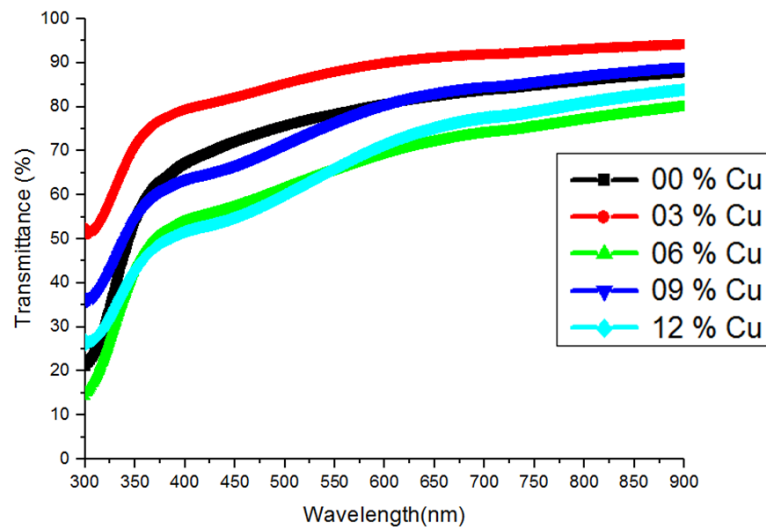


**Figure 3.44:** Transmission spectra of Cu-doped NiO thin films at different copper percentages.

The study of absorbance was in the range of (300– 900 nm). Figure 3.45 shows the relation between absorbance (A) and wavelength for Cu-doped NiO thin films. The absorbance decreases rapidly at short wavelengths (high energies) corresponding to the energy gap of the film, (when the incident photon has an energy equal or more than the energy gap value). This evident increase of energy is due to the interaction of the material electrons with the incident photons which have enough energy for the occurrence of electronic transitions, this attribute to decrease the energy gap of the film. Nickel oxide is a high band-gap semiconductor with the absorption edge in the UV region and no absorption in the visible region. This absorption is due to multiple reasons, including the structural defects and impurities; such as the presence of Ni<sup>3+</sup> ions in the oxide lattice, where it shows charge transfer transition with the consequent absorbance.

The energy gap values depend in general on the films crystal structure, the arrangement and distribution of atoms in the crystal lattice, also affected by crystal regularity. The optical energy gap ( $E_g$ ) was derived assuming allowed direct transitions between the edge of the valence and conduction band.

The band gap width of the undoped and Cu-doped NiO thin films was determined from the transmission spectra by a graphical method using Tauc's equation (1.17),

This was done by plotting a graph  $(\alpha h\nu)^2 = f(h\nu)$ , a straight line is obtained which gives the value of the direct band gap. The extrapolation of the straight line to  $(\alpha h\nu)^2 = 0$  gives value of the direct band gap of the material, and this could be seen in figure 3.46. The gap-energy values obtained for undoped and Cu-doped NiO films for all doping percentage from 0 to 12 at.%. The values estimated ranging from 3.60 to 3.43 eV and were summarized in the table 3.13.

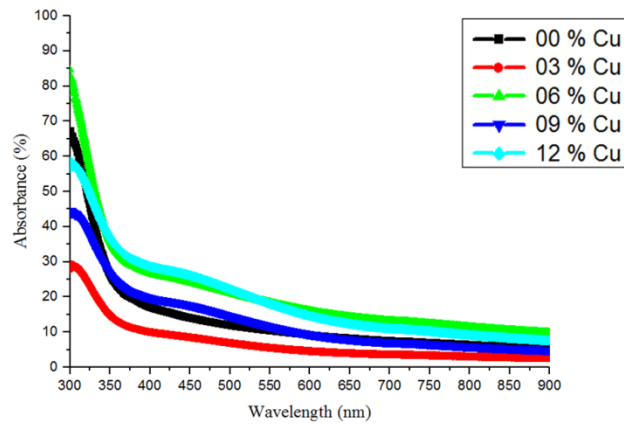


**Figure 3.45:** Absorbance spectra of Cu-doped NiO thin films at different copper percentages.

For undoped NiO film, the value of  $E_g$  is 3.60 eV, this value has a good agreement with that obtained from the NiO bulk [248]. Clearly, the values of  $E_g$  decrease with increasing Cu percentage; this change of  $E_g$  may be refer to the influence of various factors such as film thickness, crystallite size, lattice strain and presence of impurities in the films [249].

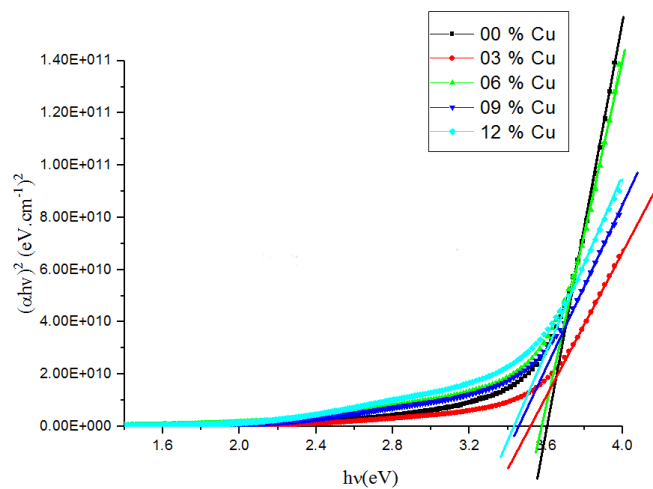


**Figure 3.46:** Plot of  $(\alpha h\nu)^2$  versus incident photon energy ( $h\nu$ ) of Cu-doped NiO thin films at different copper percentages.

**Table 3.14:** Optical and electrical parameters of Cu-doped NiO thin films at different copper percentages.

Copper percentage (at.%)	Thickness t (nm)	Urbach energy $E_U$ (eV)	Band gap energy $E_g$ (eV)	Conductivity $\sigma$ ( $\Omega\cdot\text{cm}$ ) <sup>-1</sup>
00	140	0.523	3.60	0.0214
03	104	0.591	3.53	0.1588
06	178	0.644	3.57	0.0980
09	137	0.872	3.46	0.1044
12	170	0.935	3.43	0.2916

Urbach ( $E_U$ ) gives the presentation of the tails of situational positions within the optical range gap, which is a useful parameter for assessing structural disturbance [250, 251]. Urbach energy can be calculated using equation (1.21). Figure 3.47 shows Urbach plots of the doped NiO thin films. The values of ( $E_U$ ) was obtained from the inverse of the slope of ( $\ln(\alpha)$ ) versus ( $h\nu$ ).

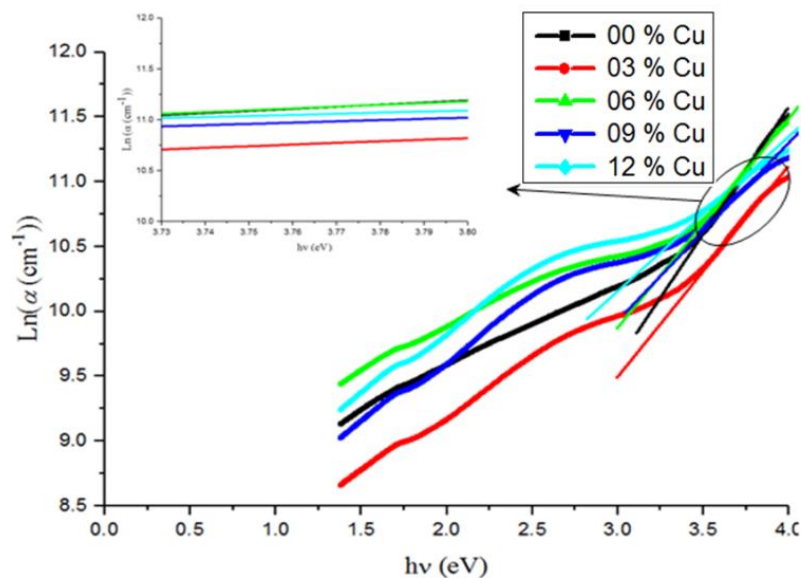


**Figure 3.47:** Plot of  $\text{Ln}(\alpha)$  versus incident photon energy ( $h\nu$ ) of Cu-doped NiO thin films at different copper percentages.

Calculated  $E_U$  values were ranging from 0.523 to 0.935 eV. It can be noted that the  $E_U$  values increase with increased the percentage of copper doping. The increasing in the values of the  $E_U$  can be attributed to the creation of localized situations of doping ions in the forbidden band gap. Although crystalline defects can contribute to the establishment of local cases within the forbidden band gap, but the effect of Cu-doping is greater and more important in this case, which is confirmed by figure 3.48. The last

figure also shows the increasing of Urbach energy values after the doping percentage Cu at.% in spite of a decrease in the values of crystalline defects such as microstrain ( $\epsilon_{\mu}$ ) and dislocation density ( $\delta$ ). Figure 3.49 shows the variation of  $E_g$  and  $E_U$  values of the undoped and Cu-doped NiO thin films. It is observed that both  $E_g$  and  $E_U$  values vary in opposite ways. The red shift in the  $E_g$  value observed for the Cu-doped NiO film is well supported with its high  $E_U$  value which confirms the increased disorderliness of these films.

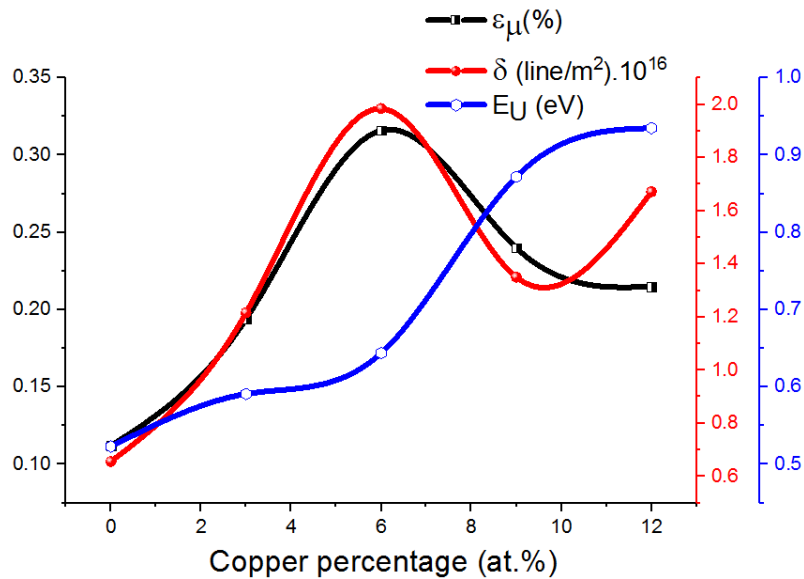


**Figure 3.48:** Variation of microstrain, dislocation density and Urbach energy of Cu-doped NiO thin films at different copper percentages.

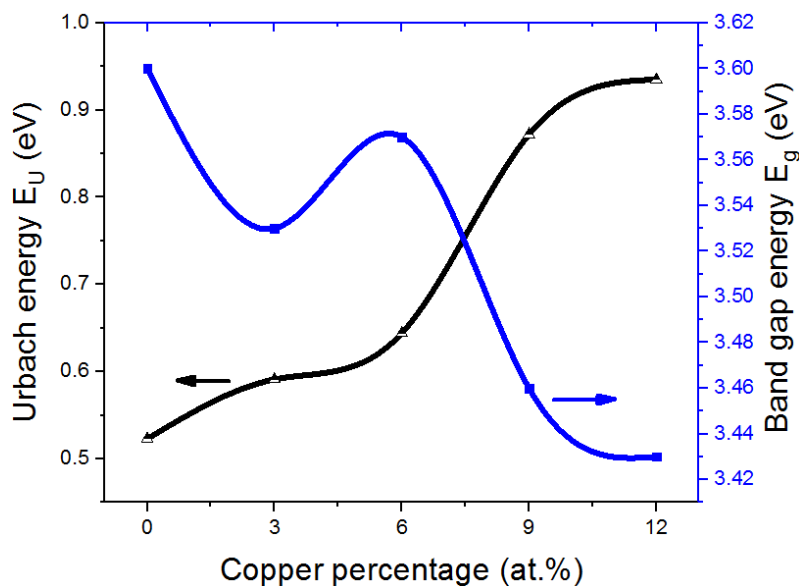


**Figure 3.49:** Variation of optical band gap energy and Urbach energy of Cu-doped NiO thin films at different copper percentages.

### 3.3.4.3.c Electrical properties

The type of the NiO thin films was determined using hot probe method (Seebeck effect). Where it was confirmed that the nature of conductivity of all films deposited were of p-type as specified in many of the literature. Resistivity of NiO films was measured by the four probe method using the relation (1.23). Figure 3.50 shows the increasing of the electrical conductivity of the films from the 0.0214 to 0.2916  $\Omega^{-1} \cdot \text{cm}^{-1}$ , when the percentage of Cu-doping is increased from 0 to 12 at.%. Where we notice a sudden increase in 3 at.% percentage, this may be due to the weak film thickness in this percentage of doping. The figure 3.50 also shows that conductivity changes in contrast to the band gap energy when the doping rate is increased. Conductivity takes the minimum value when  $D$  and  $E_g$  are minimal and takes the highest value when they are higher.

For the undoped NiO films, the conductivity may be attributed to the presence of microstructural defects existing in NiO crystallites such as nickel interstitials and oxygen vacancies which implies the formation of  $\text{Ni}^{3+}$  ions in the NiO crystal [252, 253], the microstrain and dislocation density values obtained for this film (Table 3.9) strongly supports the this fact. But for doped films, it increases with Cu-doping increasing which may be due to the substitution of  $\text{Ni}^{2+}$  by  $\text{Cu}^{2+}$  creating more acceptor levels close the valence band edge, therefore more electrical conduction as Cu-doping level increases [254, 255].

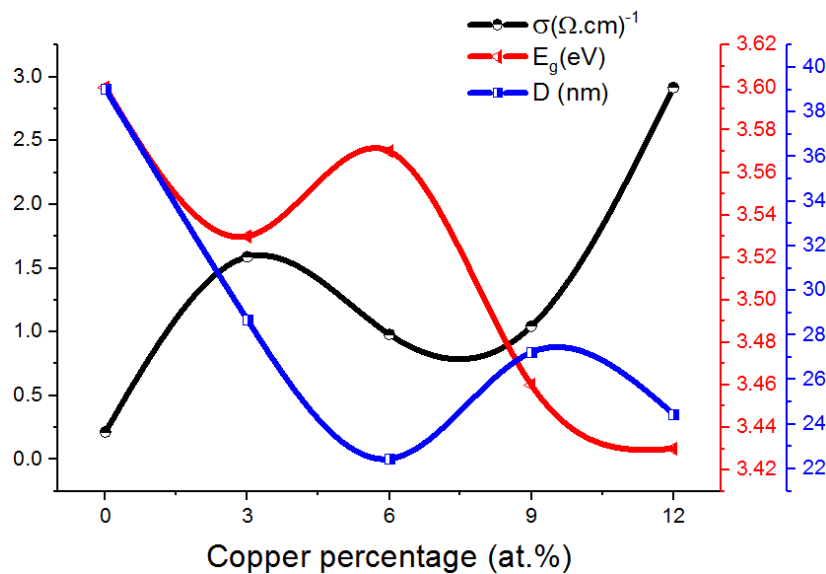


**Figure 3.50:** Variation of electrical conductivity, optical band gap energy and crystallite size of Cu-doped NiO thin films at different copper percentages.

### 3.4 Conclusion

In this chapter, we elaborated the NiO thin films, then we studied the effect of deposition parameters on the structural, optical and electrical properties of undoped and Co and Cu-doped (NiO) thin films. The XRD patterns showed that the structure of the undoped and doped NiO films is polycrystalline structure with the preferred direction (111) also showed that there was no significant shift in the direction of diffraction peaks after doping with cobalt or copper. The crystalline size is increased by thermal annealing and decreases by increasing the doping in the (NiO) samples. From the transmittance spectra, for all samples it was observed that the optical transparency values were moderate to relatively weak, it decrease by thermal annealing, by increasing the molar concentration of the precursor solution, or by increasing the percentage of doping with cobalt or copper. Cobalt or copper doping was also found to be decreasing the band gap energy for the above mentioned reasons, and its values ranged from 3.86 to 3.64 eV for undoped NiO films. For doped films, it ranged between 3.61 and 3.48 eV to cobalt doped films and between 3.60 and 3.43 eV to copper doped films. It was observed that the electrical conductivity of all samples is good and it is the P-type and it has been shown to increase by thermal annealing or by increasing the proportion of doping with cobalt or copper in general, and its value exceeded ( $0.29 \Omega^{-1} \cdot \text{cm}^{-1}$ ) when doped By 12 at.% of Copper. In the next chapter, the finest samples obtained will be used to study the sensing performance of some VOCs such as ethanol, acetone and methanol.

# Chapter Four

4/4

Gas sensing performance  
of the NiO thin films

## CHAPTER 4

# Gas sensing performance of the NiO thin films

### 4.1 Introduction

Many VOCs are present in the breath of a human and some are known to have a correlation to certain aspects of an individual's health. Further, there are many other VOCs present in the environment that are known to have adverse effects on our health. These VOCs are easily breathed in by humans since some are commonly used as ingredients in household products or in industrial processes. Therefore, it is important to monitor the concentration of these VOCs for the safety of residents and workers. Among the various VOCs, alcohol and acetone have drawn a lot of attention in the recent past [256]. Alcohol sensors with high selectivity and stability have their uses in biomedical, chemical and food industry.

The MOS chemical gas sensor devices have several unique advantages such as low cost, high sensitivity (ppm levels), small size, measurement simplicity, durability and ease of fabrication. In addition, most MOS based sensors tend to be long-lived and somewhat resistant to poisoning. For these reasons, they have rapidly grown in popularity, becoming the most widely used gas sensors available these days. All above listed characteristics have been the subject of extensive research for the past two decades. But still the quest for developing a sensor that has all the properties listed is still far from reaching an end. In the present chapter, we present the homemade gas sensor and we define the its most important components and the role of each component. Then we present the gas sensing performance for organic vapors (methanol, ethanol and acetone), that based on the undoped and Co or Cu-doped NiO thin films at 0, 3, 12 at.%.

## 4.2 gas sensor fabrication

The measurement system was set up for sensor testing, which is very important to determine the sensitivity and selectivity of each sensor to specific gases. A reasonable set of gases, as related to the planned future applications of the sensor, should be selected, which in this case are ethanol, methanol and acetone [257]. The static measurement system consists of three major components, namely a big sensing chamber, a sensing element and a sensing data system. The aim is produce a homemade gas sensor using NiO thin films as sensitive element. We illustrate photos of the fabricated gas sensor in figure 4.1. NiO thin films were firstly deposited on glass substrates by spray pyrolysis technique in the conditions previously described. We deposited silver electrodes on both ends of the samples for good electrical conductivity. The obtained gas sensor is used to sensing the organic vapors only. In the next, we define the most important components of the homemade gas sensor and the role of each component:

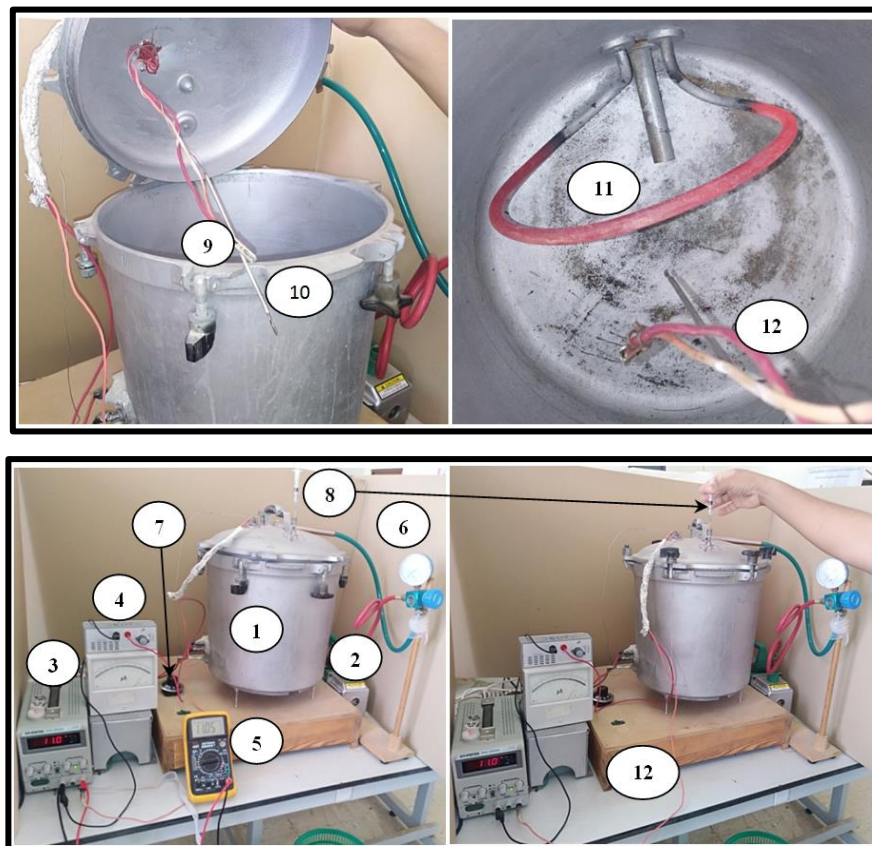


**Figure 4.1:** The most important components of the homemade gas sensor.

- 1. Sensing chamber:** It is a large pressure cooker its capacity of 22.5 liters, the process of sensing gases is carried out inside it.

2. **Vacuum pump:** It is a small primary vacuum pump used to empty the air or gas of sensing room to rehabilitate it again.
3. **DC Voltage generator:** Used to generate a continuous low current passing through the sample to be tested.
4. **Microammeter:** Used to measure the current passing through the sample.
5. **Multimeter:** Used to measure electric voltage or electrical resistance on both ends of the sample.
6. **Pressure gauge:** It measures the pressure of gas inside the sensing chamber.
7. **Temperature control scale:** Used to control the temperature of the sensing room from the inside.
8. **Syringe:** Used to inject material to be sensed.
9. **Metal pliers:** Used to hold the sample from both ends for good conduction of electricity.
10. **Thermal probe:** Used to detect the temperature inside the sensing chamber.
11. **Electrical resistance:** Used to heat the sensor chamber.
12. **Heat-resistant electrical wires:** Used for electrical conduction inside and outside the sensing chamber.

### 4.3 Gas sensing measurement

The electrical measurements were carried out at different temperatures from 60°C to 220°C, on a sample of pure NiO, two samples doped with cobalt (3, 12 at.%) and two other samples doped with copper (3, 12 at.%), This was done using an electrical circuit comprising: a DC voltage generator its voltage varies from 0 to 30 volts, a microammeter, a voltmeter, ohmmeter and standard electric wires and other heat resistant. The samples were provided with ohmic electrodes in the form of two silver bands, as shown in figure 4.2. The spacing between electrodes is 2 mm.

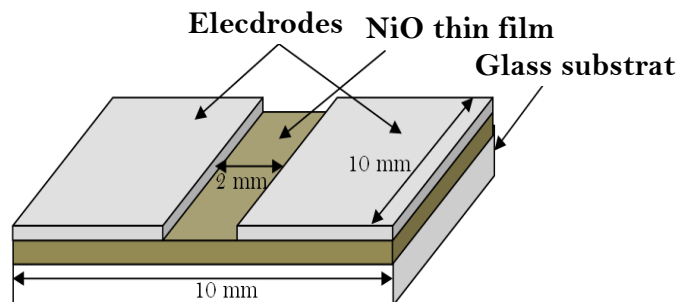


**Figure 4.2:** Schematic diagram of sensing element with two silver strips used as electrodes.

Figure 4.3 confirmed that the samples have an ohmic electrical resistance, it means the current-voltage curves are straight lines that pass of origin point.

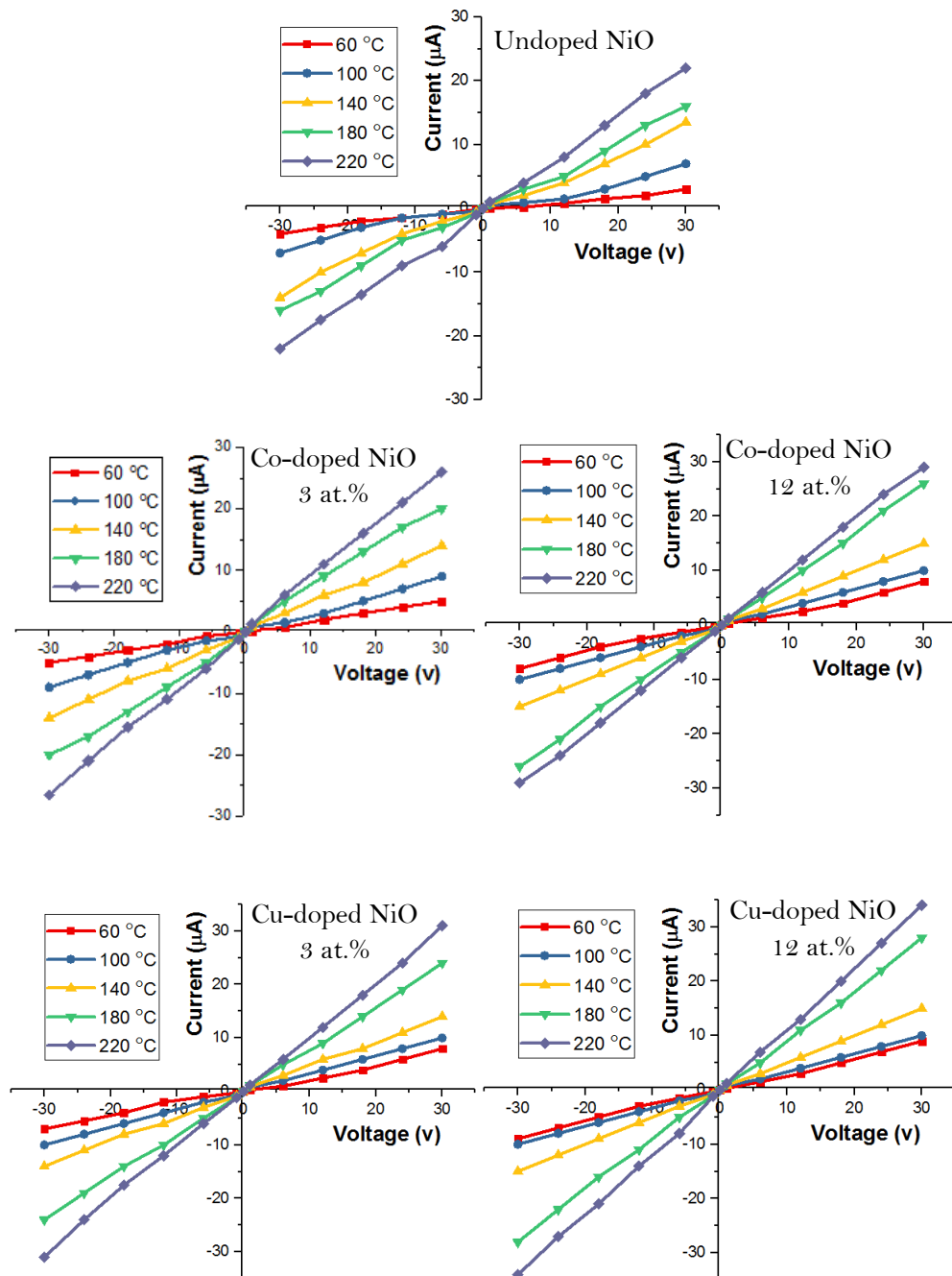


**Figure 4.3:** Voltage-current Plot (in air) of undoped and Co and Cu-doped NiO thin films at different operating temperature.

The organic vapors sensing experiments for methanol, ethanol and acetone are performed in a customized chamber with defined volume; it is the sensing chamber its capacity of 22.5 liters. The sensing samples are placed near the heat probe inside the sensing chamber to monitor real temperature. An AC power supply and temperature

control scale was connected to the heater to control the operating temperature. A schematic diagram of the gas system measurement for vapors is represented in figure 4.1. A concentration of organic vapor (methanol, ethanol or acetone) inside the system is achieved by injecting a known volume of liquid using small syringe. This volume corresponding to ppm concentration of induced volume calculated using the following equation [61, 257, 258]:

$$\text{Concentration}(\text{ppm}) = \frac{d \times V_{inj} \times R_u \times T}{M \times P \times V_{SC}} \quad (4.1)$$

Where  $d$  is the density of liquid ( $\text{kg}/\text{m}^3$ ),  $V_{inj}$  the volume of injected organic liquid (ml),  $R_u$  is universal gas constant  $\text{m}^3 \cdot \text{atm}/(\text{mol} \cdot \text{K})$ ,  $T$  is the absolute temperature (K),  $P$  is the pressure in the sensing chamber (Pa),  $V_{SC}$  is the sensing chamber volume ( $\text{m}^3$ ) and  $M$  is the molecular weight ( $\text{g}/\text{mol}$ ). The table 4.1 shows some chemical properties of the material of fumes that we want to sense.

**Table 4.1:** Some chemical properties of the methanol, ethanol and acetone [259, 260].

Material	Methanol	Ethanol	Acetone
Chemical formula	$\text{CH}_4\text{O}$	$\text{C}_2\text{H}_6\text{O}$	$\text{C}_3\text{H}_6\text{O}$
Molar mass	$32.04 \text{ g} \cdot \text{mol}^{-1}$	$46.069 \text{ g} \cdot \text{mol}^{-1}$	$58.080 \text{ g} \cdot \text{mol}^{-1}$
Appearance	Colorless liquid	Colorless liquid	Colorless liquid
Density	$0.792 \text{ g}/\text{cm}^3$	$0.7893 \text{ g}/\text{cm}^3$	$0.7845 \text{ g}/\text{cm}^3$
Melting point	$-97.6 \text{ }^\circ\text{C}$ (175.6 K)	$-114.14 \text{ }^\circ\text{C}$ (159.01 K)	$-94.7 \text{ }^\circ\text{C}$ (178.5 K)
Boiling point	$64.7 \text{ }^\circ\text{C}$ (337.8 K)	$78.24 \text{ }^\circ\text{C}$ (351.39 K)	$56.05 \text{ }^\circ\text{C}$ (329.20 K)
Vapor pressure	13.02 kPa (at $20 \text{ }^\circ\text{C}$ )	5.95 kPa (at $20 \text{ }^\circ\text{C}$ )	30.6 kPa (at $25 \text{ }^\circ\text{C}$ )

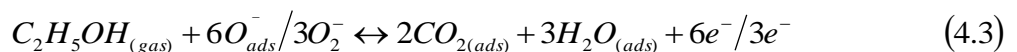
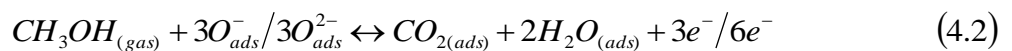
## 4.4 Principle and mechanism of gas sensor

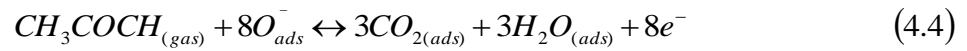
It has been reported that parameters such as grain size, thickness, film texture, porosity, grain pattern, and surface geometry are important for the properties of gas sensing of thin films of NiO. Between these parameters, grain size and porosity are two main factors that affect the gas sensing parameter of the NiO thin film. With a decrease in grain size, the area-to-volume ratio increases and the exposed surface of the film increases, respectively.

It has been shown that the gas response increases abruptly when the particle size becomes comparable to or smaller than the certain length (typically several nm) [261,

262]. In our work, it can be observed in figures 3.28 and 3.43, that the inner surfaces of the structure are very rough and have broken shells and wrinkles with well-aligned porous structures. When large tightly packed cluster of nanoparticles are exposed to a target gas, the gas cannot spread to particles in the interior of the aggregate, relatively reducing the effective surface area. However, in this work, the hollow nanostructures are much loose and porous leading to higher specific surface area. Thus, high response was obtained. The remarkably response can be attributed to the high surface area and the rapid diffusion of the target gas toward the sensing surface via porous and well-aligned nanostructures.

The gas sensing mechanism is based on the change in the conductance of the MOS sensing element. The oxygen absorbed at the surface of the materials influences the conductance of the MOS-based sensor. The oxygen absorbed depends on the type of materials and its sensing surface, particularly their chemical reaction with the gas. We know beforehand that, NiO is a p-type oxide semiconductor. The chemical reaction (reduction or oxidation) between the gas and sensing layer, states that, the electrical conductivity of p-type semiconductors increases (or decreases) when oxidizing (or reducing) gases are absorbed by their surfaces. As we know that, when NiO-based sensors are exposed to air, oxygen molecules will adsorb on the surface of NiO nanoparticle and partly transform into chemisorbed oxygen species ( $O^{2-}$ ,  $O_{ads}^-$  and  $O_2^-$ ) by capturing electrons from the conductance band of NiO [263- 265]. this is resulting in the increasing of the concentration of charge carriers (holes). In other words, the thickness of the charge accumulation layer is broadened, thus the sensors present a low resistance and an increase in their conductivity in air. In contrast, when the sensors are surrounded by the target reducing atmosphere (methanol, ethanol and acetone), the adsorbed oxygen species can react with the reducing gas and release trapped negative electrons back to the NiO conduction band, these electrons interact with the holes leading to a decrease in their concentration and reducing the number of charge carriers. This results in an increase in the resistance of the films. However, this change in resistance is proportional to the concentration of the gases. During the process, the methanol, ethanol and acetone decomposition reaction on the surface of NiO can be expressed as [263- 267]:





For Co and Cu-doped NiO, the increase of the oxygen ions quantity and the contacts between the NiO microspheres and dopant nanoparticles result in the improved increase of electron depletion [183]. By the assistance of doping, oxygen molecules can be more easily adsorbed on the surface of NiO [182]. This process increases both the quantity of adsorbed oxygen and the molecule-ion conversion rate resulting in the greater and faster degree of electron depletion from the NiO nanoparticle. Thus, the response of the Co and Cu-doped NiO nanoparticle is distinctly higher than that of the pure NiO. For the Co and Cu-doped NiO sample, it is possible to obtain an gas sensor with a higher sensitivity at relatively low concentration. What is more significant, doping is a very efficient method for improving sensing characteristics of other semi-conducting oxide gas sensors.

The films can then recover to their original state after desorption process, where the gas is withdrawn and replaced with air.

## 4.5 Gas sensing performance

In this section we present the result of the realized gas sensor based on NiO thin film. In order to characterize sensor performance towards methanol, ethanol and acetone vapors a set of characteristics parameters are investigated namely, operation temperature, sensitivity, detection limit and recovery times. The characteristic of NiO based sensor are presented below.

### 4.5.1 Gas sensing performance of undoped NiO thin films

#### 4.5.1.1 Operating temperature

The response of a semiconductor oxide gas sensor to the presence of a given gas depends on the speed of the chemical reaction on the surface of the grains and the speed of diffusion of the gas molecules to that surface which are activation processes and the activation energy of the chemical reaction is higher. In this case, at low temperatures the sensor response is restricted by the speed of the chemical reaction, and at higher temperature it is restricted by the speed of diffusion of gas molecules. The increase in sensitivity with temperature can be attributed to the fact that the thermal energy obtained was high enough to overcome the activation energy barrier to the reaction and a significant increase in electron concentration resulted from the sensing

reaction. At some intermediate temperature, the speed values of the two processes become equal, and at that point the sensor response reached it was maximum [48].

The semiconductor based sensor response is greatly influenced by its operating temperature. In fact, the adsorption of gases is directly related to the operating surface temperature of the sensing layer. In order to determine this temperature, sensor is exposed to 1000 ppm of methanol, ethanol and acetone vapors at different temperatures ranged between 60 and 220°C, the obtained responses curves are shown in figure 4.4. A typical operation temperatures corresponds to maximum response is widely reported in literature. In our case, the evolution of the sensor response indicates that this maximum is located around 110,140,170°C for methanol, acetone and ethanol respectively. Those operating temperatures are intermediary compared to other reported working temperature for sensing methanol, acetone and ethanol vapors ranged from 80 to 400°C [268]. However, we note also that undoped NiO based sensor exhibits a good sensitivity at lower operation temperature. This low operating temperature may lead to sensor power consumption reduction, thus making the device more stable, low cost with a longer life [269]. The results obtained are included in table 4.2.

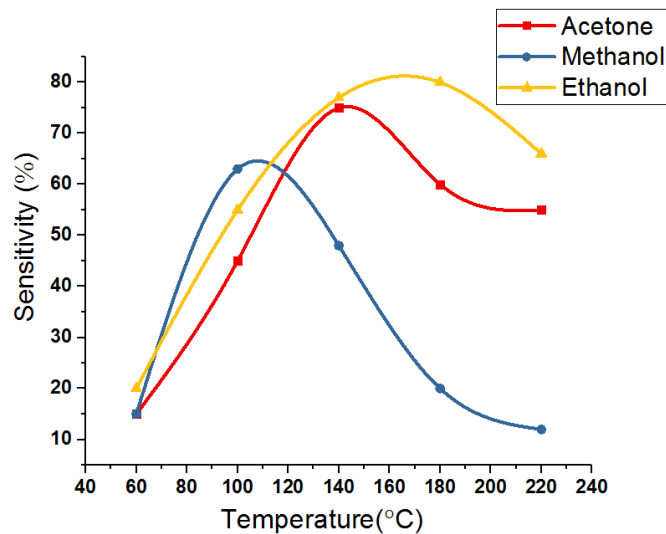


**Figure 4.4:** Response curves of undoped NiO based sensor towards methanol, ethanol and acetone (1000 ppm) at different operating temperatures.

#### 4.5.1.2 Selectivity

Figure 4.3 shows a clear difference in the operating temperature of each gas, which means that the undoped NiO based sensor can identify each of the three gases separately depending on the operating temperature. For ethanol, the optimum operating temperature is 170°C, for methanol at 110°C and for acetone at 140°C.

### 4.5.1.3 Sensitivity

The film sensitivity is the relative change of measured signal during vapor or gas exposure. The gas response of the sensor is defined as the ratio of change in the resistance of the sample when exposed to methanol, ethanol and acetone vapors on the resistance in air by the formula [174, 175]:

$$S(\%) = \frac{R_g - R_a}{R_a} \times 100 \quad (4.5)$$

Where  $R_g$  and  $R_a$  are NiO films resistances, measured in (methanol, ethanol or acetone vapors) and in air atmosphere, respectively.

In figure 4.5 we have shown the dynamic response of undoped NiO based sensor to 1000 ppm of ethanol, methanol and acetone for 220 seconds and at the operating temperatures for each gas. It is evident from the figure that the resistance increases when the sensing layer is exposed to vapors reveals that  $R_a$  is lower than  $R_g$ . The sensor exhibits high sensitivities for the ethanol, methanol and acetone; they are equals to 81, 75 and 65 % at its operating temperatures as that shown in Figure 4.3. It is well-known that the behavior of the NiO gas sensor is greatly influenced by its operating temperature, adsorption and desorption of oxygen molecules or atomic on the surface of the sensing film which leads to electrical resistance change. When the sensing film is exposed to a reducing gas (donor electron) such as the gases we used, the interaction of gases molecules with the surface chemisorbed oxygen species takes place, thereby releasing electrons. Consequently, the type of semiconductor will decide the behavior of the resistance variation [268- 270]. Hence, if the semiconductor is an n-type, the released electrons yield to resistance reduction. While in the case of p-type semiconductors, the released electrons recombine with holes to decrease the semiconductor electrical conductance and consequently the gas sensor resistance increases.

As mentioned above NiO is a p-type semiconductor due to the presence of Ni vacancy. Thereafter, if the Ni defects concentration is low, the holes concentration in NiO film is then also lower than in a p-type semiconductor. When the sensitive NiO layer is in contact with gases vapors, the electrons coming from gases reduce quickly the small holes density by recombination until saturation, for that the large density of electrons will dominate. Therefore, the NiO thin films can change from p-type to n-type when it is exposed to a reducing gas such as ethanol, methanol and acetone.

The maximum responses of undoped NiO based gas sensor for ethanol, methanol and acetone are summarized in table 4.2.

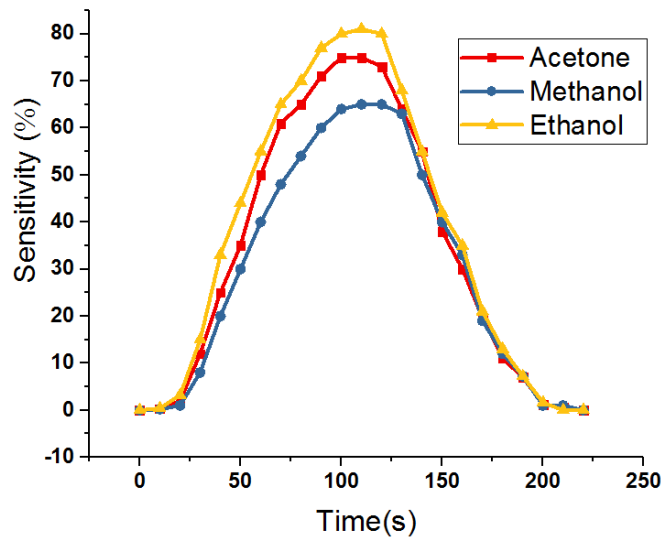


**Figure 4.5:** Response of undoped NiO based sensor towards 1000 ppm of methanol, ethanol and acetone at the optimum operating temperatures.

#### 4.5.1.4 Response and recovery times

The response and recovery times were defined as the time required to reach 90% of the final signal level and the time to return to the initial value respectively. These are important characteristics of a gas sensor. From Figure 4.5, the undoped NiO based sensor exhibits response times of 90 second for ethanol and acetone and 92 second for methanol. The recovery times are 95 second for ethanol and acetone and 85 second for methanol.

In other work, the response and recovery times are found somewhat different than ours [202, 207]. The long response and recovery times is probably the result of complex mechanisms related to adsorption and desorption of molecules when the layer is exposed to vapors or gases [179, 183]. The kinetics of each of these mechanisms is strongly influenced and controlled by the morphology and deposition conditions of the film. Modification of these conditions to obtain more porosity and decrease of the film thickness may be a suitable method to improve the response time.

#### 4.5.1.5 Detection limit

Figure 4.6 shows the variation of the sensitivity of the undoped NiO based sensor as a function of methanol, ethanol and acetone concentrations ranging from 100 to 3000 ppm at the optimum operating temperature. The sensitivity is increased when the concentration increases. This is due to the increased flow of molecules that reach adsorption sites. An increase in vapor concentration increases the surface reaction due to a larger surface coverage. Beyond a certain concentration the increase in surface re-

action will be gradual, where the saturation point on the coverage of molecules was reached and we observed constant response above certain concentration. Sensor sensitivity is somewhat small for methanol, ethanol and acetone concentrations of 300, 300 and 100 ppm, respectively. The maximum sensitivity at 2000 ppm was equal to 90% for all gases.

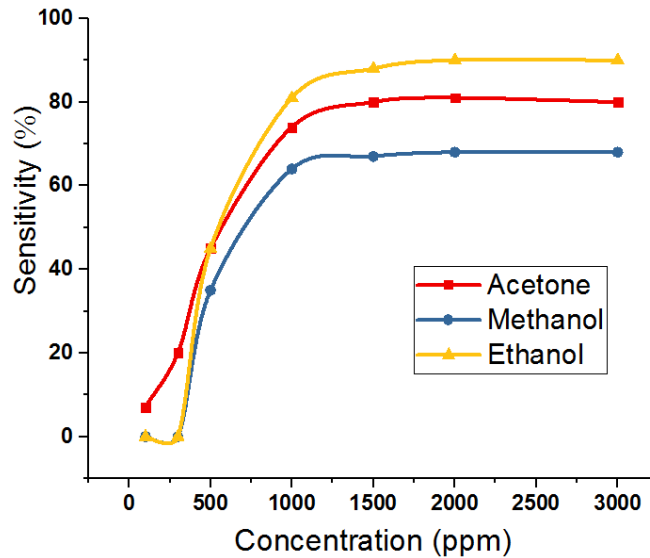


**Figure 4.6:** Variation of the sensitivity of undoped NiO based sensor as function of concentration of methanol, ethanol and acetone vapors.

#### 4.5.1.6 Stability

Stability is a property that takes into account the cloning of the device measurements in long use i.e. expressing the stability of its response after a long period of use, resulting in increased sensor resistance and reduced sensor sensitivity and selectivity. Sensor stability is a continuous response of time. Therefore, in this study it is decided to study the stability of the sensor response over time. The undoped NiO based sensor responses to 1000 ppm of acetone, ethanol and ethanol were measured at the operating temperature of each gas for 31 days. Figure 4.7 shows that the responses of undoped NiO based sensor is relatively constant for all vapors and gases and for both samples.

**Table 4.2:** Gas sensing performance of undoped NiO thin film towards methanol, ethanol and acetone vapors.

Material	Target gas	Sensitivity S%	Operating temperature (°C)	Response Time (S)	Recovery Time (S)	Detection Limit (ppm)
Undoped NiO	Ethanol	81	170	90	95	300
	Acetone	75	140	90	95	300
	Methanol	65	110	92	85	~100

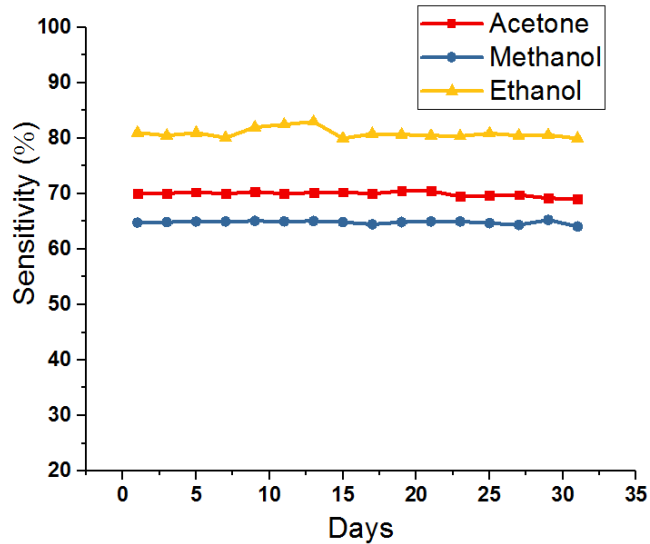


Figure 4.7: Stability characteristics of undoped NiO based sensor.

## 4.5.2 Gas sensing performance of Co-doped NiO thin films

### 4.5.2.1 Operating temperature

In figure 4.8, we reported the response curves of Co-doped NiO based sensors at a different operating temperature. The operating temperature was ranging from 60 to 220°C. We can see from Figure 4.8 (a) that the sensor shows high sensitivity about 94.6, 79.5 and 70.3 % for operating temperatures of 180, 140 and 140°C towards 1000 ppm of ethanol, acetone, and methanol gases (vapors) respectively, which means that doping of 3 at.% Co led to sensor sensitization but had a negative effect on operating temperature, which increased significantly in the case of ethanol and methanol. Figure 4.8 (b) shows that the sensor has a higher sensitivity than that shown in figure 4.8 (a) for the acetone and methanol, but its sensitivity remains almost constant for ethanol, which means that increasing the doping rate up to 12 at.% led to improved sensor sensitivity in general, where they are 94.7, 84.2 and 73.4 % for operating temperatures of 180, 140 and 140°C towards 1000 ppm of ethanol, acetone, and methanol fumes respectively.

### 4.5.2.2 Selectivity

Figure 4.8 shows a clear correlation between the operating temperature of the acetone and methanol vapors, it is 140°C, which means that the Co-doped NiO based sensors cannot distinguish between the gases clearly according to the operating tempera-

ture. It can only distinguish ethanol from them. It has a different optimum temperature, it is 110°C.

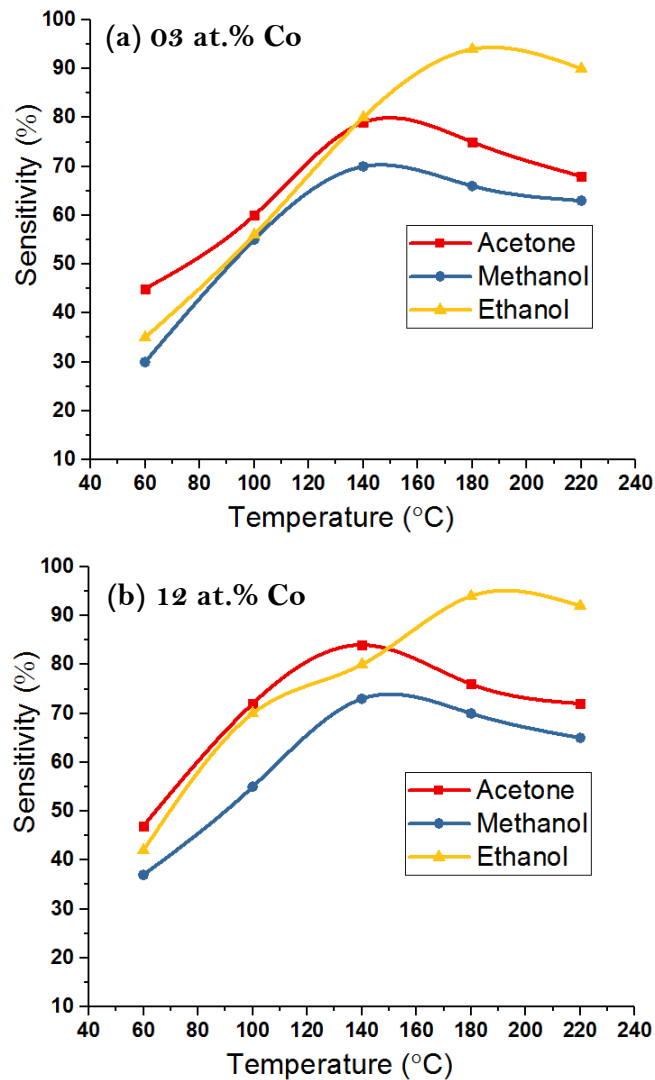


**Figure 4.8:** Response curves of Co-doped NiO based sensors towards methanol, ethanol and acetone (1000 ppm) at different operating temperatures.

#### 4.5.2.3 Sensitivity

Figure 4.9 shows the response of the Co-doped NiO-based sensors to 1000 ppm of the ethanol, acetone and methanol vapors at the optimum temperature of each gas (vapor). The dynamic responses of the Co-doped NiO-based sensors to all vapors showed a better response than those obtained from the undoped NiO and this in the two cases of doping 3 at.% (a) and 12 at.% Co (b). We also observed that sensor's resistance increases when the sensor layer is exposed to all the vapors with a sensitivity of 94.6, 79.5 and 70.3 %. For ethanol, acetone and methanol, respectively, in case of doping 3

at.% Co and 94.7, 84.2 and 73.4 %. For ethanol, acetone and methanol respectively in the case of doping 12 at.% Co. The maximum responses of Co-doped NiO based sensors for ethanol, methanol and acetone are summarized in table 4.3.

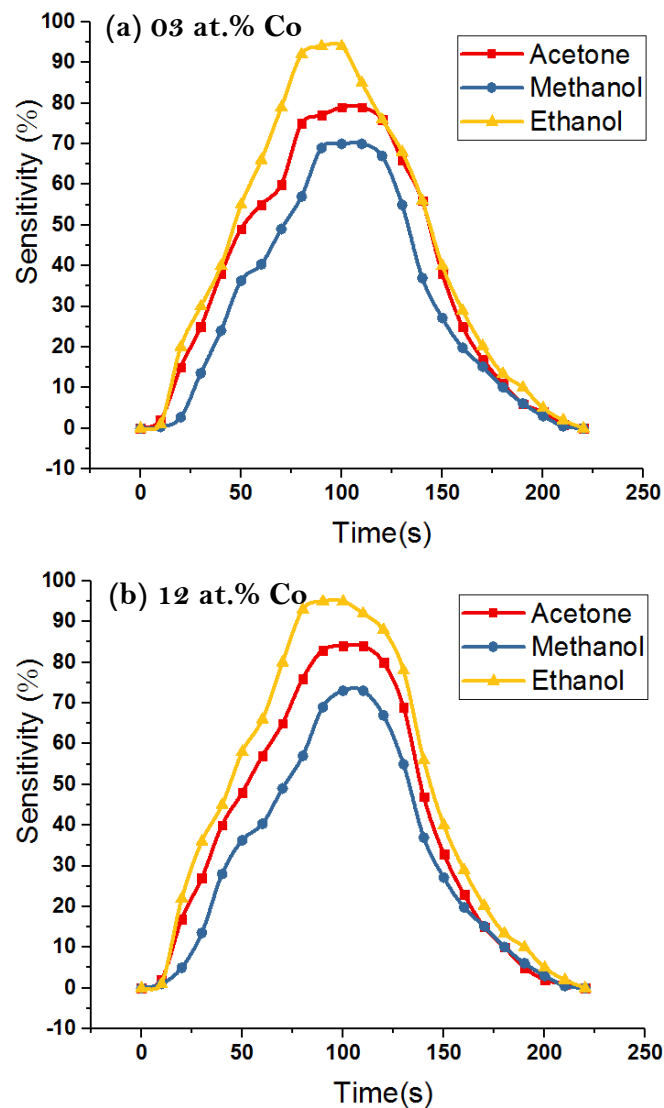


**Figure 4.9:** Response of Co-doped NiO based sensors towards 1000 ppm of ethanol, acetone and methanol at the optimum operating temperatures.

#### 4.5.2.4 Response and recovery times

From the figure 4.10 the response times of Co-doped NiO based sensors are 63.1, 65.6 and 63 seconds for ethanol, acetone and methanol and recovery times are 110.7, 87.2 and 94.4 seconds for ethanol, acetone and methanol for sample doped with 3 at.% Co. For the second sample which doped with 12 at.% Co the response times are 63.1, 70.3 and 78.8 seconds and recovery times are 95.1, 95.2 and 93.3 to ethanol, acetone and methanol. It is clear through the results of the samples that there is a clear improvement in response times, unlike recovery times that have seen relatively stable or

slightly increased ethanol status, which means that a small percentage of Co doping has accelerated the gas reaction mechanism with the sensitive layer. But relatively high rates of doping did not play the same role. We observed a good decrease in response times for doping status of 3 at.% Co. It is known that a small response time indicates a good sensor and a good sensor also has a small recovery period so that the sensor can be used repeatedly.

#### 4.5.2.5 Detection limit

The responses of the Co-doped NiO based sensors as a function of ethanol, methanol and acetone concentrations ranging from 100 to 3000 ppm were studied at the optimum operating temperatures of 180, 140 and 140°C for ethanol, methanol and acetone vapors respectively is shown in Figure 4.10. The response increases rapidly as concentration of acetone increased from 100 to 1000 ppm, after that the slope of all the graphs decreased with concentration which is due to occurrence of saturation in the response. With a small concentration of gas, exposed on a fixed surface area of a sample, there was a lower coverage of vapor molecules on the surface and hence less surface reaction occurred. Sensor sensitivity of Co-doped NiO thin film doped by 3 at.% Co to 100 ppm is about 10 % for methanol vapor and 14 % for acetone vapor and 20 for ethanol vapor, while for the doping sample 12 at.% Co the sensitivity of the sensor to 100 ppm Increased to 13 % for methanol vapor and 17 % for acetone vapor And 25 % for ethanol vapor. This increase was due to the effect of cobalt doping on the morphological and electrical characteristics of the samples, which improved the process of chemical and physical adsorption of oxygen and gas and thus improved sensitivity values. The sensitivity of our sensor remains significant even for the lowest concentrations lowest to 100 ppm for acetone, methanol and ethanol vapors, but we could not measure it because we don't have micro-syringe.

**Table 4.3:** Gas sensing performance of Co-doped NiO based sensors towards methanol, ethanol and acetone vapors.

Material	Target gas	Sensitivity S%	Operating temperature (°C)	Response Time (S)	Recovery Time (S)	Detection Limit (ppm)
Co-doped NiO (3 at.%)	Ethanol	94.6	180	63.1	110.7	<100
	Acetone	79.5	140	65.6	87.2	<100
	Methanol	70.3	140	63.0	94.4	<100
Co-doped NiO (12 at.%)	Ethanol	94.5	180	63.1	95.1	<100
	Acetone	84.2	140	70.3	95.2	<100
	Methanol	73.4	140	78.8	93.3	<100

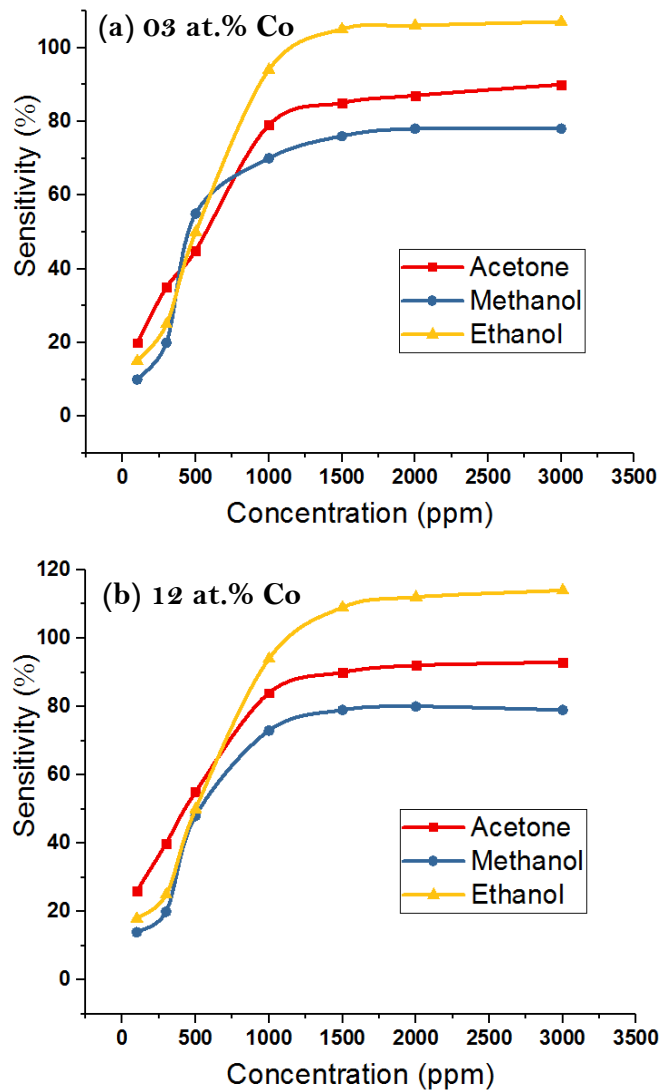


**Figure 4.10:** Variation of the sensitivity of the Co-doped NiO based sensors as function of concentration of methanol, ethanol and acetone vapors.

#### 4.5.2.6 Stability

Figure 4.11 shows the sensitivity of Co-doped NiO based sensors to 1000 ppm of acetone, ethanol and ethanol at the optimum operating temperature of each gas for 31 days. Figure 4.11 (a) shows that there is relative stability in the case of ethanol and acetone while there is relative volatility in the methanol case for an unclear reason. While figure 4.11 (b) shows that there is good stability for all gases, which means that cobalt grafting has improved stability, especially in the case of ethanol. Figure 4.10 shows that the gas sensor response is relatively constant for all vapors and gases and for both samples

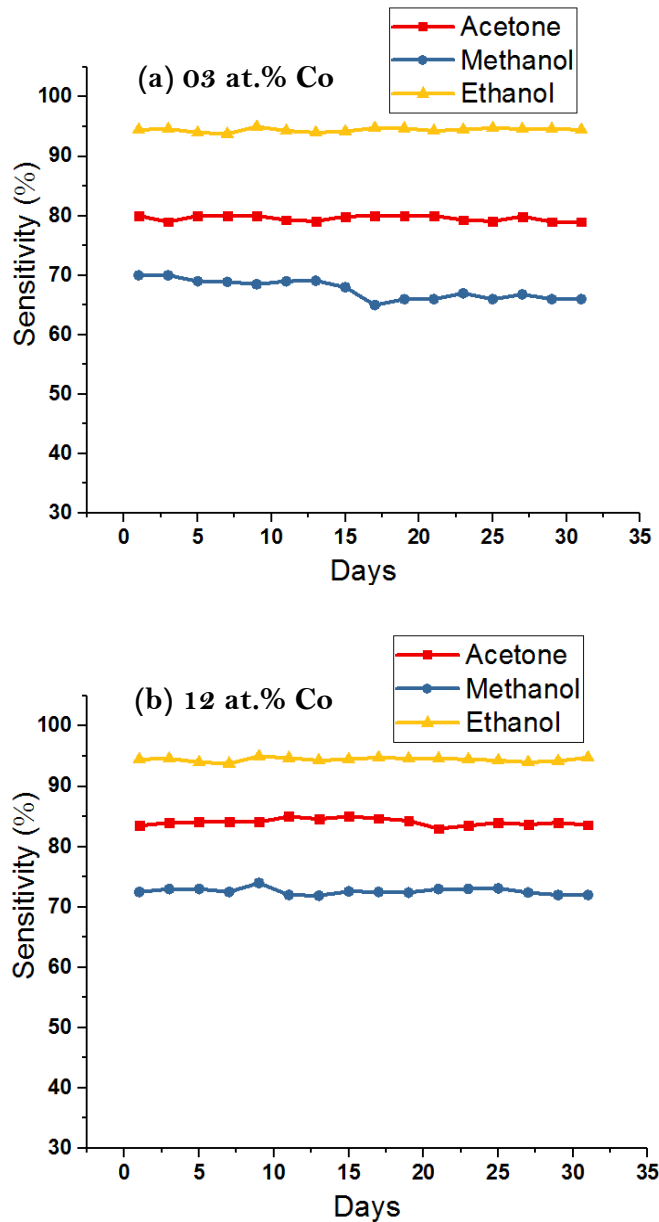


Figure 4.11: Stability characteristics of Co-doped NiO based sensors.

## 4.5.2 Gas sensing performance of Cu-doped NiO thin films

### 4.5.3.1 Operation temperature

In figure 4.12, we reported the response curves of Cu-doped NiO based sensor at a different operating temperature. The operating temperatures were ranging from 60 to 220°C. We can see from Figure 4.11 that the sensor shows high sensitivity about 102, 94.3, 77.1 % for operating temperatures of 140, 110 and 180°C towards 1000 ppm of ethanol, acetone, and methanol fumes respectively, which means that Cu doping at 3 at.% led to sensor sensitization which had a positive effect on operating temperature, which decreased significantly in the case of ethanol and acetone. But had a negative

effect in the case of methanol where its operating temperature increased significantly. Figure 4.12 (b) shows that the sensor has a higher sensitivity than that shown in Figure 4.12 (a) for all vapors, which means that increasing the doping rate up to 12 at.% led to improved sensor sensitivity in general, where they are 110.9, 97.2 and 84.8 % for operating temperatures of 140, 110 and 180°C towards 1000 ppm of ethanol, acetone, and methanol vapors respectively.

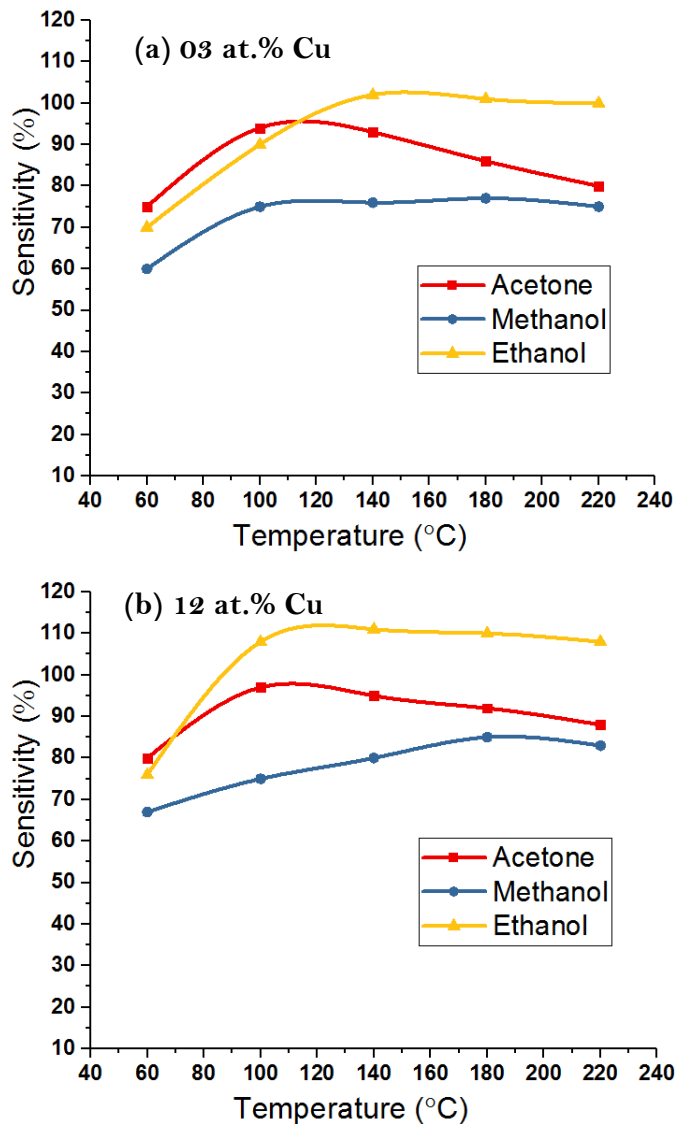


**Figure 4.12:** Response curves of Cu-doped NiO based sensor towards methanol, ethanol and acetone (1000 ppm) at different operating temperatures.

#### 4.5.3.2 Sensitivity

Figure 4.13 shows the dynamic responses of the Cu-doped NiO-based sensors to 1000 ppm of the ethanol, acetone and methanol vapors at the optimum operating temperature of each gas (vapor).

The dynamic responses of the Cu-doped NiO based sensors to all vapors showed a better response than those obtained from the undoped and Co-doped NiO based sensors this in the cases of Cu doping at 3 at.% and 12 at.%. We also observed that sensor resistance increases when the sensor layer is exposed to all the vapors with a sensitivity of 102, 94.3 and 77.1 %. For ethanol, acetone and methanol, respectively, in case of Cu doping at 3 at.% and 110.9, 97.2 and 84.8 %. For ethanol, acetone and methanol respectively in the case of Cu doping at 12 at.%. The maximum responses of Cu-doped NiO based sensors for ethanol, methanol and acetone are summarized in table 4.4.

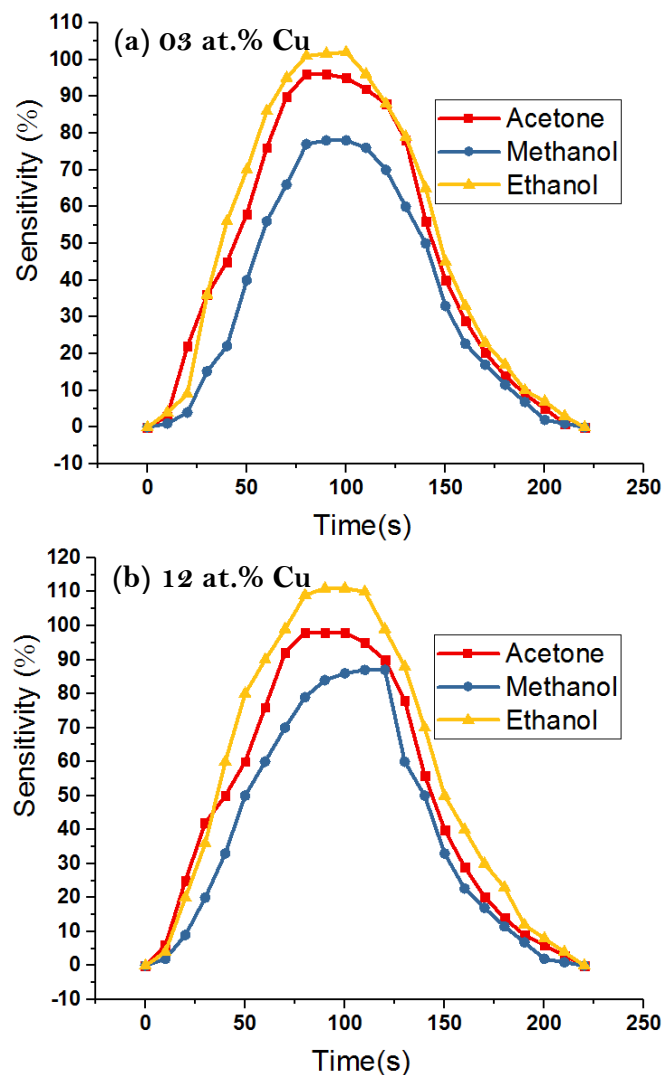


**Figure 4.13:** Responses of Cu-doped NiO based sensors towards 1000 ppm of ethanol, acetone and methanol at the optimum operating temperatures.

### 4.5.3.3 Selectivity

Figure 4.12 shows a significant difference between the operating temperatures of the three vapors: 140°C for ethanol, 110°C for the acetone and 180°C for methanol, which means that the Cu-doped NiO based sensor can clearly distinguish the gases according to the operating temperature.

### 4.5.3.4 Response and recovery times

The response and recovery times were determined for the Cu-doped NiO based sensor from the figure 4.13. The response times are 67.6, 63.3, 74.2 seconds for ethanol, acetone and methanol and recovery times are 109.5, 100.1 and 104 seconds for ethanol, acetone and methanol for sample doped with 3 at.% of Cu. For the second sample which doped with 12 at.% of Cu the response times are 72, 68.4 and 76.2 seconds and recovery times are 103.1, 101.7 and 100.2 to ethanol, acetone and methanol. It is clear through the results of the samples that there is a clear decreasing in response times, unlike recovery times that have seen increased for all vapors (gases). This means that Cu doping has accelerated the gas reaction mechanism with the sensitive layer of the Cu-doped NiO thin films.

### 4.5.3.5 Detection limit

Figure 4.14 shows the variation of the sensitivity of Cu-doped NiO based sensor as a function of acetone, methanol and ethanol concentration ranging from 100 to 3000 ppm was studied at the optimum temperature for. The response increases linearly as concentration of vapors increased from 100 to 500 ppm. The slope of all the graphs decreased with concentration which is due to occurrence of saturation in the response.

The sensitivity of Cu-doped NiO thin film doped by 3 at.% of copper to 100 ppm is about 41 % for methanol vapor, 59 % for acetone vapor and 40 for ethanol vapor, while for the doping sample 12 at.% of copper the sensitivity of the sensor to 100 ppm increased to 43 % for methanol vapor and 65 % for acetone vapor and 24 % for ethanol vapor. This increase was due to the effect of copper doping on the morphological and electrical characteristics of the films, which improved the process of chemical and physical adsorption of oxygen and gas and thus improved sensitivity values. The sensitivity of our sensor remains significant even for the lowest concentrations lowest to 100 ppm for acetone, methanol and ethanol vapors.

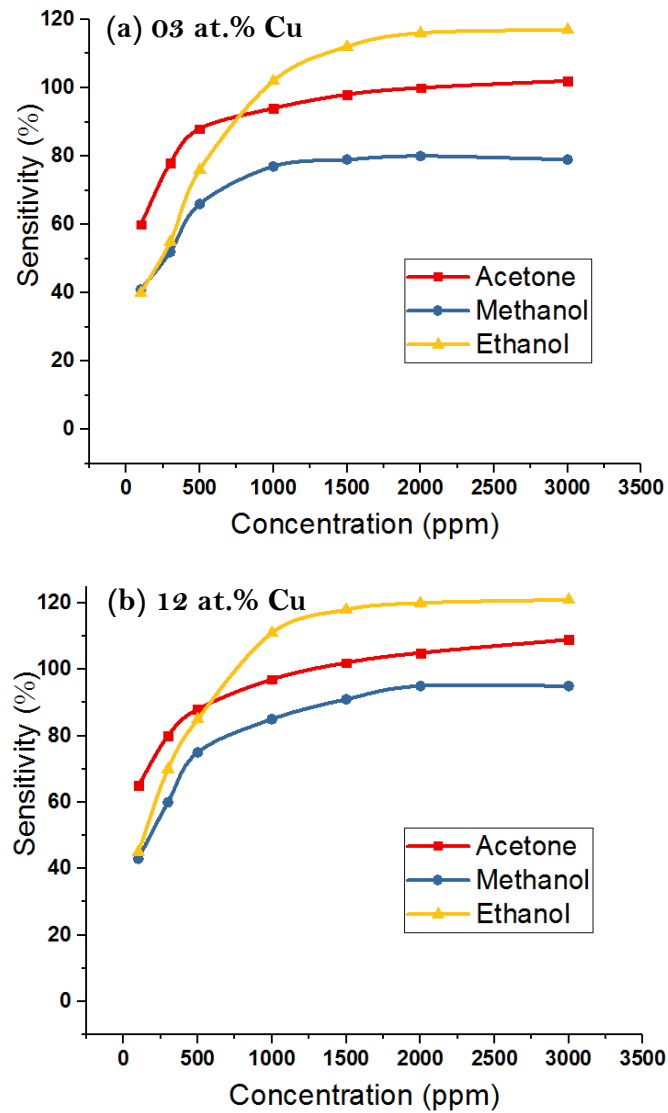


**Figure 4.14:** Variation of the sensitivity of Cu-doped NiO based sensors as function of concentration of vapors.

**Table 4.4:** Gas sensing performance of Cu-doped NiO based sensor towards methanol, ethanol and acetone vapors.

Material	Target gas	Sensitivity S%	Operating temperature (°C)	Response Time (S)	Recovery Time (S)	Detection Limit (ppm)
Cu-doped NiO (3 at.%)	Ethanol	102.0	140	67.6	109.5	<<100
	Acetone	94.3	110	63.3	100.1	<<100
	Methanol	77.1	180	74.2	104.0	<<100
Cu-doped NiO (12 at.%)	Ethanol	110.9	140	72.0	103.1	<<100
	Acetone	97.2	110	68.4	101.7	<<100
	Methanol	84.8	180	76.2	100.2	<<100

#### 4.5.1.6 Stability

The figure 4.15 shows the sensitivity of Cu-doped NiO based sensors to 1000 ppm of acetone, ethanol and ethanol at the optimum operating temperature of each gas for 31 days. Figure (a) illustrates the instability of the sensor response especially after the ninth day of figure (a) and the seventh day of figure (b), which means that the sensor is poisoned by the effect of gas, air or moisture, and is likely to have the effect of air and humidity, where air and humidity and under fairly high operating temperatures may lead to the oxidation of a part of the sensitive outer layer of the film containing Easy oxidation copper ions which prevents the interaction of the gas molecules with the film's sensitive layer.

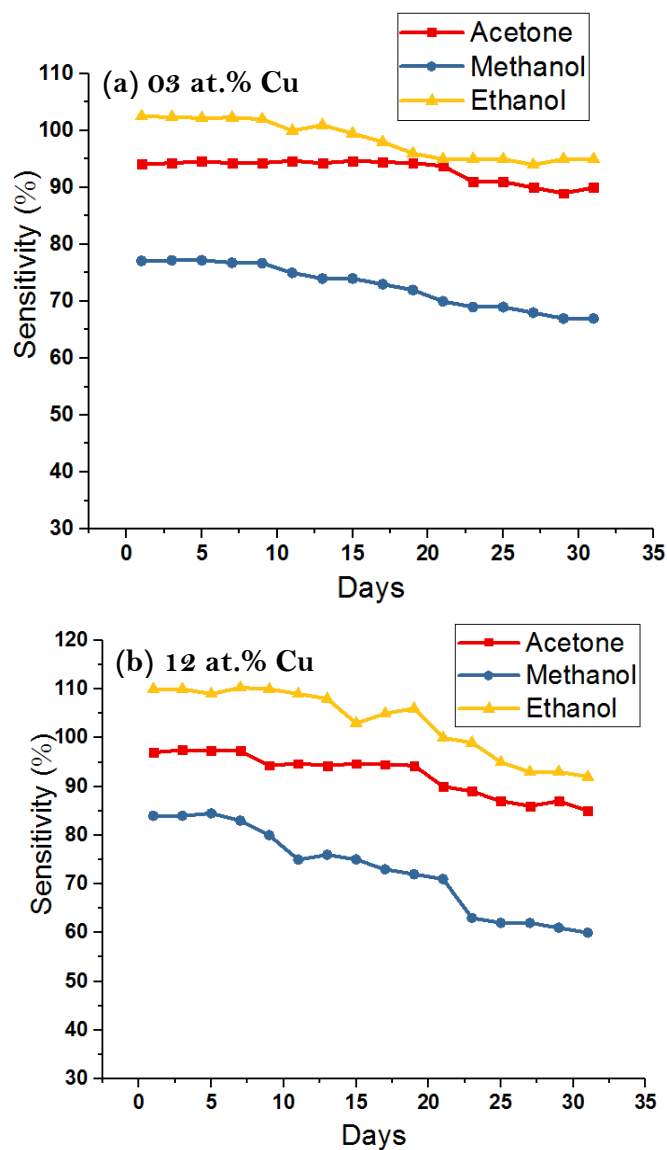
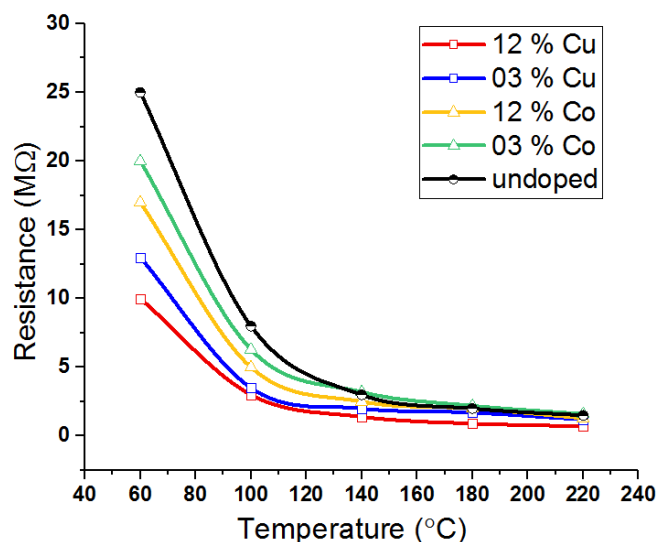


Figure 4.15: Stability characteristics of Cu-doped NiO based sensors.

## 4.6 Comparative study

### 4.6.1 Resistance

Figure 4.16 shows the electrical resistance (in air) as a function of temperature. All samples based sensor show that the electrical resistance decreases by increasing the temperature. The electrical resistance of the film in an air milieu decreases by increasing the temperature. It is known that this decrease does under the influence of oxygen adsorbed on the surface of the film oxidized by the electrons of the outer layer of the film, which generates additional holes that increase its positive conductivity and thus reduce the value of electrical resistance. This indicates that all films are semiconductor materials on the one hand and they are of p-type with large gap energy on the other hand. The figure also shows that the pure sample shows greater resistance than the other samples at all temperatures and that the use of cobalt or copper doping has reduced the value of resistance, i.e., raising the value of electrical conductivity, especially in the case of copper doping.



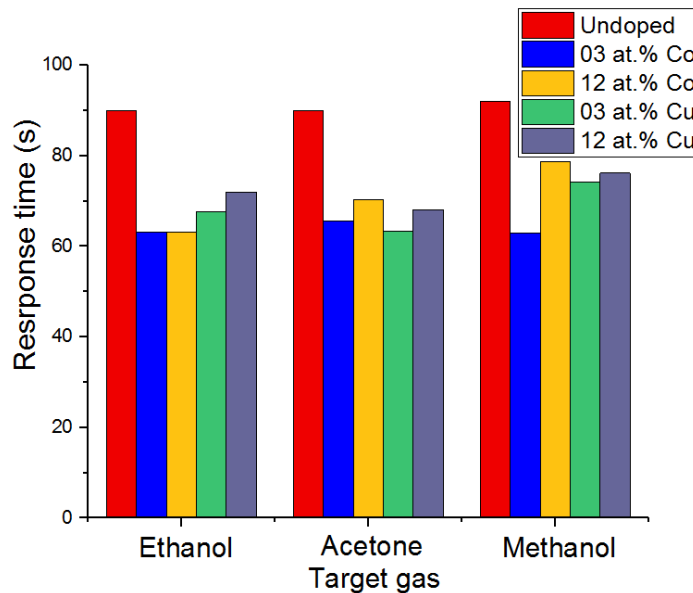
**Figure 4.16:** Variation of resistance (in air) of undoped and Co and Cu-doped NiO based sensors at different operating temperatures.

### 4.6.2 Response and recovery times

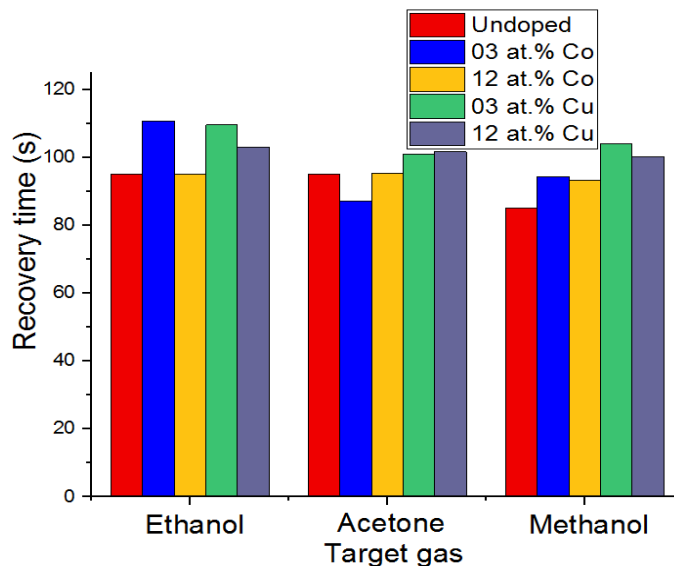
Figure 4.17 expresses the response time values for all prepared samples base sensor. From the diagram we can observe that the Co and Cu-doped NiO based sensor have lower response times (with varying between them) than the undoped NiO based sensor to all vapors. That means the doping was improving sensing properties of prepared samples.

Figure 4.18 shows the recovery times for all prepared samples base sensor. In general, it appears that the undoped NiO base sensor has lower recovery times than

the Co and Cu-doped NiO based sensor for all vapors, which means that the doping with cobalt or the copper has negatively affected the recovery time. This may be due to an increase in the roughness of the surface of the narcotic film and increase the gaps in it, which hinders the chemical recovery process, where oxygen ions or molecules adsorbed inside the gaps are delayed and thus the chemical reducing reaction is delayed.



**Figure 4.17:** Comparison between undoped and Co and Cu-doped NiO based sensors in terms of different obtained response times values.



**Figure 4.18:** Comparison between undoped and Co and Cu-doped NiO based sensors in terms of different obtained recovery times values.

### 4.6.3 Operation temperature

Figure 4.19 shows the optimum operating temperature values for the prepared samples. Note that optimum operating temperature values vary depending on the nature of the sensitive film and the vapors to be sensed. We also note that the undoped NiO based sensor has the smallest optimum operating temperature for methanol vapor, whereas the smallest optimum operating temperature for ethanol and acetone vapors are possessed by the Cu-doped NiO based sensor. We also note that the increase of the doping rate did not affect the operating temperature in both cases of doping with copper or cobalt. As we know, a sample with a smaller optimum operating temperature is preferable.

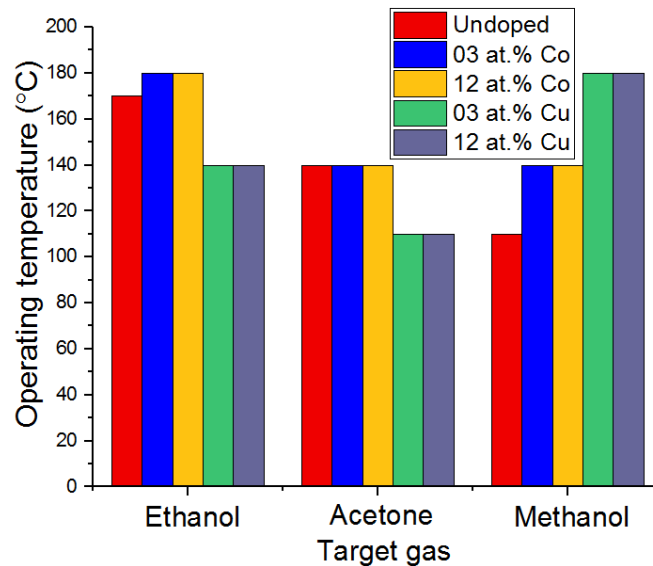


**Figure 4.19:** Comparison between undoped and Co and Cu-doped NiO based sensors in terms of different obtained optimum operating temperature values.

### 4.6.4 Sensitivity

Figure 4.20 shows the sensitivity values of the prepared samples based sensor when exposed to different vapors. All samples show greater sensitivity to ethanol, then acetone and finally methanol. Cu-doped NiO based sensor yielded better results than Co-doped NiO based sensor or undoped NiO based sensor. It is clear from the figure that the rate of doping has a significant impact on the sensitivity of films prepared where the increase in the rate of doping increased the value of sensitivity in both cases of doping studied.

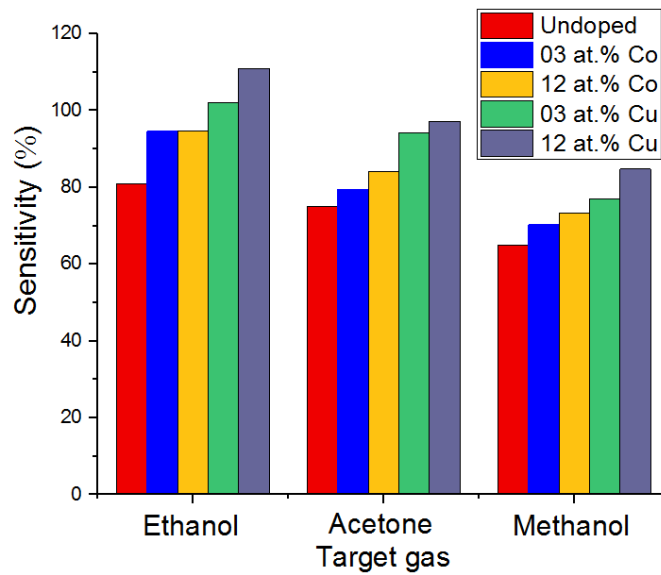


**Figure 4.20:** Comparison between undoped and Co and Cu-doped NiO based sensors in terms of sensitivity values obtained towards 1000 ppm from target gases.

#### 4.6.5 Stability

Figures 4.7, 4.11 and 4.15 show that the undoped NiO based sensor and Co-doped NiO based sensors are much better stable than the Cu-doped NiO based sensors, which means that although they have better sensitivity and better response and recovery times, they are not suitable for permanent use and therefore the Co-doped NiO based sensors are the best overall; Especially in the case 3 at.% of doping with Co.

#### 4.6.6 General comparison between our results and results of other works

The properties of the material are strongly dependent on its morphology different dimensional and morphological NiO nanostructures have been synthesized via various methods. Meanwhile, the study about optimizing the sensing properties of the NiO-based gas sensor by doping method has been developing gradually. The diverse structures of NiO (nanoparticles, nanosheets, nanotubes, hollow spheres, nanowires, etc.), appropriate doped-NiO (Al, Au, Fe, Cu, Co and Zn, etc.), and NiO composites with other MOS have been developed in recent years as a sensitive material for ethanol, acetone and methanol [271, 272]. All results obtained from us or from others reveal that doping is an effective measure to modify NiO material in order to tailor its gas sensing properties.

In tables 4.2, 4.3 and 4.4 we note that the results obtained for the sensitivity, response times, recovery times or optimal operating temperatures relatively correspond the results in table 5 in general. The difference is due to the above reasons. These results can then be adopted for use in the manufacture or development of sensors based on NiO in particular and on MOS in general.

**Table 4.5:** Results of some previous works.

Material	Vapor (Gas)	$(R_g/R_a)$	S%	OT (°C)	Time Rs/ Rc (S)	C/DL (ppm)	Ref.
			$(R_g-R_a)/R_a$				
NiO Nanoparticles (powder)	Ethanol	-	505	90	167/130	-	[273]
	Acetone	-	318	80	126/132	-	
Ultrathin NiO Nanosheets	Ethanol	3.11	211	200	64-155/93-211	200/<5	[274]
NiO nanoroses	Ethanol	9.11	811	230	18.1/19.3	5/<1	[200]
	Methanol	8.36	736	230	15.4/17.2	5/<1	
	Acetone	6.44	544	230	12.1/11.9	5/<1	
rose-like NiO nanostructure	Ethanol	8.4	740	230	21/14	5/-	[275]
Al-doped NiO nanorod-flower	Ethanol	12	120	200	48/40	100/<1	[276]
NiO/MWNTs	Ethanol	2	100	180	27/87	100/-	[277]
	Methanol	1.8	80	180	54/94	100/-	
	Acetone	1.8	80	180	25/86	100/-	
L-NiO	Ethanol	1.75	75	300	-	50/0.2	[278]
	Methanol	1.4	40	300	-	50/-	
	Acetone	1.3	30	300	-	50/-	
Fe-doped L-NiO	Ethanol	3.9	290	240	-	50/0.2	[278]
	Methanol	2.7	170	240	-	50/-	
	Acetone	3	200	240	-	50/-	
Co-doped L-NiO	Ethanol	1.5	50	240	-	50/0.2	[278]
	Methanol	1.3	30	240	-	50/-	
	Acetone	1.25	25	240	-	50/-	

## 4.7 Conclusion

In this chapter we were interested by applying the prepared films in the field of gas sensing. Five samples were selected from the prepared samples to study their sensing performance towards ethanol, acetone and methanol vapors, where all films had high ohmic resistance. Optimum operating temperatures, sensitivity, selectivity and detection limits were determined to the gas-based sensor. The undoped NiO based sensor and Co-doped NiO based sensors are much better stable than the Cu-doped

NiO based sensors, which means that although they have better sensitivity and better response and recovery times, they are not suitable for permanent use and therefore the Co-doped NiO based sensors are the best overall.

General  
conclusion  
and Future Works

# General conclusion and future works

## 1. General conclusion

The subject of this thesis is the elaboration, characterization of nanostructured NiO thin films and their application in the field of gas sensing (detection). Nickel oxide films were prepared by spray pyrolysis technique on glass substrates at temperatures above 400 °C. In order to determine the optimum conditions for laboratory preparation of samples, the effect of some preparatory parameters such as the molarity of precursor solution and thermal annealing on the structural, optical and electrical properties of nickel oxide films was studied. In addition, to enhance some of the properties of the prepared films, the incorporation of dopants into the materials is an effective way to change and improve many physical properties (structural, electrical, optical, etc.). Accordingly, the cobalt (Co) and copper (Cu) doped nickel oxide films were prepared using the above technique. The structural, optical and electrical properties of nickel oxide thin films have been shown to be strongly influenced with the percentages of cobalt or copper doping. The prepared samples were examined and characterized using X-ray diffraction meter (XRD), UV-VIS spectrometer, scanning electron microscope (SEM) and the four probes method.

The most important results obtained can be summarized as follows:

### A. Effect of precursor molarity

The SPT has been successfully employed to deposit NiO thin films with different precursor molarity (0.05, 0.10, 0.15 and 0.2 mol/L) on glass substrates at 480 °C. XRD results showed that all films have a polycrystalline cubic structure with preferential orientation according to the direction (111). The crystallite size was found between (9.72 and 46.62 nm). We have observed an improvement in the films crystallinity at 0.10 mol/L precursor molarity where the peak at position  $37.2^\circ$  corresponding to the (111) plans is very sharp, the film obtained at this molarity has higher and sharper diffraction peak indicating an improvement in peak intensity compared to other films. Transmittance spectra showed that transparency of the films ranged from 57 to 75.36 %, the band gap value of NiO films was found from 3.64 eV to 3.86 eV and Urbach energy decreases as the molarity increasing. The obtained  $E_U$  values are change between 0.472 and 0.284 eV with a different precursor molarity. This changing is attributed to

the disorder in the film due to the creation of new localized energy states near the band edges. The electrical conductivity is varied from 0.00698 to 0.08961  $\Omega^{-1}\cdot\text{cm}^{-1}$ . The high electrical conductivity is obtained for the film deposited at 0.1 mol/L. All elaborated films having p-type conductivity.

### B. Effect of annealing

Two samples of NiO thin films were prepared onto a highly cleaned glass substrates using SPT with precursor molarity of 0.15 mol/L at 480°C. After preparing the two samples, one leaves it as-deposited and the other annealed at 500°C in an electrical oven for two hours. The Both samples showed cubic crystal structure with preferential orientation according to the direction (111). It has found that the crystallite size increase from 46.62 nm for the as deposited sample to 119.89 nm for the annealed one. We have observed an improvement in the films crystallinity for the annealed sample where the peak at position  $37.2^\circ$  corresponding to the (111) plans is very sharp, the film obtained for the annealed sample has higher and sharper diffraction peak indicating an improvement in peak intensity compared to the as-deposited film. The band gap value of NiO films decreased from 3.64 eV for the as-deposited sample to 2.98 eV for the annealed one. The values of electrical conductivity and Urbach energy increased after annealing from 0.0412 to 0.0924  $\Omega^{-1}\cdot\text{cm}^{-1}$  and from 0.284 to 0.391 eV respectively. Transparency was also decreased after annealing.

### C. Effect of Coalt doped NiO thin films

Undoped and Co-doped nickel oxide thin films at 0, 3, 6, 9 and 12 at.% of Co doping have been successfully deposited on glass substrates at a temperature of about 480°C by SPT. The effect of Co doping concentration on structural, optical and electrical properties of NiO thin films was investigated. XRD characterization revealed that the undoped and Co doped NiO thin films are polycrystalline with FCC structure with preferential orientation according to the direction (111). From XRD results can be observed also a secondary phase corresponds to  $(60\bar{2})$  peak in cobalt dioxide ( $\text{CoO}_2$ ). The crystallite size ranging between 31.89 to 53.67 nm, without obvious effect of concentration of doping. SEM images show that the surfaces of deposited films have a wrinkle network structure, and are influenced by the incorporation of Co dopants. UV-VIS reveals that a decrease in the average optical transmission of the films with increased Co concentration. The optical band gap energy has been found to decreases from 3.61 to 3.48 eV with increasing Co dopant concentration from 0 to 12 at.%. The

Urbach energy has been found to increase from 0.353 to 0.915 eV with increasing Co dopant concentration from 0 to 12 at.%. The maximum value of electrical conductivity was  $0.08961 \Omega^{-1}\cdot\text{cm}^{-1}$ , it is obtained at 12 at.%. All deposited samples having p-type conductivity.

### D. Effect of copper doped NiO thin films

Undoped and Cu-doped nickel oxide thin films at 0, 3, 6, 9 and 12 at.% of Cu doping have been successfully deposited on glass substrates at a temperature of about 400 °C by SPT. The effect of Cu doping concentration on structural, optical and electrical properties of NiO thin films was investigated. XRD patterns of undoped NiO and Cu-doped NiO thin films show that all films are polycrystalline with FCC structure with preferential orientation according to the direction (111), without the appearance of a secondary phase belonging to copper and its oxides. The crystallite size was calculated using Scherrer formula and Williamson-Hall plot method, it is found that the undoped NiO sample has maximum crystallite size for two methods (22.96 and 39.03 nm respectively), without obvious effect of concentration of doping. SEM images of sample doped with 6 at.% of copper show that the deposited films are smooth and uniformly covered the whole surface of the substrate. The transmittance spectra have been recorded in the wavelength range of (300-900) nm in order to study the optical properties. The optical energy gap for allowed direct electronic transition was calculated using Tauc's equation. It is found to decrease from 3.60 to 3.43 eV with increasing Cu dopant concentration from 0 to 12 at.%. The Urbach energy has been found to increase from 0.323 to 0.935 eV with increasing Cu dopant concentration from 0 to 12 at.%. The maximum value of electrical conductivity was  $0.2916 \Omega^{-1}\cdot\text{cm}^{-1}$ , it is obtained at 12 at.%. All deposited samples having p-type conductivity.

### E. Gas sensing application

The undoped NiO sample, two samples (3 and 12 at.%) of Co-doped NiO and Cu-doped NiO were selected to study their sensitization properties for chemical vapors (ethanol, methanol and acetone). After studying the sensitivity performance of the sensors based on the selected samples, we concluded the following:

- All selected films were found to have high ohmic resistance and p-type conductivity.

- All samples show greater sensitivity to ethanol, then acetone and finally methanol. Cu-doped NiO based sensor yielded better results than Co-doped NiO based sensor or undoped NiO based sensor. It is clear from the figure that the rate of doping has a significant impact on the sensitivity of films prepared where the increase in the rate of doping increased the value of sensitivity in both cases of doping studied.
- The undoped NiO based sensor has the smallest optimum operating temperature for methanol vapor, whereas the smallest optimum operating temperature for ethanol and acetone vapors are possessed by the Cu-doped NiO based sensor. We also note that the increase of the doping rate did not affect the operating temperature in both cases of doping with copper or cobalt.
- The Co and Cu-doped NiO based sensor have lower response times (with varying between them) than the undoped NiO based sensor to all vapors. In general, the undoped NiO base sensor has lower recovery times than the Co and Cu-doped NiO based sensor for all vapors. That means the doping with cobalt or the copper improves response times the one hand but On the other hand extends the recovery time of prepared samples, which means that the doping has negatively affected the recovery time.
- the undoped NiO based sensor and Co-doped NiO based sensors are much better stable than the Cu-doped NiO based sensors, which means that although they have better sensitivity and better response and recovery times, they are not suitable for permanent use and therefore the Co-doped NiO based sensors are the best overall.

*We can conclude that all the results obtained are in agreement with the results obtained by the previous researchers and they confirm that the NiO films have a promising future in the field of gas sensing.*

## 2. Future works

According to the results of this study, the following future studies are suggested:

1. Studying the effect of Co and Cu codoped NiO thin films in order to improve several optoelectronic properties of NiO thin films.
2. Preparation of undoped and doped NiO thin films by another technique like chemical bath deposition.

## General Conclusion

---

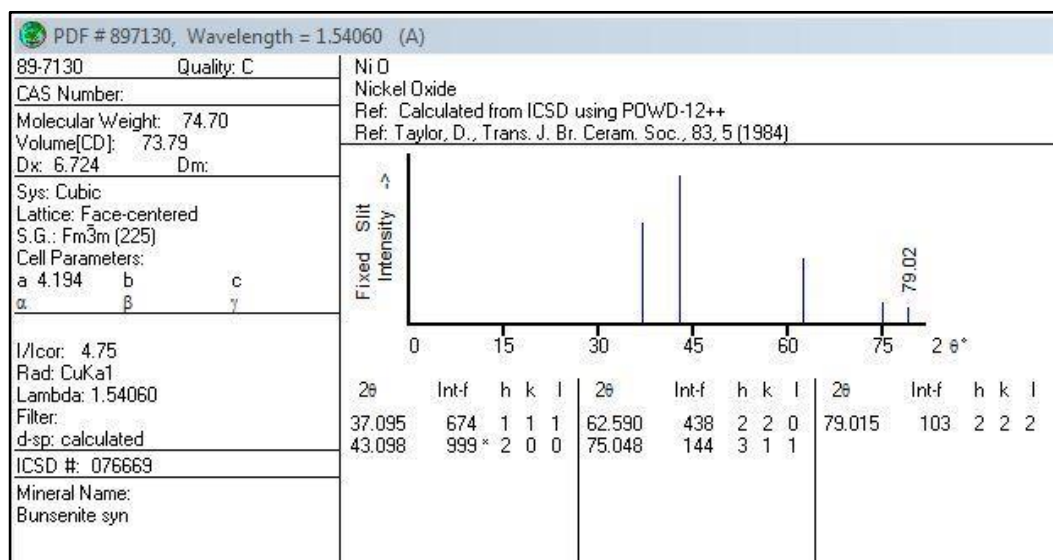
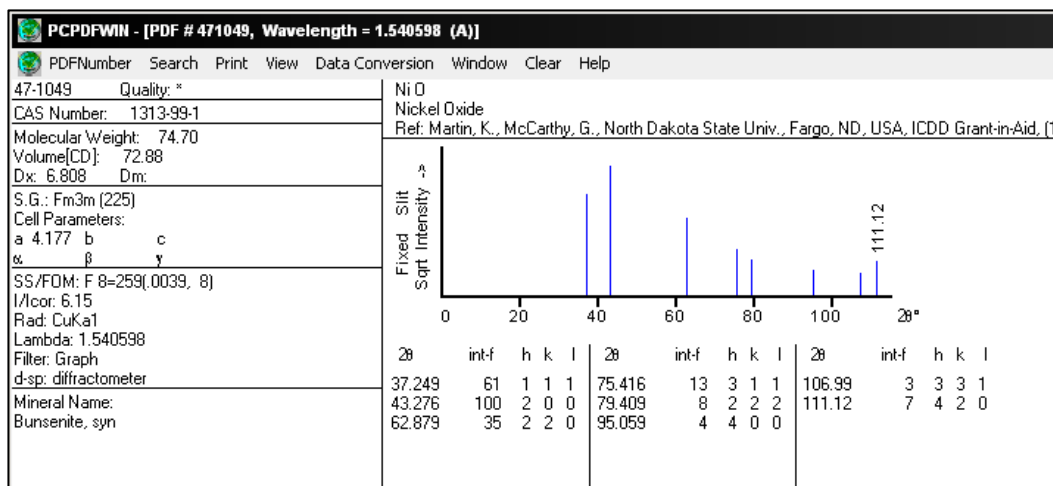
3. More extensive characterizations are necessary such as Raman spectroscopy, measurements of Hall effect, study of the current-voltage (I-V) characteristics as function of temperature, etc.
4. Studying another application of the deposited films in, PN junction, photocatalyst and antibacterial, etc.
5. Studying the magnetic properties of undoped and doped NiO thin films.

# Appendix

## A.1 JCPDS cards of Nickel Oxide (NiO)

Table A.1 presents a JCPDS cards of NiO (Joint Committee on Powder Diffraction Standards) approved in our work.

Table A.1: JCPDS cards of NiO.



## A.2 JCPDS cards of Cobalt Dioxide (Co<sub>1</sub>O<sub>2</sub>)

### Name and formula

Reference code: 98-008-7942

Compound name: Cobalt Dioxide

Common name: Cobalt Dioxide

Chemical formula: Co<sub>1</sub>O<sub>2</sub>

**Crystallographic parameters**

Crystal system: Monoclinic  
Space group: C 1 2/c 1  
Space group number: 15

a (Å): 29.9679  
b (Å): 2.8080  
c (Å): 4.9040  
Alpha (°): 90.0000  
Beta (°): 95.9110  
Gamma (°): 90.0000

Calculated density (g/cm<sup>3</sup>): 1.47  
Volume of cell (10<sup>6</sup> pm<sup>3</sup>): 410.48  
Z: 4.00

RIR: 47.27

**Subfiles and quality**

Subfiles: User Inorganic  
Quality: User From Structure (=)

**Comments**

Creation Date: 16/07/2001  
Modification Date: 30/12/1899  
Original ICSD space group: I12/A1. The coordinates are those given in the paper but the atomic distances do not agree with those calculated during testing. The coordinates are probably correct.. X-ray diffraction from single crystal. Temperature factors available

Modulated structure first part structure: collection no. 087941

Recording date: 7/16/2001

ANX formula: AX<sub>2</sub>

Z: 4

Calculated density: 1.47

R value: 0.04

Pearson code: mS12

Wyckoff code: f2

Structure TIDY: TRANS -a-c,b,a origin 0 0 1/2

Structure TIDY: REMARK Transformed from setting I 1 2/a 1.

Publication title: A bismuth cobaltite with an intrinsically modulated misfit structure: (Bi<sub>0.87</sub> Sr O<sub>2</sub>)<sub>2</sub> (Co O<sub>2</sub>)<sub>1.82</sub>

ICSD collection code: 87942

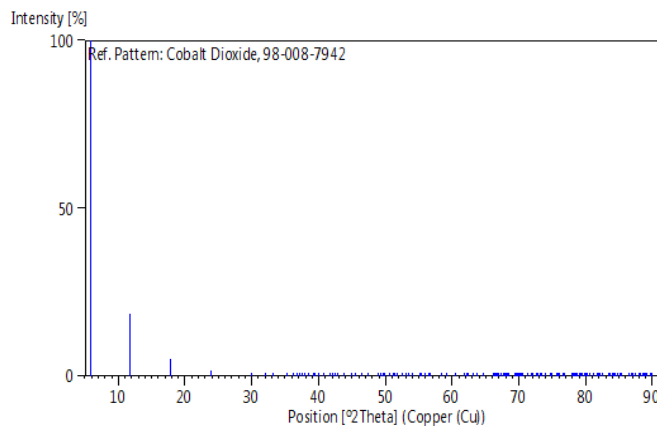
Chemical Name: Cobalt Dioxide

Second Chemical Formula: Co O<sub>2</sub>

**Peak list**

No.	h	k	l	d [Å]	2Theta[deg]	I [%]
1	2	0	0	14.90428	5.925	100.0
2	4	0	0	7.45214	11.866	18.6
3	6	0	0	4.96809	17.839	5.1
4	8	0	0	3.72607	23.862	1.5
5	10	0	0	2.98086	29.952	0.5
6	1	1	0	2.79562	31.988	0.0
7	3	1	0	2.70217	33.126	0.0
8	5	1	0	2.54032	35.303	0.0
9	12	0	0	2.48405	36.130	0.2
10	2	0	-2	2.44745	36.690	0.2
11	0	0	2	2.43896	36.822	0.4
12	1	1	-1	2.43568	36.873	0.3
13	1	1	1	2.41547	37.193	0.1
14	3	1	-1	2.39229	37.567	0.3
15	4	0	-2	2.39194	37.573	0.1
16	2	0	2	2.36839	37.960	0.6
17	7	1	0	2.34422	38.367	0.0
18	3	1	1	2.33615	38.505	0.0
19	5	1	-1	2.29473	39.228	0.2
20	6	0	-2	2.28441	39.413	0.1
21	4	0	2	2.25048	40.032	0.7
22	5	1	1	2.21365	40.727	0.0
23	7	1	-1	2.16127	41.760	0.1
24	8	0	-2	2.14436	42.105	0.1
25	9	1	0	2.14184	42.157	0.0
26	14	0	0	2.12918	42.419	0.1
27	6	0	2	2.10528	42.925	0.7
28	7	1	1	2.06763	43.746	0.1
29	9	1	-1	2.01104	45.044	0.0
30	10	0	-2	1.99078	45.528	0.1
31	8	0	2	1.95069	46.518	0.6
32	11	1	0	1.94994	46.537	0.0
33	9	1	1	1.91474	47.444	0.1
34	16	0	0	1.86304	48.845	0.1
35	11	1	-1	1.85872	48.966	0.0
36	1	1	-2	1.84671	49.306	0.0
37	12	0	-2	1.83750	49.570	0.1
38	3	1	-2	1.83629	49.604	0.0
39	1	1	2	1.82912	49.812	0.0
40	5	1	-2	1.79924	50.697	0.0
41	10	0	2	1.79901	50.704	0.4
42	3	1	2	1.78582	51.105	0.0
43	13	1	0	1.77605	51.407	0.0
44	11	1	1	1.76608	51.719	0.1
45	7	1	-2	1.74012	52.549	0.0
46	5	1	2	1.72200	53.145	0.0
47	13	1	-1	1.71339	53.433	0.0
48	14	0	-2	1.69266	54.141	0.2
49	9	1	-2	1.66529	55.105	0.0
50	12	0	2	1.65710	55.401	0.3
51	18	0	0	1.65603	55.440	0.0
52	7	1	2	1.64419	55.874	0.0
53	13	1	1	1.62765	56.492	0.1
54	15	1	0	1.62211	56.702	0.0

## **Stick Pattern**



### **A.3 Classification of target gases for sensing**

The detection or sensing of combustible or toxic gases before you reach the risk limit is considered very important and is a key component for the protection of persons and property. The gases to be detected or sensitized can be classified into three main categories [279-281].

#### **1. First category**

The most important gas in this category is the oxygen, its sensing is important to monitor of breathable atmospheres and for the control of combustion. This category can include moisture and some non-toxic and non-explosive gases but can be suffocating at high concentrations.

Normal ambient air contains an oxygen concentration of 20.8% by volume. When the oxygen level dips below 19.5% of the total atmosphere, the area is considered oxygen deficient. In oxygen-deficient atmospheres, life-supporting oxygen may be displaced by other gases, such as carbon dioxide. This results in an atmosphere that can be dangerous or fatal when inhaled. Oxygen deficiency may also be caused by rust, corrosion, fermentation or other forms of oxidation that consume oxygen. As materials decompose, oxygen is drawn from the atmosphere to fuel the oxidation process. The impact of oxygen deficiency can be gradual or sudden, depending on the overall oxygen concentration and the concentration levels of other gases in the atmosphere.

#### **2. Second category**

This category includes the flammable and explosive gases in air, its sensing is important to in order to protect against the unwanted occurrences of fire or explosion.

Combustible gas detection relies upon the detection of a gas before it reaches either its lower explosive or lower flammable limit, LEL and LFL. A hazardous area is defined based on three criteria, namely (a) depending upon type of gas, (b) ignition temperature of the gas, and (c) likelihood of gas being present in flammable concentrations. Flammability limit, thus defined, gives the proportion of combustible gases in a mixture, between which limits mixture is flammable.

- Lower Explosive Limit (LEL): The minimum concentration of gas or vapor mixed with air (percentage by volume, at room temperature) that will cause the propagation of flames when it comes in contact with a source of ignition. In common terminology, mixtures below the LEL are too lean to ignite.

- Upper Explosive Limit (UEL): The maximum concentration of gas or vapor mixed with air (percent by volume, at room temperature) that will cause the propagation of flames when it comes in contact with an ignition source. In common terminology, mixtures above the UEL are too rich to support combustion.

### 3. Third category

This category includes the toxic gases in air. A toxic gas is one which is capable of causing damage to living tissue, impairment of the central nervous system, severe illness or in extreme cases death, when ingested, inhaled or absorbed by the skin or eyes. The amounts required to produce these results vary widely with the nature of the substance and exposure time. “Acute” toxicity refers to exposure of short duration, such as a single brief exposure. “Chronic” toxicity refers to exposure of long duration, such as repeated or prolonged exposures. Toxic gas monitoring is important because some substances can’t be seen or smelled and has no immediate effects. Thus the recognition of a gas hazard via a worker’s senses often comes too late, after concentrations have reached harmful levels. The toxic effects of gases range from generally harmless to highly toxic. Some are life-threatening at even short, low-level exposures, while others are hazardous only upon multiple exposures at higher concentrations. The degree of hazard that a substance poses to a worker depends upon several factors which include the gas concentration level and the duration of exposure. Where the need is to monitor concentrations around the exposure limits, which it's often too small to exceed a few parts per million (ppm). As toxic gases can cause harm even in low concentrations, over a long period of time (chronic exposure) or in higher concentrations over a short period of time (acute exposure), different countries have established threshold limit values (TLVs) for poisonous gases in order to advance People in general and workers

in particular, protection by providing timely scientific information to occupational and environmental health professionals. The TLVs refer to those concentrations within which personnel may be exposed without known adverse effects to their health or safety; followings are the three types of TLVs:

1. Time Weighted Average (TWA) is the average concentration to which nearly all workers may be exposed over given hours of work shift/week without known adverse effects. However, many substances are sufficiently toxic that short-term exposures at higher concentrations may prove harmful or even fatal.
2. Short-Term Exposure Limit (STEL) is a time -weighted average concentration occurring over a period of not more than few minutes. It is also recommended that such circumstances should not occur many times.
3. Ceiling Limit (CL) is the concentration that should not be exceeded at any time. This is relevant for the most toxic substances or those that produce an immediate irritant effect.

Table A.2 shows the values of the most important Gas exposure limits of some toxic or flammable gases.

**Table A.2:** Gas exposure limits for some toxic and flammable gases [279- 281].

Gas or Vapor	Acetone	Ethane	Ethanol	Methane	Methanol	Propane
<b>Chemical Formula</b>	C <sub>3</sub> H <sub>6</sub> O	C <sub>2</sub> H <sub>6</sub>	C <sub>2</sub> H <sub>6</sub> O	CH <sub>4</sub>	CH <sub>4</sub> O	C <sub>3</sub> H <sub>8</sub>
<b>Relative Density (vs.Air)+</b>	Heavier	Slightly heavier	Heavier	Lighter	Heavier	Heavier
<b>Combustible</b>	yes	yes	yes	yes	yes	yes
<b>LEL (% by vol)</b>	2.5	3.0	3.3	5.0	6.0	2.1
<b>UEL (% by vol)</b>	12.8	12.5(15.5)	19	15	36	9.5
<b>ACGIHT LV-TWA (ppm)<sup>2</sup></b>	500	A	1000	A	200	2500
<b>ACGIHT LV- STEL (ppm)</b>	750	A	-	A	250	-
<b>OSHA - PEL (ppm)</b>	1000	-	1000	-	200	1000
<b>NIOSH - IDLH (PPM)</b>	2500	A	3300	A	6000	2100
<b>Autoignition Temp (°C)</b>	456	472	363	537	464	450

# References

**References**

- [1] J. F. Chang, H. H. Kuo, I. C. Leu and M. H. Hon, "The effects of thickness and operation temperature on ZnO:Al thin film CO gas sensor", *Sensors and Actuators B: Chemical*, Vol. 84, No. 2-3, (2002), 258-264.
- [2] I. M. Ibrahim, Y. R. Hathal, F. T. Ibrahim and M. H. Ali, "Etching effect on sensing behavior of CuO:NiO/PS Hydrogen gas sensor", *International Journal of Scientific and Engineering Research*, Vol. 6, No. 7, (2015), 1664-1668.
- [3] V. M. Aroutiounian, "Hydrogen detectors", *International Scientific Journal for Alternative Energy and Ecology*, Vol. 23, No. 3, (2005), 21-31.
- [4] V. M. Aroutiounian, "Semiconductor metal Oxide hydrocarbon gas Sensors", *International Scientific Journal for Alternative Energy and Ecology*, Vol. 47, No. 3, (2007), 33-42.
- [5] Wang, P. Yang, X. Wei and Z. Zhou, "Preparation of NiO two-dimensional grainy films and their high-performance gas sensors for ammonia detection", *Nanoscale. Res. Lett.*, Vol. 10, No. 119, (2015), 1-6.
- [6] V. S. Kalyamwar and F. C. Raghuvanshi, "TiO<sub>2</sub> modified ZnO thick film resistors as ammonia gas sensors", *Advanced Materials Letters*, Vol. 4, No. 12, (2013), 895-898.
- [7] A.K. Srivastava, "Detection of volatile organic compounds (VOCs) using SnO<sub>2</sub> gas-sensor array and artificial neural network", *Sensors and Actuators B: Chemical*, Vol. 96, No. 1-2, (2003), 24-37.
- [8] L. Valentini, I. Armentano, J. M. Kenny, C. Cantalini, L. Lozzi, and S. Santucci, "Sensors for sub-ppm NO<sub>2</sub> gas detection based on carbon nanotube thin films", *Applied Physics Letters*, Vol. 82, No. 6, (2003), 961-963.
- [9] S. T. Shishiyanu, T. S. Shishiyanu and O. I. Lupan, "Novel NO<sub>2</sub> gas sensor based on cuprous oxide thin films", *Sensors and Actuators B: Chemical*, Vol. 113, N. 1, (2006), 468-476.
- [10] V. S. Kalyamwar, F. C. Raghuvanshi, N. L. Jadhao and A. J. Gadewar, "Zinc Oxide Nano-structure Thick Films as H<sub>2</sub>S Gas Sensors at Room Temperature", *Journal of Sensor Technology*, Vol. 3, (2013), 31-35.
- [11] D. Jundale, S. Pawar, M. Chougule, P. Godse, S. Patil, B. Raut, S. Sen, and V. Patil, "Nano-crystalline CuO Thin Films for H<sub>2</sub>S Monitoring: Microstructural and Optoelectronic Characterization", *Journal of Sensor Technology*, Vol. 1, (2011), 36-46.
- [12] A. Thamri, H. Baccar, F. E. Annanouch, E. Llobet and A. Abdelghani, "Methanol Ethanol and Acetone Sensing Using AACVD-grown Tungsten Oxide Nanoneedles", *Journal of Nanomedicine & Nanotechnology*, Vol. 7, No. 3, (2016), 1-6.
- [13] G. S. Aluri, A. Motayed, A. V. Davydov, V. P. Oleshko, K. A. Bertness, N. A. Sanford and R. V. Mulpuri, "Methanol ethanol and hydrogen sensing using metal oxide and metal (TiO<sub>2</sub>-Pt) composite nanoclusters on GaN nanowires: a new route towards tailoring the selectivity of nanowire/nanocluster chemical sensors", *Journal of Nanotechnology*, Vol. 23, No. 17, (2012), 1-12.
- [14] R. C. Boldú, "Gas sensor microsystems based on nanostructured layers via anodic oxidation", *Doctoral Thesis, Rovira I Virgili University*, (2012), Spain.
- [15] M. U. Qadri, "Tungsten oxide nanostructures and thin films for optical gas sensors", *Doctoral Thesis, Rovira I Virgili University*, (2014), Spain.
- [16] A. Gaddari, "Nouvelle méthode d'élaboration par voie sol-gel des couches minces de dioxyde d'étain : Applications à la détection à température ambiante d'ozone et d'ammoniac", *doctoral Thesis, (Franche-Comté University + Cadi Ayyad University)*, (2013), Maroc.
- [17] T. Shigemori, "Gas sensors status and future trends for safety applications", *The 14th International Meeting on Chemical Sensors*, DOI 10.5162/IMCS2012/PT1.

## References

---

- [18] A. Martucci, N. Bassiri and M. Guglielmi, "NiO-SiO<sub>2</sub> Sol-Gel Nanocomposite Films for Optical Gas Sensor", *Journal of Sol-Gel Science and Technology*, Vol. 26, No. 1-3, (2003), 993-996.
- [19] T. T. Le Dang and M. Toneyzer, "Polycrystalline NiO nanowires: scalable growth and ethanol sensing", *Procedia Engineering*, Vol. 120, (2015), 427-434.
- [20] B. Ghaddab, "Developpement d'un capteur de gaz à base de couche hybride dioxyde d'étain /nanotubes de carbone", *Doctoral Thesis, Franche-Comté University*, (2015), France.
- [21] A. Star, V. Joshi, S. Skarupo, D. Thomas and J. C. P. Gabriel, "Gas sensor array based on metal-decorated carbon nanotubes", *The Journal of Physical Chemistry B*, Vol. 110, No. 42, (2006), 21014-21020.
- [22] K. A. Chebout, R. T. Ighil, K. Mhammedi, S. Sam and N. Gabouze, "V<sub>2</sub>O<sub>5</sub> nanorods as CO<sub>2</sub> gas sensing devices", *Journal of Engineering and Technology*, Vol. 7, No. 1, (2018), 24-29.
- [23] C. Jin, S. Park, H. Kim, T. Ko and C. Lee, "Enhanced NO<sub>2</sub> Gas-sensing Properties of SnO<sub>2</sub> Nanorods with a TiO<sub>2</sub> Capping", *Journal of Korean Physical Society*, Vol. 61, No. 9, (2012), 1370-1375.
- [24] R. S. Zeferino, M. B. Flores and U. Pal, "Photoluminescence and Raman scattering in Ag-doped ZnO nanoparticles", *Journal of Applied Physics*, Vol. 109, No. 1, (2011), 1-6.
- [25] M. Aliahmada, A. Rahdar and Y. Azizi, "Synthesis of Cu doped NiO nanoparticles by chemical method", *Journal of Nanostructures*, Vol. 4, (2014), 145-152.
- [26] A. Rahdar, M. Aliahmad and Y. Azizi, "NiO nanoparticles: Synthesis and characterization", *Journal of Nanostructures*, Vol. 5, No. 2, (2015), 145-151.
- [27] D. Yang, "Nanocomposite films for gas sensing", *Journal of Advances in Nanocomposites - Synthesis, Characterization and Industrial Applications*, Vol. 37, (2011), 858-883.
- [28] R. Srivastava, "Nanocomposite NiFe<sub>2</sub>O<sub>4</sub>-Fe<sub>2</sub>O<sub>3</sub>-NiO thick film liquefied petroleum gas sensor", *International Journal Innovative Research in Science, Engineering and Technology*, Vol. 2, No. 11, (2013), 6567-6571.
- [29] M. Jothibas, C. Manoharan, S. Dhanapadian and S. J. Jeyakumar, "Influence of Precursor Concentration on Sprayed In<sub>2</sub>O<sub>3</sub> Thin Films", *Asian Journal of Chemistry*, Vol. 25, (2013), 59-64.
- [30] J. Wöllenstein, M. Scheulin, N. Herres, W.J. Becker and H. böttner, "Gas sensitive behavior and morphology of reactive evaporated V<sub>2</sub>O<sub>5</sub> thin films", *Sensor and Materials*, Vol. 15, No. 5, (2003), 239-246.
- [31] A. S. Garde, "Gas Sensing Properties of WO<sub>3</sub> Thick Film Resistors Prepared by Screen Printing Technique", *International Journal of Chemical and Physical Sciences*, Vol. 5, No. 3, (2016), 1-13.
- [32] H. Benelmadjat, B. Boudine, O. Halimi, and M. Sebais, "Fabrication and characterization of pure and Sn/Sb-doped ZnO thin films deposited by sol-gel method", *Optics & Laser Technology*, Vol. 41, No. 5, (2009), 630-633.
- [33] M. Suche, S. Christoulakis, K. Moschovis, N. Katsarakis and G. Kiriakidis, "ZnO transparent thin films for gas sensor applications", *Thin Solid Films*, Vol. 515, (2006), 551-554.
- [34] J. Xu, Q. Pan b, Y. Shun and Z. Tian, "Grain size control and gas sensing properties of ZnO gas sensor", *Sensors and Actuators B: Chemical*, Vol. 66, No. 1-3, (2000), 277-279.
- [35] M. M. Abdullah, M. H. Suhail and S. I. Abbas, "Fabrication and Testing of SnO<sub>2</sub> Thin Films as a Gas Sensor", *Arch. Appl. Sci. Res*, Vol. 4, N. 3, (2012), 1279-1288.
- [36] R. H. Bari, S. B. Patil1 and A. R. Bari, "Synthesis, characterization and gas sensing performance of Sol-Gel prepared nanocrystalline SnO<sub>2</sub> thin film", *International Journal of Smart Sensing and Intelligent Systems*, Vol. 7, No. 2, (2014), 610-629.

## References

---

- [37] M. Guziewicz, P. Klataa, J. Grochowska, K. Golaszewskaa, E. Kaminskaa, J.Z. Domagala, B.A. Witkowskib, M. Kandylac, Ch. Chazimanolisd, M. Kompitsasc and A. Piotrowskaa, "Hydrogen Sensing Properties of Thin NiO Films Deposited by RF Sputtering", *Procedia Engineering*, Vol. 47, (2012), 746-749.
- [38] Y. Ogo, H. Hiramatsu, K. Nomura, H. Yanagi, T. Kamiya, M. Hirano and H. Hosono, "Channel thin-film transistor using p-type oxide semiconductor SnO", *Applied Physics Letter*, Vol. 93, (2008), 1-3.
- [39] F.K. Mugwang, P.K. Karimi, W.K. Njoroge, O. Omayio and S. M. Waita, "Optical characterization of Copper Oxide thin films prepared by reactive dc magnetron sputtering for solar cell applications", *International Journal of Thin Film Science*, Vol. 2, No. 1, (2013), 15-24.
- [40] T. Minami, T. Miyata, and Y. Nishi, "Relationship between the electrical properties of the n-oxide and p-Cu<sub>2</sub>O layers and the photovoltaic properties of Cu<sub>2</sub>O-based heterojunction solar cells", *Solar energy materials and solar cells*, Vol. 147, (2016), 85-93.
- [41] D. S. Murali, S. Kumar, R. J. Choudhary, A. D. Wadikar, M. K. Jain and A. Subrahmanyan, "Synthesis of Cu<sub>2</sub>O from CuO thin films: Optical and electrical properties", *AIP Advances*, Vol. 5, (2015), 1-5.
- [42] S. Kalpana, S. S. Krishnan, T. S. Senthil and S.V. Elangovan, "Cobalt doped Zinc oxide nanoparticles for photocatalytic applications", *Journal of Ovonic Research*, Vol. 13, No. 5, (2017), 263-269.
- [43] A. Chowdhuri, D. Haridas, K. Sreenivas and V. Gupta, "Mechanism of trace level H<sub>2</sub>S gas sensing using RF Sputtered SnO<sub>2</sub> thin films with CuO catalytic overlayer", *International Journal on Smart sensing and intelligent systems*, Vol. 2, No. 4, (2009), 540-548.
- [44] H. Gong, J. Q. Hu, J. H. Wang, C. H. Ong and F. R. Zhu, "Nano-crystalline Cu-doped ZnO thin film gas sensor for CO", Vol. 115, No. 1, (2006), 247-251.
- [45] Y. J. Choi, Z. Seeley, A. Bandyopadhyay, S. Bose, S. A. Akbar, "Aluminum-doped TiO<sub>2</sub> nano-powders for gas sensors", *Sensors and Actuators B*, Vol.124, (2007), 111-117.
- [46] O. Lupan, S. Shishiyanu, L. Chow and T. Shishiyanu, "Nanostructured zinc oxide gas sensors by successive ionic layer adsorption and reaction method and rapid photothermal processing", *Thin Solid Films*, Vol. 516, (2008), 3338-3345.
- [47] S. Alamdari, M. S. Ghamsari and M. J. Tafreshi, "Synthesis, Characterization, and Gas Sensing Properties of In-doped ZnO Nanopowders", *Nanochemistry Research*, Vol. 2, N. 2, (2017), 198-204
- [48] A. V. Rajgure, "Synthesis and Characterization of nanocrystalline ZnO gas sensor", *Doctoral Thesis, Solapur University*, (2014), India.
- [49] N. Dufour, "Conception et réalisation d'un multicapteur de gaz intégré à base de plateformes chauffantes sur silicium et de couches sensibles à oxyde métallique pour le contrôle", *doctorat Thesis, Toulouse university*, (2013), France.
- [50] I. D. Farrukh, R. M. Kevin and E. S. Mohammed, "Morphology and property control of NiO nanostructures for supercapacitor applications", *Nanoscale Research Letters*, Vol. 8, No. 1, (2013), 1-7.
- [51] J. S. Anandh, M. Haris and P. Immanuel, "Structural and Optical Properties of Pure NiO and Li-Doped Nickel Oxide Thin Films by Sol-Gel Spin Coating Method", *International Journal of Science and Research*, Vol. 23, (2014), 58-87.
- [52] A. A. G. Attieh, M. S. A. Wahabab, A. A. Farghalibc and P. M. Z. Hasana, "Structural optical and photo-catalytic activity of nanocrystalline NiO thin films", *Materials Research Bulletin*, Vol. 7, (2016), 71-75.
- [53] M. S. Amir, H. J. Ahalapitiya and S. Gamini, "Surface and gas sensing properties of nanocrystalline nickel oxide thin films", *Applied Surface Science*, Vol. 276, (2013), 291-297.

## References

---

- [54] D. G. Enrico and M. Alessandro, "Sol-Gel Thin Films for Plasmonic Gas Sensors", *Sensors*, Vol. 15, No. 7, (2015), 16910-16928.
- [55] D. Y. Jianga, J. M. Qina, X. Wangb, S. Gaoa, A. C. Lianga and J. X. Zhaoa, "Optical properties of NiO thin films fabricated by electron beam evaporation", *Vacuum*, Vol. 86, N. 8, (2012), 1083-1086.
- [56] H. Ivan, L. Jozef, S. Helmut and V. Peter, "properties of sputtered NiO thin films", *Journal of Electrical Engineering*, Vol. 53, No. 11-12, (2002), 339-342.
- [57] V. Julijana, P. G. Margareta, N. Metodija and S. Nace, "Studies on Electrochromism of Chemically Deposited Nickel Oxide Thin Films", *Silpakorn University Science and Technology Journal*, Vol. 5, N. 1, (2011), 34-42.
- [58] C. K. Romana and B. Peter, "Sol-Gel Prepared NiO Thin Films for Electrochromic applications", *Acta. Chim. Slov*, Vol. 53, (2006), 136-147.
- [59] J. H. Ahmed, "Study of optical and electrical properties of Nickel Oxide (NiO) thin films deposited by using a spray pyrolysis technique", *Journal of Modern Physics*, Vol. 5, No. 18, (2014), 2184-2191.
- [60] P. S. Patil, L. D. Kadam, "Preparation and characterization of spray pyrolyzed nickel oxide (NiO) thin films", *Applied Surface Science*, Vol. 199, No. 1-4, (2002), 211-221.
- [61] M. L. Zeggar, "Cupric Oxide thin films deposition for gas sensor application", *Doctoral Thesis, frères Mentouri Constantine1 University*, (2016), Algeria.
- [62] S. Yahiaoui, "L'effet de la molarité des différentes sources d'étain sur les propriétés des couches minces d'oxyde d'étain SnO<sub>2</sub> élaborées par Spray Ultrasonique", *Magister Thesis, Biskra University*, (2014), Algeria.
- [63] D. Royer and E. Dieulesaint, "Ondes élastiques dans les solides (Génération, interaction acousto-optique, applications)", *Edition Masson, Tome 2*, (1999), France.
- [64] G. Williams and G. S. V. Coles, "The Gas-Sensing Potential of Nanocrystalline Tin Dioxide Produced by a Laser Ablation Technique", *MRS Bulletin*, Vol. 24, No. 6, (1999), 25-29.
- [65] David C. Look, D. C. Reynolds, C. W. Litton, R. L. Jones, D. B. Eason, and G. Cantwell, "Characterization of homoepitaxial p-type ZnO grown by molecular beam epitaxy", *Applied Physics Letter*, Vol. 81, No. 10, (2002), 1830-1832.
- [66] A. M. Reddya, A. S. Reddyb and P. S. Reddya, "Annealing effect on the physical properties of dc reactive magnetron sputtered nickel oxide thin films", *Physics Procedia*, Vol. 49, (2013), 9-14.
- [67] P.J. Kelly and R.D. Arnell, "Magnetron sputtering: a review of recent developments and applications", *Vacuum*, Vol. 56, (2000), 159-172.
- [68] M. Leskelä, and M. Ritala, "Atomic layer deposition (ALD): from precursors to thin film structures". *Thin Solid Films*, Vol. 409, No. 1, (2002), 138-146.
- [69] D. Perednis and L. J. Gauckler, "Thin film deposition using spray pyrolysis", *Journal of Electroceramics*, Vol. 14, (2005), 103-111.
- [70] S. A. Mahmoud, S. Alshomer and M. A. Tarawnh, "Structural and optical dispersion characterization of sprayed Nickel Oxide thin films", *Journal of Modern Physics*, Vol. 2, (2011), 1178-1186.
- [71] R. C. Korošec and P. Bukovec, "Sol-Gel Prepared NiO thin films for electrochromic applications", *Acta Chim. Slov*, Vol. 53, (2006), 136-147.
- [72] F. Y. Yang, Kai Liu, Kimin Hong, D. H. Reich, P. C. Searson and C. L. Chien "Large magnetoresistance of electrodeposited Single-Crystal Bismuth thin films", *Science*, Vol. 284, No. 5418, (1999), 1335-1337.
- [73] J. C. Osuwa and G. I. Onyejiuwa, "Structural and electrical properties of annealed Nickel Oxide (NiO) Thin Films prepared by chemical bath deposition", *Journal of Ovonic Research*, Vol. 9, No. 1, (2013), 9-15.

## References

---

- [74] Y.Z. Liu, C.C. Wang and M. Chu, "Low threshold 1.3- $\mu\text{m}$  InGaAsP/InP lasers prepared by a single-step liquid-phase epitaxy", *Journal of Applied Physics*, Vol. 63, (1988), 2151-2151.
- [75] D. J. Estes and M. Mayer, "Electroformation of giant liposomes from spin-coated films of lipids", *Colloids and Surfaces B: Biointerfaces*, Vol. 42, (2005), 115-123.
- [76] P. Baudry, A. C. M. Rodrigues, M. A. Aegerter and L. O. Bulhões, "Dip-coated  $\text{TiO}_2$ - $\text{CeO}_2$  films as transparent counter-electrode for transmissive electrochromic devices". *Journal of Non-Crystalline Solids*, Vol. 121, (1990), 319-322.
- [77] A. V. Moholkar, S. M. Pawar, K. Y. Rajpure, P. S. Patil and C. H. Bhosale, "Properties of highly oriented spray-deposited fluorine-doped tin oxide thin films on glass substrates of different thickness", *Journal of Physics and Chemistry of Solids*, Vol. 68, (2007), 1981-1988.
- [78] D. Perednis and L. J. Gaukler, "Thin film deposition using spray pyrolysis", *Journal of Electroceramics*, Vol. 14, (2005), 103-111.
- [79] R. Chamberlin, J. S. Skaraman, "Chemical spray deposition process for inorganic films", *Journal of electrochemical Society*, Vol. 113, No. 1, (1966), 86-89.
- [80] J. C. Viguie and J. Spitz, "Chemical vapor deposition at low temperatures", *Journal of electrochemical Society*, Vol. 122, (1975), 585-588.
- [81] W. Kern and B. Tracy, "Titanium dioxide antireflection coating for silicon solar cells by spray deposition", *United States*, Vol. 41, No. 4, (1980), 133-180.
- [82] P. S. Patil, "Versatility of chemical spray pyrolysis technique", *Materials Chemistry and Physics*, Vol. 59, No. 3, (1999), 185-198.
- [83] S. M. Sabnis, P. A. Bhadane, P. G. Kulkarni, "Process flow of spray pyrolysis technique", Vol. 4, No. 5, (2013), 07-11.
- [84] L. Filipovic et al, "Methods of simulating thin film deposition using spray pyrolysis techniques", *Microelectronic Engineering*, Vol. 117, (2014), 57-66.
- [85] A. J. Kelly, "Charge injection electrostatic atomizer modeling Aerosol", *Aerosol Science and Technology*, Vol. 12, No. 3, (1990), 526-537.
- [86] A. Nakaruk and C. Sorrell, "Conceptual model for spray pyrolysis mechanism: fabrication and annealing of Titania thin films", *Coatings Technology and Research*, Vol. 7, No. 5, (2010), 665-676.
- [87] D. Perednis and L. J. Gauckler, "Solid oxide fuel cells with electrolytes prepared via spray pyrolysis", *Solid State Ionics*, Vol. 166, No. 3-4, (2004), 229-239.
- [88] W. Li and E. J. Davis, "Measurement of the thermophoretic force by electrodynamic levitation: Microspheres in air", *Journal of Aerosol Science*, Vol. 26, No. 7, (1995), 1063-1083.
- [89] L. Filipovic, S. Selberherr, G. C. Mutinati, E. Brunet, S. Steinhauer, A. Köck, J. Teva, J. Kraft, J. Siegert and F. Schrank, "Modeling spray pyrolysis deposition", *Proceedings of the World Congress on Engineering*, Vol. 2, No. 3-5, (2013), 1-6.
- [90] C. Falcony, M. A. A. Frutis and M. G. Hipólito, "Spray pyrolysis technique; High-K dielectric films and luminescent materials: A Review", *Micromachines*, Vol. 414, No. 9, (2018), 1-33.
- [91] F. F. Fachini, "Effects of the initial droplet temperature on the vaporization process at high pressure", *Journal of the Brazilian Society of Mechanical Sciences and Engineering*, Vol. 29, No. 1, (2007), 91-98.
- [92] W. Siefert, " Properties of thin  $\text{In}_2\text{O}_3$  and  $\text{SnO}_2$  films prepared by corona spray pyrolysis, and a discussion of the spray pyrolysis process", *Thin Solid Films*, Vol. 120, No. 4, (1984), 275-282.
- [93] L. Filipovic, Member, S. Selberherr, G. C. Mutinati, E. Brunet, S. Steinhauer, A. Köck, J. Teva, J. Kraft, J. Siegert, F. Schrank, C. Gspan and W. Grogge, "A Method for simulating spray pyrolysis deposition in the level set framework", *Engineering Letters*, Vol. 21, No. 4, (2013), 1-17.

## References

---

- [94] H. H. Afify, S. A. Nasser and S. E. Demian, "Influence of substrate temperature on the structural, optical and electrical properties of ZnO thin films prepared by spray pyrolysis", *Materials Science: Materials in Electronics*, Vol. 2, No. 3, (1991), 152-156.
- [95] N. Lehraki, M. S. Aida, S. Abed, N. Attaf, A. Attaf and M. Poulain, "ZnO thinfilms deposition by spray pyrolysis: Influence of precursor solution properties", *Current Applied Physics*, Vol. 30, (2012), 1-5.
- [96] J. C. Vigué, "Chemical vapor deposition at low temperatures", *Journal of Electrochemical Society*, Vol. 122, No. 4, (1975), 585-588.
- [97] S. Senroy, "Characterization of copper oxide, titanium oxide and copper doped titanium oxide thin films prepared by spray pyrolysis technique", *Doctoral Thesis, Bangladesh University*, (2016), Bangladesh.
- [98] D. W. Pashley, "The nucleation, growth, structure and epitaxy of thin surface films", *Advances in Physics*, Vol. 14, No. 55, (1965), 327-416.
- [99] J. L. McCormick and J. W. Westwater, "Nucleation sites for dropwise condensation", *Chemical Engineering Science*, Vol. 20, No. 12, (1965), 1021-1036.
- [100] K.L. Chopra, "Growth of Sputtered vs Evaporated Metal Films", *Journal of Applied Physics*, Vol. 37, N. 9, (1966), 3405-3410.
- [101] U. Gösele and K. N. Tu, "Growth kinetics of planar binary diffusion couples: "Thin film case" versus "bulk cases"", *Journal of Applied Physics*, Vol. 53, No. 4, (1982), 3252-3260.
- [102] K. Reichelt, "Nucleation and growth of thin films", *J. Vacuum*, Vol. 38, No. 12, (1988), 1083-1099.
- [103] A. Beggas, "Elaboration and characterization of chalcogenide thin films by chemical bath deposition technique", *Doctoral Thesis, Biskra University*, (2018), Algeria.
- [104] M. Thomson, "The Modification of Thin Film Surface Structure via Low Temperature Atmospheric Pressure CVD Post Process Treatment Material", *Doctoral Thesis, Salford Greater Manchester University*, (2013), United Kingdom.
- [105] J. A. Nielsen and D. McMorrow, "Element of modern X-ray physics", WILY Edition, Second Edition, ISBN: 978-0-470-97394-3, (2011).
- [106] V. Saravanakannan and T. Radhakrishnan, "Structural, electrical and optical characterization of CuO thin films prepared by spray pyrolysis technique", *International Journal of ChemTech Research*, Vol. 6, No. 1, (2014), 306-310.
- [107] A. Rahdar, M. Aliahmadb and Y. Azizi, "NiO Nanoparticles: Synthesis and Characterization", *Journal of Nanostructures*, Vol. 5, (2015), 145-151.
- [108] L. Cattin, B. A. Reguig, A. Khelil, M. Morsli, K. Benchouk and J. C. Berne`de, "Properties of NiO thin films deposited by chemical spray pyrolysis using different precursor solutions", *Applied Surface Science*, Vol. 254, (2008), 5814-5821.
- [109] O. Belahssen, M. Ghougali and A. Chala, "Effect of iron doping on physical properties of NiO thin films", *Journal of Nano-and Electronic Physics*, Vol. 10, No. 2, (2018), 1-4.
- [110] M. Mekhnache, A. Drici, L. S. Hamideche, H. Benzarouk, A. Amara, L. Cattin, J. C. Bernede and M. Guerioune, "Properties of ZnO thin films deposited on (glass, ITO and ZnO: Al) substrates", *Superlattices and Microstructures*, Vol. 49, No. 5, (2011), 510-518.
- [111] M. V. Kumar, S. Muthulakshmi, A. A. Paulfrit, J. Pandiarajan, N. Jeyakumaran and N. Prithivikumaran, "Structural and optical behavior of thermally evaporated p-Type Nickel Oxide thin film for Solar Cell Applications", *International Journal of ChemTech Research*, Vol. 6, No. 13, (2014), 5174-5177.
- [112] M. Karunakaran, S. Maheswari, K.Kasirajan and S. Dineshraj, "Physical properties of nanocrystalline Tin Oxide thin film by chemical spray syrolysis method", *International Journal for Research in Applied Science & Engineering Technology*, Vol. 4, No. 7, (2016), 691-695.

## References

---

- [113] A. F. Saleh, "Structural and morphological studies of NiO thin films prepared by Rapid thermal oxidation method", *International Journal of Application or Innovation in Engineering & Management*, Vol. 2, No. 1, (2013), 16-21.
- [114] Y. Z. Dawood, M. H. Hassoni and M. S. Mohamad, "Effect of solution concentration on some optical properties of indium oxide doped with SnO<sub>2</sub> thin films prepared by chemical spray pyrolysis technique", *International Journal of Pure and Applied Physics*, Vol. 2, No. 1, (2014), 1-7.
- [115] S. Ilican, M. caglar, Y. caglar, "Determination of the thickness and optical constants of transparent indium-doped ZnO thin films by the envelope method", *Materials Science-Poland*, Vol. 25, No. 3, (2007), 709-718.
- [116] M. caglar, Y. caglar, S. Ilican, "The determination of the thickness and optical constants of the ZnO crystalline thin film by using envelope method", *Optoelectronics and Advanced Materials*, Vol. 8, No. 4, (2006), 1410-1413.
- [117] L. Reimer, "Scanning Electron Microscopy: Physics of image formation and microanalysis", Springer-Verlag, Second Edition, ISBN 3-540-63976-4, (1998).
- [118] E. Suzuki, "High-resolution scanning electron microscopy of immunogold-labelled cells by the use of thin plasma coating of osmium". *Journal of Microscopy*, Vol. 208, No. 3, (2002), 153-157.
- [119] A. R. Xarouco de Barros, "Development of p-type oxide semiconductors based on tin oxide and its alloys: application to thin film transistors", Master Thesis, Lisbon University, (2014), Portugal.
- [120] S. Benhamida, "Caractérisation Des Couches Minces D'oxyde De Nickel (NiO) Elaboré Par Spray Pyrolyse", Doctoral Thesis, Biskra University, (2018), Algeria.
- [121] P. Miles, "High transparency infrared materials - A technology update", *Optical Engineering*, Vol. 15, (1976), 451-459.
- [122] A. V. Rajgure, "Synthesis and Characterization of nanocrystalline ZnO gas sensor", Doctoral Thesis, Solapur University, (2014), India.
- [123] B. A. Ezekoye and C.E. Okeke, "Optical properties in PbHgS ternary thin films deposited by solution growth method", *The Pacific Journal of Science and Technology*, Vol. 7. No. 2, (2006), 108-113.
- [124] A. D. A. Buba and J. S. A. Adelabu, "Optical and Electrical Properties of Chemically Deposited ZnO Thin Films", *The Pacific Journal of Science and Technology*, Vol. 11, No. 2, (2010), 429-434.
- [125] S. S. Roy and J. Podder, "Synthesis and optical characterization of pure and Cu doped SnO<sub>2</sub> thin films deposited by spray pyrolysis", *Journal of Optoelectronics and Advanced Materials*, Vol. 12, No. 7, (2010), 1479 -1484.
- [126] F. N. AlShammary, "Optical characteristics of NiO thin film on glass formed by Chemical spray pyrolysis", *Journal of Kufa – Physics*, Vol. 2, No. 1, (2010), 22-27.
- [127] S. Sriram and A. Thayumanavan, "Structural, optical and electrical properties of NiO thin films prepared by low cost spray pyrolysis technique", *International Journal of Materials Science and Engineering*, Vol. 1, No. 2, (2013), 118-121.
- [128] N. N. Jandow, "Effects of Cu-doping on optical properties of NiO", *International Letters of Chemistry, Physics and Astronomy*, Vol. 48, (2015), 155-162.
- [129] K. Boubaker, "A physical explanation to the controversial Urbach tailing universality, *The European Physical Journal Plus*", Vol. 126, No. 10, (2011), 1-4.
- [130] F. N. C. Anyaegbunam and C. Augustine, "A study of optical band gap and associated Urbach energy tail of chemically deposited metal oxides binary thin film", *Digest Journal of Nanomaterials and Biostructures*, Vol. 13, No. 3, (2018), 847-856.

## References

---

- [131] K. Anandan and V. Rajendran, "Effect of Fe Doping in NiO Semiconductor Nanoparticles and Studies on Their Structural, Magnetic and Optical Properties: Synthesized Via the Precipitation Process", *International Journal of Advanced Trends in Engineering and Technology*, Vol. 2, No. 2, (2017), 1-5.
- [132] S. Bebramache, Y. Aoun, S. Lakel, B. Benhaoua and C. Torchi, "The calculate of optical gap energy and urbach energy of  $\text{Ni}_{1-x}\text{Co}_x\text{O}$  thin films", *Journal of Sādhanā*, Vol. 44, N. 26, (2019), 1-6.
- [133] M. V. Nikolić, V. Blagojevi, K. M. Paraskevopoulos, T. T. Zorba, D. Vasiljevi-Radovi, P. M. Nikoli and M. M. Risti, "Far infrared properties of sintered NiO", *Journal of the European Ceramic Society*, Vol. 27, (2007), 469-474.
- [134] H. Benzscour, "Synthèse d'un oxyde transparent conducteur (OTC) par pulvérisation chimique (ZnO, NiO)", *Magistere Thesis*, Badji Mokhtar University, (2008), Algeria.
- [135] S. Perusin, "Conséquences de l'oxydation haut température sur l'injection de défauts et le comportement mécanique des matériaux métalliques", *Doctoral Thesis*, Toulouse University, (2004), France.
- [136] J. D. Desai, S. K Min, K. D. Jung and O. S. Joo, "Spray pyrolytic synthesis of large area  $\text{NiO}_x$  thin films from aqueous nickel acetate solutions", *Applied Surface Science*, Vol. 253, No. 4, (2006), 1781-1786.
- [137] P. D. Hoon, "Optimization of nickel oxide-based electrochromic thin films", *Doctoral Thesis*, Bordeaux 1 University, (2010), France.
- [138] P. Puspharajah, S. Radhakrishna, and A. K. Arof, "Transparent conducting lithium-doped nickel oxide thin films by spray pyrolysis technique", *Journal of Materials Science*, Vol. 32, (1997), 3001-3006
- [139] A. M. Soleimanpour, "Synthesis, fabrication and surface modification of nanocrystalline nickel oxide for electronic gas sensors", *Doctoral Thesis*, Toledo University, (2013), U.S.A.
- [140] J. P. Neumann, T. Zhong and Y. A. Chang, "The Ni-O (Nickel-Oxygen) system", *Bulletin of Alloy Phase Diagrams*, Vol. 5, No. 2, (1984), 141-144.
- [141] V. Marcio, P. S. Renan and I. C. Susana, "Synthesis and characterization of stable Co and Cd doped nickel hydroxide nanoparticles for electrochemical applications", *Ultrasonics Sonochemistry*, Vol. 16, No.1, (2009), 35-40,
- [142] P. S. Patil, L. D. Kadam, "Preparation and characterization of spray pyrolyzed nickel oxide (NiO) thin films", *Applied Surface Science*, Vol. 199, (2002), 211-221.
- [143] S. Stanescu, "Les 'glissements de type écoulement' dans les marnes noires des Alpes du Sud. Morphologie, fonctionnement et modélisation hydro-mécanique", *Doctorat Thesis*, Louis Pasteur – StrasbourgI University, (2002), France.
- [144] T. M. Schuler, D. L. Ederer, S. Itza-Ortiz, G. T. Woods, T. A. Callcott and J. C. Woicik, "Character of the insulating state in NiO: A mixture of charge transfer and Mott-Hubbard character", *Phys. Rev. B - Condens. Matter Mater. Phys.*, Vol. 71, No. 11, (2005), 1-7.
- [145] N. F. Mott, "The basis of the electron theory of metals, with special reference to the transition metals", *Proceedings of the Physical Society. Section A*, Vol. 62, No. 7, (1949), 416-422.
- [146] J. Hubbard, "Exchange splitting in ferromagnetic nickel", *Proceedings of the Physical Society*, Vol. 84, No. 4, (1964), 55-464.
- [147] S. Lany, J. Osorio-Guillén and A. Zunger, "Origins of the doping asymmetry in oxides: Hole doping in NiO versus electron doping in ZnO", *Phys. Rev. B -Condens. Matter Mater. Phys.*, Vol. 75, No. 24, (2007), 1-4.
- [148] B. E. Saracin, "Structural and optoelectronic properties of sol-gel derived nickel oxide thin films", *Doctoral Thesis*, Middle East Technical University, (2017), Turkey.

## References

---

- [149] J. G. Aiken and A. G. Jordan, "Electrical transport properties of single crystal nickel oxide", *Journal of Physics and Chemistry of Solids*, Vol. 29, No. 12, (1968), 2153-2167.
- [150] H. W. Ryu, G. P. Choi, G. J. Hong and J. S. Park, "Growth and surface morphology of textured NiO thin films deposited by off-axis RF magnetron sputtering", *Japanese Journal of Applied Physics*, Vol. 43, No. 8A, (2004), 5524-5525.
- [151] G. A. Sawatzky and J. W. Allen, "Magnitude and origin of the band gap in NiO", *Physical Review Letters*, Vol. 53, No. 24. (1984), 2339-2342.
- [152] P. Lunkenheimer, A. Loidl, C. R. Ottermann, and K. Bange, "Correlated barrier hopping in NiO films", *Physical Review B*, Vol. 44, No. 11, (1991), 5927-5930.
- [153] M. R. Waugh, "The Synthesis, Characterisation and Application of Transparent Conducting Thin Films", *Doctorate Thesis, College London University*, (2011), England.
- [154] S. Pongha, P. Thongbai, T. Yamwong and S. Maensiri, "Giant dielectric response and polarization relaxation mechanism in (Li, V)-doped NiO", *Scripta Materialia*, Vol. 60, (2009), 870-873.
- [155] P. Mallick<sup>1</sup> and N. C. Mishra, "Evolution of structure, microstructure, electrical and magnetic properties of Nickel Oxide (NiO) with transition metal ion doping", *American Journal of Materials Science*, Vol. 2, No. 3,( 2012), 66-71.
- [156] D. Y. Jianga, J. M. Qina , X. Wangb, S. Gaoa, A. C. Lianga and J. X. Zhaoa, "Optical properties of NiO thin films fabricated by electron beam evaporation", *Vacuum*, Vol. 86, No. 8, (2012), 1083-1086.
- [157] H. Ivan, L. Jozef, S. Helmut and V. Peter, "properties of sputtered NiO thin films", *Journal of Electrical Engineering*, Vol. 53, No. 11-12, (2002), 339-342.
- [158] V. Julijana, P. G. Margareta, N. Metodija and S. Nace, "Studies on electrochromism of chemically deposited Nickel Oxide thin films", *Silpakorn University Science and Technology Journal*, Vol. 5, No. 1, (2011), 34-42.
- [159] C. K. Romana and B. Peter, "Sol-Gel Prepared NiO Thin Films for Electrochromic applications", *Acta Chimica Slovenica*, Vol. 53, ( 2006),136-147.
- [160] J. H. Ahmed, "Study of optical and Electrical Properties of Nickel Oxide (NiO) Thin Films Deposited by Using a Spray Pyrolysis Technique", *Journal of Modern Physics*, Vol. 5, (2014), 2184-2191.
- [161] K. O. Ukoba, A. C. Eloka-Eboka and F. L. Inambao, "Review of nanostructured NiO thin film deposition using the spray pyrolysis technique", *Renewable and Sustainable Energy Reviews*, Vol. 82, (2018), 2900-2915.
- [162] A. V. Rajgure, "Synthesis and characterization of nanocrystalline ZnO gas sensor, Doctoral Thesis", *Solapur University*, (2014), India.
- [163] S. M. Kanan, O. M. El-Kadri, I. A. Abu-Yousef and M. C. Kanan, "Semiconducting metal oxide based sensors for selective gas pollutant detection", *Sensors*, Vol. 9, No. 10, (2009), 8158-8196.
- [164] N. Dufour, "Conception et réalisation d'un multicapteur de gaz intégré à base de plateformes chauffantes sur silicium et de couches sensibles à oxyde métallique pour le contrôle", *Doctoral Thesis, Toulouse University*, (2013), France.
- [165] B. Ghaddab, "Developpement d'un capteur de gaz a base de couche hybride dioxyde d'étain / nanotubes de carbone", *Doctoral Thesis, Franche-Comté University*, (2015), France.
- [166] G. Noubel, "Élaboration des couches minces sensibles à la présence de vapeur d'eau par polymérisation plasma", *Doctoral Thesis, Constantine University*, (2011), Algeria.
- [167] G. F. Fine, L. M. Cavanagh, A. Afonja and R. Binions, "Metal oxide semi-conductor gas sensors in Environmental Monitoring", *Sensors*, Vol. 10, No. 6, (2010), 5469-5502.

## References

---

- [168] C. M. Ghimbeu, "Préparation et caractérisation de couches minces d'oxydes métalliques semiconducteurs pour la détection de gaz polluants atmosphériques", Doctoral Thesis, University of Paul Verlaine de Metz, (2007), France.
- [169] X. Liu, S. Cheng, H. Liu, S. Hu, D. Zhang and H. Ning, "A survey on gas sensing technology", *Sensors*, Vol. 12, No. 7, (2012), 9635-9665.
- [170] P. D. Hoon, "Optimisation of Nickel Oxide- based electrochromic thin films", Doctoral Thesis, Bordeaux1University, (2010), France.
- [171] R. Nisha, "Development of semiconductor metal oxide gas sensors for the detection of NO<sub>2</sub> and H<sub>2</sub>S gases", Doctoral Thesis, Cochin University of Science and Technology, (2014), India.
- [172] A. Gaddari, "Nouvelle méthode d'élaboration par voie sol-gel des couches minces de dioxyde d'étain : Applications à la détection à température ambiante d'ozone et d'ammoniac", Doctoral Thesis, Franche-Comté University, (2013), France.
- [173] E. E. Basse, "Development and characterization of metal oxide gas sensor", Doctoral Thesis, Auckland University of technology, (2014), New Zealand.
- [174] S. T. Shishiyanu, T. S. Shishiyanu and O. I. Lupan, "Novel NO<sub>2</sub> gas sensor based on cuprous oxide thin films", *Sensors and Actuators B: Chemical*, Vol. 113, No. 1, (2006), 468-476.
- [175] O. Lupan, S. Shishiyanu, L. Chow and T. Shishiyanu, "Nanostructured zinc oxide gas sensors by successive ionic layer adsorption and reaction method and rapid photothermal processing", *Thin Solid Films*, Vol. 516, No. 10, (2008), 3338-3345.
- [176] J. Flueckiger, F. K. Ko and K. C. Cheung, "Microfabricated formaldehyde gas sensors", *Sensors*, Vol. 9, (2009), 9196-9215.
- [177] A. S. Garde, "Gas Sensing Properties of WO<sub>3</sub> Thick Film Resistors Prepared by Screen Printing Technique", *International Journal of Chemical and Physical Sciences*, Vol. 5, No. 3, (2016), 1-13.
- [178] C. C. Cesar, "Elaboration et caractérisation d'un réseau de nanofils de ZnO par méthode hydrothermale et son application à la détection de gaz", Doctoral thesis, Paris-Est University, (2013), France.
- [179] L. T. Hoa, H. N. Tien, and S. H. Hur, "Fabrication of Novel 2D-NiO Nanosheet rached on 1D-ZnO Nanorod Arrays for Gas Sensor Application", *Journal of Nanomaterials*, Vol. 2014, (2014), 1-6.
- [180] A. M. Soleimanpour, "Synthesis, fabrication and surface modification of nanocrystalline nickel oxide for electronic gas sensors", Doctoral Thesis, Toledo University, (2013), U.S.A.
- [181] A. M. Soleimanpour, A. H. Jayatissa and G. Sumanasekera, "Surface and gas sensing properties of nanocrystalline nickel oxide thin films", *Applied Surface Science*, Vol. 276, (2013), 291- 297.
- [182] A. M. Soleimanpour, "Synthesis oxides with gas sensing properties", Doctoral Thesis, Romanian Academy University, (2017), Romania.
- [183] J. Wang, P. Yang, X. Wei and Z. Zhou, "Preparation of NiO two-dimensional grainy films and their high-performance gas sensors for ammonia detection", *Nanoscale Research Letters*, Vol. 10, N. 119, (2015), 1-6.
- [184] C. Wang, "Metal organic chemical vapor deposition of indium oxide for ozone sensing", Doctoral Thesis, Albert-Ludwigs University, (2009), German.
- [185] V. E. Bochenkov and G. B. Sergeev, "Sensitivity, Selectivity and Stability of Gas-Sensitive Metal-Oxide Nanostructures", *Metal Oxide Nanostructures and their Applications*, Vol. 3, (2010), 31-52.
- [186] T. T. Le Dang and M. Tonzzer, "Polycrystalline NiO nanowires: scalable growth and ethanol sensing", *Procedia Engineering*, Vol. 120, (2015), 427- 434.

## References

---

- [187] A. V. Rajgure, "Synthesis and characterization of nanocrystalline ZnO gas sensors", Doctoral Thesis, University of Solapur, (2014), India.
- [188] S. Ozdemir, "Formation, characterization, and flow dynamics of nanostructure modified sensitive and selective gas sensors based on porous silicon", Doctoral Thesis, Georgia Institute of Technology, (2011), U.S.A.
- [189] P. Shankar and J. B. B. Rayappan, "Gas sensing mechanism of metal oxides: The role of ambient atmosphere, type of semiconductor and gases - A review", *Science Letters Journal*, Vol. 126, No. 4, (2015), 1-18.
- [190] A. Singla, "Fabrication of NO<sub>x</sub> gas sensor using Zn<sub>1-z</sub>Ni<sub>z</sub>CO<sub>2</sub>O<sub>4</sub> (z=0.1-1.0) nanoparticles", Master Thesis, National Institute of Technology, (2015), India.
- [191] D. D. Lee and D. S. Lee, "Environmental gas sensors", *IEEE Sensors Journal*, Vol. 1, No. 3, (2001), 214-224.
- [192] J. Mathyan, D. Sivalingam, J. B. Gobalakrishnan and J. B. B. Rayanppan, "Spray coated nanostructured Nickel Oxide thin films for ethanol sensing", *Journal of Applied Sciences*, Vol. 12, No. 16, (2012), 1686-1960.
- [193] K. Christos, "Nanostructured semiconducting Metal Oxides and applications as Gas Sensors: Synthesis, Characterization and Evaluation", Master Thesis, Patras University, (2017), Greece.
- [194] S. Basu and P. K. Basu, "Nanocrystalline Metal Oxides for Methane Sensors: Role of Noble Metals", *Journal of Sensors*, Vol. 2009, (2009), 1-20.
- [195] F. O. Hassni, "Couches minces d' d'oxydes spinelles et de nanocomposites spinelle-CuO a propriétés semiconductrices destinées à la réalisation de capteurs de gaz", Doctorat Thesis, Toulouse University, (2009), France.
- [196] A. Rothschild and Y. Komem, "The effect of grain size on the sensitivity of nanocrystalline metal-oxide gas sensors", *Journal of Applied Physics*, Vol. 95, No. 11, (2004), 6374-6380
- [197] G. Sakai, N. S. Baik, N. Miura and N. Yamazoe, "gas sensing properties of tin oxide thin films fabricated from hydrothermally treated nanoparticles dependence of CO and H<sub>2</sub> response on film thickness", *sensors and Actuators B: Chemical*, Vol. 77, No. 1-2, (2001), 116-121.
- [198] G. Neri, "First Fifty Years of Chemoresistive Gas Sensors", *Chemosensors*, Vol. 3, (2015), 1-20.
- [199] S. R. Nalagem, A. Chougule, S. Sen and V. B. Patil, "Novel method for fabrication of NiO sensor for NO<sub>2</sub> monitoring", *Journal of Materials Science: Materials in Electronics*, Vol. 24, No. 1, (2013), 368-375.
- [200] Y. Zhang, L. Xie, C. Yuan, C. Zhang, S. Liu, Y. Peng, H. Li and M. Zhang, "Preparation of 3D rose-like nickel oxide nanoparticles by electrodeposition method and application in gas sensors", *Journal of Materials Science: Materials in Electronics*, Vol. 27, No. 2, (2016), 1817-1827.
- [201] L. Wang, J. Deng, T. Fei and T. Zhang, "Template-free synthesized hollow NiO-SnO<sub>2</sub> nanospheres with high gas-sensing performance", *Sensors and Actuators B: Chemical*, Vol. 164, No. 1, (2012), 90- 95.
- [202] M. M. Goma, G. Reza Yazdi, M. Rodner, G. Greczynski, M. Boshta, M. B. S. Osman, V. Khranovskyy, J. Eriksson and R. Yakimova, "Exploring NiO nanosize structures for ammonia sensing", *Journal of Materials Science: Materials in Electronics*, Vol. 29, No. 14, (2018), 11870-11877.
- [203] C. Cantalini, M. Post, D. Buso, M. Guglielmi and A. Martucci, "Gas sensing properties of nanocrystalline NiO and Co<sub>3</sub>O<sub>4</sub> in porous silica sol-gel films", *Sensors and Actuators B: Chemical*, Vol. 108, No. 1-2, (2005), 184-192.

## References

---

- [204] H. Steinebach, S. Kannan, L. Rieth and F Solzbacher, "H<sub>2</sub> gas sensor performance of NiO at high temperatures in gas mixtures", *Sensors and Actuators B: Chemical*, Vol. 151, No. 1, (2010), 162-168.
- [205] G. Thangamani, K. Deshmukh, M. B. Ahamed, K.Chidambaram, K.C. Saranya and SK. K. Pasha, "Facile synthesis of Nickel Oxide nanoparticles using solvothermal method and their implementation in sensor applications", *International Journal of ChemTech Research*, (2015), 70-76.
- [206] R. C. Korošec and P. Bukovec, "Sol-Gel prepared NiO thin films for electrochromic applications", *Acta Chimica Slovenica*, Vol. 53, (2006), 136-147.
- [207] S. Capone, A. Forleo, L. Francioso, R. Rella, P. Siciliano, J. Spadavecchia, D. S. Presicce and A. M. Taurino, "Solid state gas sensors: State of the art and future activities", *Optoelectronics and Advanced Materials*, Vol. 5, No. 5, (2003), 1335-1348.
- [208] J. D. Desai, "Nickel oxide thin films by spray pyrolysis". *Journal of Materials Science: Materials in Electronics*, Vol. 27, No. 12, (2016), 12329-12334.
- [209] N. F. A. Shammery, "Optical characteristics of NiO thin film on glass formed by chemical spray pyrolysis", *Journal of Kufa – Physics*, Vol.2, No.1, (2010), 22-27.
- [210] R. Sharma, A. D. Acharya, S.B. Shrivastava, T. Shripathi, V. Ganesan, "Preparation and characterization of transparent NiO thin films deposited by spray pyrolysis technique", *Optik*, Vol. 125, No.22, (2014), 6751-6756.
- [211] R. Barir, B. Benhaoua, S. Benhamida, A. Rahal, T. Sahraoui and R. Gheriani, "Effect of precursor concentration on structural optical and electrical properties of NiO thin films prepared by spray pyrolysis", *Journal of Nanomaterials*, Vol. 2017, (2017), 1-10.
- [212] S. Joishy, and B. V. Rajendra, "Effect of substrate temperature and molarity on optical and electrical properties of mixed structured Zn<sub>0.80</sub>Cd<sub>0.20</sub>O thin films", *Journal of Electronic Materials*, Vol. 47, No. 11, (2018), 6681-6690.
- [213] M.A. Islam, M.S. Hossain, M.M. Aliya, M.M. Aliyu, J. Husna, M.R. Karim, K. Sopian, N. Amin, "Comparison of structural and optical properties of CdS thin films grown by CSVT, CBD and sputtering techniques", *Energy Procedia*, Vol. 33, (2013), 203 - 213.
- [214] N. Khedmi, M. Ben Rabeh, M. Kanzari, "Structural morphological and optical properties of SnSb<sub>2</sub>S<sub>4</sub> thin films grown by Vacuum Evaporation Method", *Journal of Materials Science & Technology*, Vol. 30, (2014),1006-1011.
- [215] P. M. Ponnusamy, S. Agilan, N. Muthukumarasamy, T. S. Senthil, G. Rajesh, M.R. Venkatraman, and D. Velauthapillai, "Structural, optical and magnetic properties of undoped NiO and Fe-doped NiO nanoparticles synthesized by wet-chemical process", *Materials Characterization*, Vol. 114, No. 2, (2016) 166-171.
- [216] N. A. Bakr, S. A. Salman and A. M. Shano, "Effect of Co Doping on Structural and Optical Properties of NiO Thin Films Prepared By Chemical Spray Pyrolysis Method, *International Letters of Chemistry, Physics and Astronomy*", Vol. 2, (2015),15-30.
- [217] S. Hassanien and A. A. Akl, "Optical characteristics of iron oxide thin films prepared by spray pyrolysis technique at different substrate temperatures", *Applied Physics A*, Vol.124, No. 11,(2018), 2-16
- [218] H. Moualkia, S. Hariecha and M. S. Aida, "Structural and optical properties of CdS thin films grown by chemical bath deposition", *Thin Solid Films*, Vol. 518, (2009), 1259-1262.
- [219] S. Chandramohan, A. Kanjilal, J. K. Tripathi, S. N.Sarangi, R. Sathyamoorthy, and T. Som, "Structural and optical properties of Mn-doped CdS thin films prepared by ion implantation", *Journal of Applied Physics*, Vol. 105, No. 12, (2009), 1-4.
- [220] P. S. Patil and L. D. Kadam, "Preparation and characterization of spray pyrolyzed nickel oxide (NiO) thin films", *Applied surface science*, Vol. 199, (2002), 1-4.
- [221] J. E. Dominguez, L. Fu, and X. Q. Pana, "Effect of crystal defects on the electrical prop-

## References

---

- erties in epitaxial tin dioxide thin films", *Applied Physics Letters*, Vol. 81, No. 27, (2002), 5168-5170.
- [222] R. Charma, A.D. Acharya, S. Moghe, B. Shrivastava, M. Gangrade, V. Shripathi, V. Ganesan, "Effect of cobalt doping on microstructural and optical properties of nickel oxide thin films", *Materials Science in Semiconductor Processing*, Vol. 23, (2014), 42-49.
- [223] M. Ghougali, O. Belahssen, A. Chala, "Structural, optical and electrical properties of NiO nanostructure thin film", *Journal of Nano-and Electronic Physics*, Vol. 8, No. 4, (2016), 1-4
- [224] M. Ghougali, O. Belahssen, A. Chala, "Effect of annealing in physical properties of NiO nanostructure thin film", *Journal of Nano-and Electronic Physics*, Vol. 9, No. 3, (2017), 1-3.
- [225] P. S. Patil, L. D. Kadam, "Preparation and characterization of spray pyrolyzed nickel oxide (NiO) thin films", *Applied surface science*, Vol. 199, No. 1-4, (2002), 211-221.
- [226] R. D. Shannon, "Revised effective ionic radii and systematic studies of interatomic distances in halides and chalcogenides", *Acta Crystallographica Section A*, Vol. 32, No. 5, (1976), 751-767.
- [227] N. A. Bakr, S. A. Salman and A. M. Shano, "Effect of Co doping on structural and optical properties of NiO thin films prepared by chemical spray pyrolysis method", *International Letters of Chemistry, Physics and Astronomy*, Vol. 41, ( 2015),15-30.
- [227] D. Sathisha and K. G. Naik, "Synthesis and characterization of cobalt doped nickel oxide thin films by spray pyrolysis method", *American Institute of Physics AIP Conference Proceedings*. 1953, (2018), 1-4.
- [228] L. J. Kennedy, P. Magesan, J. J. Vijaya, M. Umapathy and U. Aruldoss, "Biomaterials doped nanocrystalline nickel oxide as efficient humidity, sensor: A green approach", *Materials Science and Engineering: B*, Vol.190, (2014), 13-20.
- [229] D. Nečas, and P. Klapetek, "Gwyddion: an open-source software for SPM data analysis", formerly *Central European Journal of Physics*, Vol. 10, No. 1, (2012), 181-188.
- [230] H. Gao, and T.Qiang, "Fracture Surface Morphology and Impact Strength of Cellulose/PLA Composites", *Materials*, Vol. 10, (2017), 1-11.
- [231] M. N. Armenise, C. E. Campanella, C. Ciminelli, F. Dell'Olio and V. M. N. Passaro, "Phononic and photonic band gap structures: modelling and applications", *Physics Procedia*, Vol. 3, (2010), 357-364.
- [232] O. K. Ukoba, F. Inambao and A. E. Eboka, "Influence of annealing on properties of spray deposited nickel oxide films for solar cells", *Energy Procedia*, Vol. 142, (2017), 244-252.
- [233] M. Ghougali , O. Belahssen, A. Chala, "Effect of iron doping on physical properties of NiO thin films", *Journal of Nano-Electron. Physics*, Vol. 10, No. 2, (2018), 1-4.
- [234] H. Soonmin, "Preparation and Characterization of Nickel Oxide Thin Films: A review ", *International Journal of Applied Chemistry*, Vol. 12, No. 2, (2016), 87-93.
- [235] S. I. Abbas and A. Q. Ubaid, "Structural, optical and photoluminescence properties of nanocrystalline NiO thin films", *Journal of Advances in physics*, Vol. 6, No.1, (2014),1016-1023.
- [236] C. Lokhande, K. Gadave, "Chemical deposition of MnS thin films from thiosulphate bath", *Turkish Journal of Physics*, Vol.18, (1994), 83-87.
- [237] F. Al-Shaikley, "Electrical and optical properties dependence on annealing temperature for CdS thin films", *Indian Journal of Applied. Research*, Vol. 3, (2013), 544-548.
- [238] W. Zhang, S. H. Brongersma, T. Clarysse, V. Terzieva, E. Rosseeel, W. Vandervorst and K. Maex, "Surface and grain boundary scattering studied in beveled polycrystalline thin copper films", *Journal of Vacuum Science & Technology B: Microelectronics and Nanometer Structures*, Vol.22, No. 4, (2004), 1830-1833.
- [239] F. D. Paraguay, L. W. Estrada, N. D. R. Acosta, E. Andrade, M. M. Yoshida, "Growth,

## References

---

structure and optical characterization of high quality ZnO thin films obtained by spray pyrolysis", *Thin Solid Films*, Vol. 350, (1999), 192-202 .

[240] J. D. Bayan and D. R. Gametin, "Doped semiconductor nanocrystals: synthesis, characterization, physical properties and applications", *Progress in Inorganic chemistry*, Vol. 47, (2005), 47-126.

[241] L. Znaidi, T. Touam, D. Vrel, N. Souded, S. Ben Yahia, O. Brinza, A. Fischer, and A. Boudrioua, "AZO thin films by Sol-Gel process for integrated optics", *Coatings*, Vol. 3, (2013) 126-139.

[242] S. Ilican, M. Caglar and Y. Caglar, "Determination of the thickness and optical constants of transparent indium-doped ZnO thin films by the envelope method", *Materials Science-Poland*, Vol. 25, No. 3, (2007), 709-718.

[243] A. K. Zak, W. H. A. Majid, M. E. Abrishami and R. Yousefi, "X-ray analysis of ZnO nanoparticles by Williamson-Hall and size-strain plot methods", *Solid State Sciences*, Vol. 13, (2011), 251-256.

[244] Y. Taraka Prabhu, K. V. Rao, V. S. S. Kumar and B. S. Kumari, "X-Ray Analysis by Williamson-Hall and Size-Strain Plot Methods of ZnO Nanoparticles with Fuel Variation", *World Journal of Nano Science and Engineering*, Vol. 4, (2014), 21-28.

[245] T. S. Moss, "The interpretation of the properties of indium antimonide", *Proceedings of the Physical Society. Section B*, Vol. 67, No. 10, (1954), 775-782.

[246] E. Burstein, "Anomalous optical absorption limit in InSb", *Physical Review*, Vol. 93, No. 3, (1954), 632-633.

[247] A. P. Roth and D. F. Williams, "Properties of zinc oxide films prepared by the oxidation of diethyl zinc", *Journal of Applied Physics*, Vol. 52, No. 11, (1981), 6685-6692.

[248] E. Avendaño, L. Berggren, G.A. Niklasson, C.G. Granqvist and A. Azens, "Electrochromic materials and devices: brief survey and new data on optical absorption in tungsten oxide and nickel oxide films", *Thin Solid Films*, Vol. 496, (2006) 30-36.

[249] M. Ben Amor, A. Boukhachem, K. Boubaker and M. Amlouk, "Structural, optical and electrical studies on Mg-doped NiO thin films for sensitivity applications", *Materials Science in Semiconductor Processing*, Vol. 27, (2014), 994-1006.

[250] X. Chen, L. Zhao and Q. Niu, "Electrical and Optical Properties of p-Type Li,Cu-Codoped NiO Thin Films", *Journal of Electronic Materials*, Vol. 41, No. 12, (2012), 3382-3386.

[251] G. D. Cody, T. Tiedje, B. Abeles, T. D. Moustakas, B. Brooks and Y. Goldstein, "Disorder and the optical-absorption edge of Hydrogenated amorphous Silicon", *Physical Review Letters*, Vol. 47, No. 20, (1981) 1480-1483.

[252] S. Benramache, A. Rahal and B. Benhaoua, "The effects of solvent nature on spray-deposited ZnO thin film prepared from Zn (CH<sub>3</sub>COO)<sub>2</sub>, 2H<sub>2</sub>O", *Optik*, Vol. 125, (2014), 663-666.

[253] S. Nandy, B. Saha, M. K. Mitra and K. K. Chattopadhyay, "Effect of oxygen partial pressure on the electrical and optical properties of highly (200) oriented p-type Ni<sub>1-x</sub>O films by DC sputtering", *Journal of Materials Science*, Vol. 42, (2007), 5766-5772.

[254] M. Jlassi, I. Sta, M. Hajji and H. Ezzaouia, "Optical and electrical properties of nickel oxide thin films synthesized by sol-gel spin coating", *Materials Science in Semiconductor Processing*, Vol. 21, (2014), 7-13.

[255] H. L. Chen, Y. M. Lu and W. S. Hwang, "Thickness dependence of electrical and optical properties of sputtered Nickel oxide films", *Thin Solid Films*, Vol. 514, (2006), 361-365.

[256] A. Thakur, "Exploring pure and modified ZnO nanoflowers based acetone and Ethanol Gas Sensors", *Master Thesis, International Institute of Information Technology Hyderabad*, (2019), India

## References

---

- [257] T. Seesaard, P. Lorwongtragool and T. Kerdcharoen, "Development of fabric-based chemical gas sensors for use as wearable electronic noses", *Sensors*, Vol. 15, (2015), 1885-1902.
- [258] V. Aroutiounian, Z. Adamyan, A. Sayunts, E. Khachatryan, A. Adamyan, K. Hernadi, Z. Nemeth and P. Berki, "Comparative Study of VOC sensors based on ruthenated MWCNT/SnO nanocomposites", *International Journal of Emerging Trends in Science and Technology*, Vol. 1, No. 8, (2014), 1309-1319.
- [259] M. Parmar and K. Rajanna, "Copper (II) oxide thin film for methanol and ethanol sensing", *International Journal on Smart Sensing and Intelligent Systems*, Vol. 4, No. 4, (2011), 710-725.
- [260] A. Malinowski and D. dan Wardzińska, "Catalytic conversion of furfural towards fuel Biocomponents", *CHEMIK*, Vol. 66, No. 9, (2012), 982-990.
- [261] J. H. Lee, "Gas sensors using hierarchical and hollow oxide nanostructures: Overview", *Sensors and Actuators B: Chemical*, Vol. 140 (2009), 319-336.
- [262] L. Wang, J. Deng and T. Fei, "Tong Zhang, Template-free synthesized hollow NiO-SnO<sub>2</sub> nanospheres with high gas-sensing performance", *Sensors and Actuators B: Chemical*, Vol. 164, (2012), 90-95.
- [263] W. Zeng, B. miao, L. lin and J. xie, "Facile synthesis of NiO nanowires and their gas sensing performance", *Transactions of Nonferrous Metals Society of China*, Vol. 22, (2012), 100-104.
- [264] J. A. Dirksen, K. Duval, and T. A. Ring, "NiO thin-film formaldehyde gas sensor", *Sensors and Actuators B: Chemical*, Vol. 80, No. 2, (2001), 106-115.
- [265] L. Wang, Z. Lou, T. Fei, and T. Zhang, "Enhanced acetone sensing performances of hierarchical hollow Au-loaded NiO hybrid structures", *Sensors and Actuators B: Chemical*, Vol. 161, No. 1, (2012), 178-183.
- [266] C. Wang, J. Liu, Q. Yang, P. Sun, Y. Gao, F. Liu and G. Lu, "Ultrasensitive and low detection limit of acetone gas sensor based on W-doped NiO hierarchical nanostructure", *Sensors and Actuators B: Chemical*, Vol. 220, (2015) 59-67.
- [267] J. Qin, Z. Cui, X. Yang, S. Zhu, Z. Li and Y. Liang, "Synthesis of three-dimensionally ordered macroporous LaFeO<sub>3</sub> with enhanced methanol gas sensing properties", *Sensors and Actuators B: Chemical*, Vol. 209, (2015), 706-713.
- [268] Q. Tan, J. Fang, W. Liu, J. Xiong, and W. Zhang, "Acetone sensing properties of a gas sensor composed of carbon nanotubes doped with iron oxide nanopowder", *Sensors*, Vol. 15, No. 11, (2015), 28502-28512.
- [269] M. Y. Chuang, Y. T. Lin, T. W. Tung, L. Y. Chang, H. W. Zan and H. F. Meng, "Room-temperature-operated organic-based acetone gas sensor for breath analysis", *Sensors and Actuators B: Chemical*, Vol. 260, (2018), 593-600.
- [270] T. F. Du, Y. M. Zhang, J. Zhang, Z. Q. Zhu, and Q. J. Liu, "High Sensitive and Selective Acetone Gas Sensor Using Molecular Imprinting Technique Based on Ag-LaFeO<sub>3</sub>", *Materials Science Forum*, Vol. 852, (2016), 760-765.
- [271] J. W. Yoon, H. J. Kim, I. D. Kim and J. H. Lee, "Electronic sensitization of the response to C<sub>2</sub>H<sub>5</sub>OH of P-Type NiO nanofibers by Fe doping", *Nanotechnology*, Vol. 24, (2013), 44405-44412.
- [272] C. Wang, J. Liu, Q. Yang, P. Sun, Y. Gao, F. Liu, J. Zheng and G. Lu, "Ultrasensitive and Low Detection Limit of Acetone Gas Sensor Based on W-Doped NiO Hierarchical Nanostructure", *Sensors and Actuators B: Chemical*, Vol. 220, (2015), 59-67.
- [273] G. Thangamani, K. Deshmukh, M. B. Ahamed, K. Chidambaram, K. C. Saranya and SK. K. Pasha, "Facile Synthesis of Nickel Oxide Nanoparticles using Solvothermal Method and Their implementation in Sensor Applications, *International Journal of ChemTech Research*", Vol. 8, No. 5, (2015), 70-76.

## References

---

- [274] Z. Changhui, F. Jiecai, Z. Zhenxing and X. Erqing, "Enhanced ethanol sensing performance of porous ultrathin NiO nanosheets with neck-connected Networks, RSC Advances", Vol. 3, (2013), 4018-4023.
- [275] Y. Zhang, L. Z. Xie, , H. R. Li, P. Wang, S. Liu, Y. Q. Peng and M. Zhang, "Facile Synthesis of Rose-Like NiO Nanoparticles and Their Ethanol Gas-Sensing Property", Chinese Physics Letters, Vol. 32, No. 9, (2015), 1-4.
- [276] C. Wang, X. Cui, J. Liu, X. Zhou, X. Cheng, P. Sun, G. Lu, "Design of Superior Ethanol Gas Sensor Based on Al-Doped NiO Nanorod-Flowers", ACS Sensors", Vol. 1, No. 2, (2015), 131-136.
- [277] N. Chen, Q. Li, Y. Li, D. Deng, X. Xiao and Y. Wang, "Facile Synthesis and Gas Sensing Performances Based on Nickel Oxide Nanoparticles/Multi-Wall Carbon Nanotube Composite", Journal of Materials Science: Materials in Electronics, Vol. 26, (2015), 8240-8248.
- [278] X. Sun, X. Hu, Y. Wang, R. Xiong, X. Li, J. Liu, H. Ji, X. Li, S. Cai and C. Zheng, "Enhanced Gas-Sensing Performance of Fe-Doped Ordered Mesoporous NiO with Long-Range Periodicity", The Journal of Physical Chemistry C, Vol. 119, (2015), 3228-3237.
- [279] RAE Systems by Honeywell 877-723-2878, "Guide to atmospheric testing in confined spaces", [www.raesystems.com](http://www.raesystems.com).
- [280] MSA, The Safety Company, "Gas Detection Handbook", fifth edition, ID 5555-312-MC /Aug 2007, [www.msagasdetection.com](http://www.msagasdetection.com).
- [281] RIKEN KEIKI Co. Ltd., "Gas Detection Hand book", TDEO 109-0, Tokyo, 174-9744 (Japan), [www.rikenkeiki.co.jp](http://www.rikenkeiki.co.jp)

## ABSTRACT

This work has been based on the chemical spray pyrolysis technique, it is a very attractive method, that for its ease and low cost on the one hand and the quality of the films prepared by it on the other hand, it is used to produce thin films for different applications including the most important (MOS)-based gas sensors, Such as (NiO)-based gas sensors. At first, a comprehensive study is presented on the effect of deposition parameters on the structural, optical and electrical properties of undoped and Co and Cu-doped (NiO) thin films; the finest samples obtained are then used in the sensor to study their sensing performance for some Volatile organic gases such as ethanol, acetone and methanol. In the following we summarize the most important results obtained:

- The XRD patterns showed that the structure of the undoped and doped NiO films is polycrystalline structure with the preferred direction (111) also showed that there was no significant shift in the direction of diffraction peaks after doping with cobalt or copper. The crystalline size (D) is increased by thermal annealing and decreases by increasing the doping in the (NiO) samples. From the transmittance spectra, for all samples it was observed that the optical transparency values were moderate to relatively weak, it decrease by thermal annealing, by increasing the molar concentration of the precursor solution, or by increasing the percentage of doping with cobalt or copper. Cobalt or copper doping was also found to be decreasing the band gap energy for the above mentioned reasons, and its values ranged from 3.86 to 3.64 eV for undoped NiO films. For doped films, it ranged between 3.61 and 3.48 eV to cobalt doped films and between 3.60 and 3.43 eV to copper doped films. It was observed that the electrical conductivity of all samples is good and it is the P-type and it has been shown to increase by thermal annealing or by increasing the proportion of doping with cobalt or copper in general, and its value exceeded ( $0.29 \Omega^{-1} \cdot \text{cm}^{-1}$ ) when doped By 12 at.% of Copper.
- Five samples were selected from the prepared samples to study their sensing performance towards ethanol, acetone and methanol vapors, where all films had high ohmic resistance. Optimum operating temperatures, sensitivity, selectivity and detection limits were determined to the gas-based sensor.

**Keywords:** Spray Pyrolysis Technique (SPT); NiO Thin Films; Metal-Oxide-Semiconductors (MOS); Gas Sensor; Sensing Mechanism in (MOS).

## Résumé

Ce travail est basé sur la technique de la pyrolyse chimique par pulvérisation, c'est une méthode très attrayante en raison de sa simplicité et de son faible coût d'une part, et la qualité des films préparés d'autre part, qui lui permet de produire des films minces pour différentes applications, les plus importantes étant les capteurs de gaz à base de (MOS), tels que les capteurs de gaz à base (NiO). Au début, une étude complète est présentée sur l'effet des paramètres de dépôt sur les propriétés structurales, optiques et électriques des couches minces de (NiO) non dopées et dopées au Co et au Cu ; Les échantillons les plus fins obtenus sont puis utilisées dans le capteur pour étudier leurs performances de détection de certains gaz organiques volatils tels que l'éthanol, l'acétone et le méthanol. Nous résumons ci-dessous les principaux résultats obtenus:

- Les diagrammes XRD ont montré que la structure des films de NiO non dopés et dopés est polycristalline avec la direction préférée (111), a également montré qu'il n'y avait pas de décalage significatif dans la direction des pics de diffraction après dopage au cobalt ou au cuivre. La taille cristalline (D) est augmentée par recuit thermique et diminue en augmentant le dopage dans les échantillons (NiO). A partir des spectres de transmittance, il a été observé pour tous les échantillons que les valeurs de transparence optique étaient modérées à relativement faibles, elle diminuait par recuit thermique, en augmentant la concentration molaire de la solution de précurseur ou en augmentant le pourcentage de dopage au cobalt ou au cuivre. Il a également été constaté que le dopage au cobalt ou au cuivre diminuait l'énergie de la bande interdite pour les raisons susmentionnées, et que ses valeurs allaient de 3.86 à 3.64 eV pour les films de NiO non dopés. Pour les films dopés, il a varié entre 3,61 et 3.48 eV pour les films dopés au cobalt et entre 3.60 et 3.43 eV pour les films dopés au cuivre. Il a été observé que la conductivité électrique de tous les échantillons est bonne et qu'il s'agit du type p; il a été démontré qu'elle augmentait par recuit thermique ou par augmentation de la proportion de dopage au cobalt ou au cuivre en général, et sa valeur dépassait ( $0.29 \Omega^{-1} \cdot \text{cm}^{-1}$ ) lorsqu'il est dopé par 12 at.% de cuivre.
- Cinq échantillons ont été sélectionnés parmi les échantillons préparés pour étudier leurs performances de détection vers les vapeurs d'éthanol, d'acétone et de méthanol, où tous les films présentaient une résistance ohmique élevée. Les températures de fonctionnement, la sensibilité, la sélectivité et les limites de détection optimales ont été déterminées pour le capteur à base de gaz.

**Mots-clés:** Technique de Pyrolyse par Pulvérisation (SPT); Couches Minces de NiO; Semi-Conducteurs des Oxydes Métallique (MOS); Détecteur de Gaz; Mécanisme de Détection dans (MOS).

## الملخص

لقد استند هذا العمل على تقنية الانحلال الكيميائي الحراري بالرش فهي طريقة جذابة للغاية، و ذلك لسهولةها و وقلة تكلفتها من جهة و جودة الأفلام المحضرة بها من جهة أخرى، فهي تستخدم لإنتاج أغشية رقيقة من أجل تطبيقات مختلفة من أهمها أجهزة استشعار الغاز القائمة على (MOS)، مثل أجهزة استشعار الغاز القائمة على أكسيد النيكل (NiO). في البداية، يتم تقديم دراسة شاملة حول تأثير معلمات الترسيب على الخصائص الهيكلية والبصرية والكهربائية للأغشية الرقيقة من أكسيد النيكل (NiO) غير المطعمة (النقية) و المطعمة بالكوبالت والنحاس؛ ثم تستخدم أجود العينات التي تم الحصول عليها في جهاز الاستشعار لدراسة أدائها الاستشعاري عن بعض الغازات (الأبخرة) العضوية المتطايرة مثل الإيثانول والأسيتون والميثانول. في ما يلي نلخص أهم النتائج التي تم الحصول عليها:

- أظهرت أنماط حيود الأشعة السينية (XRD) أن بنية أفلام أكسيد النيكل (NiO) غير المطعمة و المطعمة متعددة التبلور ذات الاتجاه المفضل (111) و أوضحت أيضا أنه ليس هناك تحولا كبيرا في توجهات قمم الانعراج بعد التطعيم باستخدام الكوبالت (Co) أو النحاس (Cu). كما أن القدر الحبيبي (D) يزداد بالتلدين الحراري و يتناقص بزيادة نسبة التطعيم في عينات أكسيد النيكل (NiO). من أطيايف النفاذية، لوحظ أن قيم الشفافية الضوئية متوسطة إلى ضعيفة نسبيا بالنسبة لجميع العينات، وهي تتناقص بالتلدين الحراري أو بزيادة التركيز المولي لمحلول السلائف أو بزيادة نسبة التطعيم بالكوبالت (Co) أو بالنحاس (Cu). و قد وجد أيضا أن طاقة الفجوة تتناقص للأسباب السالفة الذكر، و قد تراوحت قيمها بين (3.86 eV و 3.64 eV) بالنسبة لأفلام أكسيد النيكل (NiO) غير المطعمة، أما بالنسبة للأفلام المطعمة فقد تراوحت بين (3.61 eV و 3.48 eV) للأفلام المطعمة بالكوبالت و بين (3.60 eV و 3.43 eV) بالنسبة للأفلام المطعمة بالنحاس. وقد لوحظ أن الناقلية الكهربائية لجميع العينات جيدة و هي من النوع P و تبين أنها تزداد بالتلدين الحراري أو بزيادة نسبة التطعيم بالكوبالت (Co) أو النحاس (Cu) عموما، و قد تعدت قيمتها ( $0.29 \Omega^{-1}.cm^{-1}$ ) عند التطعيم بنسبة (12 at.%) من النحاس (Cu).
- تم اختيار خمس عينات من بين العينات المحضرة من أجل دراسة أدائها الاستشعاري تجاه بخار الإيثانول و الأستون و الميثانول حيث تُحقق من أن لجميع الأفلام مقاومة أومية عالية، وقد تم تحديد درجات حرارة التشغيل المثلى و حساسية و انتقائية و حدود الكشف للمستشعر الغازي المعتمد عليها.

**الكلمات المفتاحية:** تقنية الانحلال الحراري بالرش (SPT)؛ أفلام أكسيد النيكل (NiO) الرقيقة؛ أشباه موصلات الأكاسيد المعدنية (MOS)؛ مستشعر الغاز؛ آلية الاستشعار في (MOS).

# Publications

## Structural, Optical and Electrical Properties of NiO Nanostructure Thin Film

M. Ghougali<sup>1,2,3</sup>, O. Belahssen<sup>1,2,\*</sup>, A. Chala<sup>1,2</sup>

<sup>1</sup> Material Sciences Department, Faculty of Science, University of Biskra, Algeria

<sup>2</sup> Physic Laboratory of Thin Films and Applications (LPCMA), University of Biskra, Algeria

<sup>3</sup> Laboratory of exploitation and valorization the azalea energetics sources (LEVRES), Faculty of exact Science, University of El-Oued, Algeria

(Received 17 July 2016; revised manuscript received 19 December 2016; published online 23 December 2016)

Nickel oxide was deposited on highly cleaned glass substrates using spray pneumatic technique. The effect of precursor molarity on structural, optical and electrical properties has been studied. The XRD lines of the deposited NiO were enhanced with increasing precursor molarity due to the improvement of the films crystallinity. It was shown that the crystalline size of the deposited thin films was calculated using Debye-Scherrer formula and found in the range between 9 and 47 nm. The optical properties have been discussed in this work. The absorbance ( $A$ ), the transmittance ( $T$ ) and the reflectance ( $R$ ) were measured and calculated. Band gap energy is considered one of the most important optical parameter, therefore measured and found ranging between 3.64 and 3.86 eV. The NiO thin film reduces the light reflection for visible range light. The increase of the electrical conductivity to maximum value of  $0.0896 (\Omega \text{ cm})^{-1}$  can be explained by the increase in carrier concentration of the films. A good electrical conductivity of the NiO thin film is obtained due to the electrically low sheet resistance. NiO can be applied in different electronic and optoelectronic applications due to its high band gap, high transparency and good electrical conductivity.

**Keywords:** NiO thin films, XRD, Optical constants, Electrical conductivity.

DOI: [10.21272/jnep.8\(4\(2\)\).04059](https://doi.org/10.21272/jnep.8(4(2)).04059)

PACS numbers: 73.61. – r, 78.20. – e,  
78.66. – w

### 1. INTRODUCTION

Nickel oxide (NiO) is the most investigated metal oxide and it has attracted considerable attention because of its low cost material, and also for its applications in several fields such as a catalyst, transparent conducting oxide, photodetectors, electrochromic, gas sensors, photovoltaic devices, electrochemical supercapacitors, heat reflectors, photo-electrochemical cell, solar cells and many opto- electronic devices [1-7]. NiO is an IV group and it can be used as a transparent p-type semiconductor layers, it has a band gap energy ranging from 3.45 eV to 3.85 eV [8]. Band gap energy is significant to adjust the energy level state of NiO.

The reduction in particle size to nanometer scale results more interesting prosperities in compared with their bulk properties [9]. Therefore, there are several techniques have been used for synthesis and manipulation of nanostructures NiO such as the thermal evaporation, sputtering, pulse laser ablation, thermal decomposition, electrochemical deposition and sol-gel methods etc. Among of these techniques, sol-gel has some advantages such as high purity of raw materials and a homogeneous solution hence easy control over the composition of the deposited films. In this work, a low cost sol-gel/spray pneumatic technique was used to prepare pure NiO nanoparticles thin films with various precursor concentrations. The structural properties of the produced nickel oxide thin films have been examined. The absorption, transmittance and reflectance spectra of the produced thin films for the NiO are also measured in range between 300-1100 nm. Moreover, the optical band gap is determined as a function of the precursor concentrations.

### 2. EXPERIMENTAL DETAILS

#### 2.1 Preparation of Samples

NiO thin films were prepared onto a highly cleaned glass substrates using sol-gel spray pneumatic technique. Nickel nitrate was dissolved in 50ml of water as a solvent and chloride acid was used as a stabilizer for the all samples in this work. The produced mixture (Sol) was stirred at 60 °C for 2 h in order to obtain a clear and homogenous solution then the mixture was cooled down at room temperature and placed at dark environment for 48 h to have the final (Gel). The glass substrates were cleaned by detergent and by alcohol mixed with deionized water.

#### 2.2 Deposition of Thin Films

The coating was dropped into glass substrates at 480 °C that sprayed during 2 min by pneumatic nebulizer system which transforms the liquid to a stream formed with uniform and fine droplets, followed by the films dried on hot plate at 120 °C for 10 min in order to evaporate the solvent.

#### 2.3 Devices and Measurements

The X-ray diffraction (XRD) spectra of the NiO were measured to verify the structure. X-ray diffraction (XRD) was measured by using BRUKER-AXS-8D diffractometer with Cu K $\alpha$  radiation ( $\lambda = 1.5406 \text{ \AA}$ ) operated at 40 KV and 40 mA in the scanning range of ( $2\theta$ ) between 20° and 80°. The spectral dependence of the NiO transmittance ( $T$ ) and the absorbance ( $A$ ), on

\* [belahssenokba@gmail.com](mailto:belahssenokba@gmail.com)

the wavelength ranging 300-1100 nm are measured using an ultraviolet-visible spectrophotometer (Perkin-Elmer Lambda 25). The reflectance ( $R$ ) was calculated by the well-known equation as ( $T + R + A = 1$ ). Whereas the electrical conductivity of the films was measured in a coplanar structure of four golden stripes on the deposited film surface; the measurements were performed with Keithley model 2400 low voltage source meter instrument.

### 3. RESULTS AND DISCUSSIONS

#### 3.1 Structural Properties

Fig. 1 shows the spectra of the grown NiO nanoparticles with 4 XRD lines, showing the broadening of the line which is a characteristic of the formation of nanoparticles. The X-ray diffraction was used in this work in order to understand the structure of the deposited NiO thin films with different precursor concentrations.

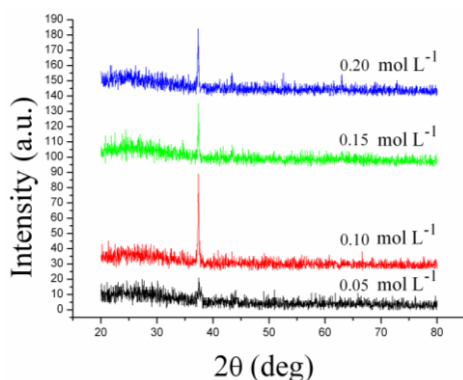


**Fig. 1** – XRD patterns of the deposited NiO thin films on glass substrate at different precursor concentrations

The indexed peak (111) at  $2\theta = 37.1^\circ$  correspond to

the cubic structure of NiO nanoparticles which are consistent with the JCPDS (No.47-1049). Figure shows that the diffraction intensity increased for precursor molarity  $0.10 \text{ mol L}^{-1}$ ; it shows that the best crystalline quality of the film is achieved for this precursor molarity. The crystalline size was calculated using Debye-Scherrer formula [10]:

$$D = \frac{0,9\lambda}{\beta \cos \theta} \quad (1)$$

where  $\lambda$  is the wavelength of the X-rays used ( $1.5406 \text{ \AA}$ ),  $\beta$  is the full width at half maximum (FWHM) and  $\theta$  is the diffraction angle.

The increasing of the diffraction peaks may indicate to the resulted of the NiO in good crystallinity [11]. The crystallite size of the NiO thin films were calculated using the well-known Debye-Scherer's formula Eq. (3.1), the average of the NiO thin films ranging between 9.72 and 46.62 nm. The changing in the crystallites size leads to the changes in optical properties i.e. band gap energy increased with decreasing crystallites size as shown in Fig. 2.

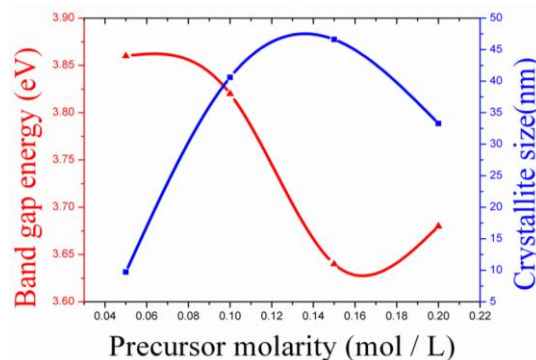


**Fig. 2** – The variation of crystallite size and band gap energy NiO thin films as a function of the precursor molarity

**Table 1** – Structural, optical and electrical parameters of NiO thin film at different precursor molarity

Precursor molarity ( $\text{mol L}^{-1}$ )	Crystallite size (nm)	Band gap energy (eV)	Conductivity ( $\Omega \text{ cm}$ ) <sup>-1</sup>
0.05	9,72	3,86	0.03306
0.10	40,61	3,82	0.08961
0.15	46,62	3,64	0.04125
0.20	33,29	3,68	0.00698

#### 3.2 Optical Properties

Fig. 3 shows the optical absorption spectra of NiO nanoparticles. The absorption edge of  $0.05 \text{ mol/L}$  was found to be at  $326 \text{ nm}$  and of  $0.20 \text{ mol/L}$  was found to be at  $343 \text{ nm}$ . The absorption spectra of  $0.05 \text{ mol/L}$  show that the absorption edge is slightly shifted towards shorter wavelength when compared to other precursor concentration. The absorption edge of a degenerate semiconductor is shifted to shorter wavelengths with increasing carrier concentration. This shift predicts that there is an increase in band gap value ( $E_g = 3.86 \text{ eV}$ ), which is due to the reduction in particle size ( $D = 9.72 \text{ nm}$ ). The fundamental absorption, which corresponds to the electron transition from the valance band to the conduction band, can be used to determine

the nature and value of the optical band gap. The optical absorption study was used to determine the optical band gap of the nanoparticles, which is the most familiar and simplest method.

The absorption coefficient ( $\alpha$ ) and the incident photon energy ( $h\nu$ ) are related by the expression [12]:

$$(\alpha h\nu) = C(h\nu - E_g)^n \quad (2)$$

where  $\alpha$  is the absorption coefficient,  $C$  is a constant,  $h\nu$  is the photon energy,  $\nu$  is the frequency of the incident radiation,  $h$  is the Planck's constant, exponent  $n$  is 0.5 for direct band allowed transition ( $h\nu = 1239/\lambda(\text{nm})^\circ(\text{eV})$ ) and  $E_g$  the band gap energy of the semiconductor.

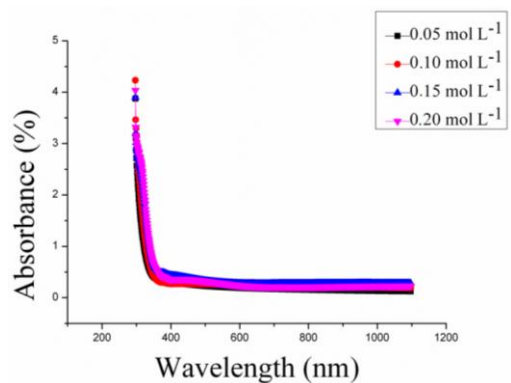


Fig. 3 – Absorbance spectra of NiO samples for different precursor molarity

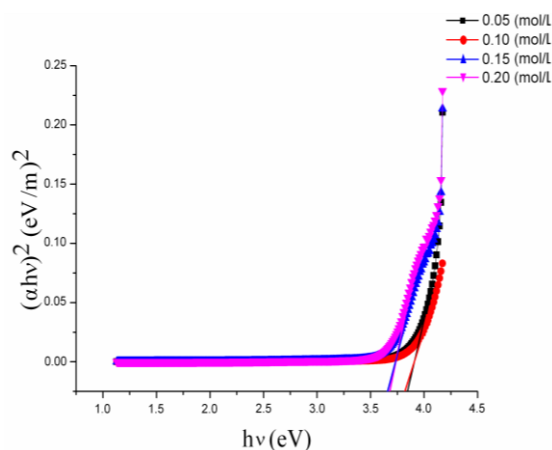


Fig. 4 – Plot of  $(\alpha hv)^2$  versus incident photon energy ( $h\nu$ ) of NiO nanoparticles

As it was shown in (Fig. 4) a typical variation of  $(\alpha hv)^2$  as a function of photon energy ( $h\nu$ ) of NiO nanoparticles Eq. (2), used for deducing optical band gap  $E_g$ . The optical band gap values have been determined by extrapolating the linear portion of the curve to meet the energy axis ( $h\nu$ ) [13]. The band gap values were given in Table 1.

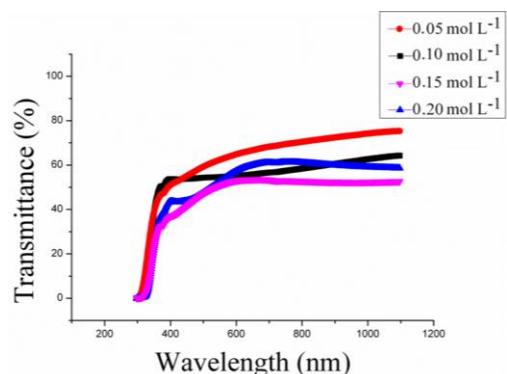


Fig. 5 – Transmission spectra of NiO samples for different precursor molarity

For a transmittance study (Fig. 5), the NiO layer showed very high transmittance of 75.36 %, averaged in the wavelength ( $\lambda$ ) of 300-1100 nm. Suppression of light

reflection at a surface is an important factor to absorb more photons in semi-conductor materials. We obtained the reflectance profiles of NiO-coated (Fig. 6). The averaged reflectance values (300-1100 nm) were significantly lower than 0.203 %. Moreover, NiO-coating drives a substantially suppressed reflectance under 0.20 % in  $500 \text{ nm} < \lambda < 1100 \text{ nm}$ . This notifies that the NiO-coating is an efficient design scheme to introduce the incident light into substrate.

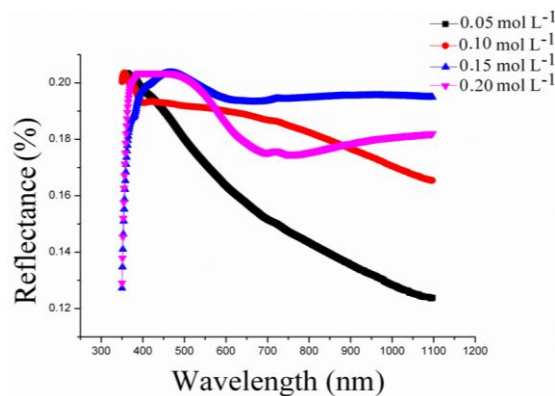


Fig. 6 – Reflectance profiles of NiO thin film for different precursor molarity

### 3.3 Electrical Properties

The electrical properties of the NiO films are summarized in Table 1. Fig. 7 shows the variation of the electrical conductivity  $\sigma$  of NiO thin films as a function as precursor molarity. As can be seen, deposited films have good conductivity. The maximum recorded value was  $0.0896 (\Omega \text{ cm})^{-1}$  for the NiO thin film deposited using the molarity  $0.10 \text{ mol L}^{-1}$ . The increase of the electrical conductivity can be explained by the increase in the carrier concentration. Patil et al. [14] have reported that the increase of the electrical conductivity is due to the increase in activation energy with increasing film thickness. This was explained by difference in the experimental conditions of spraying solution, spray rate and cooling of the substrates during decomposition. However, with  $0.10 \text{ mol L}^{-1}$  precursor molarity, the crystal structure of the film is significantly improved and the grain size is increased, leading to a reduced concentration of structural defects such as dislocations and grain boundaries. Thus, the decrease of the concentration of crystal defects leads in the increase of free carrier concentration. The improvement of crystal quality reduces the carrier scattering from structural defects, leading to higher mobility.

## 4. CONCLUSION

The spray pneumatic technique has been successfully employed to deposit NiO thin films with different concentrations precursor on glass substrates. All the films showed cubic crystal structure with preferential orientation according to the direction (111). The maximum crystallite size was found (46.62 nm). We have observed an improvement in the films crystallinity at  $0.10 \text{ mol L}^{-1}$  precursor molarity where the peak at position

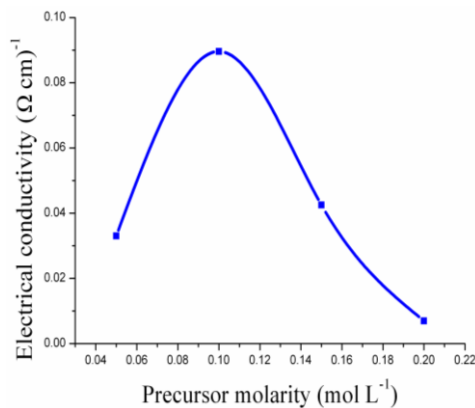


**Fig. 7** – Variation of the electrical conductivity of NiO thin films with the precursor molarity

37.1° corresponding to the (111) planes is very sharp, the film obtained at this concentration has higher and sharper diffraction peak indicating an improvement in

## REFERENCES

1. M.A. Abbasi, Z.H. Ibupoto, A. Khan, O. Nur, M. Willander, *Mater. Lett.* **108**, 152 (2013).
2. M.D. Irwin, D.B. Buchholz, A.W. Hains, R.P.H. Chang, T.J. Marks, *Proceedings of the National Academy of Sciences*, art. No 0711990105, **105** (2008).
3. J. Kim, J.-H. Yun, Y.C. Park, W.A. Anderson, *Mater. Lett.* **75**, 99 (2012).
4. M.-J. Park, J.-Y. Jung, S.-M. Shin, J.-W. Song, Y.-H. Nam, D.-H. Kim, *Thin Solid Films* **599**, 54 (2016).
5. K.C. Wang, P.S. Shen, M.H. Li, S. Chen, M.W. Lin, P. Chen, *ACS Appl. Mater. Interfaces* **6**(15), 11851 (2014).
6. J.H. Yun, J. Kim, Y.C. Park, S.J. Moon, W.A. Anderson, *Thin Solid Films* **547**, 17 (2013).
7. S. Ahn, A.H. Tuan, S. Kim, C. Park, C. Shin, Y.J. Lee, *Mater. Lett.* **132**, 06 (2014).
8. D. Zaouk, Y. Zaatar, R. Asmar, *Microelectron. J.* **37**,5 (2006).
9. A.A. Al-Ghamdi, W.E. Mahmoud, J. Yaghmour, F.M. Al-Marzouki, *J. Alloy. Compd.* **486**, 1 (2009).
10. B.D. Cullity, *Elements of X-ray Diffraction* (Addison-Wesley Publishing Co. Inc.: New York: 1976).
11. R. Charma, A.D. Acharya, S. Moghe, B. Shrivastava, M. Gangrade, V. Shripathi, V. Ganesan, *Mater. Sci. Semicond. Process.* **23**, 42 (2014).
12. R. Sharma, A.D. Acharya, S.B. Shrivastava, M. M. Patidarc, M. Gangrade, T. Shripathic, V. Ganesan, *Optik* **127**(1), 11 (2016).
13. P.M. Ponnusamy, S. Agilan, N. Muthukumarasamy, T.S. Senthil, G. Rajesh, M.R. Venkatraman, D. Velauthapillai, *Mater. Charact.* **114**, 166 (2016).
14. P.S. Patil, L.D. Kadam, *Appl. Surf. Sci.* **199**, 1 (2002).

peak intensity compared to other films. The band gap value of NiO films was found from 3.64 eV to 3.86 eV. The high transmittance (75.36 %), low reflectance under 0.20 %, widened band gap and good conductivity (0.0896 (Ω cm)<sup>-1</sup>) obtained for NiO thin films make them promising candidate for optoelectronic devices as well as window layer in solar cell applications.

## ACKNOWLEDGEMENTS

Authors wish to thank Mr. Brahim Gasmi for his assistance in XRD data acquisition from (LPCMA), University of Biskra, Algeria and Pr. Tibarmacine from the university of Biskra, Algeria.

Authors are grateful to the Editor-in-Chief of the Journal of Nano- and Electronic Physics Protsenko Ivan Yuhymovych for a critical reading of the manuscript and his valuable comments.

## Short Communication

### Effect of Annealing in Physical Properties of NiO Nanostructure Thin Film

M. Ghougali<sup>1,2,3</sup>, O. Belahssen<sup>1,2,\*</sup>, A. Chala<sup>1,2</sup>

<sup>1</sup> *Material Sciences Department, Faculty of Science, University of Biskra, Algeria*

<sup>2</sup> *Physic Laboratory of Thin Films and Applications (LPCMA), University of Biskra, Algeria*

<sup>3</sup> *Laboratory of exploitation and valorization the azalea energetics sources (LEVRES), Faculty of exact Science, University of El-Oued, Algeria*

(Received 19 March 2017; revised manuscript received 15 May 2017; published online 30 June 2017)

Nickel oxide was deposited on highly cleaned glass substrates using spray pneumatic technique. The effect of precursor molarity on structural, optical and electrical properties has been studied. The XRD lines of the deposited NiO were enhanced with increasing precursor molarity due to the improvement of the films crystallinity. It was shown that the average of the crystalline size of the deposited thin films was calculated using Debye-Scherrer formula and found 46.62 for as-deposited sample and 119.89 nm for the annealed one. The optical properties have been discussed in this work. The absorbance ( $A$ ), the transmittance ( $T$ ) and the reflectance ( $R$ ) were measured and calculated. Band gap energy is considered one of the most important optical parameter, therefore measured and found ranging ranging 3.64 for as-deposited sample and 2.98 eV for the annealed one. The NiO thin film reduces the light reflection for visible range light. The increase of the electrical conductivity to maximum value of  $0.09241 (\Omega \text{ cm})^{-1}$  can be explained by the increase in carrier concentration of the films. A good electrical conductivity of the NiO thin film is obtained due to the electrically low sheet resistance. NiO can be applied in different electronic and optoelectronic applications due to its high band gap, high transparency and good electrical conductivity.

**Keywords:** NiO thin films, XRD, Optical constants, Electrical conductivity.

DOI: [10.21272/jnep.9\(3\).03043](https://doi.org/10.21272/jnep.9(3).03043)

PACS numbers: 73.61. – r, 78.20. – e, 78.66. – w

## 1. INTRODUCTION

Nickel oxide (NiO) is the most investigated metal oxide and it has attracted considerable attention because of its low cost material, and also for its applications in several fields such as a catalyst, transparent conducting oxide, photodetectors, electrochromic, gas sensors, photovoltaic devices, electrochemical supercapacitors, heat reflectors, photo-electrochemical cell, solar cells and many opto- electronic devices [1–11]. NiO is an IV group and it can be used as a transparent p-type semi-conductor layers, it has a band gap energy ranging from 3.45 eV to 3.85 eV [12]. Band gap energy is significant to adjust the energy level state of NiO.

The reduction in particle size to nanometer scale results more interesting prosperities in compared with their bulk properties [13]. Therefore, there are several techniques have been used for synthesis and manipulation of nanostructures NiO such as the thermal evaporation, sputtering, pulse laser ablation, thermal decomposition, electrochemical deposition and spray methods etc. Among of these techniques, spray has some advantages such as high purity of raw materials and a homogeneous solution hence easy control over the composition of the deposited films.

In this work, a low cost spray pneumatic technique was used to prepare pure NiO nanoparticles thin films with  $0.15 \text{ mol L}^{-1}$  precursor molarity. The structural properties of the produced nickel oxide thin films have been examined. The absorption, transmittance and reflectance spectra of the produced thin films for the NiO are also measured in range between 300-900 nm.

Moreover, the optical band gap is determined as a function of the precursor concentrations.

## 2. EXPERIMENTAL DETAILS

### 2.1 Preparation of Samples

NiO thin films were prepared onto a highly cleaned glass substrates using sol-gel spray pneumatic technique. Nickel nitrate was dissolved in 50 ml of water as a solvent and chloride acid was used as a stabilizer for the all samples in this work. The produced mixture was stirred at  $60^\circ\text{C}$  for 2 h in order to obtain a clear and homogenous solution then the mixture was cooled down at room temperature and placed at dark environment for 48 h. The glass substrates were cleaned by detergent and by alcohol mixed with deionized water.

### 2.2 Deposition of Thin Films

The coating was dropped into glass substrates at  $480^\circ\text{C}$  that sprayed during 2 min by pneumatic nebulizer system which transforms the liquid to a stream formed with uniform and fine droplets, followed by the films dried on hot plate at  $120^\circ\text{C}$  for 10 min in order to evaporate the solvent.

### 2.3 Devices and Measurements

The X-ray diffraction (XRD) spectra of the NiO were measured to verify the structure. (XRD) was measured by using BRUKER-AXS-8D diffractometer with Cu K $\alpha$  radiation ( $\lambda = 1.5406 \text{ \AA}$ ) operated at 40 KV and 40 mA

\*[belahssenokba@gmail.com](mailto:belahssenokba@gmail.com)

in the scanning range of ( $2\theta$ ) between  $20^\circ$  and  $80^\circ$ . The spectral dependence of the NiO transmittance ( $T$ ) and the absorbance ( $A$ ), on the wavelength ranging 300-1100 nm are measured using an ultraviolet-visible spectrophotometer (Perkin-Elmer Lambda 25). The reflectance ( $R$ ) was calculated by the well-known equation as ( $T + R + A = 1$ ). Whereas the electrical conductivity of the films was measured in a coplanar structure of four golden stripes on the deposited film surface; the measurements were performed with Keithley model 2400 low voltage source meter instrument.

### 3. RESULTS AND DISCUSSIONS

#### 3.1 Structural Properties

Fig. 1 shows the spectra of the grown NiO nanoparticles with 2 XRD lines, showing the broadening of the peak which is a characteristic of the formation of nanoparticles. The X-ray diffraction was used in this work in order to understand the structure of the as-deposited and the annealed NiO thin.

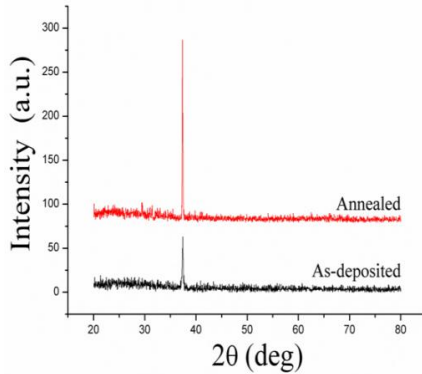


**Fig. 1** – XRD patterns of the as-deposited and annealed NiO thin films

The indexed peak (111) at  $2\theta = 37.1^\circ$  correspond to the cubic structure of NiO nanoparticles which are consistent with the JCPDS (No.47-1049). Fig. 1 shows that the diffraction intensity increased for annealed sample; it shows that the best crystalline quality of the film is achieved for this annealed sample. The crystalline size was calculated using the well-known Debye-Scherrer for(1)

$$D = \frac{0.9}{\beta \cos \theta}$$

where  $\lambda$  is the wavelength of the X-rays used (1.5406 Å),  $\beta$  is the full width at half maximum (FWHM) and  $\theta$  is the diffraction angle.

The increasing of the diffraction peaks may indicate to the resulted of the NiO in good crystallinity [15]. The crystalline size is found in the range of 46.62 nm for as-deposited sample and 119.89 nm for annealed one. The changing in the crystallites size leads to the changes in optical properties i.e. band gap energy increased with decreasing crystallites size as shown in Fig. 2.

#### 3.2 Optical Properties

Fig. 2 shows the optical absorption spectra of NiO

nanoparticles. The absorption spectra of as-deposited sample show that the absorption edge is slightly shifted towards shorter wavelength when compared to the annealed one. The absorption edge of annealed sample is shifted to longer wave-lengths. This shift predicts that there is a decrease in band gap value ( $E_g = 2.98$  eV), which is due to an enlargement in particle size ( $D = 119.89$  nm). The fundamental absorption, which corresponds to the electron transition from the valance band to the conduction band, can be used to determine the nature and value of the optical band gap. The optical absorption study was used to determine the optical band gap of the nanoparticles, which is the most familiar and simplest method.

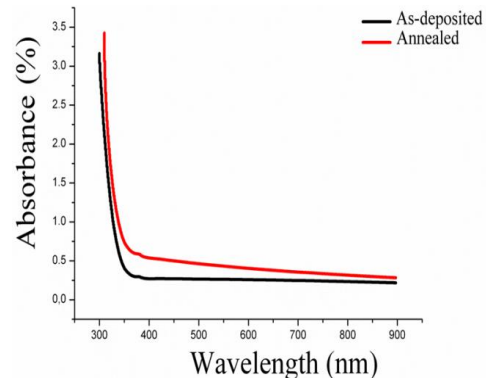


**Fig. 2** – Absorbance spectra of the as-deposited and annealed NiO thin films  $D = \frac{0.9}{\beta \cos \theta}$

The absorption coefficient ( $\alpha$ ) and the incident photon energy ( $h\nu$ ) are related by the expression [16]:

$$(\alpha h\nu) = C(h\nu - E_g)^n \quad (2)$$

where  $\alpha$  is the absorption coefficient,  $C$  is a constant,  $h\nu$  is the photon energy,  $\nu$  is the frequency of the incident radiation,  $h$  is the Planck's constant, exponent  $n$  is 0.5 for direct band allowed transition ( $h\nu = 1239/\lambda(\text{nm})(\text{eV})$ ) and  $E_g$  the band gap energy of the semiconductor.

As it was shown in Fig. 3a typical variation of  $(\alpha h\nu)^2$  as a function of photon energy ( $h\nu$ ) of NiO nanoparticles Eq. (2), used for deducing optical band gap  $E_g$ . The optical band gap values have been determined by extrapolating the linear portion of the curve to meet the energy axis ( $h\nu$ ) [17]. The band gap values were given in Table 1.

For a transmittance study (Fig. 4), the as-deposited NiO showed high transmittance, averaged in the wavelength ( $\lambda$ ) of 300-900 nm. Suppression of light reflection at a surface is an important factor to absorb more photons in semiconductor materials.

The reflectance profiles of NiO coated as deposited and annealed are shown in Fig. 5. The averaged reflectance values were significantly lower than 0.203 %. Moreover, NiO coating drives a substantially suppressed reflectance under 0.20 % in  $400 \text{ nm} < \lambda < 900 \text{ nm}$ . This notifies that the NiO coating is an efficient design scheme to intro-duce the incident light into substrate.

### 3.3 Electrical Properties

The electrical properties of the NiO films are summarized in Table 1. The as-deposited films have good conductivity  $0.04125 (\Omega \text{ cm})^{-1}$ , after annealing the conductivity increase at  $0.09241 (\Omega \text{ cm})^{-1}$ . The increase

**Table 1** – Structural, optical and electrical parameters of as-deposited and annealed NiO thin film

Sample	Crystallite size (nm)	Band gap energy (eV)	Conductivity $(\Omega \text{ cm})^{-1}$	reduces the carrier scattering from structural defects, leading to higher mobility.		
As-deposited	46.62	3.64	0.04125			
Annealed	119.89	2.98	0.09241			

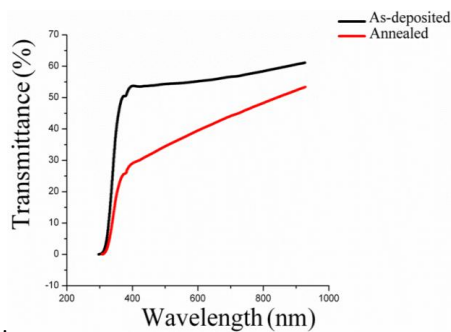


**Fig. 3** – Transmission spectra of the as-deposited and annealed NiO thin films

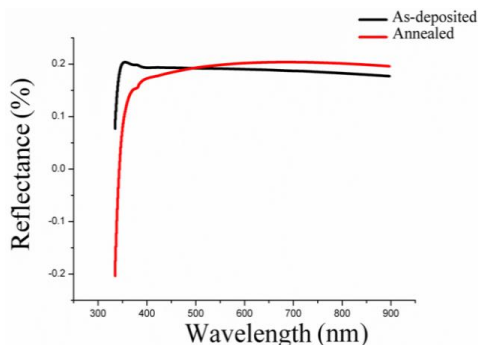


**Fig. 4** – Reflectance profiles of the as-deposited and annealed NiO thin films

### REFERENCES

- M.A. Abbasi, Z.H. Ibupoto, A. Khan, O. Nur, M. Willander, *Mater. Lett.* **108**, 149 (2013).
- M.D. Irwin, D.B. Buchholz, A.W. Hains, R.P.H. Chang, T.J. Marks, *Proceedings of the National Academy of Sciences ID No 0711990105*, **105** (2008).
- M. Ghogali, O. Belahssen, A. Chala, *J. Nano- Electron. Phys.* **8** No 4, 04059 (2016).
- J. Kim, J.-H. Yun, Y.C. Park, W.A. Anderson, *Mater. Lett.* **75**, 99 (2012).
- M.-J. Park, J.-Y. Jung, S.-M. Shin, J.-W. Song, Y.-H. Nam, D.-H. Kim, *Thin Solid Films* **599**, 54 (2016).
- K.C. Wang, P.S. Shen, M.H. Li, S. Chen, M.W. Lin, P. Chen, *ACS Appl. Mater. Interfaces* **6**, No.15, 11851 (2014).
- S. Benramache, O. Belahssen, H. Ben Temam, *J. Semicond.* **35**, No.7, 073001 (2014).
- J.H. Yun, J. Kim, Y.C. Park, S.J. Moon, W.A. Anderson, *Thin Solid Films* **547**, 17 (2013).
- A. Alshahrie, I.S. Yahia, A. Alghamdi, P.Z. Al Hassan, *Optik* **127**, 5105 (2016).
- S. Ahn, A.H. Tuan, S. Kim, C. Park, C. Shin, Y.J. Lee, *Mater. Lett.* **132**, 06 (2014).
- O. Belahssen, H. Ben Temam, S. Lakel, B. Benhaoua, S. Benramache, S. Gareh, *Optik* **126**, 1487 (2015).
- D. Zaouk, Y. Zaatar, R. Asmar, *Microelectron. J.* **37**, 1276 (2006).
- A.A. Al-Ghamdi, W.E. Mahmoud, J. Yaghmour, F.M. Al-Marzouki, *J. Alloy. Compd.* **486**, 9 (2009).
- B.D. Cullity, *Elements of X-ray Diffraction* (Addison-Wesley Publishing Co. Inc.: New York: 1976).
- R. Charma, A.D. Acharya, S. Moghe, B. Shrivastava, M. Gangrade, V. Shripathi, V. Ganesan, *Mater. Sci. Semicond. Process.* **23**, 42 (2014).
- R. Sharma, A.D. Acharya, S.B. Shrivastava, M.M. Patidarc, M. Gangradec, T. Shripathic, V. Ganesan, *Optik* **127**, 4661 (2016).
- P.M. Ponnusamy, S. Agilan, N. Muthukumarasamy, T.S. Senthil, G. Rajesh, M.R. Venkatraman, D. Velauthapillai, *Mater. Character.* **114**, 166 (2016).
- P.S. Patil, L.D. Kadam, *Appl. Surf. Sci.* **199**, 211 (2002).

of the electrical conductivity can be explained by the increase in the carrier concentration. Patil et. al. [18] have reported that the increase of the electrical conductivity is due to the increase in activation energy. This was explained by the crystal structure of the film which is increased, leading to a reduced concentration of structural defects such as dislocations and grain boundaries. Thus, the decrease of the concentration of crystal defects leads in the increase of free carrier concentration. The improvement of crystal quality

reduces the carrier scattering from structural defects, leading to higher mobility.

### 4. CONCLUSION

The spray pneumatic technique has been successfully employed to deposit NiO thin films with  $0.15 \text{ mol} \cdot \text{L}^{-1}$  concentration precursor on glass substrates. The films showed cubic crystal structure with preferential orientation according to the direction (111). It has found that the crystallite size increase from 46.62 nm for the as-deposited sample to 119.89 nm for the annealed one. We have observed an improvement in the films crystallinity for the annealed sample where the peak at position  $37.1^\circ$  corresponding to the (111) plans is very sharp, the film obtained for the annealed sample has higher and sharper diffraction peak indicating an improvement in peak intensity compared to the as-deposited film. The band gap value of NiO films decreased from 3.64 eV for the as-deposited sample to 2.98 eV for the annealed one. The high transmittance, low reflectance under 0.20 %, widened band gap and good conductivity obtained for NiO thin films make them promising candidate for optoelectronic devices as well as window layer in solar cell applications.

### ACKNOWLEDGEMENTS

Authors wish to thank Mr. Brahim Gasmı for his assistance in XRD data acquisition from (LPCMA), University of Biskra, Algeria and Pr. Tibarmacine from the university of Biskra, Algeria. Authors are grateful to the Editor-in-Chief of the Journal of Nano- and Electronic Physics Protsenko Ivan Yuhymovych for a critical reading of the manuscript and his valuable comments.

## Effect of Iron Doping on Physical Properties of NiO Thin Films

O. Belahssen<sup>1,2,\*</sup>, M. Ghougali<sup>1,2,3</sup>, A. Chala<sup>1,2</sup>

<sup>1</sup> Material Sciences Department, Faculty of Science, University of Biskra, Algeria

<sup>2</sup> Physic Laboratory of Thin Films and Applications (LPCMA), University of Biskra, Algeria

<sup>3</sup> Laboratory of exploitation and valorization the azalea energetics sources (LEVRES), Faculty of exact Science, University of El-Oued, Algeria

(Received 31 July 2017; published online 29 April 2018)

Nickel-iron oxide was deposited on highly cleaned glass substrates using spray pneumatic technique. The effect of iron percentage on structural, optical and electrical properties has been studied. The crystalline size of the deposited thin films was calculated using Debye-Scherrer formula and found in the range between 8.8 and 27.6 nm. The optical properties have been discussed in this work. The absorbance ( $A$ ), the transmittance ( $T$ ) and the reflectance ( $R$ ) were measured and calculated. Band gap energy is considered one of the most important optical parameter, therefore measured and found ranging between 3.81 and 3.98 eV. The NiO:Fe thin film reduces the light reflection for visible range light. The increase of the electrical conductivity to maximum value of  $0.470 \cdot 10^{-4} (\Omega \text{ cm})^{-1}$  for 6 % Fe can be explained by the increase in carrier concentration of the films. A good electrical conductivity of the NiO:Fe thin film is obtained due to the electrically low sheet resistance. NiO:Fe can be applied in different electronic and optoelectronic applications due to its high band gap, high transparency and good electrical conductivity.

**Keywords:** NiO thin films, XRD, Optical constants, Electrical conductivity.

DOI: [10.21272/jnep.10\(2\).02039](https://doi.org/10.21272/jnep.10(2).02039)

PACS numbers: 73.61.Jc, 78.66.Bz

### 1. INTRODUCTION

Nickel oxide (NiO) is the most investigated metal oxide and it has attracted considerable attention because of its low cost material, and also for its applications in several fields such as a catalyst, transparent conducting oxide, photodetectors, electrochromic, gas sensors, photovoltaic devices, electrochemical supercapacitors, heat reflectors, photo-electrochemical cell, solar cells and many opto- electronic devices [1-9]. NiO is an IV group and it can be used as a transparent p-type semiconductor layers, it has a band gap energy ranging from 3.45 eV to 3.85 eV [10]. Band gap energy is significant to adjust the energy level state of NiO.

Several techniques have been used for synthesis and manipulation of nanostructures NiO:Fe such as the thermal evaporation, sputtering, pulse laser ablation, thermal decomposition, electrochemical deposition and sol-gel methods etc. Among of these techniques, sol-gel has some advantages such as high purity of raw materials and a homogeneous solution hence easy control over

In this work, a low cost spray pneumatic technique was used to prepare pure NiO:Fe nanoparticles thin films with various iron percentages. The structural properties of the produced nickel oxide doped iron thin films have been examined. The absorption, transmittance and reflectance spectra of the produced thin films for the NiO:Fe are also measured in range between 300-1100 nm. Moreover, the optical band gap is determined as a function of the iron percentages.

### 2. EXPERIMENTAL DETAILS

#### 2.1 Preparation of Samples

NiO:Fe thin films were prepared onto a highly cleaned glass substrates using spay pneumatic tech-

nique. Nickel nitrate was dissolved in 50 ml of water as a solvent, iron nitrate was dissolved in 50 ml of water too and chloride acid was used as a stabilizer for the all samples in this work. The precursor molarity and iron nitrate concentration are  $0.20 \text{ mol L}^{-1}$ . The produced mixture was stirred at  $60^\circ \text{C}$  for 2 h in order to obtain a clear and homogenous solution then the mixture was cooled down at room temperature and placed at dark environment for 48 h. The glass substrates were cleaned by detergent and by alcohol mixed with deionized water.

#### 2.2 Deposition of Thin Films

The coating was dropped into glass substrates at  $480^\circ \text{C}$  that sprayed during 2 min by pneumatic nebulizer system which transforms the liquid to a stream formed with uniform and fine droplets.

#### 2.3 Devices and Measurements

The X-ray diffraction (XRD) spectra of the NiO:Fe were measured to verify the structure. X-ray diffraction (XRD) was measured by using BRUKER-AXS-8D diffractometer with Cu K $\alpha$  radiation ( $\lambda = 1, 5406 \text{ \AA}$ ) operated at 40 kV and 40 mA in the scanning range of ( $2\theta$ ) between  $20^\circ$  and  $80^\circ$ . The spectral dependence of the NiO:Fe transmittance ( $T$ ) and the absorbance ( $A$ ), on the wavelength ranging 300-1100 nm are measured using an ultraviolet-visible spectrophotometer (Perkin-Elmer Lambda 25). The reflectance ( $R$ ) was calculated by the well-known equation as ( $T + R + A = 1$ ). Whereas the electrical conductivity of the films was measured in a coplanar structure of four golden stripes on the deposited film surface; the measurements were performed with Keithley model 2400 low voltage source meter instrument.

\* [belahssenokba@gmail.com](mailto:belahssenokba@gmail.com)

### 3. RESULTS AND DISCUSSIONS

#### 3.1 Structural Properties

The X-ray diffraction was used in this work in order to understand the structure of the deposited NiO:Fe thin films with different iron percentages. XRD patterns of all the deposited samples of Nickel-Iron Oxide thin films are shown in figure 1. From the figure, it can be noticed that all the patterns exhibit diffraction peaks around  $2\theta \sim 37^\circ$ , referred to (111) favorite direction which is in agreement with the Joint Committee of Powder Diffraction Standards (JCPDS) card number 47-1049. The position of the peaks leads to the conclusion that the films are, in nature, with a cubic crystalline structure, which is in agreement with other reports [11, 12].

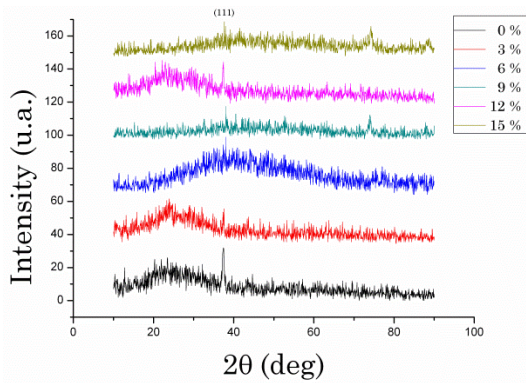


Fig. 1 – XRD patterns of the deposited NiO:Fe thin films on glass substrate at different iron percentages

The lattice constant  $a$  of Fe doped NiO thin films, is calculated using equation (1):

$$d_{(hkl)} = \frac{a}{\sqrt{(h^2 + k^2 + l^2)}}, \quad (1)$$

where  $(h, k, l)$  is the Miller indices of the planes and  $d_{hkl}$  is the interplanar spacing.

It can be observed that no peaks correspond to the Fe doping exist in the XRD patterns. In fact, doping with low concentration impurities does not result in the appearance of new XRD peaks, but instead leads to a shift in the lattice parameters of the host material. This shift may arise from the strain induced when the dopant is incorporated into the crystal lattice [13]. The strain  $\varepsilon$  values in the films were estimated from the observed shift, in the diffraction peak between their positions in the XRD spectra via the formula (2):

$$\varepsilon = \frac{a - a_0}{a_0} \cdot 100 \quad (2)$$

where  $\varepsilon$  is the mean strain in NiO:Fe thin films (Table 1),  $a$  is the lattice constant of NiO:Fe thin films and  $a_0$  the lattice constant of bulk (standard  $a_0 = 0, 4177$  nm).

The crystalline size was calculated using Debye-Scherrer formula [14]:

$$D = \frac{0.9\lambda}{\beta \cos \theta} \quad (3)$$

where  $\beta$  is the full width at half maximum (FWHM) and  $\theta$  is the diffraction angle.

The crystallite size of the NiO:Fe thin films were calculated using the well-known Debye-Scherrer's formula Eq. (3), the average of the NiO:Fe thin films ranging between 8.8 and 27.6 nm. The changing in the crystallites size leads to the changes in optical properties.

Fig. 2 shows the variation of the crystallite size and mean strain as a function of percentage of Fe. The crystallite size increases when the stain decreases and inversely.

The changing in the crystallites size leads to the changes in optical properties i.e. band gap energy increases with decreasing crystallites size as shown in Fig. 3.

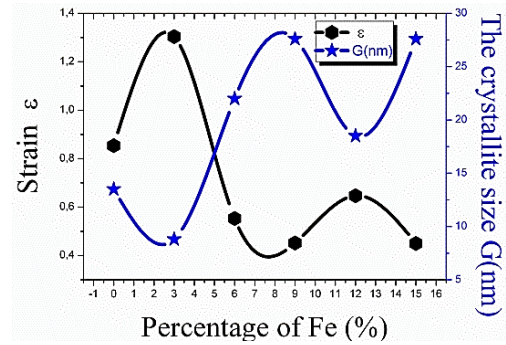


Fig. 2 – The variation of crystallite size and mean strain of Fe doped NiO thin films as a function of the percentage of Fe

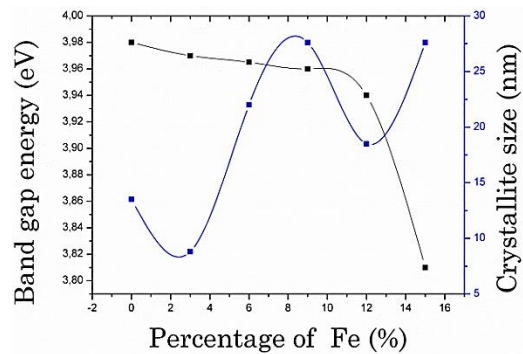


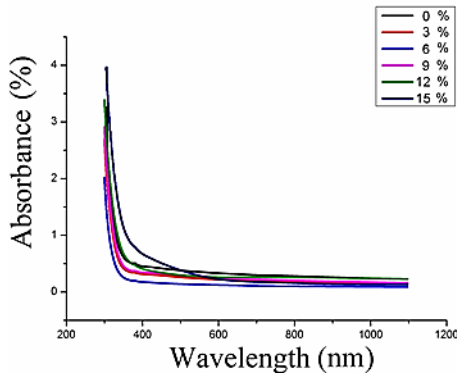
Fig. 3 – The variation of crystallite size and band gap energy of NiO:Fe thin films as a function of the percentage of Fe

#### 3.2 Optical Properties

Fig. 4 shows the optical absorption spectra of NiO:Fe nanoparticles. The absorption spectra of 6 % Fe show that the absorption edge is slightly shifted towards shorter wavelength when compared to other absorption spectra. The absorption edge of a degenerate semiconductor is shifted to shorter wavelengths with increasing carrier concentration. This shift predicts that there is an increase in band gap value ( $E_g = 3.965$  eV). The fundamental absorption, which corresponds to the electron transition from the valance band to the conduction band, can be used to determine the nature and value of the optical band gap. The optical absorption study was used to determine the optical band gap of the nanoparticles, which is the most familiar and simplest method.

**Table 1** – Structural, optical and electrical parameters of NiO:Fe thin film at different iron percentages

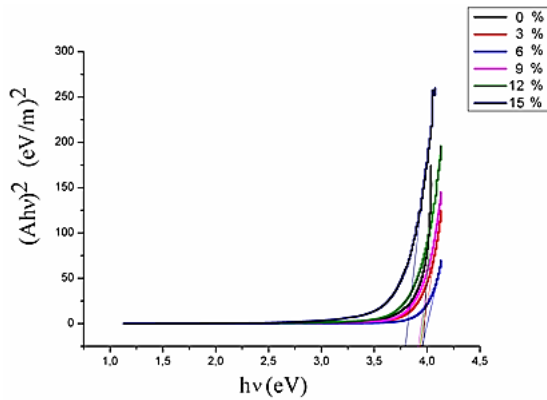
Percentage Fe (%)	Crystallite size (nm)	Strain $\epsilon$ (%)	Band gap energy (eV)	Conductivity $10^{-4} (\Omega \text{ cm})^{-1}$
0	13.5	0.854	3.980	0.366
3	8.8	1.304	3.970	0.295
6	22.0	0.553	3.965	0.470
9	27.6	0.452	3.960	0.303
12	18.5	0.647	3.940	0.283
15	27.6	0.450	3.810	0.279

**Fig. 4** – Absorbance spectra of NiO samples for different percentage of Fe

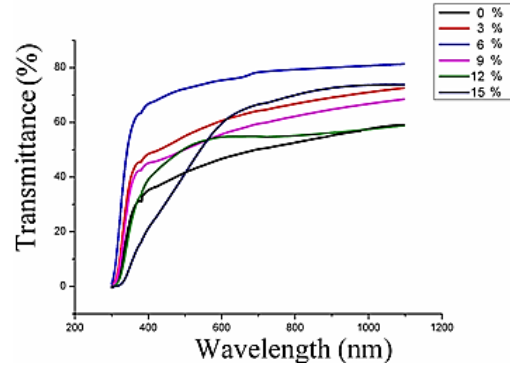
The absorption coefficient ( $\alpha$ ) and the incident photon energy ( $h\nu$ ) are related by the expression 2 [12]:

$$(\alpha h\nu) = C(h\nu - E_g)^n \quad (2)$$

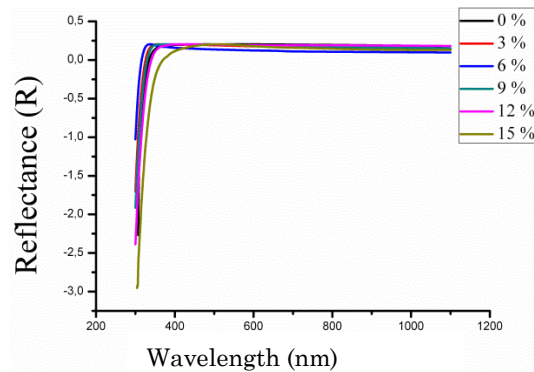
where  $\alpha$  is the absorption coefficient,  $C$  is a constant,  $h\nu$  is the photon energy,  $\nu$  is the frequency of the incident radiation,  $h$  is the Planck's constant, exponent  $n$  is 0.5 for direct band allowed transition ( $h\nu = 1239/\lambda(\text{nm})$  (eV)) and  $E_g$  the band gap energy of the semiconductor.

**Fig. 5** – Plot of  $(\alpha h\nu)^2$  versus incident photon energy ( $h\nu$ ) of NiO:Fe nanoparticles for different percentage of Fe

As it was shown in (Fig. 5) a typical variation of  $(\alpha h\nu)^2$  as a function of photon energy ( $h\nu$ ) of NiO:Fe nanoparticles Eq. (2), used for deducing optical band gap  $E_g$ . The optical band gap values have been determined by extrapolating the linear portion of the curve to meet the energy axis ( $h\nu$ ) [15]. The band gap values were given in Table 1.

**Fig. 6** – Transmission spectra of NiO:Fe samples for different percentage of Fe

For a transmittance study (Fig. 6), the NiO:Fe layer showed very high transmittance of 80 % for 6 % iron concentration, averaged in the wavelength ( $\lambda$ ) of 300-1100 nm. Suppression of light reflection at a surface is an important factor to absorb more photons in semiconductor materials. We obtained the reflectance profiles of NiO:Fe coated (Fig. 7). The averaged reflectance values (300-1100 nm) were significantly lower than 20 %. Moreover, NiO:Fe coating drives a substantially suppressed reflectance under 20 % in  $500 \text{ nm} < \lambda < 1100 \text{ nm}$ . This notifies that the NiO:Fe coating is an efficient design scheme to introduce the incident light into substrate.

**Fig. 7** – Reflectance profiles of NiO:Fe thin film for different percentage of Fe

### 3.3 Electrical Properties

The electrical properties of the NiO:Fe films are summarized in Table I. Fig. 8 shows the variation of the electrical conductivity  $\sigma$  of NiO:Fe thin films as a function as percentage of Fe. As can be seen, deposited films have good conductivity. The maximum recorded value was  $0.470 \cdot 10^{-4} (\Omega \text{ cm})^{-1}$  for the NiO:Fe thin film depos-

ited using 6 % iron concentration. The increase of the electrical conductivity can be explained by the increase in the carrier concentration. Patil et al. [16] have reported that the increase of the electrical conductivity is due to the increase in activation energy with increasing film thickness. This was explained by difference in the experimental conditions of spraying solution, spray rate and cooling of the substrates during decomposition. However, with  $0.20 \text{ mol L}^{-1}$  precursor molarity, the crystal structure of the film is significantly improved and the grain size is increased, leading to a reduced concentration of structural defects such as dislocations and grain boundaries. Thus, the decrease of the concentration of crystal defects leads in the increase of free carrier concentration. The improvement of crystal quality reduces the carrier scattering from structural defects, leading to higher mobility.

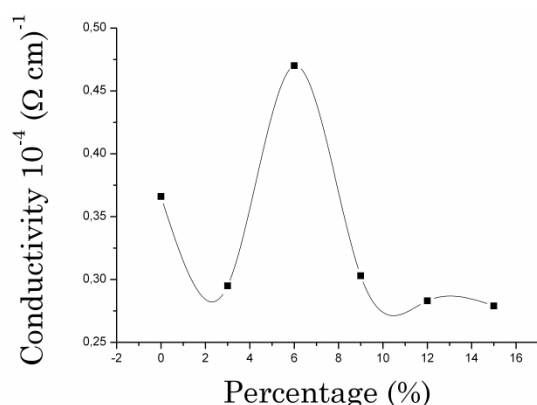


**Fig. 8** – Variation of the electrical conductivity of NiO:Fe thin films as a function of the percentage of Fe

## REFERENCES

- M.A. Abbasi, Z.H. Ibupoto, A. Khan, O. Nur, M. Willander, *Mater. Lett.* **108**, 152 (2013).
- M.D. Irwin, D.B. Buchholz, A.W. Hains, R.P.H. Chang, T.J. Marks, *Proc. National Academy Sci.* **105**, art. No 0711990105 (2008).
- M. Ghougali, O. Belahssen, A. Chala, *J. Nano- Electron. Phys.* **8** No 4, 04059 (2016).
- J. Kim, J.-H. Yun, Y.C. Park, W.A. Anderson, *Mater. Lett.* **75**, 99 (2012).
- M.-J. Park, J.-Y. Jung, S.-M. Shin, J.-W. Song, Y.-H. Nam, D.-H. Kim, *Thin Solid Films* **599**, 54 (2016).
- K.C. Wang, P.S. Shen, M.H. Li, S. Chen, M.W. Lin, P. Chen, *ACS Appl. Mater. Interf.* **6**, 11851 (2014).
- J.H. Yun, J. Kim, Y.C. Park, S.J. Moon, W.A. Anderson, *Thin Solid Films* **547**, 17 (2013).
- S. Ahn, A.H. Tuan, S. Kim, C. Park, C. Shin, Y.J. Lee, *Mater. Lett.* **132**, 332 (2014).
- M. Ghougali, O. Belahssen, A. Chala, *J. Nano- Electron. Phys.* **9** No 3, 03043 (2017).
- D. Zaouk, Y. Zaatar, R. Asmar, *Microelectron. J.* **37**, 11 (2006).
- A.R. Balu, V.S. Nagarethinam, N. Arunkumar, M. Suganya, *J. Electron. Dev.* **13**, 739 (2012).
- R. Sharma, A.D. Acharya, S.B. Shrivastava, M.M. Patidarc, M. Gangradec, T. Shripathic, V. Ganesan, *Optik* **127**, 4661 (2016).
- J. Daniel Bayan, Daniel R. Gametin, *Prog. Inorgan. Chem.* **47** (2005).
- B.D. Cullity, *Elements of X-ray Diffraction* (Addison-Wesley Publishing Co. Inc.: New York: 1976).
- P.M. Ponnusamy, S. Agilan, N. Muthukumarasamy, T.S. Senthil, G. Rajesh, M.R. Venkatraman, D. Velauthapillai, *Mater. Character.* **114**, 166 (2016).
- P.S. Patil, L.D. Kadam, *Appl. Surf. Sci.* **199**, 211 (2002).

## 4. CONCLUSION

The spray pneumatic technique has been successfully employed to deposit NiO:Fe thin films with different iron concentrations on glass substrates. All the films showed cubic crystal structure with preferential orientation according to the direction (111). The maximum crystallite size was found (27.06 nm). We have observed an improvement in the films crystallinity at  $0.10 \text{ mol L}^{-1}$  precursor molarity where the peak at position  $37.1^\circ$  corresponding to the (111) plans is very sharp, the film obtain at this concentration has higher and sharper diffraction peak indicating an improvement in peak intensity compared to other films. The band gap value of NiO:Fe films was found from 3.810 eV to 3.980 eV. The high transmittance (80 %), low reflectance under 20 %, widened band gap and good conductivity ( $0.470 \cdot 10^{-4} (\Omega \text{ cm})^{-1}$ ) obtained for NiO:Fe thin films make them promising candidate for optoelectronic devices as well as window layer in solar cell applications.

## ACKNOWLEDGEMENTS

Authors wish to thank Mr. Brahim Gasmi for his assistance in XRD data acquisition from (LPCMA), University of Biskra, Algeria and Pr. Tibarmacine from the university of Biskra, Algeria.

Authors are grateful to the Editor-in-Chief of the Journal of Nano- and Electronic Physics Protsenko Ivan Yuhymovych for a critical reading of the manuscript and his valuable comments.

# ABSTRACT

This work has been based on the chemical spray pyrolysis technique, it is a very attractive method, that for its ease and low cost on the one hand and the quality of the films prepared by it on the other hand, it is used to produce thin films for different applications including the most important (MOS)-based gas sensors, Such as (NiO)-based gas sensors. At first, a comprehensive study is presented on the effect of deposition parameters on the structural, optical and electrical properties of undoped and Co and Cu-doped (NiO) thin films; the finest samples obtained are then used in the sensor to study their sensing performance for some Volatile organic gases such as ethanol, acetone and methanol. In the following we summarize the most important results obtained:

- The XRD patterns showed that the structure of the undoped and doped NiO films is polycrystalline structure with the preferred direction (111) also showed that there was no significant shift in the direction of diffraction peaks after doping with cobalt or copper. The crystalline size ( $D$ ) is increased by thermal annealing and decreases by increasing the doping in the (NiO) samples. From the transmittance spectra, for all samples it was observed that the optical transparency values were moderate to relatively weak, it decrease by thermal annealing, by increasing the molar concentration of the precursor solution, or by increasing the percentage of doping with cobalt or copper. Cobalt or copper doping was also found to be decreasing the band gap energy for the above mentioned reasons, and its values ranged from 3.86 to 3.64 eV for undoped NiO films. For doped films, it ranged between 3.61 and 3.48 eV to cobalt doped films and between 3.60 and 3.43 eV to copper doped films. It was observed that the electrical conductivity of all samples is good and it is the P-type and it has been shown to increase by thermal annealing or by increasing the proportion of doping with cobalt or copper in general, and its value exceeded ( $0.29 \Omega^{-1} \cdot \text{cm}^{-1}$ ) when doped By 12 at.% of Copper.
- Five samples were selected from the prepared samples to study their sensing performance towards ethanol, acetone and methanol vapors, where all films had high ohmic resistance. Optimum operating temperatures, sensitivity, selectivity and detection limits were determined to the gas-based sensor.

**Keywords:** Spray Pyrolysis Technique (SPT); NiO Thin Films; Metal Oxide Semiconductors (MOS); Gas Sensor; Sensing Mechanism in (MOS).